Title

Digital autoradiography and small-scale dosimetry techniques for alpha-particle radiopharmaceutical therapy

Author

Peter, Robin

Publication Date

2024

Peer reviewed|Thesis/dissertation

Digital Autoradiography and Small-Scale Dosimetry Techniques for Alpha-Particle Radiopharmaceutical Therapy

By

Robin Peter

A dissertation submitted in partial satisfaction of the

requirements for the degree of

Doctor of Philosophy

in

Engineering — Nuclear Engineering

in the

Graduate Division

of the

University of California, Berkeley

Committee in charge:

Professor Youngho Seo, Co-Chair
Professor Kai Vetter, Co-Chair
Professor Steven Conolly

Fall 2024

Digital Autoradiography and Small-Scale Dosimetry Techniques for Alpha-Particle Radiopharmaceutical Therapy

Abstract

Digital Autoradiography and Small-Scale Dosimetry Techniques for Alpha-Particle Radiopharmaceutical Therapy

by

Robin Peter

Doctor of Philosophy in Engineering — Nuclear Engineering

University of California, Berkeley

Professor Youngho Seo, Co-Chair

Professor Kai Vetter, Co-Chair

Alpha-particle radiopharmaceutical therapy (αRPT) is a cancer treatment modality that aims to minimize toxicity to normal tissues by guiding cytotoxic alpha-emitting radionuclides to cancer cells with biomolecular targeting. The short range of the alpha-particle theoretically allows a perfectly targeted agent to spare healthy tissue, but it can also result in heterogeneous energy deposition in tumors and organs. Data explaining the effect of dose heterogeneity on treatment efficacy and toxicity are still lacking. The ability to predict treatment outcomes and efficiently develop αRPT agents requires clarity in the dose-effect relationship at the microscopic scale and tools to facilitate such investigations.

This dissertation describes the implementation of small-scale dosimetry techniques using an iQID digital autoradiography system and provides three examples of their use in preclinical studies of αRPT agents. Device characterization, quantitative corrections, image processing, Monte Carlo kernel simulations, and histological correlation are discussed. Preclinical imaging throughput is increased through slice minimization algorithms with quantifiable uncertainty costs. These approximations also enable a sampling method for 3D small-scale dosimetry that presents comprehensive views of the absorbed dose distributions within whole organs and tumors. The developed methods are demonstrated in the assessment of ^{211}At in canine lymph nodes, ^{225}Ac in murine kidneys and tumor xenografts, and ^{225}Ac in murine liver micrometastases. These data, which show nonuniform patterns of absorbed dose in tissues and tumors, emphasize that the development of αRPT agents and optimization of tumor and organ doses require consideration of small-scale effects. Finally, progress towards isotope separation in iQID autoradiography using charged particle discrimination or coincident gamma-ray detection is reported. The role of this work is described in the context of growing interest in dosimetry-based, patient-tailored radiopharmaceutical prescriptions.

To my dad, who emailed my first paper to his oncologist in excitement, and to my mom, who fortunately does not have an oncologist and shared it at the farmers' market instead.

Contents

List of Figures

List of Tables

Acknowledgments

I am sincerely grateful to all those individuals who made this work possible and helped me grow as a person and professional.

To my advisors, Profs. Kai Vetter and Youngho Seo, I could not ask for more supportive academic "parents." Thank you for all your conversations, ideas, feedback, 1:00 AM reassurance emails, and for always wanting the best for me. I would also like to express gratitude to committee member Prof. Steve Conolly for his insight and support.

To Brian Miller and Javier Caravaca Rodriguez, I sincerely appreciate your mentorship. Thank you for fielding my many questions to catch me up to speed, for your willingness to troubleshoot technical details with me, and for general perspectives and life advice along the way.

To the other graduate students, postdoctoral fellows, and research scientists in the Berkeley radiation detection, UCSF physics research, and UCSF molecular imaging laboratories, thank you for the ideas, encouragement, thought-provoking discussions, and assistance with experiments. I am fortunate to count many of you among my good friends.

Preface

Structure of the dissertation

Chapter 1 provides an introduction to alpha-particle radiopharmaceutical therapy (αRPT) and related concepts. Chapter 2 is part review, articulating macrodosimetry workflows and gamma spectroscopy approaches, and part report, detailing the specific methods used for gamma-ray biodistribution studies in this dissertation. We return to literature review briefly in Chapter 3 to contextualize the need for small-scale dosimetry and digital autoradiography. Chapter 4 compiles the methods, tools, and technical details used for αRPT dosimetry with an iQID digital autoradiography system. These methods are applied to preclinical studies in Chapters 5–7. Chapter 5 discusses a study of ^{211}At-radioimmunotherapy conditioning in canines; Chapter 6 proposes a 3D mode of digital autoradiography for the study of whole tumors and kidneys in mice treated with ^{225}Ac agents; and Chapter 7 highlights the utility of 3D digital autoradiography for assessing tumor micrometastases within normal liver tissue. Chapter 8 reports progress towards isotope separation in digital autoradiographs using simultaneous gamma- or beta-particle detection. We summarize the work and discuss future outlook in Chapter 9.

Box 0: Asides. Side calculations and remarks not directly relevant to the main line of discussion are included in box inserts like this one.

List of original papers

All text in this dissertation was originally written by me for inclusion here or in one of the three manuscripts below. Source material is indicated in each relevant chapter. Background information and discussion sections from the three articles have been disseminated throughout.

Paper 1: Peter, R. *et al.* Small-Scale (Sub-Organ and Cellular Level) Alpha-Particle Dosimetry Methods Using an iQID Digital Autoradiography Imaging System. *Sci Rep* **12,** 17934 (2022)

Paper 2: Peter, R., Bidkar, A. P., *et al.* 3D Small-Scale Dosimetry and Tumor Control of ^{225}Ac Radiopharmaceuticals for Prostate Cancer. *Sci Rep* **14,** 19938 (2024)

Paper 3: Bidkar, A. P., Peter, R., *et al.* Effective Treatment of Prostate Cancer Micrometastases Using CD46-targeted ^{225}Ac Therapy. *In revisions* (2024)

Data collection

This work would not be possible without the expertise of several talented bioengineers and radiochemists who have done the heavy lifting in animal and sample handling. Credit for specific aspects of data collection go to the following parties. All other experiments and content were carried out and produced by me.

- Chapter 2: ^{225}Ac and ^{134}Ce samples were prepared by KNB. ^{227}Th and ^{223}Ra samples were prepared by RAS. Hidex measurements were conducted by KNB and RAS. 3D-printed sample holders were designed by SD and BH. HPGe and CZT measurements were done by me.
- Chapters 4–5: Lymph node autoradiography data from Paper 1 was previously collected by the team at Fred Hutchinson Cancer Research Center in [4] and analyzed by me. ^{225}Ac calibration swatches were pipetted by KNB and imaged and analyzed by me. H&E images and raw ^{225}Ac autoradiography tissue data were prepared and acquired by APB.
- Chapter 6: H&E images and raw ^{225}Ac autoradiography tissue data were prepared and acquired by APB with minor assistance from me. Biodistribution data was collected by APB and KNB.
- Chapter 7: H&E images and raw ^{225}Ac autoradiography tissue data were prepared and acquired by APB.
- Chapter 8: I conducted all experiments.

Abbreviations and affiliations:[1] KNB: Kondapa Naidu Bobba, UCSF Postdoctoral Researcher. RAS: Ramya Ambur Sankaranarayanan, UCSF Postdoctoral Fellow. SD: Shixian Du, UCSF MS student in Biomedical Imaging. BH: Benjamin Huang, UC Berkeley Assistant Research Specialist. APB: Anil P. Bidkar, UCSF Postdoctoral Fellow.

[1] At time of data collection.

Chapter 1

Alpha-particle radiopharmaceutical therapy

This chapter reviews key motivations, concepts, and challenges related to alpha-particle radiopharmaceutical therapy (αRPT). The state of the field and the role of αRPT in cancer treatment are described at a high level (Sec. 1.1), then fundamental alpha- (α-) particle characteristics such as range and energy deposition are explained in the context of an anti-cancer therapeutic agent (Sec. 1.2). Section 1.3 discusses the risk of recoil progeny redistribution by isotope. Current practices and deficits in RPT treatment planning, and specific challenges for αRPT in image-based dosimetry, are considered in Sec. 1.4. Finally, Sec. 1.5 summarizes the role of preclinical dosimetry in facilitating the clinical translation of αRPT.

1.1 A need for non-toxic systemic cancer treatments

Cancer treatment is advancing. Between 1975 and 2016, the five-year survival rate for cancer patients across all disease sites rose steadily from 50% to 72% (Fig. 1.1) [6]. Still, cancer caused nearly one-fifth of all deaths in the United States in 2022. For people under 65 years of age, it is the leading cause, surpassing heart disease, accidents, stroke, and other chronic diseases.

While advances in screening and treatment techniques continue to improve patient outcomes, there is a stark gap between what medicine can accomplish for early-detected lesions compared to metastatic ones. Among the five most common forms, cancer detected while still confined to a single primary site (localized) has a five-year survival rate of 77.5%. If the cancer has metastasized to other distant locations, the prognosis decreases to 17.8% [5]. Localized therapies, such as surgery and anatomically targeted external radiation (known as radiation therapy, external-beam radiation therapy, EBRT, or XRT), are inherently ill posed to handle a myriad of lesions.

Figure 1.2, from [7], shows the relative distributions of treatment types by stage for female breast cancer as an example. Disease with greater metastatic spread must generally be

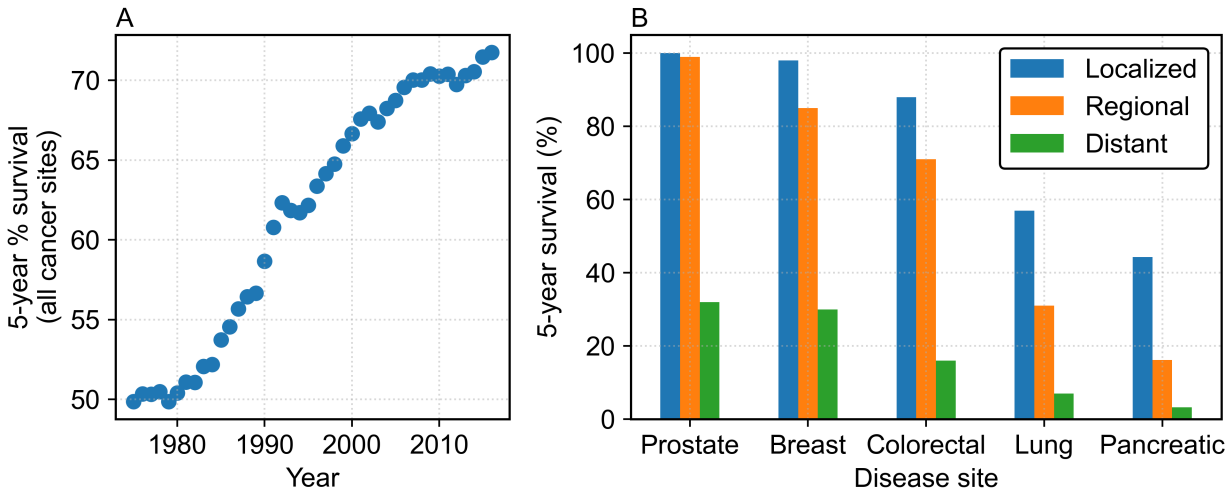

Figure 1.1: (A) Thirty-year trend of increasing cancer survival rates illustrates progress in screening and treatment. (B) Five-year survival prognosis for five of the most common forms of cancer by stage at diagnosis, showing gap between early- and late-detected lesions. Data from the U.S. Cancer Statistics Data Visualizations tool [5] and the SEER Database [6].

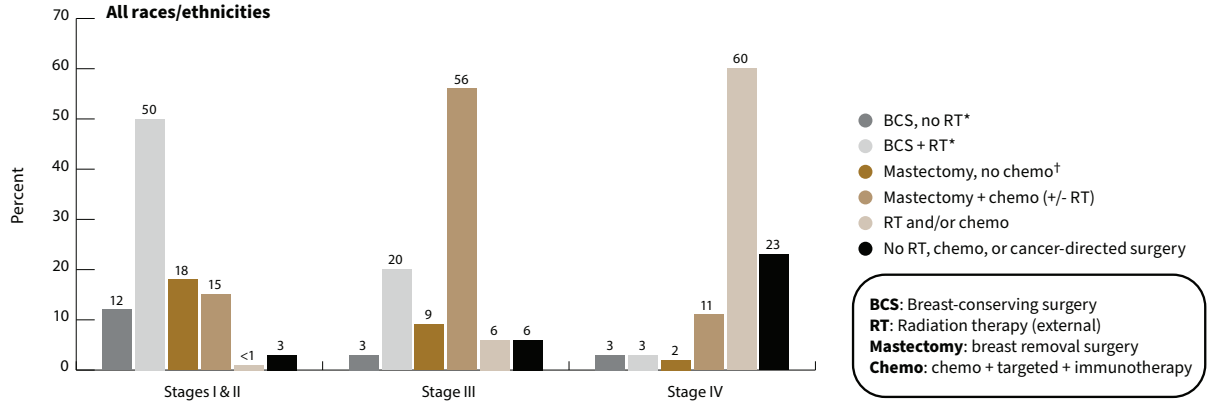

Figure 1.2: Female breast cancer treatment patterns by stage, 2018, from [7], with added legend. Localized treatments (BCS/mastectomy surgeries, as well as RT) are less suitable for disseminated disease than systemic treatments (chemotherapy, targeted therapies, and immunotherapy are grouped by the reference as "chemo"). Cancer stage I corresponds to localized disease, stages II-III may have regional spread, and stage IV is metastatic disease.

Box 1.1: RPT vs. TRT. Radiopharmaceutical therapies are also sometimes called targeted radionuclide therapy (TRT), especially in the context of targeted α-particle therapy (TAT). Some literature differentiates TRT from RPT in that RPT agents can be incorporated through purely physiologic mechanisms, whereas TRT utilizes an engineered targeting vehicle. $^{223}RaCl_2$, which localizes to bone because radium is a calcium analogue, is an example of a radiopharmaceutical that is not "targeted" under this definition. Some literature also distinguishes RPT from selective internal radiation therapy (SIRT), such as ^{90}Y microsphere embolization, where glass or resin spheres containing radioactivity are injected directly into a tumor-supplying artery and lodge in tumor capillaries [11, 12]. We do not differentiate between these three mechanisms and generally use RPT to encompass all.

treated with systemic modalities, mainly chemotherapy, but the five-year survival prognosis remains below one in three with modern medicine. Systemic drug treatment may fail if patients develop resistance or discontinue therapy due to side effects resulting from damage to healthy tissue [8–10]. Considerable research and clinical effort in recent decades has produced several new classes of therapy that aim to eradicate tumor cells with minimal effect on surrounding normal tissues, including targeted therapies and immunotherapy.

Radiopharmaceutical therapy (RPT, Box 1.1) is a type of targeted therapy that uses a biological or molecular targeting strategy to selectively deliver radioactive isotopes to tumor sites with, ideally, minimal localization in healthy tissue. For example, a specific antigen or protein receptor may be over-expressed on cancer cells relative to normal cells. An antibody or molecule that binds to that receptor can be chemically attached to a radioactive element, so that when the compound is injected into the bloodstream it preferentially localizes on lesions. Radioactive emissions from the nuclide deposit cytotoxic doses in nearby cells with efficacy on par with or greater than external-beam radiation and chemotherapy. The targeting strategy, radioisotope, and chelation technique binding the two can be optimized for each application, so there is an enormous permutation space of possible radiopharmaceuticals (RPs) currently being investigated. As a consequence, RPT research is highly multidisciplinary. A team of biologists, radiochemists, physicists, and oncologists is needed throughout the development pipeline to identify the targeting mechanism, produce and isolate the isotope, develop the chelation chemistry, quantify activity, conduct dosimetry, and assess the therapeutic efficacy and toxicity of the drug at preclinical and clinical stages.

Radiopharmaceutical therapy with beta- (β-) particle emitters (βRPT) has been in clinical use for over half a century with ^{131}I, a natural choice to treat thyroid disease due to its physiologic accumulation there. Wider adoption of βRPT compared to other RPT modalities has occurred partially due to historical familiarity and isotope availability, but also because of the tendency for popular βRPT isotopes to emit imageable photon signal that can be used for verification and dosimetry. Other common βRPT isotopes include ^{90}Y (hepatic malignancies), ^{153}Sm (palliative care for bone metastases), and ^{177}Lu, approved by the U.S. Food

Box 1.2: Auger electrons. Radioisotopes that emit Auger electrons after electron capture or internal conversion are also of interest for RPT, but few agents have been examined in clinical trials with none obtaining regulatory approval for patient care [22]. Most Auger electrons deposit relatively low energies (sub-keV) over extremely short ranges (500 nm), yielding relatively high LET (4–26 keV/µm) [23]. Auger electrons are also often released in dense cascades rather than isolated emissions, resulting in complex and highly cytotoxic damage to target structures [22]. Proponents suggest that Auger RPT efficacy may rival αRPT, with several advantages: 1) isotopes can be produced simply and cheaply in cyclotrons, 2) sub-keV recoil energy negates progeny redistribution toxicity; and 3) lower range provides even greater potential for targeting selectivity. However, like αRPT, the latter advantage may hinge on the targeting accuracy and require micro-scale dosimetry assessments for verification.

and Drug Administration (FDA) in 2018 for treatment of gastroenteropancreatic neuroendocrine tumors (GEP-NETs) and in 2022 for metastatic castration-resistant prostate cancer (mCRPC).

Alpha-particle radiopharmaceutical therapy (αRPT) has experienced burgeoning interest more recently, receiving its first FDA approval in 2013 for $^{223}RaCl_2$, which provides palliative treatment for bone metastases from metastatic castration-resistant prostate cancer. The Phase III ALSYMPCA clinical trial referenced in the decision demonstrated an overall survival extension of 3.6 months over placebo in patients recurrent after or ineligible for docetaxel, the only chemotherapy with any demonstrated survival benefit for mCRPC at the time [13–15]. A follow-up 2016 trial confirmed similar improvements, even in patients treated with modern hormone therapies [15, 16]. Today, there are nearly thirty commercially and academically sponsored clinical trials involving αRPT that are either recruiting or ongoing (Table 1.1, [17]).

Compared to βRPT, αRPT may have potential advantages in cytotoxic efficacy and targeting selectivity due to the short range and high linear energy transfer of the alpha- (α-) particle emission. Patients that have developed resistance to βRPT may be treatable with the more-cytotoxic αRPT [18–21]. However, these α-particle characteristics also give rise to a host of challenges not widely experienced in βRPT: extremely low treatment activities that produce low imaging signal and demand the development of new imaging techniques and systems for verification and dosimetry; recoiling progeny nuclei that can be toxic to non-targeted locations; and micro-scale dose heterogeneities, for which our existing dosimetry models are ill suited. This chapter briefly reviews how these potentials and challenges alike emerge from physical properties of the α-particle. The issue of micro-scale dose heterogeneity is a key topic of this dissertation and is discussed at length in Chapter 3 and onward.

Table 1.1: Active and recruiting clinical trials using αRPT, simplified from [17]. Center line separates commercially sponsored trials (above) from investigator-sponsored trials (below). Entries without site-specific disease indicate that the target is expressed on multiple types of cancer cells.

Trial	Isotope	Target	αRP	Cancer	Phase
NCT03276572	^{225}Ac	PSMA	^{225}Ac-J591	Prostate	I
NCT04506567	^{225}Ac	PSMA	^{225}Ac-J591	Prostate	I/II
NCT04576871	^{225}Ac	PSMA	^{225}Ac-J591	Prostate	I
NCT04886986	^{225}Ac	PSMA	^{225}Ac-J591	Prostate	I/II
NCT04946370	^{225}Ac	PSMA	^{225}Ac-J591	Prostate	I/II
NCT05567770	^{225}Ac	PSMA	^{225}Ac-J591	Prostate	I
NCT03746431	^{225}Ac	IGF-1R	^{225}Ac-FPI-1434	Metastatic	I/II
NCT05605522	^{225}Ac	NTSR1	^{225}Ac-FPI-2059	Solid	I
NCT05219500	^{225}Ac	PSMA	^{225}Ac-FPI-2265	Prostate	II
NCT04147819	^{227}Th	HER2	BAY2701439	Solid	I
NCT05720130	^{212}Pb	PSMA	^{212}Pb-ADVC001	Prostate	I/II
NCT04597411	^{225}Ac	PSMA	^{225}Ac-PSMA-617	Prostate	I
NCT04644770	^{225}Ac	hK2	^{225}Ac-DOTA-h11B6	Prostate	I
NCT03466216	^{212}Pb	SSTR2	^{212}Pb-DOTAMTATE	NET	I
NCT05153772	^{212}Pb	SSTR2	^{212}Pb-DOTAMTATE	NET	II
NCT05477576	^{225}Ac	SSTR2	RYZ101	GEP-NET	III
NCT05595460	^{225}Ac	SSTR2	RYZ101 + BSC	Lung	I
NCT05283330	^{212}Pb	GRPR1	^{212}Pb-DOTAM-GRPR1	Solid	I
NCT03441048	^{225}Ac	CD33	^{225}Ac-lintuzumab	Leukemia	I
NCT03867682	^{225}Ac	CD33	^{225}Ac-lintuzumab	Leukemia	I/II
NCT05275946	^{211}At	Thyroid	TAH-1005	Thyroid	I
N/A	^{211}At	NET	^{211}At-MABG	Adrenal	I
NCT04083183	^{211}At	CD45	^{211}At-BC8-B10	HCT transplant	I/II
NCT03670966	^{211}At	CD45	^{211}At-BC8-B10	HCT transplant	I/II
NCT04579523	^{211}At	CD38	^{211}At-OKT-B10	Multiple myeloma	I
NCT04466475	^{211}At	CD38	^{211}At-OKT-B10	Multiple myeloma	I
NCT05363111	^{225}Ac	CD38	^{225}Ac-DOTA-daratumuab	Multiple myeloma	I
NCT05204147	^{225}Ac	CEA	^{225}Ac-DOTA-M5A	Metastatic	I

Box 1.3: Production and availability. One of the main barriers to translation and further development of αRPT is limited and expensive production. For example, the primary source of ^{225}Ac is a fixed and highly restrictive quantity of ^{229}Th generators supplied by ^{233}U stockpiles amassed during nuclear weapons development in the mid-20th century. Accelerator production methods are being investigated but continue to face challenges with co-produced contaminants, infrastructure, and cost [24, 25]. Full review of production developments for αRPT is beyond the scope of this work but has been conducted by other authors [24, 26, 27].

1.2 Physical and biological concepts

1.2.1 Charged particle range in tissue

The α-particle ($^4He^{2+}$) and other heavy charged particles (defined by mass $m >> m_e$, the electron mass) primarily lose energy through Coulomb interactions with orbital electrons in matter.[1] If orbital electrons were table-tennis balls, the α-particle would be a bowling ball by mass comparison. It travels along a straight trajectory, relatively unperturbed by the continuous stream of minor excitation and ionization events along its path. The α-particle is thus characterized by its energy, which corresponds to a finite range representing the maximum penetration of the particle in that medium. For therapeutic α-particles of 5 – 9 MeV, the range in water-like tissue is approximately 35 – 100 µm, spanning only a few cell diameters [28].

The less massive electron is more easily perturbed along its trajectory and has higher velocity for the same energy, resulting in a longer and more convoluted path, typically spanning several millimeters in tissue [29]. Figure 1.3 [30] illustrates the range advantage of αRPT over βRPT for treatment of small lesions using a scanning micron electrograph to inspect cancerous micrometastases on the peritoneum of a mouse. Assuming a target location on the surface of a cancer cell, the α-particle range is better suited to the scope of the metastases and delivers less cross-dose to the surrounding tissue than the longer-range β-particle. Because of the range discrepancy, literature often describes αRPT as a modality with minimal toxicity and enhanced tissue sparing.

However, the short range is only advantageous for tissue sparing if the targeting mechanism delivers the radioisotope exclusively to tumor cell surfaces as intended. Nonspecific uptake, including redistribution of progeny (Sec. 1.3), deposits cytotoxic α-particle dose to healthy structures despite the short range. Even relatively low doses to normal tissues may be toxic if the short range results in dense regions of localized dose in critical sub-structures. Additionally, the range has historically been regarded as a disadvantage for the treatment of medium- to large-scale tumors, which may suffer from incomplete tumor penetration under

[1] Elastic collisions with nuclei in the medium occur but contribute negligibly to the energy loss. The nuclear stopping power for a 5 MeV electron in water represents 0.08% of the total [28].

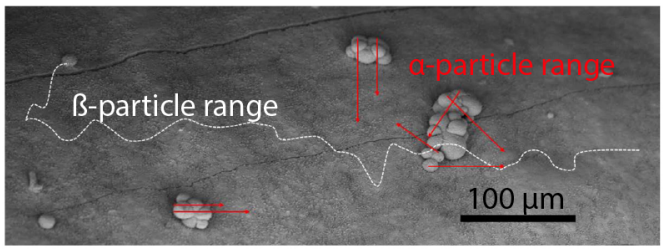

Figure 1.3: Scanning electron microscopy micrograph of micrometastases shows the potential advantage for αRPT over βRPT by minimizing cross-fire dose to healthy tissue, from [30], with added annotations. Used under the Creative Commons Attribution License (CC BY 4.0).

αRPT or require greater treatment activities to compensate. These micro-scale effects must be evaluated during drug discovery and preclinical testing if αRPT is to make a safe and efficient translation to clinical use.

1.2.2 Linear energy transfer

The rate of energy loss in a medium is quantified by the linear stopping power $S = -dE/dx$, which for our purposes is proportional to $1/E$ for an α-particle of energy E (Box 1.4). In medical physics settings, this quantity is more commonly discussed as the linear energy transfer (LET) L_Δ of a particle, defined as

$$L_\Delta = \frac{dE_\Delta}{dx}. \tag{1.1}$$

The LET differs from the stopping power only in that secondary electrons with kinetic energy greater than the threshold Δ are excluded from consideration [31].[2] The concept is designed to quantify the amount of energy deposited as high-density ionization events near the particle track itself, which are more likely to cause biological damage. Unrestricted LET, or just LET, has no cutoff Δ imposed, and is thus identical to S.

LET can also be defined to include only processes from collisional processes, rejecting contributions from radiative ones [32]. These *bremsstrahlung* emissions, produced when charged particles are deflected from their trajectory in nuclear interactions, are not guaranteed to deposit energy locally along the charged-particle track and may escape the medium entirely without effect. This distinction is not meaningful for α-particles, which travel in straight paths with negligible losses to nuclear interactions. For β-particles of therapeutic energies up to $\sim 2.3\,\text{MeV}$ (^{90}Y), the fraction of radiative losses S_r to collisional losses S_c in tissue is still minimal, approximately

$$\frac{S_r}{S_c} \simeq \frac{EZ}{700} \leq \frac{(2.3)(7.5)}{700} = 2\%. \tag{1.2}$$

In this equation [32], E is given in MeV and we have assumed the effective atomic number to be $Z = 7.5$ in tissue. The various formulations of LET and stopping power are thus functionally similar when discussing α-particles.

[2]The quantity dE_Δ is conventionally defined as an energy loss, such that LET and stopping power are both positive quantities.

Box 1.4: Bethe-Bloch and Bragg peak. The full Bethe-Bloch formula describing the stopping power of charged particles in matter is a function of particle velocity and charge, as well as the density and atomic number of the medium [33, 34]. For heavy charged particles, the inverse relation between S and E produces a characteristic track pattern known as the *Bragg peak*: the rate of energy loss increases as the particle slows, so the majority of energy is deposited at the end of the track. This phenomenon is of particular importance to ion-beam radiation therapies, including proton therapy, but has lesser impact in radiopharmaceuticals because the $1/r^2$ falloff of an isotropic emitter provides a stronger counter-effect (Sec. 4.6).

The increased mass, lower velocity, and high Coulombic interaction rate of α-particles—which produce their characteristic short range—also result in high LET ($\sim 100\,\mathrm{keV/\mu m}$), about 500 times greater than the LET of β-particles ($\sim 0.2\,\mathrm{keV/\mu m}$). In a purely physical sense, without yet considering biological effects, α-particles are orders of magnitude more effective than β-particles at depositing energy locally. Significantly lower quantities of radioactive material can be used to treat a region to a specific dose.

1.2.3 Absorbed dose and biological efficacy

The word *dose* in this dissertation refers to the radiation mean absorbed dose D:

$$D = \frac{1}{m}\int dE = \frac{\bar{E}}{m}, \tag{1.3}$$

or the quotient of the mean absorbed energy $\bar{E}$ evaluated in a region of mass m with units of Gy (J/kg). This term is distinct from the administered quantity of a drug, which is quantified in RPT by the administered or injected *activity*.

Under this definition, dose is an expected value within the region being considered and is fundamentally non-stochastic. The region may be defined as a whole tumor or organ, as in macrodosimetry, or in a single voxel, as in small-scale dosimetry (Ch. 3). It is also a purely physical quantity, independent of the biological effect or radiation type. In radiation-based therapies, dose is the key metric that links the intensity of administered treatment to treatment outcomes. However, the biological mechanism of cell death is related to the ionization density described above, such that α- and β-particles can deposit the same dose with different cytotoxicities.

Microscopic radiobiology remains an area of active research, but DNA damage is generally agreed to be the main source of cell death from radiation. Where β-particles and secondary electrons from photons largely ionize the surrounding water media, leading to DNA damage through indirect chemical reactions, densely ionizing α-particles can directly damage the DNA strand itself to produce double-strand breaks. These damaging events are

less susceptible to the oxygen concentration, repair mechanisms, and chemical radiosensitizers and radioprotectors—all complications of photon- and β-particle radiobiology [35]. The greater efficacy and direct DNA damage of α-particle radiation are major motivators for the development of αRPT, which has been demonstrated to overcome β-particle radioresistance in vitro and in patients [18–21, 36].

Three quantities in literature that have been used to describe the effect of particle type on biological effect are the quality factor Q, radiation weighting factor w_R, and relative biological effectiveness (RBE). All three were developed with radiation protection in mind, rather than therapy. The quality factor Q is an archaic quantity, selected by a committee of experts, that largely relates to the linear energy transfer. Its modern replacement is w_R, similarly defined by consensus recommendation. The product of the dimensionless w_R with the absorbed dose is termed the equivalent dose $H_T = w_R D$ in units of Sv. While the Sv shares the same base units as the Gy, it is differentiated to reflect the inclusion of a scalar factor. The Committee on Medical Internal Radiation Dose (MIRD) and International Commission on Radiation Units and Measurements (ICRU) periodically release material containing their latest recommendations for these quantities [31, 37]. The current recommended w_R values for photons, β-particles, and α-particles are 1, 1, and 20, respectively.

RBE is an experimentally determined value defined as the ratio of absorbed doses for two radiation types that achieve the same biological effect x:

$$\text{RBE} = \left.\frac{D_R}{D_T}\right|_x, \tag{1.4}$$

where R is a selected reference radiation with well-characterized effects, and T is the radiation type being tested.

Unfortunately, the historical evolution of these quantities has resulted in some confusion for their use in αRPT dosimetry. RBE and w_R are both used to quantify stochastic effects, such as cancer induction in healthy tissues, rather than the deterministic effects of therapeutic applications—tumor kill, organ toxicity, etc. [37]. A "deterministic RBE" has been proposed (but not distinguished with an alternative name), with a value of 5 recommended by committee review for α-particles, but human studies of RBE with αRPT are lacking. A growing number of animal models place the deterministic α-particle RBE in the range of 1–10 against a variety of reference radiations (^{90}Y, ^{60}Co, ^{177}Lu, x-rays) [31, 38–41]. The high variability of the quantity reflects a still poor understanding of the radiobiological dependence on different experimental endpoints, geometries, and microscopic dose distributions. Experimental, theoretical, and anecdotal evidence all indicate that α-particles have greater biological effect per Gy than photons or β-particles, but the magnitude and conditional dependence remain unclear.

1.2.4 Nuclear recoil

The energy released in α-particle decay is split as kinetic energy between the emitted α-particle and the resulting progeny nucleus in a process called nuclear recoil. The distribution

of kinetic energy can be computed with classical kinematics through conservation of energy and momentum as

$$T_\alpha = \frac{Q}{1 + m_\alpha / m_{X'}} \approx Q\left(1 - \frac{4}{A}\right), \tag{1.5}$$

where T_α is the kinetic energy of the α-particle, Q is the net energy released in the transition, and m_α and $m_{X'}$ are the masses of the α-particle and progeny nucleus, respectively. The simplification to mass number A is applicable when $A >> 4$. The recoil energy is typically on the order of 2% of the Q-value, around 100 keV, resulting in very short ranges of the recoiling nucleus in tissue, on the order of nanometers. Nuclear recoil from β-decay is less easily modeled because the energy is split between three constituents (β-particle, antineutrino, and decay nucleus), but the effect is generally minimal (∼1 eV). The nuclear recoil phenomenon complicates the dose delivery and toxicity profile of αRPT agents, as discussed in the following section.

1.3 Selected isotopes and recoil risk

Reviews of radioisotopes relevant for αRPT have already been conducted by several authors [24, 26, 42, 43]. The calculus to select an optimal αRPT isotope considers availability, cost, half-life, chemistry, decay chain, emission energy, imaging potential, and personnel safety, among other factors. Table 1.1 indicates that ^{225}Ac is the primary isotope of interest commercially (aside from the clinically viable ^{223}Ra), while ^{211}At is mainly being investigated at academic centers. ^{212}Pb has also garnered interest in commercial spheres due to continued production limitations for ^{225}Ac (Box 1.3) [44].

All αRPT isotopes currently in clinical trials have complex decay chains with progeny that also emit radiation. These *in vivo generators* can be advantageous for therapy [45]. A parent isotope with desirable chelation chemistry or physical half-life can be used as a vehicle to direct dose-delivering progeny, which themselves are not required to have such characteristics [46].

The cost of this advantage is complication of the target pathway and radiopharmaceutical pharmacokinetics due to nuclear recoil. As described above, α-decay imparts recoil energy on the order of 100 keV to the product nucleus due to conservation of energy and momentum (Eqn. 1.5). Taking the enthalpy of a chemical bond to be around 200 kcal/mol ≈ 10 eV [47], the recoiling nucleus will certainly dissociate from any chemical bond constructed with the parent. The free α-emitting progeny is not bound to the targeting mechanism and may redistribute elsewhere in the biological system through diffusion, convection, or blood transport [43]. Sites that preferentially accumulate these progeny are at risk for excess toxicity. For example, radium has an affinity for bone surfaces as a calcium analogue, whereas bismuth is preferentially concentrated and retained in kidneys while clearing from the body [48, 49].

Certain isotopes contend with this challenge more than others—namely, those with long-lived α-emitting progeny. Progeny that emit only β-particles and γ-rays contribute near

negligible dose in the αRPT context because of the low treatment activities (50–100 kBq/kg). Short-lived progeny are unlikely to relocate prior to decay, even if freed from a chemical chelator. If the progeny have no natural affinities, or the parent is well incorporated into the targeted tissue structure, the effect of diffusion-mediated redistribution can be minimal. For several of the medically interesting α-particle radionuclides, however, recoil concerns may impact their clinical viability.

The recoil considerations for selected α-emitting isotopes are summarized below. Figure 1.4 shows simplified decay chains for several in vivo generators used for αRPT with a focus on identification of long-lived α-emitting progeny. Gamma-ray emissions below 500 keV with at least 10% intensity, which may be valuable for imaging, are also indicated. The energy and half-life of each isotope, along with current literature examining the potential for progeny redistribution and toxicity, are briefly discussed. All nuclear data are collected from NuDat 3.0, a nuclear database maintained by the U.S. National Nuclear Data Center (NNDC) [50].

^{211}At: ^{211}At decays through two possible pathways to stable ^{207}Po. The α-emission from ^{211}At in the ^{211}At $\longrightarrow$ ^{207}Bi $\longrightarrow$ ^{207}Pb branch breaks chemical chelation, but the subsequent decay emits positrons or photons with minimal dose. In the alternate ^{211}At $\longrightarrow$ ^{211}Po $\longrightarrow$ ^{207}Pb branch, the initial electron capture (EC) decay and short half-life of ^{211}Po (0.5 s) make destabilization and redistribution prior to the α-emission unlikely.

Although there are no long-lived α-emitting progeny to cause off-target toxicity, deastatination, or the release of free ^{211}At in vivo due to instability of the compound, is a concern for ^{211}At-based αRPT [51, 52]. Research into the mechanisms underlying deastatination and fabrication methods to reduce it are ongoing [53].

^{212}Pb: ^{212}Pb itself decays through β- rather than α-emission. It is an in vivo generator of ^{212}Bi, which decays through two α/βor β/αchains to stable ^{208}Pb. ^{212}Bi and its short-lived progeny are the main contributors to dose, so the ability to secure ^{212}Bi localization to the intended target is paramount.

Most β-particle therapy agents, including ^{177}Lu and ^{90}Y, are characterized by one-step β-decay processes with minimal nuclear recoil ($\sim$1 eV) and without radioactive progeny. Unlike these, the β-decay of ^{212}Pb leaves progeny ^{212}Bi in an excited state that relaxes through either γ-emission or internal conversion (IC) of up to 300 keV [54]. Emission of an IC electron, and the subsequent cascade of Auger electrons and x-rays that follow due to the new orbital vacancy, can destabilize the new complex between the decay nucleus and chelator. Breakup of a ^{212}Pb-DOTA complex during decay to ^{212}Bi-DOTA has been observed in solution at a rate of $36 \pm 2\,\%$ [54].

Nonetheless, concerns about progeny redistribution have been largely resolved with the introduction of tetraamide cyclen (TCMC or DOTAM), a chelator with higher stability than DOTA. ^{212}Pb-TCMC-trastuzumab has been tested in humans without serious hematological, renal, or liver toxicity, providing some evidence that progeny redistribution may not be an issue at treatment dosages [55, 56].

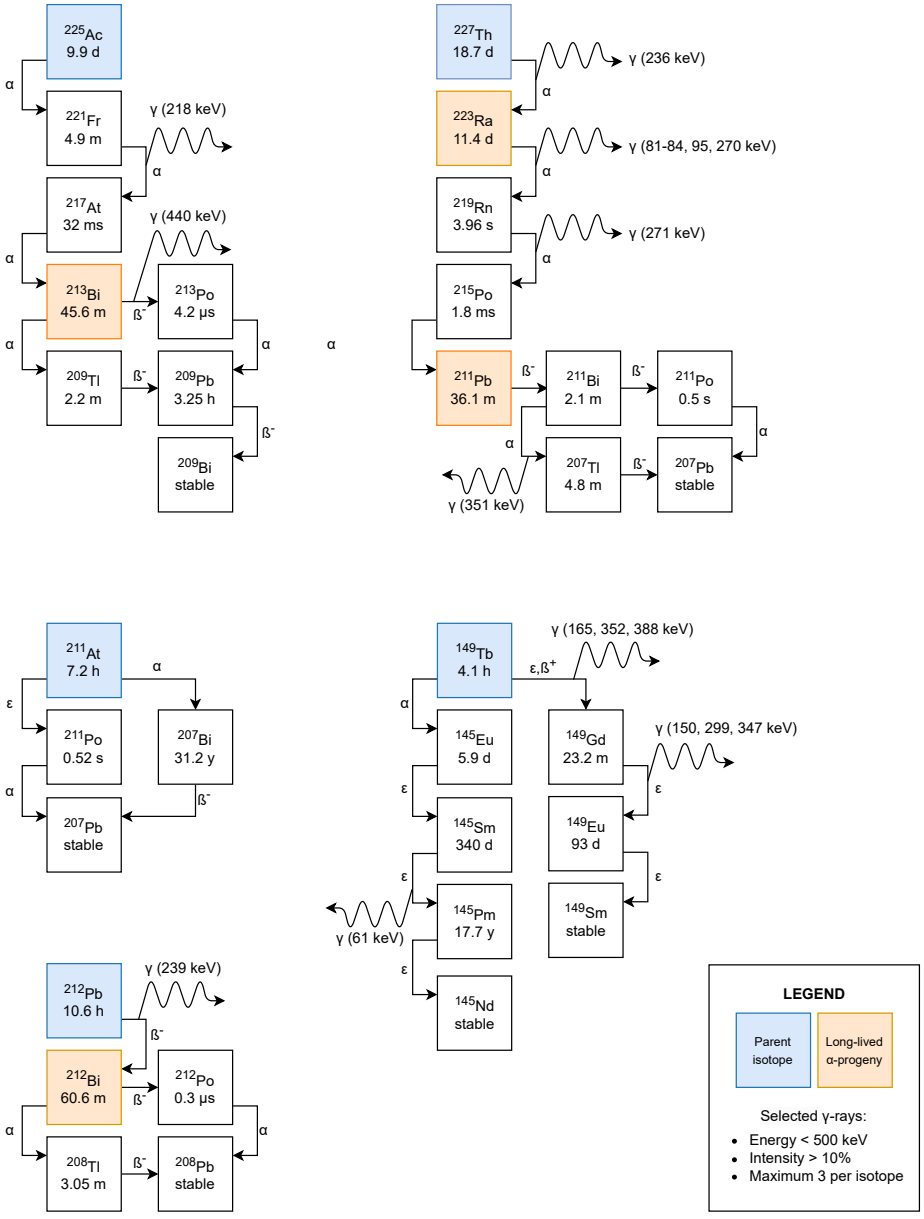

Figure 1.4: Simplified decay chains for selected in vivo generators for αRPT.

^{225}Ac: The decay chain of ^{225}Ac involves the emission of four α-particles through seven of eight possible radioisotopes to stable ^{209}Bi. Of these, α-emitting ^{213}Bi is the main toxicity risk due to its 45.6 m half-life, which leaves sufficient time for the freed progeny to circulate to another location before decay. ^{221}Fr, which has a 4.8 m half-life, has been investigated for off-target toxicity to a lesser extent. The intermediary ^{217}At ($t_{1/2} = 32\,\text{ms}$) almost exclusively decays in the same location as its direct parent ^{221}Fr.

Many preclinical studies over the past two decades have observed relocalization of ^{213}Bi to the kidneys after treatment with various ^{225}Ac-conjugates [57–60], but in vivo imaging of the time-dynamic progeny distribution remains challenging. A recent compartment model based on pharmacokinetic reports from the International Commission on Radiological Protection (ICRP) was consistent with these findings and calculated a 13.5% increase in kidney dose due to progeny redistribution compared to a "stationary" decay chain in a simulation of free ^{225}Ac in human anatomy [61]. However, clinically reported instances of ^{225}Ac-associated nephrotoxicity are somewhat few and often include patients with pre-existing kidney disease [62, 63]. Patients treated with ^{225}Ac-PSMA-617 usually exhibit treatment-ending xerostomia before nephrotoxicity due to expression of PSMA in salivary glands, but long-term monitoring is still pending [19, 64].

^{213}Bi: Although progeny ^{213}Bi is a redistribution concern for ^{225}Ac αRPT, ^{213}Bi itself as a targeted in vivo generator does not have any long-lived α-emitting progeny. The α-emission from ^{213}Bi in the $^{213}\text{Bi} \longrightarrow {}^{209}\text{Tl} \longrightarrow {}^{209}\text{Pb}$ decay branch breaks chemical chelation, but ^{209}Tl and ^{209}Pb are β-emitters with negligible dose at αRPT activities. In the other branch, the emission of a β-particle before the rapid α-decay of ^{213}Po ($t_{1/2} = 4.2\,\mu\text{s}$) does not pose a redistribution risk.

^{223}Ra: The dominant formulation of ^{223}Ra for αRPT does not involve chemical chelation. ^{223}Ra is an analogue for calcium and, when injected as $^{223}\text{RaCl}_2$, preferentially binds to bone surfaces. No chemical complex is broken by α-emission, but the decay progeny are not calcium analogues and may be considered independent from the targeting mechanism.

Similar to ^{225}Ac, the decay chain of ^{223}Ra involves the emission of four α-particles through seven of eight possible radioisotopes to stable ^{207}Pb. Most of the progeny are short-lived, with the exception of ^{211}Pb ($t_{1/2} = 36.1\,\text{min}$). ^{211}Pb is a β-emitter, but decays to ^{211}Bi, which contains α-emissions in both of its decay branches.

Several studies in mice and humans have reported no significant redistribution of ^{211}Bi away from the bone-targeted parent site [65–68]. The relatively good safety profile and the lack of nonhematologic toxicities in patients clinically treated with ^{223}Ra strongly suggests that ^{211}Bi redistribution is minimal [69].

^{227}Th: Unlike its progeny ^{223}Ra, ^{227}Th can be conjugated with stable chelator complexes to facilitate targeting to non-osseous lesions. The half-life of ^{223}Ra is long ($t_{1/2} = 11.4\,\text{d}$), and significant relocalization to the bone occurs after the primary ^{227}Th α-decay. Some

bone dose is therefore inevitable. Fortunately, the relatively good patient tolerance to ^{223}Ra allows a limited therapeutic window in which a ^{227}Th-based αRPT can be administered without hematologic toxicity [70]. Since ^{223}Ra is itself an FDA-approved αRP, the natural bone affinity of the radioactive progeny has also been utilized to develop a doubly-targeted bone-seeking agent, ^{227}Th-EDTMP [71].

^{149}Tb: Only the $^{149}\text{Tb} \longrightarrow {}^{145}\text{Eu}$ branch of the ^{149}Tb decay yields α-particles. After the 16.7% α-decay from ^{149}Tb itself, the only α-emission from progeny comes from ^{145}Pm with an intensity on the order of $1 \times 10^{-7}\%$. ^{149}Tb is thus a theoretically appealing αRPT candidate for its absence of dose due to redistributed progeny, imageable γ-rays and positrons (via PET), and potential diagnostic surrogates. Production challenges and lack of availability have limited the ability to investigate it in preclinical and clinical studies [72].

1.4 RPT treatment planning and verification

Dosimetry, the measurement and calculation of the dose absorbed by tissues, is a crucial component of radiation-based therapies. Decades of clinical experience with external-beam radiation have emphasized the value of dosimetry in the clinical workflow, including pre-therapy imaging and simulations to adapt treatment plans to patient-specific anatomy; quality assurance to maintain replicability of dose delivery; and in vivo verification to ensure the validity of the treatment. Absorbed dose to tissue is highly predictive of EBRT outcomes such as tumor control and side effects, so physicians, dosimetrists, and physicists go to lengths to optimize a patient's treatment plan and verify that it is carried out as intended.

In contrast, the clinical standard practice for administration of ^{223}Ra is as follows [73]:

1. Weigh the patient to determine mass M.
2. Compute the activity to be administered as $A = (55\,\text{kBq/kg})(M)$.
3. Administer activity A.

Although a bare-bones protocol such as this can be advantageous to reduce cost, complexity, and patient inconvenience, treatment optimization is severely underutilized, especially compared to modern standards for EBRT. In this formulation, the treatment endpoint is the prescription activity rather than a desired lesion absorbed dose or dose limit for any particular structure. Biological variation between individuals can result in substantially different patterns of uptake, clearance, and therefore response. To understand why more complex treatment planning and verification are not utilized requires review of existing RPT dosimetry data.

Evidence strongly supports a correlation between RPT absorbed doses and biological outcomes, as found in a meta-study of 79 published βRPT articles, but data explicitly articulating the relationship are still scarce [74]. Correlation has been observed between dosimetry and secondary metrics, such as platelet counts for bone marrow toxicity or prostate-specific

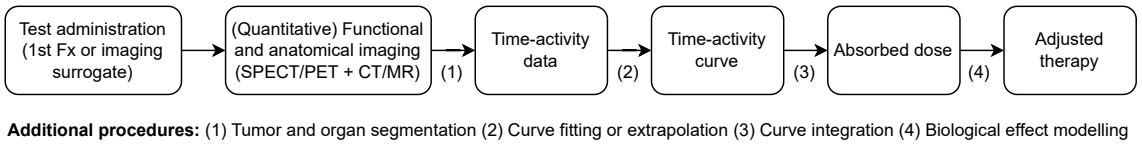

Figure 1.5: Generalized image-based RPT dosimetry workflow, based on [76].

antigen (PSA) levels for prostate cancer. However, the field has still not witnessed a clinical trial clearly illustrating that RPT dosimetry predicts overall survival better than standard non-radiation metrics (e.g., blood cell counts to monitor bone marrow toxicity) [75]. Maximum-tolerated absorbed dose (MTAD) and prescribed tumor-absorbed dose (PTAD) approaches have been suggested but applied in only a few cases [76]. The exception is treatment with ^{90}Y microspheres, for which a significant body of clinical evidence has prompted recommendations that treatment prescriptions be verified and modulated according to post-therapy imaging and dosimetry [77].

The scarcity of clinical dosimetry data, even for approved βRPT agents, has stemmed in part from a lack of dosimetry tools and protocols. Reports and teaching materials that delineate standardized techniques for RPT dosimetry have emerged only recently [31, 76]. O'Donoghue and colleagues suggest a framework using functional nuclear medicine imaging (planar/SPECT/PET) and anatomic imaging (CT/MR) with an MTAD or PTAD approach (Fig. 1.5). However, this paradigm and much of the literature for quantitative RPT dosimetry are generally reported with βRPT in mind. The physical and biological properties of αRPT discussed in Sec. 1.2 generate additional challenges in the proposed workflow, particularly in quantitative imaging and linking dosimetry metrics with outcomes.

1.4.1 Imaging and dosimetry challenges in αRPT

Diagnostic nuclear medicine imaging is mechanistically similar to RPT but uses a trace amount of imageable radioisotope instead of a therapeutic. Isotopes that emit gamma- (γ-) rays are common, as are those that emit positrons (β^+) which subsequently annihilate and emit 511-keV photons. These long-range electromagnetic quanta have relatively low absorption in the patient and can escape for detection in clinical scanning equipment. Imaging systems are defined by the expected radiation, where planar γ-camera or single-photon emission computed tomography (SPECT) systems may be used for γ-rays, and positron emission tomography (PET) systems are used for β^+-emitters. In RPT dosimetry, the imaged radiation is produced by either the therapeutic isotope itself (e.g., ^{177}Lu emits a 208 keV γ-ray) or a surrogate diagnostic conjugate sharing the same chemistry. Here, we summarize several of the major challenges and efforts for image-based verification and dosimetry of αRPT agents.

Sensitivity: Alpha-particles travel only several cell diameters in tissue, so in vivo images of αRPs in patients or animals are constructed from signal produced by photons (γ-rays, x-

rays, or annihilation photons from β^+ emission) in the decay chain, when available. The high cytotoxicity of α-particles compared to β-particles or secondary electrons from EBRT implies lower injected activities for treatment (Sec. 1.2). αRPT trials are currently being studied in patients at activities of 1–10 MBq, compared to several hundred MBq for a typical ^{99m}Tc bone scan or several GBq for βRPT. Thus, imageable signals are several orders of magnitude lower than the levels for which clinical nuclear medicine equipment is designed. Furthermore, γ- and x-ray emissions from αRPT isotopes are not necessarily optimal for imaging, sometimes exhibiting low branching ratios or high energies with lower detection rate and increased collimator penetration in SPECT systems. Each of these factors contributes to reduced signal-to-noise ratio (SNR) and impaired image quality. The deficiency is so great that imaging with standard systems cannot generally be accomplished within acquisition times tolerable for patients in the clinical setting, or within anesthesia time limits in the preclinical setting, without severe penalties to image quality.

Resolution: Clinical SPECT systems are limited to spatial resolutions of several millimeters, with sub-mm resolution reserved for specialized pinhole preclinical SPECT systems [78, 79]. Conventional SPECT also employs a physical collimator to define the direction of incidence of photon signal from the patient. More restrictive collimators improve spatial resolution but discard more events, further exacerbating the sensitivity challenge. Most modern PET systems do not use physical collimators and obtain higher sensitivity than SPECT, but are fundamentally limited to around 1.8 mm full-width half-maximum (FWHM) (clinical) and 0.7 mm FWHM (preclinical) spatial resolution due to positron range and non-collinearity of annihilation photon pairs [80]. With the exception of ^{149}Tb, common αRPT isotopes do not emit positrons in their decay chains, so the applicability of PET to αRPT imaging is mostly limited to diagnostic surrogates. Overall, it is rare that even a preclinical system can exhibit millimeter-spatial resolution when imaging αRPT activities in reasonable times (sub-hours). The combination of the resolution and sensitivity issues create a substantial challenge for regular implementation of macroscopic (i.e., organ-scale) αRPT dosimetry. Resolution limits are an even greater concern when assessing the dosimetric effects of the short range of the α-particle ($< 100\,\mu$m). Micro-scale dose heterogeneities that can occur within organs or tumors are entirely unresolvable by any in vivo imagers currently available (Ch. 3).

Imaging surrogates: Image quality challenges can be partially circumvented through use of PET and SPECT imaging surrogates, which are chemically similar diagnostic RPs that may be injected at higher activities to obtain tracer distributions correlated with the αRP kinetics. Some potential diagnostic substitutes for ^{225}Ac include ^{133}La or ^{134}Ce/^{134}La for PET, or ^{226}Ac for SPECT. Familiar PET and SPECT isotopes, such as ^{18}F and ^{68}Ga, can also be chemically chelated to the same targeting moiety as the radiopharmaceutical and are commonly seen in αRPT imaging [19]. However, these tracers are not optimal for quantitative dosimetry because dissimilarities in chemical properties between the isotopes

can induce uncertainty in uptake and pharmacokinetics [27]. Overall, the utility of surrogate imaging techniques is limited by the chemical similarity of the surrogate to the therapeutic isotope, the complication of dosimetry (requiring studies to correlate imaging biokinetics to therapeutic absorbed dose), and the lack of information provided by the surrogate about the distribution of recoil progeny [81].

Clinical efforts: Quantitative planar imaging of ^{223}Ra itself is possible, though noisy enough that a ^{99m}Tc bone scan may be required to delineate regions of interest [67, 82, 83]. However, a greater challenge to ^{223}Ra dosimetry is the micro-scale resolution issue: ^{223}Ra treats bone metastases, which are frequently sub-clinical disease not easily resolvable in gamma camera scans or anatomical imaging. The lack of information about the lesion mass and extent restrict the ability to convert even a quantitative activity image to actionable dosimetry. Several investigators have reported ^{225}Ac imaging feasibility with clinical SPECT scanners in technical reports of one or two patients [84–86], but ^{18}F-PSMA-I&T and ^{68}Ga-PSMA-11 PET are more common because of their superior image quality for non-quantitative verification [19]. Planar imaging of ^{212}Pb in three patients showed gross differences between abdominal and extra-abdominal uptake, but blood and urine samples were ultimately more informative [87].

Preclinical efforts and specialized systems: A number of specialized systems are being investigated for in vivo imaging of αRPT agents at sub-millimeter resolution in the preclinical setting. The Alpha-SPECT-Mini is a CdTe-based pinhole SPECT that reports around 0.75 mm spatial resolution and sensitivity sufficient for live in vivo imaging of 55.5 kBq (1.5 µCi) free ^{225}Ac in a mouse [88]. The system distinguishes signal from ^{225}Ac (100 keV) and several progeny: ^{209}Tl (117 keV), ^{221}Fr (218 keV), and ^{213}Bi (440 keV).

Other systems are also being developed with an emphasis on sensitivity using cadmium zinc telluride (CdZnTe, or CZT) in several form factors: a four-head preclinical CZT SPECT [89], CZT Compton camera [90], and a collimatorless planar CZT camera [91]. These proofs of concept have remained mostly confined to phantom and ex vivo murine measurements, but show promise for in vivo feasibility with improved collimator design, reconstruction, or geometry.

Frame et al quantified the distribution of ^{225}Ac and its progeny in mice bearing tumor xenografts using a specialized dual-modality imager with two high-purity germanium (HPGe) double-sided strip detectors (DSSDs) in two configurations: a masked coded aperture system suited for the ^{221}Fr 218-keV γ-ray, and a two-layer Compton imager optimized for the ^{213}Bi 440-keV γ-ray [92]. Mice that received 18.5 kBq (0.5 µCi) of an ^{225}Ac-based RP were euthanized prior to the imaging session, which used 8-10 h per modality. Images were insufficient to segment organs in the abdominal cavity, but modifications to the detector geometry and reconstruction algorithm may improve resolution to levels sufficient for segmentation.

Modeling biological effects: Two factors render αRPT dosimetry metrics non-trivial for clinical interpretation. The dense ionization of α-particle tracks results in complex DNA damage that is more cytotoxic than dose induced by β-particles or photons (Sec. 1.2). Furthermore, the short range of the α-particle results in micro-scale dose heterogeneities unlike the fairly uniform dose distributions created by external photon beams. It is still unclear how these nonuniformities impact biological outcomes in different organ and tumor systems. Unlike EBRT, in which many years of clinical experience affords confidence to clinicians that a given prescribed dose yields a specific outcome, the field of RPT lacks a database of concrete causal relationships between absorbed dose and therapeutic or toxic effect. βRPT also suffers this deficiency, as discussed above, but the problem is more challenging to solve in αRPT due to the α-particle range and cytotoxicity.

1.5 The role of preclinical dosimetry

Growing commercial and academic interest in αRPT reflects an unmet need for non-toxic, systemic anti-tumor therapies in the space of available cancer treatments. The short range and high LET of the α-particle paint an appealing profile: a drug cytotoxic enough to overcome chemo- and radio-resistance, with selectivity to avoid healthy tissue damage and toxic side effects. However, these same properties create imaging and dosimetry challenges that limit our ability to develop and understand these drugs.

The potential to spare normal tissue relies on the targeting mechanism, but verification through direct imaging of γ-rays is impaired by low injected activities and often sub-optimal photon emissions. Recoiling decay products are difficult to track and can induce toxicity in non-targeted locations. Current treatment protocols, which use fixed or scalar activity tables without dosimetric information, make treatment outcome subject to biological variability between patients. Information about the effects of α-particle dose is needed to create a dosimetry-based framework, but micro-scale dose inhomogeneities obscure the relation. It should not be overlooked that clinical results with αRPT are already promising. However, translation as a standard-of-care curative therapy will likely require that these knowledge gaps be filled.

Dosimetry studies in the preclinical setting are required for efficient drug discovery and safe clinical translation (Fig. 1.6). The greater spatial resolution and sensitivity afforded by preclinical imagers allows better characterization and selection of αRPT drug candidates prior to the clinical phase, as well as investigation of the biodistribution and toxicity risk of recoiled progeny. Since each targeted αRP is suitable for a different cancer setting, the preclinical stage is mandatory to identify the best drug candidates for human trials and reject sub-optimal ones. Crucially, ex vivo imaging is currently the only possible approach to observe micro-scale dose inhomogeneities. Quantification of these effects is not only required to fully evaluate preclinical drug targeting and efficacy, but also to build models that relate measured α-particle dose to observable biological outcomes. Ex vivo dosimetry methods can be applied to clinical biopsies [66, 93], but such procedures are irregular and highly

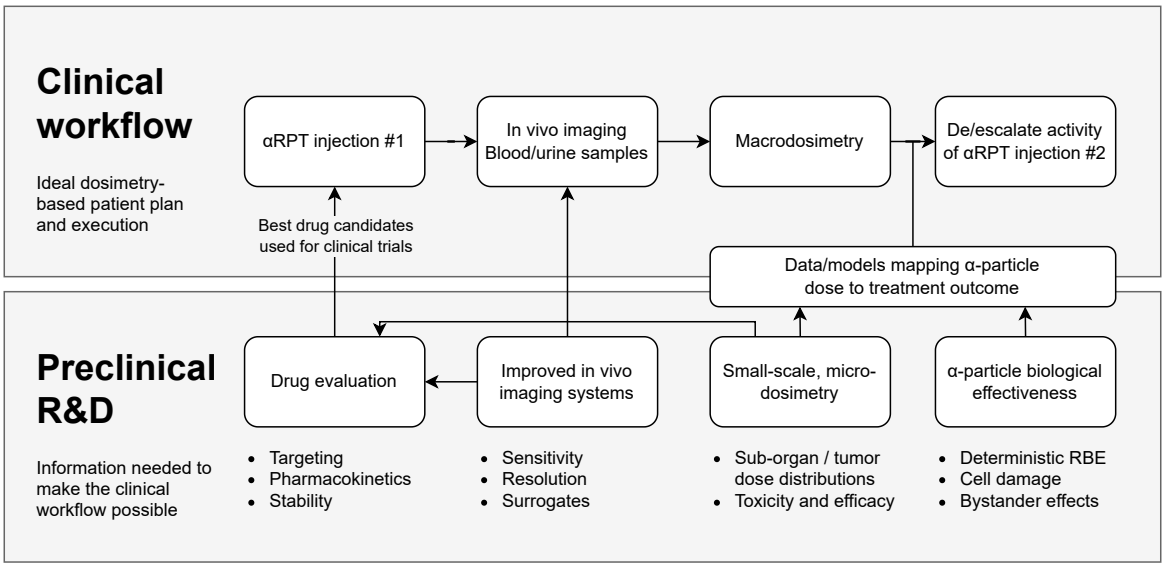

Figure 1.6: Role of preclinical research, including in vivo and ex vivo small-scale dosimetry, in the clinical translation of αRPT.

invasive. Animal studies are thus the main means by which the spatial-dose-effect relation unique to α-particle emitters can be understood. These data are fundamentally necessary if personalized dosimetry-based treatment planning and verification are to be realized in αRPT. The remainder of this dissertation details dosimetry protocols and outcomes in various animal studies of α-particle radiopharmaceuticals with a focus on small-scale effects.

Chapter 2

Macroscopic dosimetry in preclinical radiopharmaceutical studies with ex vivo gamma-ray spectroscopy

Gamma-ray counting ("gamma counting")[1] is the most common method to quantify the macroscopic (organ- and tumor-level) distribution and pharmacokinetics of αRPs in preclinical mouse studies. To assess a mouse subject through gamma counting, the subject is euthanized and dissected, and individual organs and tumors are counted in a radiation-detection device calibrated to provide a corresponding radioactivity reading for a given counts-per-time measurement. This procedure is carried out at several time points over the course of a research study to assess how the radiopharmaceutical navigates the biological system.

In this chapter, we review the uses for gamma counting over quantitative imaging in αRPT, fundamental dosimetry concepts, and workflows for gamma counting in radiopharmaceutical studies. We also discuss how these methods are applied to preclinical studies in this dissertation.

2.1 Gamma counting in αRPT

Gamma counting is the simplest and most common dosimetry procedure for radiochemistry laboratories studying αRPT. Although non-invasive in vivo quantification through PET, SPECT, or other advanced imaging modes is desirable, the minimal quantities of injected radioactive material used in αRPT creates sensitivity requirements unmet by traditional imagers. Adaptation and improvement of quantitative imaging systems to the challenges of αRPT, and the development of new technologies that may be better suited to the modality, are areas of active research.

[1] Gamma counting is sometimes described synonymously with **scintillation counting.** However, many gamma counting studies use non-scintillator semiconductor detectors, especially when superior energy resolution is required. We therefore use the term gamma counting to encompass both approaches.

Well-type gamma counters provide higher sensitivity than most in vivo imaging systems, assisted by the geometric advantage of an unobstructed sample inside near-4π detector coverage. Commercial gamma-counters generally have high throughput, are easy to operate, and do not require physics or nuclear engineering expertise to interpret the data (although such knowledge is beneficial for in-depth analysis). Complex image reconstruction is not required. This simplicity is a boon for laboratories focused on other aspects of radiopharmaceutical development, such as the radiochemistry or biological models. Until in vivo imaging technology has advanced sufficiently, the highly sensitive and user-friendly gamma counter is likely to remain the most common technology for αRPT preclinical radioactivity assessment. Clinical studies may also utilize gamma counting for blood and urine samples to evaluate blood and renal clearance [94].

The inherent drawback of gamma counting compared to in vivo imaging is that the animal must be sacrificed to conduct a measurement. Biological variability between subjects is unavoidable, and only a single snapshot in time is obtained. The results cannot inform adjustment of the treatment dosage unless the measurement is carried out with tissue biopsies or blood or urine samples. Gamma counting also does not provide any information about the spatial distribution of radioactivity within samples, which is highly relevant to the study of αRPT.

Below, we discuss the general workflow for preclinical gamma-counting studies using a commercial NaI(Tl) gamma counter (Hidex Automatic Gamma Counter (AMG)), and the specific methods for device characterization and calibration, data collection, dosimetry analysis, and multiple-isotope separation used for studies in this dissertation.

2.2 Hidex AMG

The Hidex AMG is an automated system comprising a lead-shielded, 3-in well-type NaI(Tl) gamma counter with a sample balance and Microsoft Windows 10 PC interface. A 1×3 inch NaI(Tl) crystal surrounds the sample holder and is coupled to an equivalently sized photomultiplier tube (PMT). Racks of samples are provided by the user to the machine, which pulls single tubes in order for measurement in the well. 55 mm lead shielding surrounds the detector system in 4π solid angle coverage, with an additional 80 mm of shielding between the detector and the input rack conveyor. Compatible sample vials up to 13 mm × 95 mm (diameter × height) can be used. Performance specifications provided by the vendor are summarized in Table 2.1.

2.3 Biodistribution data

Simple biodistribution (BioD) analyses compare total counts between samples, while complexity and robustness can be added by utilizing more of the information supplied by the device. For example, use of an isotope-specific energy window, or region of interest (ROI),

Table 2.1: Performance specifications of the Hidex AMG, from [95].

Parameter	**Vendor Specification**
Energy range	5–2000 keV
Counting efficiency	78% at 28.4 keV
	47% at 320 keV
	6% at 662 keV
Energy resolution	<30% at 28.4 keV
	<9.5% at 662 keV
Maximum count rate	10 million cpm

can improve the selectivity of the analysis, and normalization to the mass of the sample better characterizes the pharmacokinetic distribution. Many spectroscopic gamma counters provide the entire pulse-height energy spectrum and the mass of each measured sample in addition to the programmed counting protocols.

The standard approach for preclinical BioD studies is a measurement that yields the percentage injected activity per gram (%IA/g) of the radiopharmaceutical in each tissue or tumor of the mouse subject.[2] %IA/g for a sample k is computed as

$$(\%\mathrm{IA/g})_k = 100\left(\frac{A_k}{A_I}\right)\Big/ m_k, \tag{2.1}$$

where A_k and A_I denote the activity in sample k and the total activity injected, respectively, and m_k is the mass of the sample in grams.

A_k can be measured by a programmed isotope-specific protocol in a commercial gamma counter that tracks counts. Inputs to the protocol are the measurement time, isotope, and energy window—a specific ROI (e.g. 450–580 keV), or an open window spanning the detection range (e.g. 0–2000 keV). These parameters are saved under a given protocol name to be re-used between calibrations and studies of the same isotope. Some example acquisition parameters for the Hidex AMG are provided in Table 2.2.

Multiple racks of 10 samples each can be queued in the Hidex AMG for automatic measurement. The output is a sequential list of counts per minute (cpm) from the specified ROI, and mass if requested, for each sample in order. Based on the half-life of the isotope, the Hidex AMG automatically applies an exponential decay correction to the start of the run for each count value. The decay-corrected count figure is used as input to a look-up table or calibration curve and yields A_k, then a one-step calculation determines %IA/g for the series.

[2]The figure "%ID/g", or percentage injected dose per gram, is actually more common, but we find this term misleading because the word *dose* is overloaded in contexts that also handle radioactivity. We use %IA/g to emphasize that the gamma counter provides a measure of activity (Bq) which is distinguished from the absorbed dose (Gy).

Table 2.2: Example acquisition parameters for a Hidex AMG biodistribution gamma-counting study.

Parameter	Quantity	Notes
Measurement time	60 s	per sample
Isotope	^{18}F	half-life used for automatic decay correction
Energy window	409–613 keV	20% energy window around 511 keV

2.4 Spectroscopic methods

The programmed-window method is straightforward and effective for single-isotope sources in a well-calibrated detector. More robust methods are needed when

- the isotope has multiple emissions, or a multi-isotope co-injection is used. Consideration must be given to the energy windows and the impact of cross-talk between energies.
- the isotope has a complex decay series, which may contain radioactive progeny not in equilibrium with the parent. The relative distribution between parent and progeny may change over time, even during the measurement. The single-isotope decay correction becomes inaccurate.
- the energy calibration of the device is known to drift. A specified ROI will therefore select a slightly different piece of the spectrum from one measurement to the next.

These situations are most easily addressed by using the spectral data from the device. There is abundant literature for a variety of applications of gamma-ray spectroscopy. The spectroscopy procedure used in this work includes energy calibration, background subtraction, Gaussian fitting in a ROI to determine counts, and decay- or multi-isotope corrections.

Energy calibration. Figure 2.1 illustrates the need for and application of energy calibration to the Hidex AMG. Three samples of ^{134}Ce in solution were measured within several hours using the same device, with gain drift causing displacement of the 511 keV and 1022 keV peaks of up to 30 keV. (^{134}Ce is an in vivo generator PET agent being investigated as a surrogate diagnostic pair for ^{225}Ac, and decays via electron capture to positron-emitting ^{134}La.) Calibration re-scales the spectrum such that each peak is correctly centered at the known energy.

Our calibration procedure consists of the following steps:

1. Provide user input for the peak-finding algorithm: known peak energies E, allowed energy search range, minimum peak signal-to-noise ratio (SNR), and energy discrepancy tolerance dE.

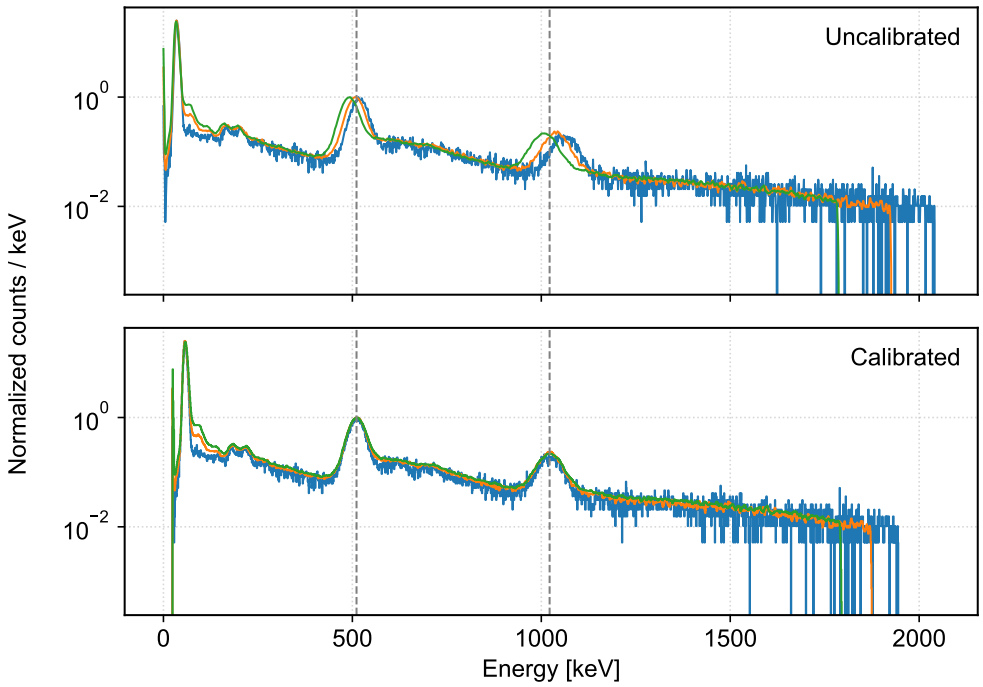

Figure 2.1: Example of on-the-fly Hidex energy calibration using ^{134}Ce. Three samples of ^{134}Ce measured in a span of several hours exhibit significant gain drift over the 511 keV and 1022 keV annihilation photon peaks. Calibration re-scales the spectrum such that each peak is correctly centered at the known energy (gray dashed lines).

2. Use a one-dimensional peak-finding algorithm, such as `Scipy.signal.find_peaks`, to locate maxima in the spectrum.
3. From found maxima at energies E', select those within dE of E to use for calibration.
4. Use a least-squares linear fit function to map signal value to energy.
5. Apply the calibration function to the spectrum.

The advantage of this approach is that the energy calibration can be applied to any spectrum after acquisition, regardless of the drift at the specific measurement time, allowing users to take advantage of the automatic, serial-rack measurement capabilities of the Hidex AMG. This type of calibration is possible because the injected isotope is functionally always known for biodistribution experiments (as compared to, for example, gamma-ray spectroscopy in nuclear security and search applications).

Efficiency calibration curve and dead time effects. An efficiency calibration curve converts the measured quantity (cpm) to true sample activity, accounting for detector geometry, efficiencies, and isotope branching ratios. For an isotope to be used in an animal study, one prepares an array of known-activity samples, commonly through serial dilution,

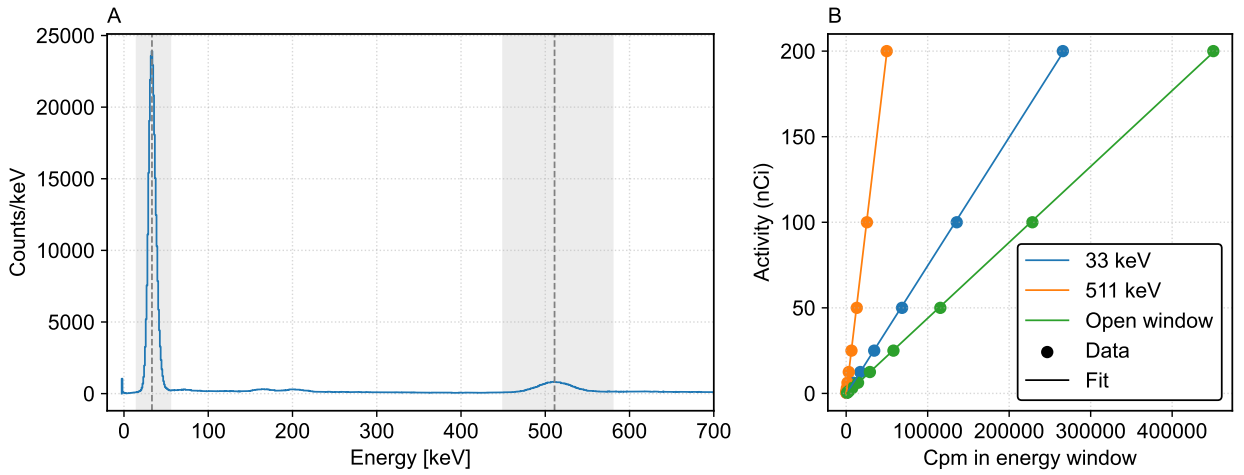

Figure 2.2: Example Hidex AMG efficiency calibration curve for ^{134}Ce for each of two energy windows and an open window. (A) Example energy spectrum for a 60 s acquisition of 200 nCi of ^{134}Ce, with energy windows around the 33.0–33.4 keV and 511 keV lines displayed. (B) Calibration curves for each energy window and an open window (0–2000 keV) at a range of activities prepared through serial dilution (0.4–200 nCi).

and measures them in the device using the counting and analysis procedure to be used in the study. The activity of the original sample is measured using an argon gas dose calibrator, or provided by industry measurements.

An example efficiency calibration curve for ^{134}Ce is shown in Fig. 2.2. Aside from the annihilation peaks at 511 keV and 1022 keV, a weak 607 keV gamma-ray from ^{134}La and characteristic x-rays at 33 keV (21.3%) and 33.4 keV (38.8%) are also emitted. A window around the x-rays, annihilation photons, or an open window (0–2000 keV) can be used for calibration, as long as the selection is consistent between calibration and experiment.

At sufficiently low activities (below $\sim 0.5\,\mu\text{Ci} = 18.5\,\text{kBq}$), an ideal calibration is linear, as in the ^{134}Ce example in Fig. 2.2. Higher activities induce non-negligible rate effects in the detector (Fig. 2.3). A nonparalyzable detector model can be used to predict the behavior of the device as

$$n = \frac{m}{1 - m\tau} \quad \Longrightarrow \quad m = \frac{n}{1 + n\tau}, \tag{2.2}$$

where n is the true interaction rate in the detector, which is proportional to the true activity of the sample; m is the recorded count rate; and τ is the dead-time of the system [32].

Background correction. Extensive lead shielding in the Hidex AMG substantially lowers the measured radiation background, but it still warrants consideration. This is particularly true when measuring low activities or multiple emissions in which higher-energy gamma-rays can down-scatter into lower-energy ROIs. Additionally, the spectrum will con-

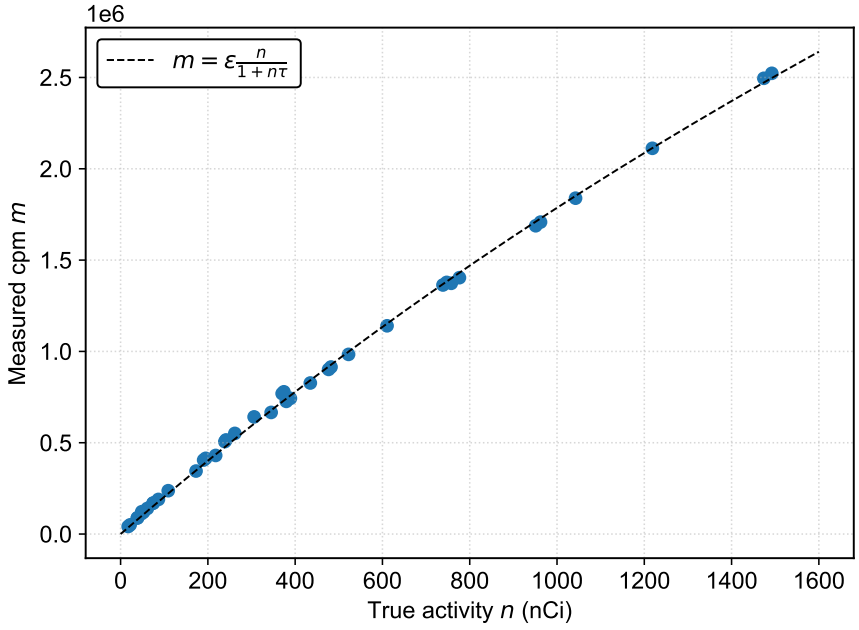

Figure 2.3: Hidex AMG calibration curve for ^{134}Ce with a nonparalyzable detector model using an open window. Non-linearity is evident at higher activities.

tain background counts in the 80–90 keV range corresponding to characteristic x-rays from lead. These effects were handled in four ways in our studies.

1. Exclude the characteristic x-ray range. This was generally appropriate for our studies, but in some cases one may wish to utilize overlapping ^{225}Ac x-rays as additional signal.
2. Measure a blank sample as background and subtract it from each spectrum. This has an effect of around one or two counts per 1-keV bin in a 60 s acquisition.
3. Measure a blank vial and sum all counts in the open window. Compute the minimum detectable activity (MDA) and Currie decision threshold L_C, and assign any measured spectrum below L_C an activity of zero.
4. For multiple-energy emissions, handle downscatter background with a secular equilibrium calibration or with Gaussian fitting.

When discussing MDA, we use the formalism in Knoll [32]. Assuming Gaussian distributed counts and background measurement N_B, the Currie decision threshold $L_C = 2.33\sqrt{N_B}$ ensures 95% specificity (5% false positive rate). If fewer than $N_B + L_C$ counts are present, we say that no activity is detected above background. We also discard measurements with fewer than 30 total counts as the Gaussian assumption breaks down.

If background is a result of downscatter from a higher-energy emission, and the emission is either from the same isotope or an isotope in secular equilibrium, then the amount of downscatter background is also proportional to the quantity of isotope present. A standard

linear efficiency calibration will still be accurate, albeit with a higher slope. In the case where the higher-energy window is from an isotope not in secular equilibrium, then the downscatter background can be approximated with a constant, linear, or exponential function beneath the Gaussian photopeak. More complex modeling for non-equilibrium isotope chains is discussed in Section 2.6.

2.5 Macroscopic dosimetry

The MIRD (Committee on Medical Internal Radiation Dose) S-value formalism provides a framework to calculate the absorbed dose rate in a structure using knowledge of the activity in surrounding structures, which can be measured with quantitative imaging or gamma spectroscopy. Characteristics of the radioisotope decay are also required. The structure in which the dose rate is to be calculated is considered the target region r_T, and it receives energy from surrounding radioactive source regions r_S. The instantaneous dose rate in r_T is

$$\begin{aligned}\dot{D}(r_T,t) &= \sum_{r_S} A(r_S,t)S(r_T \leftarrow r_S,t) \\ &= \sum_{r_S}\left[A(r_S,t)\frac{1}{m(r_T,t)}\sum_i E_i Y_i \phi(r_T \leftarrow r_S, E_i, t)\right]. \end{aligned} \tag{2.3}$$

The variables included are defined as:

$$\begin{aligned} r_T &= \text{target region} \\ r_S &= \text{source region} \\ A(r_S,t) &= \text{activity in source region at time } t \\ S(r_T \leftarrow r_S,t) &= S\text{-value for effect of } r_S \text{ on } r_T \text{ at time } t \\ m(r_T,t) &= \text{mass of target region at time } t \\ i &= \text{index for individual emissions for a given isotope} \\ E_i &= \text{mean energy of the } i\text{th emission} \\ Y_i &= \text{branching ratio of the } i\text{th emission} \\ \phi(r_T \leftarrow r_S, E_i, t) &= \text{geometry-dependent absorbed fraction of the emission from } r_S \text{ in } r_T. \end{aligned}$$

The equation simplifies considerably when evaluating α-particle radiopharmaceuticals at the organ level since dose can be assumed to derive from and entirely deposit within the tissue. Therefore, the source and target region are the same ($r_T = r_S$), only self-dose contributes, and the absorbed fraction $\phi(E_i,t) = 1$. Equation 2.3 reduces to

$$\dot{D}(r_T,t) = A(r_T,t)\frac{1}{m(r_T,t)}\sum_i E_i Y_i. \tag{2.4}$$

Quantities E_i and Y_i can be obtained from nuclear databases for the isotope of interest, and $A(r_T, t)$ and $m(r_T, t)$ are equivalent to A_k and m_k as measured in the gamma counter in our previous nomenclature.

In biodistribution studies, this calculation occurs on a macroscopic scale in which r_T is a whole tissue or organ.[3] Macroscopic dosimetry is useful to identify overall pharmacokinetics and targeting properties of radiopharmaceuticals. Limitations of macroscopic dosimetry for αRPT are discussed in Chapter 3.

2.5.1 Dosimetry over time

Equation 2.4 provides the instantaneous dose rate in a target region at a single moment in time. The total absorbed dose in the structure over the course of treatment is the time-integrated dose rate,

$$D(r_T) = \int_0^\infty \dot{D}(r_T, t)dt, \tag{2.5}$$

where the bounds $t = [0, \infty)$ indicate that the full effects of an injection at $t = 0$ are evaluated.

A number of approaches can be taken to integrate $\dot{D}(r_T, t)$, including fitting with analytical integration, numerical methods, and compartment modeling [31, 76, 96]. The diversity in methods reflects a wide variety in the characteristics of pharmacokinetic data. Assumptions about uptake patterns for one data set may not apply to another. Some data may be sparse in time, such as a single patient imaging measurement, while other data may be abundant, as in a multi-time-point preclincal study. A single-exponential model might be sufficient in some cases, whereas others may require multi-exponential or piecewise functions for a reasonable fit.

In this work, the measured dose-rate data $\dot{D}(r_T, t)$ are fit to single-exponential, multi-exponential, or piecewise functions, then the fit function is numerically integrated using trapezoidal sums with the `numpy` (Python) function `numpy.trapz`. At least 1000 trapezoids are used for each curve to bring the discrete computation closer to a continuous integral. The upper integration bound is replaced with $6.6t_{\text{eff}}$, or 6.6 effective half-lives of the exponential fit function, which is the time for clearance and decay to bring the remaining activity below 1% of the starting value. Conceptually, t_{eff} models the biological clearance half-life t_b and physical half-life of the radionuclide t_p simultaneously as

$$\frac{1}{t_{\text{eff}}} = \frac{1}{t_b} + \frac{1}{t_p}. \tag{2.6}$$

The specific fit functions and bounds used for each study are described in their relevant sections.

[3] The MIRD formalism is also most commonly used for macroscopic dosimetry, but is not in principle restricted to any spatial scale. Eqn. 2.3 is limited by the spatial resolution of the activity measurement and structure delineation (Ch. 3).

Box 2.1: Time-activity vs. time-dose-rate curves. The dosimetry procedure we have described so far consists of three steps: 1) measure activity, 2) calculate dose rate, and 3) integrate for dose. Most literature surrounding RPT dosimetry describes a different order, analogous to 1-3-2: measure activity, integrate to obtain the time-integrated activity (formerly termed the *cumulated activity*), then calculate dose. Both procedures are valid in the macroscopic framework. We use the 1-2-3 approach because it translates more easily to small-scale ex vivo dosimetry procedures using dose kernel or Monte Carlo calculations at each time point (Ch. 3).

2.6 Multiple-isotope separation

The study and development of αRPs can involve the use or measurement of more than one radioisotope, usually due to a parent-progeny decay series, multiple co-injection, or an imaging surrogate. ^{225}Ac-based RPs, for example, must handle the emissions from progeny ^{221}Fr and ^{213}Bi individually due to the potential for redistribution. Several studies have also investigated the potential for "cocktail therapies," in which multiple modes of RPT are combined in a single subject, such as simultaneous treatment with β-emitting ^{177}Lu and α-emitting ^{225}Ac [97]. In each case, study and verification of both isotopes requires disentanglement of the two different signals by gamma-ray spectroscopy. The demands for each such study are influenced by the energies, emission types, and crosstalk between isotopes, and can be handled through the use of analytical decay equations, data-driven statistical methods, or semiconductor detectors with high spectral resolution.

We are particularly interested in the study of ^{225}Ac, for which there are several applications of gamma-ray spectroscopy due to the emission of several x- and γ-rays in its complex decay chain. In this dissertation, quantitative separation of ^{213}Bi from its parent ^{225}Ac is necessary. We articulate the method used for ^{225}Ac/^{213}Bi separation in later studies using the Hidex AMG here. Then, we describe a short investigation characterizing two semiconductor detectors for improved separation in co-injection applications.

2.6.1 ^{225}Ac and ^{213}Bi

The growth and decay of parent and progeny isotopes in decay chains are governed by the Bateman equations [98], which incorporate exponential decay laws and the half-lives of each isotope into a set of differential equations. In gamma-ray biodistribution measurements, biological processes halt at the time of animal sacrifice, and the decay of any existing isotopes in that instant follow these decay laws.

For a two-isotope decay chain with parent half-life $t_a = \ln 2/\lambda_a$ and progeny half-life $t_b = \ln 2/\lambda_b$, a measurement at time t post-sacrifice provides $A_a(t)$ and $A_b(t)$, the respective parent and progeny activities. These are related to $A_a(0)$ and $A_b(0)$ at the instant of sacrifice

$(t = 0)$ by solutions to the Bateman equations [99]:

$$A_a(t) = A_a(0)e^{-\lambda_a t} \tag{2.7}$$

$$A_b(t) = A_a(0)\frac{\lambda_b}{\lambda_b - \lambda_a}(e^{-\lambda_a t} - e^{-\lambda_b t}) + A_b(0)e^{-\lambda_b t}. \tag{2.8}$$

The decay chain of ^{225}Ac is shown in Fig. 2.4. Although the decay series is complex, passing through six decays through two pathways to stable ^{209}Bi, simplification to a relation between ^{225}Ac and ^{213}Bi is desirable due to the non-negligible 45.6 min half-life of ^{213}Bi and its potential for redistribution and off-target toxicity. Time-sensitive gamma counting and analysis with the Bateman equations can quantify the redistribution of free ^{213}Bi between organs.

In gamma counting measurements, we assume secular equilibrium between ^{225}Ac ($t_{1/2}$ = 9.9 d) and ^{221}Fr ($t_{1/2}$ = 4.8 min), and between ^{221}Fr and ^{217}At ($t_{1/2}$ = 32 ms), but not between ^{225}Ac and ^{213}Bi ($t_{1/2}$ = 45.6 min). This assumption is valid for measurements occurring between 30 min and 5 h after sacrifice (after six ^{221}Fr half-lives, but before six ^{213}Bi half-lives, have elapsed), and allows us to treat ^{225}Ac and ^{213}Bi activities as direct parent and progeny.

We may manipulate Eqns. 2.7–2.8 slightly to obtain the relation between $A_a(t)$ and $A_b(t)$:

$$\frac{A_b(t)}{A_a(t)} = \left(\frac{A_b(0)}{A_a(0)} - \frac{\lambda_b}{\lambda_b - \lambda_a}\right)e^{-(\lambda_b - \lambda_a)t} + \frac{\lambda_b}{\lambda_b - \lambda_a} \tag{2.9}$$

All measurements correspond to animals sacrificed at the same time post-injection. Eqn. 2.9 is equivalent to

$$A_b(0) = A_b(t)e^{\lambda_b t} - \frac{\lambda_b}{\lambda_b - \lambda_a}A_a(t)(e^{\lambda_b t} - e^{\lambda_a t}). \tag{2.10}$$

$A_b(t)/A_a(t) = 1$ is the condition that describes secular equilibrium between ^{225}Ac and ^{213}Bi at any time t. For tissues with $A_b(t)/A_a(t) > 1$, the difference between the total activities at sacrifice, $A_b(0) - A_a(0)$, is the quantity of free ^{213}Bi present at that moment (e.g. due to redistribution from other tissues).

Equation 2.9 is a convenient form to apply as an empirical fit to data at multiple time points; for example, in a sequential BioD measurement of organs from multiple animals sacrificed at the same time, or a sequential counting of the same animal. The equation can be written as $A_b(t)/A_a(t) = Ce^{-(\lambda_b - \lambda_a)t} + D$, where C is the fit parameter, and the desired ratio $A_b(0)/A_a(0) = C + \lambda_b/(\lambda_b - \lambda_a)$. Note that the decay coefficient in the exponent, $\lambda_b - \lambda_a$, is not a free parameter and is constrained to the half-lives of ^{213}Bi and ^{225}Ac. If only a single measurement is available, the analytical decay correction in Eqn. 2.10 can be used. This analytical correction is illustrated in Fig. 2.4 for initial conditions with and without free ^{213}Bi in the tissue at the time of sacrifice.

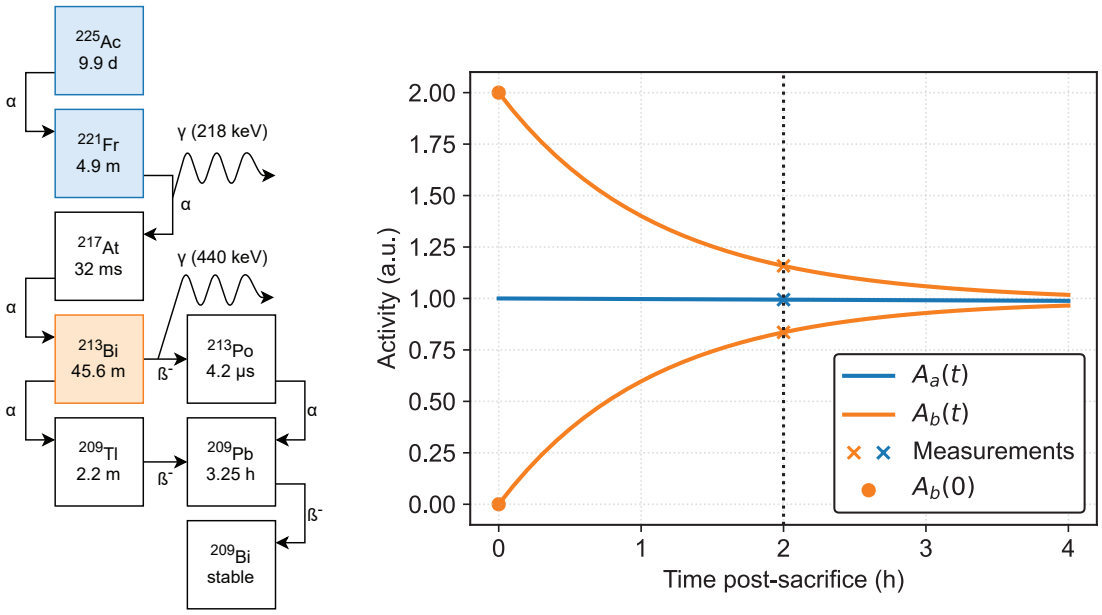

Figure 2.4: ^{225}Ac decay chain (left) and algebraic ^{213}Bi decay correction (right). Measured counts of the two gamma-rays from ^{221}Fr and ^{213}Bi (×) are used to calculate the free ^{213}Bi activity at the time of sacrifice (•). Activity curves for two possible initial conditions are shown, representing tissues with (above) and without (below) free ^{213}Bi present.

The method discussed above is similar to that in Seoane et al [100] but is expressed in different formalism that eases generalization to other parent-progeny isotopes. The ratio $A_b(t)/A_a(t)$ in Eqn. 2.9 is useful to check whether deviation from secular equilibrium is observed and determine which initial condition shown in Fig. 2.4 is relevant. Eqn. 2.10, with $A_a(0)$ subtracted as discussed, reduces to Seoane Eqn. 7 in the case where $\lambda_b/(\lambda_b - \lambda_a) \longrightarrow 1$ (1.003 for ^{225}Ac and ^{213}Bi).

2.6.2 Semiconductor detectors for ex vivo tissue measurements

Eqns. 2.9 and 2.10 rely on accurate measurements of $A_a(t)$ and $A_b(t)$, typically obtained using separate energy windows in the same gamma counting acquisition. The Hidex AMG is sufficient for separation between ^{225}Ac and ^{213}Bi, but some multiple-isotope applications contain gamma-ray emissions that are challenging to distinguish with NaI(Tl). In such cases, semiconductor detectors offer superior energy resolution for peak separation. Fig. 2.5 illustrates the difference between a mixed sample of unknown quantities of ^{227}Th and ^{223}Ra as measured in the NaI(Tl) Hidex AMG as compared to an HPGe detector. NaI(Tl) blurs the ^{223}Ra and ^{227}Th peaks in the 250–300 keV range and results in a summed lump that

is challenging to disentangle. Use of a semiconductor detector provides clearly distinguished energy lines in the same region so that straightforward ROI methods can be applied.

Semiconductor detectors are significantly more expensive than NaI(Tl) systems and have historically been less flexible due to liquid-nitrogen or bulky mechanical cooling requirements. The rise of room-temperature semiconductors such as CZT in the medical physics space has prompted the development of commercial benchtop semiconductor gamma-spectroscopy systems [101], but most available semiconductor detectors are still designed and produced for the broader radiation detection industry. We have adapted two such systems for use in preclinical biodistribution studies and briefly report their characteristics here.

Although most of the work in this dissertation investigates ^{225}Ac and ^{213}Bi and can be conducted with the Hidex AMG, we included this brief investigation to illustrate the potential and limitations of the systems for αRPT. Superior energy resolution from semiconductor detectors can also be utilized for the separation of ^{225}Ac from co-injected ^{134}Ce, eliminating overlap between the ^{213}Bi energy peak at 440 keV and the β^+ annihilation peak at 511 keV. Our group has conducted preliminary efforts towards ^{225}Ac/^{134}Ce co-injections and ^{227}Th/^{223}Ra separation using the capabilities of these systems. These data are currently unpublished and not included here.

ORTEC HPGe IDM-200-V. The ORTEC IDM-200-V Interchangeable Detector Module (IDM) is a self-contained, mechanically cooled HPGe detector system designed as a modular piece for use in nuclear security, radiation survey, and industrial monitoring applications (Fig. 2.6). Each module contains a 85 mm × 30 mm (diameter × length) coaxial HPGe crystal with a Stirling cooler (no liquid nitrogen required).

The specific two units in our possession were previously used for RadMAP, a vehicle-based mobile radiation survey system for mapping urban environments [102]. A traffic accident occurred that resulted in damage to the detector systems on board, so the system performance is somewhat degraded relative to the commercial specifications.

H3D M400 CZT detector. The H3D M400 Custom Integrable Detector Module is a self-contained CZT spectrometer similarly designed as a modular, portable piece for use in radiation surveys, laboratory experiments, and medical imaging. Because CZT is a room-temperature semiconductor, the entire module is significantly smaller than the HPGe IDM (Fig. 2.7C). Four 11 px×11 px CZT crystals, each approximately 20.9 mm×20.9 mm×10 mm, are arranged in quadrants and allow 3D position sensing of events in the volume. The imaging capabilities of the device are not utilized in the current application as a gamma counter.

Custom 3D-printed sample holder. Neither the ORTEC IDM nor the H3D M400 were designed for biodistribution tissue measurements and, unlike the Hidex AMG, both lack a well-defined sample container. This component is essential for dosimetry to ensure identical geometric efficiency as well as practical stability between measurements. We designed a

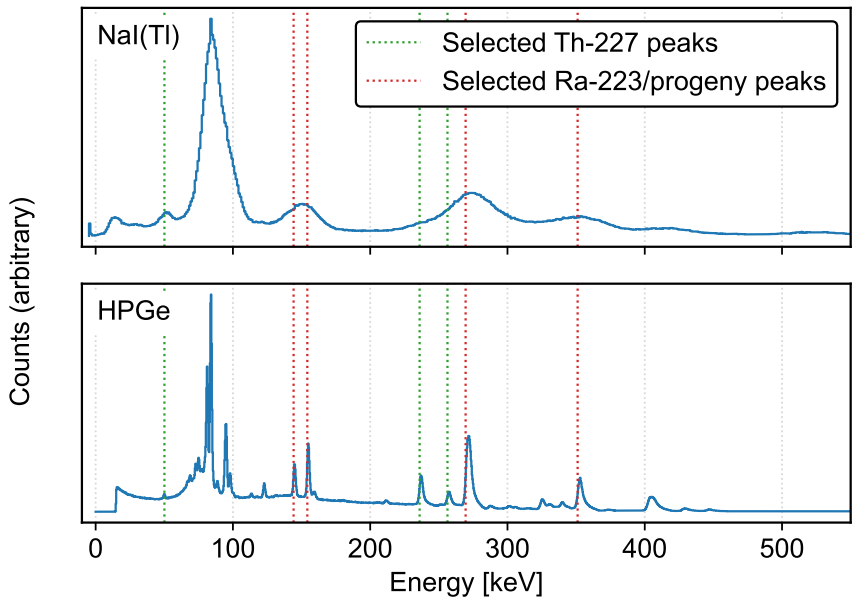

Figure 2.5: Comparison of NaI(Tl) and HPGe detectors for purposes of isotope separation using a mixed sample containing ^{227}Th and ^{223}Ra.

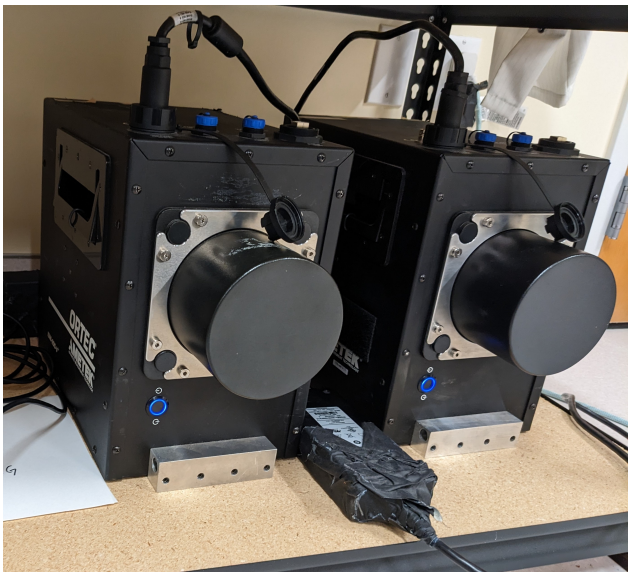

Figure 2.6: ORTEC IDM-200-V detector systems.

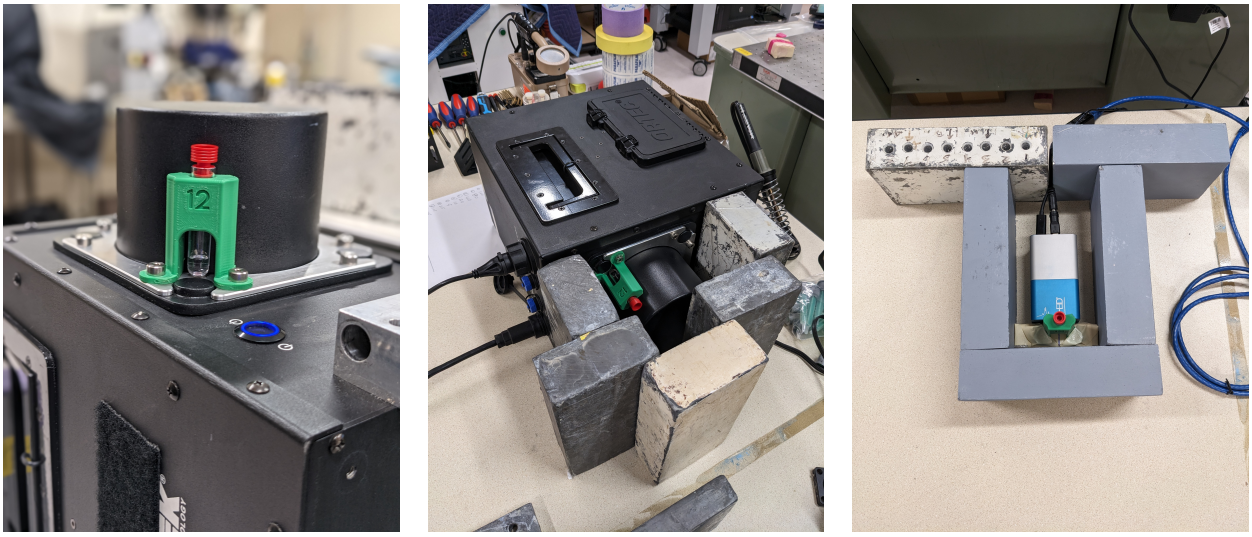

(A) 3D-printed sample holder affixed to the HPGe IDM.

(B) Sideways HPGe IDM orientation with lead shielding.

(C) Shielded BioD set-up using CZT M400 system.

Figure 2.7: 3D printed sample holder facilitates preclinical biodistribution measurements with semiconductor detectors.

sample holder,[4] attachable to the base plate of the IDM, that we 3D-printed from polylactic acid (PLA) using an Ultimaker device (Fig. 2.7A). The internal bore accommodates a standard cappable 12-mm diameter polystyrene test tube used in Hidex BioD studies. The holder is designed such that the sample tube is in contact with the external cap of the detector to minimize distance to the crystal.

Since the sample holder is secured to the IDM with screws, the entire system can be placed sideways such that the crystal is lower to the surface of the platform. This orientation offers a more favorable geometry for shielding with standard $2 \times 4 \times 8$ inch lead bricks (Fig. 2.7B). The same sample holder was also used for a shielded BioD setup using the H3D M400 CZT system by elevating it such that the bottom of the tube aligned with the center of the detector face (Fig. 2.7C).

Background reduction. The initial system setup in Fig. 2.7A had the IDM positioned on a stand such that the base of the crystal was aligned with an adjacent table that supported a single $2 \times 4 \times 8$ inch lead brick from one direction (towards the preclinical imaging facility, believed to be the dominant source of background). The system adjustment in Fig. 2.7B with the IDM on its side allowed for more complete shielding coverage. Some consistency in the geometric position of the sample was sacrificed (e.g., liquid samples no longer collected in the

[4] All design and fabrication credits go to Shixian Du, graduate student at UCSF, and Benjamin Huang, research scientist at UC Berkeley.

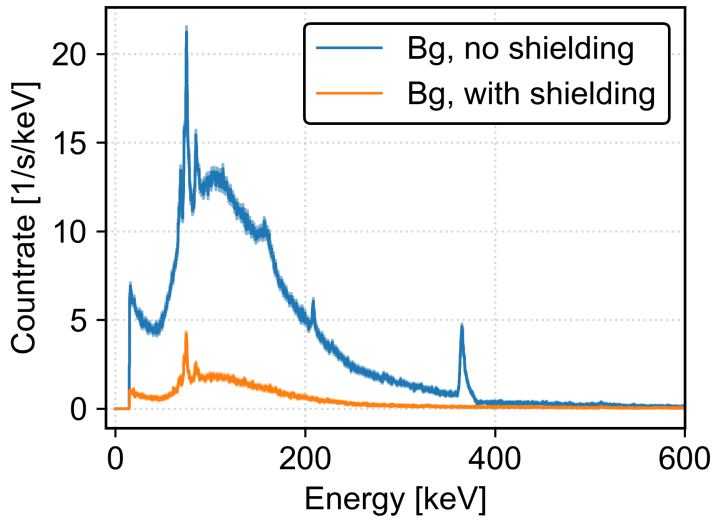

Figure 2.8: Side-sitting detector configuration with lead brick shielding (Fig. 2.7B) reduces the background count rate in the laboratory from 1982 ± 2 cps to 304 ± 1 cps.

bottom of the tube), but the background rate was significantly improved, from 1982 ± 2 cps to 304 ± 1 cps (Fig. 2.8).

Energy resolution and sensitivity comparison. The relative energy resolution and sensitivity of the HPGe ORTEC IDM and CZT H3D M400 were compared to the NaI Hidex AMG to evaluate their potential for use in ^{225}Ac and ^{134}Ce co-injection biodistribution studies. Figure 2.9 explores the energy resolution of the three detector systems using standard vials prepared with 37 kBq (1 µCi) of each isotope (^{225}Ac and ^{134}Ce) as measured using an argon gas dose calibrator.[5] The NaI gamma counter showed significant overlap between the peaks at 440 keV (^{213}Bi) and 511 keV (annihilation photons from ^{134}La β^+ emissions), obscuring each of the two signals (Fig. 2.9A). The CZT and HPGe detectors distinguished both of these peaks, as well as the weak 465 keV emission from ^{209}Tl between them.

A Gaussian model was fit to each peak to quantify the FWHM energy resolution in Fig. 2.9B. The CZT and damaged HPGe detectors were comparable and both superior to the NaI detector. Since cooled HPGe detectors typically serve as the gold standard for energy resolution, we attribute reduced performance to the vehicle accident described previously. Characterization of these devices at the time of initial purchase showed spectral resolution better than that in this investigation, achieving 0.2% (1.3 keV) FWHM at 662 keV. A symmetric Gaussian is also unlikely to be the best model for peaks in either semiconductor detector. The CZT detector showed characteristic low-energy tails due to hole trapping and incomplete charge collection, whereas the damaged HPGe detector exhibited high-energy

[5] There is some evidence that gas-based dose calibrators are inaccurate at this activity level, so the 1-µCi measure should be treated as approximate. Since the same vials were used for all systems, the relative comparisons are accurate.

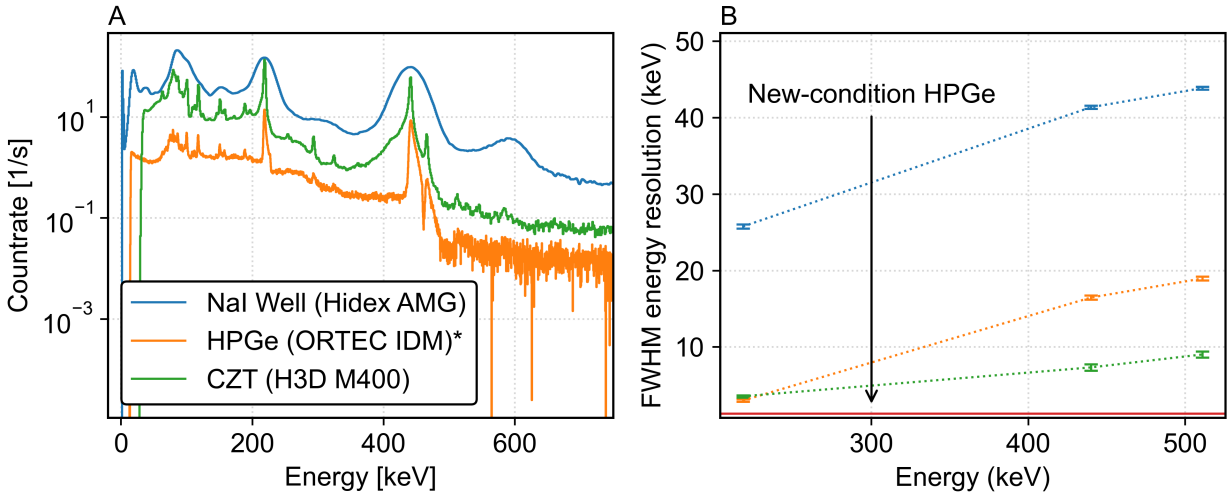

Figure 2.9: Energy resolution and sensitivity comparison between Hidex NaI(Tl), ORTEC IDM HPGe, and H3D M400 CZT detectors for separation of ^{225}Ac and ^{134}Ce. (A) Log-scale energy spectra of mixed samples containing 37 kBq (1 µCi) of each isotope. *The performance of the HPGe detector suffered due to its sub-par condition. (B) Comparison of energy resolution at the ^{221}Fr, ^{213}Bi, and annihilation peaks. Uncertainty propagates one standard deviation of the fit parameters. An HPGe detector in new condition has been observed previously with spectral resolution of 1.3 keV FWHM at 662 keV (red line extended for visual clarity).

tailing.[6] Nonetheless, both systems showed improvement over traditional NaI for separation of the two peaks of interest for ^{225}Ac/^{134}Ce co-injection.

Conversely, at 218 keV and 440 keV, the detection efficiency of the Hidex AMG was approximately 26 times greater than the HPGe IDM and 9 times greater than the CZT M400. This result was expected, due to the superior geometric efficiency provided by the Hidex AMG as an instrument designed for high-sensitivity ex vivo tissue studies. The CZT M400 showed superior sensitivity than the HPGe IDM due to the higher stopping power of CZT relative to HPGe and similar geometric configurations.

2.7 Summary

Gamma counting is a powerful tool for ex vivo studies of α-particle radiopharmaceuticals that also emit photons. We reviewed the general protocols for biodistribution measurements and macroscopic dosimetry with details regarding the main spectroscopy system used in

[6] We expect low-energy tails in semiconductor detectors and are unsure of the cause of the high-energy "tails" in the damaged detectors.

this dissertation, the NaI(Tl) Hidex AMG. A procedure to quantify the relative amounts of ^{225}Ac and ^{213}Bi in a non-equilibrium state was described for use in subsequent chapters. We additionally reported the characteristics of two simple gamma counting setups using commercially available semiconductor detectors and a custom 3D-printed sample holder. As expected, these systems performed better than the NaI(Tl) Hidex AMG in spectral resolution, but came with a sensitivity trade-off due to the less favorable sample geometry relative to a well counter.

Chapter 3

αRPT dosimetry at smaller scales

Macroscopic dosimetry techniques, such as ex vivo biodistribution measurements, are used to evaluate the pharmacokinetics, targeting, and effects of αRPs by organ or tumor site. They are common in preclinical drug discovery studies, and most estimates provided by in vivo PET and SPECT imaging systems with greater-than-millimeter spatial resolution similarly treat organs and tumors as monolithic structures for dose evaluation. However, macroscopic dosimetry provides an incomplete picture of αRPT. The short range of the α-particle, which gives αRPT the potential for selective targeting, can also result in heterogeneous patterns of energy deposition within tissues. Inhomogeneous dose can produce unexpected results for therapy or toxicity if treated the same way as uniform dose distributions from external-beam radiation. Tools are therefore needed that evaluate dose on a *small-* or *micro*-scale. In this chapter, we introduce and review the concepts of dose heterogeneity (Sec. 3.1), small-scale dosimetry (Secs. 3.2, 3.4), and autoradiography (Sec. 3.3) to contextualize the methods and examples in the remainder of this dissertation.

3.1 Dose heterogeneity

Much of our understanding about radiation effects in tissues is derived from clinical experience with external-beam photon and electron radiation, using treatment plans optimized to deliver uniform dose to cancerous volumes. Unlike external-beam radiation therapy (EBRT), RPT does not have granular control over the delivery of the source radiation after its administration in a patient. Dose heterogeneity in αRPT is a phenomenon resulting from the physical characteristics of α-particle emissions and nonuniformity of target expression. The targets of RPT, most commonly antigens and cell membrane protein receptors, can exhibit nonuniform expression on cells [29]. Therapeutic radioisotopes will thus also be nonuniformly distributed. Since α-particles have a short range, each site of α-emission has a small sphere of influence in which energy is deposited, resulting in localized pockets of dose within tissues. Compared to photons and electrons (from EBRT or βRPT), α-particles also have very high LET, exacerbating the difference between dosed and undosed regions.

Photon and electron therapies deliver dose uniformly (to a good approximation) to subcellular structures because secondary electrons and β-particles travel several millimeters through tissue. In contrast, the α-particle path may or may not intercept DNA structures in the cell nucleus, depending on the emission location and direction. The same outcome is not guaranteed for all cells, because stochasticity affects whether a particle traverses a DNA strand, whether a single- or double-strand break is induced, whether repair occurs, etc. This stochasticity affects other types of radiation, but the low activities in αRPT render the modality more subject to randomness than βRPT or EBRT. Tronchin et al summarize the issue succinctly: "assuming a uniform activity distribution to determine mean absorbed doses will not always provide physically or biologically meaningful information, and can be poor predictors of the biological effect of alpha-particle radiation [103]." We investigate several examples of dose heterogeneity in the preclinical studies in this dissertation.

One clinically relevant example of dose heterogeneity has been observed in the treatment of bone-metastatic prostate cancers using ^{223}Ra. Macroscopic dosimetry of red marrow dose in trials of ^{223}Ra does not necessarily correlate with patient hematological toxicity, either under- and over-predicting toxicity in different instances. In one study, compartment models calculated that 1.5 Gy absorbed dose would be delivered to marrow over the course of a standard six-injection treatment [104]. When the RBE of α-particles was considered, the equivalent dose surpassed the clinical toxicity threshold at 2 Gy (based on studies of ^{131}I βRPT patients [105]), but minimal toxic effects were actually observed in patients [13]. A different study utilizing planar imaging and blood samples estimated marrow absorbed doses below the 2 Gy threshold in all patients, yet observed severe anemia in several and forced cancellation of the treatment course due to side effects [106]. A small-scale model was required to explain that preferential localization of ^{223}Ra on only the surface of the bone marrow could be responsible for the discrepancies [107].[1]

3.2 What's in a name? Small-scale, sub-organ, micro-scale, and micro-dosimetry

So far, we have described two highly related but subtly different effects of the α-particle range on dose distributions: (1) the combination of biological heterogeneity and short range lead to inhomogeneities in uptake and energy deposition, and (2) the sparsity of emissions and similarity between target structure size and particle range yield stochastic variations from cell to cell. These two ideas are easily conflated such that the terms sub-organ, small-scale, micro-scale, and microdosimetry are often used interchangeably in literature. The most correct terminology would explicitly separate the concepts of spatial scale and stochasticity.[2]

[1] Remarks: This model suggested that only a thin layer of bone marrow is irradiated by α-particles, which only resolves the discrepancy in case where macroscopic dose overpredicts toxicity. In the second study, it is unclear whether the < 2 Gy specification was RBE-corrected or not, which could explain the discrepancy.

[2] It could well be argued that the inhomogeneous binding of radiopharmaceuticals is also a stochastic process, but for convenience we are referring to energy and particle-track modeling here.

Box 3.1: Tumor heterogeneity. Dose heterogeneity in the context of αRPT dosimetry is different from the concept of tumor heterogeneity commonly discussed in cancer biology. The latter describes that morphological or physiological differences can occur within tumors, between tumors in an individual, or between tumors across individuals [108, 109]. The former specifically refers to non-uniform distributions of dose within a structure (organ or tumor). To illustrate, suppose that two tumors in the same subject treated with αRPT are evaluated. If one exhibits large variations between highly dosed and undosed sub-regions, then it demonstrates dose heterogeneity. If the other is uniformly saturated, then subject as a whole shows tumor heterogeneity as defined by the different tumor responses. It is possible and likely that intratumoral heterogeneity can result in dose heterogeneity in αRPT.

For example, one would not have "small-scale dosimetry" or "microdosimetry," but perhaps "small-scale deterministic dosimetry" and "micro-scale stochastic dosimetry." These descriptions are somewhat onerous, so we use the following shorthands in this work:[3]

- **Macroscopic dosimetry** (or just **dosimetry**)**:** *macroscopic deterministic dosimetry*, or assessments of absorbed dose characterizing entire organs or tumors.
- **Sub-organ dosimetry:** *sub-organ deterministic dosimetry*, or assessments of absorbed dose evaluated at spatial scales smaller than a whole organ or tumor. (Note that the "sub-organ" shorthand does not preclude tumor dosimetry.)
- **Small-scale dosimetry:** *small-scale deterministic dosimetry*, or assessments of absorbed dose evaluated at spatial scales on the order of the α-particle range, not greater than several hundred microns. Generally requires ex vivo imaging with autoradiography or digital autoradiography.
- **Micro-scale dosimetry:** *micro-scale deterministic dosimetry*, or assessments of absorbed dose evaluated at a high degree of spatial resolution. This term can be redundant with small-scale dosimetry but usually implies higher spatial resolution, at the sub-cellular or cellular scale.
- **Microdosimetry:** *micro-scale stochastic dosimetry*, assessments of stochastic energy deposition at the sub-cellular or cellular scale. Stochastic dosimetry can be conducted at greater spatial scales, but this is the most common meaning of the term.[4]

[3] This nomenclature was presented by R. Bastiaannet in his microdosimetry talk at AAPM 2024 [110].

[4] In fact, there is precedent for differentiation between nanodosimetry (DNA-level stochastic dosimetry) and microdosimetry (cellular level stochastic dosimetry) [111].

The biological effects of αRPT will be well understood when each spatial scale is linked in a complete, robust model: when an in vivo imaging measurement (macrodosimetry) can accurately predict the sub-organ distributions seen in ex vivo measurements (small-/micro-scale), which can in turn extrapolate cellular and biological effects thanks to modeling of DNA damage (microdosimetry). Comprehensive reviews for past and current approaches to analytical, Monte Carlo, and track-structure microdosimetry modeling are provided by Hoffman and Tronchin [103, 111]. Here, we are concerned with the development and distribution of replicable methods for small-scale experimental measurements, interfacing with the macroscopic and microscopic boundaries where possible. The work in this dissertation entirely consists of non-stochastic dosimetry spanning macroscopic, sub-organ, and small-to-micro scales.

Let us consider the macro-to-micro boundary in more detail. Conventional in vivo imaging methods lack the spatial resolution to resolve small- or micro-scale activity distributions (cutting-edge specialized systems may be approaching sub-organ: Sec. 1.4). The endeavor to understand the basic science and characteristics of specific αRPs at the micro-scale thus requires ex vivo measurements and models that translate observations to human outcomes. For example, if a comprehensive preclinical study finds that a particular αRP delivers 80% of kidney activity to the cortex and 20% to the medulla (we have used arbitrary numbers), then a macroscopic in vivo measurement of activity A can be modeled as $0.8A$ and $0.2A$ for the two sub-structures, respectively. This macro-to-micro approach has been discussed in literature and modeled in select cases [29, 107], but the data still remain sparse. In rare instances where a biopsy can be collected from patients treated with αRPT, direct small-scale dosimetry is possible. Benabdallah et al have recently conducted small-scale dosimetry in seven patients treated with ^{223}Ra for bone-metastatic castration-resistant prostate cancer [66].

3.3 Autoradiography principles and systems

Autoradiography is the primary tool to study intratumoral and sub-organ dose heterogeneity in preclinical αRPT studies at therapeutic injected activities [112, 113]. Compared with in vivo preclinical PET or SPECT imaging, ex vivo digital autoradiography (DAR) offers higher spatial resolution ($< 100\,\mu$m) and sensitivity (up to 50%, geometry-limited) due to the contact imaging geometry and high efficiency for α-particle detection. The ability to directly image the therapeutic α-particle also simplifies quantitative dosimetry and avoids inaccuracies from the use of imaging surrogates [81].

Autoradiography utilizes radioactive signal produced in the sample itself ("auto") to construct an image ("radiogram"), which can be achieved through a variety of techniques and systems [114, 115]. Most commonly, the sample is placed in direct contact with the detection medium so that the location of energy deposition in the detector is nearly identical to the spatial position of emission in the sample. Over time, a 2D image of the emission location is accumulated without the need for complex reconstruction.

Two quantities fundamentally affect the degree to which interpretation of the detector

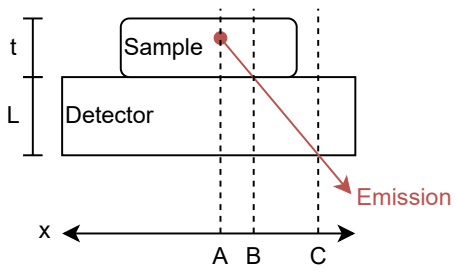

Figure 3.1: Autoradiography geometry with sample thickness t and detector thickness L. $x = A$ is the true spatial location of the emission, whereas $x = B$ represents the uncertainty of the measurement due to the sample thickness and particle range. The emission may deposit energy over the range from B to C inside the detector to further blurring effect.

interaction location as the emission location is accurate: (1) the thickness of the sample t and (2) the range of the particle R (Fig. 3.1). Particles emitted from point A enter the detector face at point B, a distance $\sqrt{R^2 - z^2}$ away from A where z is the vertical position in the tissue running from 0 to t. The maximum difference $B - A$, projected into the plane of the image, is R, in the limit where the emission occurs exactly at the interface and the particle travels parallel to the image plane. Energy is deposited over the region between points B and C such that the detector thickness L also affects the spatial resolution of the image, but we consider this to be a property of specific systems rather than a fundamental limit. Oblique emissions can be blocked to improve the spatial resolution of the system with microcapillary array plates, similar to the use of a parallel-hole collimator in traditional SPECT [116].

3.3.1 Digital autoradiography systems

Comprehensive reviews of analog and digital autoradiography systems describing their principles, advantages, and disadvantages have been conducted by Miller, Örbom, and Bäck [113, 115]. Both phosphor-screen and phosphor-storage-type analog systems can have excellent resolution across large fields of view accommodating whole-body (animal) samples. For quantitative dosimetry of αRPs, however, single-particle DAR is currently favored because it removes restrictions on dynamic range, improves quantitative workflows and postprocessing, and enables temporally sensitive analyses.

Single-particle DAR can be executed with scintillator-, semiconductor-, and gas-based systems. All form factors are capable of sufficiently high spatial resolution for small-scale dosimetry (20–80 µm), with the highest resolutions (sub-µm, visible particle tracks) achieved by cooled direct-detection and scintillator-EMCCD systems [117, 118]. The drawback of most solid-state or cooled-CCD systems is a restricted field of view (FOV) that bottlenecks practical use in preclinical drug development (under 2 cm^2 active area). So-called scientific CCD camera systems have long been in use in astronomy, physics, and basic science research and can be implemented in large-area (8 cm × 8 cm) configurations while maintaining superior energy and spatial resolution, but these have not been broadly demonstrated for RPT applications [119, 120]. Gas autoradiographs have shown the largest active imaging areas among commercial digital systems, up to 23 cm × 23 cm. Semiconductor and gas detectors

can generally accommodate higher count-rates and temporal precision (sub-ms) compared to CCD/CMOS-based imagers (∼10 ms).

Readers are directed to Miller's review for specifications of currently available commercial imagers [113]. Several selected systems are discussed below with attention to particle discrimination capabilities, which are of interest to the study of αRPs that are in vivo generators (Sec. 1.3). Separation of isotopes can be achieved through measurement timing, selective attenuation, or energy discrimination:

- **Measurement timing:** Over two separate acquisitions before and after the decay of the shorter-lived nuclide, different intensities indicate the regions which originally contained that isotope. This method has been demonstrated in a dual-isotope ^{125}I/^{99m}Tc study in rats [121], and, relevantly, identification of non-equilibrium ^{225}Ac progeny in mice [58].

- **Attenuation:** Two acquisitions are collected, one with a selectively attenuating filter for one of the isotopes. For example, use of a copper foil blocks 99.9% of low-energy ^{35}S electrons but only 30% of medium-energy ^{32}P electrons, resulting in a phosphorus-enhanced image [122]. Two acquisitions are required.

- **Energy:** Sufficient energy resolution can discriminate charged-particle emissions of different energies as fingerprints for different isotopes. Semiconductor autoradiographs, which directly utilize ionized charge as signal, provide higher energy resolution than their scintillator-based counterparts and are best suited for this method. The data is acquired in a single image.

The Biomolex 700 Imager, a double-sided silicon strip detector (DSSD), has been characterized and used mostly for β-particle detection rather than αRPT, although imaging capabilities have been shown for ^{211}At in mice [123, 124]. The device has spatial resolution of 154 µm in the field of view of a standard microscope slide (75 mm × 25 mm), with energy resolution sufficient for segmentation of the 35-keV ^{125}I γ-ray from ^{131}I β-emissions.[5] Incorporation of more complex modeling and mixed temporal-energy segmentation enabled separation of ^{125}I/^{131}I/^{18}F and ^{18}F/^{177}Lu/^{99m}Tc mixtures [124].

The Timepix series is a line of CMOS read-out chips developed at CERN in collaboration with Medipix, now commercialized by Advacam. These devices can be bonded to a variety of semiconductor sensor materials, most commonly silicon, and have a degree of application-specific modularity enabled by the choice of tiled, large-FOV (14.3 cm × 14.3 cm), slow-readout (10 FPS) or fast, small-FOV (1.4 cm × 1.4 cm) systems. Timepix has been utilized in a wide variety of applications in microscopic medical imaging, radio- and brachytherapy, and space dosimetry, with one study to date investigating ^{227}Th for αRPT in a small-FOV configuration with particle-track resolution [125]. The acquisition was quantitative but uncalibrated, and could in principle be adapted for quantitative dosimetry. Although the measured α-particle energy spectrum was consistent with expectations for the range of

[5] The energy resolution can be estimated from Fig. 7 of [124], approximately 10 keV FWHM at 140 keV.

emissions in the ^{227}Th decay chain, the low counts in the study preclude evaluation of the energy discrimination capabilities for α-particles [126].

The ionizing-radiation quantum imaging detector (iQID) camera (QScint Imaging Solutions, LLC) is a scintillation-based DAR system that has been utilized for numerous preclinical αRPT studies to date [1, 4, 127]. Its main advantage is practicality and commercial support. Its relatively large FOV (12.6–50.3 cm^2) enables simultaneous imaging of 10–30 tissue slices in an acquisition while maintaining good spatial resolution (20–40 µm effective pixel size) and high efficiency for alpha-particle detection. Use of different scintillators and attenuation materials can emphasize specific signals, such as selective blocking of α-particles to identify β-particles from a joint source [128]. iQID has poor energy resolution for charged particles, but the intensity of scintillation light can in principle be used to discriminate large differences in particle energy to reject noise, separate ^{241}Am α-particles from ^{252}Cf fission fragments [128], or identify differences in α- or β-particle distribution [129]. Particle discrimination with iQID is explored in more depth in Chapter 8.

The first iteration of **the scintillation-based alpha-camera** developed by Bäck and Jacobsson was not a single-particle imager, but linearity between accumulated pixel intensity and activity enabled quantitative imaging via calibration with samples measured with a γ-counter [130]. A second-generation system incorporates an EMCCD camera, allowing for single-particle imaging with spatial resolution estimated at 20–35 µm FWHM [115]. Unlike most digital autoradiographs, the FOV is optically adjustable and can accommodate whole-body mouse autoradiography at the cost of spatial resolution.[6] Although it has been utilized for a range of αRPT drug development studies, the system is not commercially available, and its particle discrimination capabilities have not been estimated.

3.4 From autoradiography to dosimetry

The past decade has witnessed a shift in the use of autoradiography from qualitative confirmation of targeted structures to quantitative measurements of absorbed dose. However, even quantitative autoradiography produces only two-dimensional estimates of activity in a single plane, whereas dose is an energy density that receives contributions from emissions in a three-dimensional structure. DAR dosimetry is therefore an exercise in modeling as well as instrumentation. Several approaches to this challenge are discussed in literature, including use of a Gaussian smoothing filter, spherical shell projections, or source-specific Monte Carlo simulations [123, 131]. However, the conceptually simplest approach for αRPT is to consecutively slice and measure a thin volume of tissue spanning the range of the α-particle of interest so that all possible geometric contributors to cross-dose are measured. One implementation of this procedure, as well as its limitations and several alternatives, are discussed in Chapter 4.

The International Commission on Radiation Units and Measurements (ICRU) has identified three main methodologies by which absorbed dose can be calculated from an activity

[6] iQID also has this capability with a fiber-optic stage extender, but only up to 80 mm FOV diameter.

measurement in RPT [31]: direct Monte Carlo (MC), dose point kernel (DPK) convolution, and the MIRD S-coefficient (or S-value) formalism (described in Chapter 2). All three fundamentally rely on an MC simulation, with increasing layers of abstraction that add practicality at the cost of accuracy. None of the approaches are inherently macro- or microscopic by nature, but there are connotations about scale depending on how they are most commonly implemented in the field. To describe each in brief:

- **Direct Monte Carlo:** a 3D activity distribution measurement in a volume is entered into a validated MC framework, which is a computerized simulation program that enforces first-principles physics rules to predict interactions of radiation with matter. The longer the simulation is run, the more statistically accurate the quantitative estimates become. The premiere tool for micro-scale and microdosimetry.
- **Dose point kernel:** MC simulation (or, sometimes, an analytical method) is used to compute a DPK, a normalized distribution of the energy deposition from a particular radiation source in a homogeneous medium. Absorbed dose is calculated via convolution of the DPK with the 3D activity distribution measurement. The most common tool for small-scale dosimetry, and frequently used for clinical dosimetry of βRPT.
- **MIRD S-values:** MC simulation is used to compute the relative dose from each relevant spatial structure to each other one, normalized to the structure's internal source activity (most commonly applied between organs). Then, an activity distribution measurement is parsed to evaluate the activity of each region that should be used in the formalism described in Chapter 2. Generally a macroscopic dosimetry method, although increasing efforts are being made to simulate smaller-scale S-values.

Since the S-value method pre-calculates all relevant parameters, it is often regarded as the most practical and closest to a clinical standard, particularly for nuclear medicine imaging and βRPT. Implementation assumes uniform distribution of dose within source (activity-having) and target (dose-receiving) regions, usually organs. Because this approach can be inaccurate in αRPT, recent efforts have increasingly investigated S-values for sub-organ, micro-scale, and even cellular-scale structures [107, 123, 127, 132]. Regardless of the spatial scales involved, the S-value method fundamentally assumes that a consistent geometry between source and target regions is maintained across subjects and patients.

The DPK method limits the computation to a single MC simulation and the convolution. Unlike the S-value approach, it accounts for the specific anatomical geometry of the subject or patient, and therefore is the most common method for personalized dosimetry (clinically) and sample-specific dosimetry (preclinically) [31]. One important nuance is that use of the single kernel for all cases renders this a non-stochastic method. Although the DPK approach is particularly advantageous for handling the heterogeneous *source* distributions found in αRPT, it is ill posed to describe heterogeneous *media*. DPK convolution is the main dose calculation method used in this dissertation, with specific implementation details and considerations discussed in Chapter 4.

Direct Monte Carlo is the most accurate method of the three and must be used if neither S-values nor DPK convolution are relevant to the dosimetry application. MC also regularly appears in experimental studies in which DPK or S-values may not have been rigorously validated yet, and is the main tool for the study of stochastic dosimetry methods.

3.5 Summary

In this chapter, we briefly reviewed the key concepts and motivations underlying small-scale deterministic dosimetry with autoradiography. The short range of the α-particle and inhomogeneous distribution of biomarkers give rise to dose heterogeneity within target and off-target structures. External-beam models based on uniform dose distributions fail to accurately predict toxicity and therapeutic efficacy for these inhomogeneous dose distributions. Therefore, new data and models are required to accurately characterize small-scale dose distributions and their biological effects. The remainder of this dissertation is dedicated to the development and demonstration of small-scale dosimetry methods and their implementation in preclinical studies of αRPs.

Chapter 4

Small-scale α-particle dosimetry methods with iQID digital autoradiography

This chapter describes methodology for small-scale α-particle dosimetry with an iQID camera digital autoradiography system, including characterization of the device, quantitative corrections, and routine and novel post-processing methodologies. We draw from Papers 1 and 2, in which these procedures were developed for specific use cases (^{211}At in a canine model and ^{225}Ac in a murine model, respectively) but remain broadly applicable to DAR dosimetry studies [1, 2]. Generalizable concepts and protocols are discussed through these specific examples, with some additional detail not published in either manuscript. For preclinical findings and results, see Chapters 5 and 6.

4.1 Overview of the workflow

Alpha-particle dosimetry with digital autoradiography is a multi-step process involving sample preparation, radiation detection, image processing, and data analysis. Figure 4.1 provides a simplified overview of these steps. To quantify the presence of an α-emitting radioisotope in a tissue, the sample is sectioned into thin slices which are affixed to the acquisition stage of the digital autoradiography device. An image containing α-particle emissions from all samples on the stage is acquired over several hours or overnight. Post-processing tools re-align the discrete slice images into an activity stack, which undergoes a dose-rate computation such as dose kernel convolution to quantify the self- and cross-dose-rates of slices in the stack. The output is a dose-rate image of the slice at the center of the stack, or in the middle of the original tissue sample. Further analysis, such as dose-rate-volume histograms, time-dose-rate-curves, pathological and histological correlation and comparison, and tumor control probability, can be conducted on dose-rate images.

Each of these sub-protocols—sample preparation, digital autoradiography, image pro-

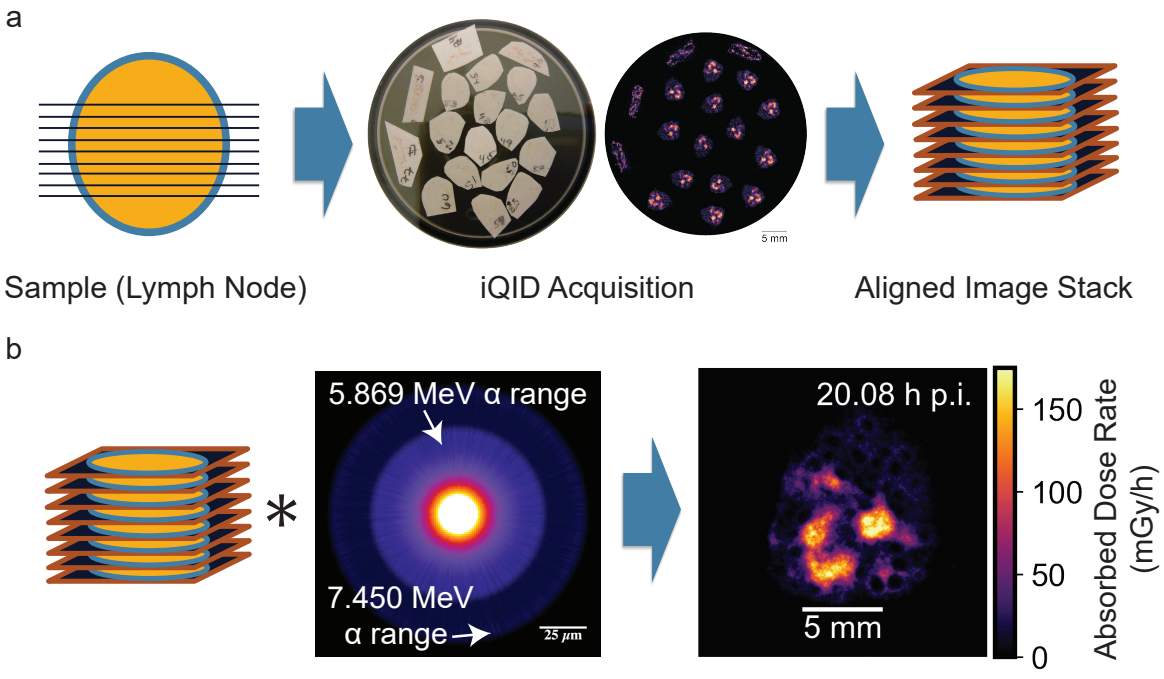

Figure 4.1: Overview of dosimetry with iQID digital autoradiography. (A) Thin (10–20 µm) cryosections are cut from a tissue biopsy or dissected organ (e.g., canine lymph node), imaged in 2D with an iQID device, and registered into a 3D volume. (B) Convolution of the registered activity image stack with a 3D Monte Carlo dose kernel produces dose-rate maps of canine lymph node slices.

cessing, dose-rate computation, and dosimetry analysis—can be individually optimized for the task at hand. In some cases, these procedures may not be standardized in the field and are active areas of research. We describe our approaches and rationales for each of these steps in detail.

4.2 Sample preparation

Alpha-particle dosimetry is conducted on cohorts of animals that have received a known quantity of an αRP to assess the distribution and effect of the drug in a biological model. The treated subjects are either biopsied or euthanized at specified time-points over the next several hours, days, or sometimes weeks to investigate the presence of the αRP in various tissues of interest at that time. Organs or tumors collected from the subject are placed into an optical cutting temperature medium (OCT, Tissue-Tek) and frozen at −10 °C. In time-sensitive measurements such as those measuring redistributed progeny (Ch. 8), the procedure can be hastened with the use of liquid nitrogen for flash-freezing. The frozen

samples are then sliced in a cryotome to the designated slice thickness. 10–20 µm slice thickness is typical for αRPT measurements to maximize α-particle escape and detection efficiency. However, thinner slices are more delicate and prone to tearing and stretching than thicker slices.

4.3 iQID camera system

The iQID camera device comprises a disposable scintillator in direct contact with a microchannel plate image intensifier and lens that projects scintillation light onto a 4 megapixel (2448 px × 2048 px) Point Grey Research Grasshopper®3 camera with a CMOSIS CMV4000 CMOS sensor [128]. Alpha-particles generated in the tissue escape and deposit in the scintillation screen, which can be selected based on application. ZnS:Ag (EJ-440; Eljen Technology) is the most common scintillator for α-particle imaging thanks to its commercial availability and extremely high light yield (95,000 photons/MeV) [133]. The scintillation light is amplified with a spatial-information-preserving image intensifier and imaged onto the CMOS sensor using a CCTV camera lens. Each α-particle interaction event appears in an image frame as a small cluster of contiguous pixels on the CMOS camera. Multiple α-particle events may be present in a single image frame and are processed using centroid estimation into single events in listmode data with spatial and temporal information. iQID is thus an event-by-event measurement device in which one count is recorded per detected α-decay. Real-time iQID image previews and acquisition settings are viewed in a LabVIEW™ acquisition software provided with the device. A top-down view of tissue samples on the iQID device, and the subsequent iQID event image, can be seen in Fig. 4.1A (center).

4.3.1 Device characterization and calibration

Device characterization based on previous publications is summarized in Table 4.1 [128, 134]. The intrinsic efficiency of iQID for alpha particles between 3.70 and 7.95 MeV using ZnS:Ag was measured to be 98% ± 1% in a 4π geometry [134], or one-half that for the 2π geometry typically used for tissue studies. Images are measured at 20–30 frames per second (FPS), corresponding to 33–50 ms exposure time, although high-FPS applications are discussed in Chapter 8. A calibration scale can be used to determined the effective pixel size (Fig. 4.2). The default 40-mm diameter field-of-view (FOV) is expandable up to 80 mm using a fiber optic taper and is inversely related to the spatial resolution (19.5–39 µm effective pixel size). At the larger diameter, 10–30 tissue slices can fit on the stage, enabling concurrent imaging of one or two complete mouse organs or tumors.

To calibrate the device for ^{225}Ac experiments at UCSF China Basin, an array of droplet samples of known radioactivity was prepared and measured to characterize the quantitative accuracy. The same method can be used for any water-soluble radiometal being investigated.

Solutions of 185 Bq/µL were prepared from stock dilution and serially diluted by factors of two down to 5.78 Bq/µL with small volumes reserved at each dilution. 2-µL droplets of

Table 4.1: iQID camera[a] characteristics, summarized from [128] and [134].

Characteristic	**Quantity**	**Notes**
Spatial resolution	32.3 µm LSF FWHM	at 24.4 µm effective px size
	64.1 µm LSF FWHM	at 62.0 µm effective px size
Field of view	40 mm	19.5 µm effective px size
	80 mm (expander attachment)	39.0 µm effective px size
Intrinsic efficiency	0.984	Composite α source[b]
Geometric efficiency	0.50	1.0 with scintillator sandwich [128]
Frame rate	25 FPS (40 ms frame window)	Full FOV maximum: 90 FPS
Energy resolution	Poor: insufficient to distinguish α-particles of 5-8 MeV	

[a]The prototype camera in these studies is similar to the now commercialized iQID Nsight Medium.
[b]NIST-traceable electroplated disc source containing Pu-239, Am-241 and Cm-244 (Eckert & Ziegler Analytics), with α particles ranging from 3.70 to 7.95 MeV.

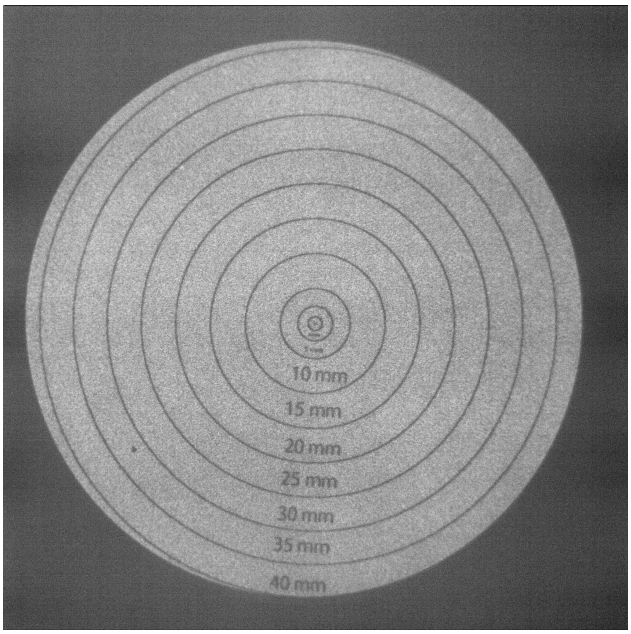

Figure 4.2: Concentric circle scale imaged under the iQID optical camera to calibrate imaged pixels to physical distance (45.3 px/mm in this example).

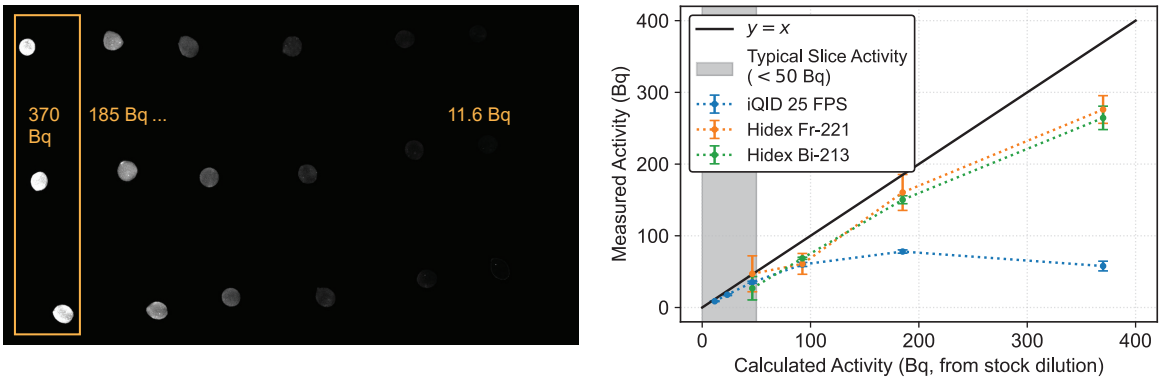

Figure 4.3: iQID calibration of ^{225}Ac using serial dilutions. (Left) iQID image showing relative count intensity of serial dilution droplets from 370 to 11.56 Bq. (Right) Calibration curve of iQID measured activity at 25 FPS after geometric efficiency and radioactive decay correction, compared to activity measured using Hidex NaI(Tl) gamma-counter at 218 keV (^{221}Fr) and 440 keV (^{213}Bi). Activities below 46.25 Bq were not recorded in Hidex due to sensitivity limitations.

each concentration were prepared ($N = 3$ per concentration), counted in a Hidex NaI(Tl) automatic gamma counter (60 s, 175–250 keV and 385–490 keV windows with Gaussian and linear background fits), pipetted onto ZnS:Ag scintillator paper, and evaporated in a fume hood at room temperature, leaving circular samples of 370, 185, 92.5, 46.25, 23.13, and 11.56 Bq as calculated from the stock dilution (Fig. 4.3). ^{225}Ac was provided as a dissolved chloride salt in water, and therefore it did not vaporize at room temperature during the procedure. The swatch was measured in iQID at 25 FPS for 24 h.

For activities below 46.25 Bq, the mean spatial pileup loss was $23.8\% \pm 0.7\%$, yielding an absolute efficiency of 38% when including 50% geometric efficiency. Greater saturation occurred at higher activities beyond the range of tissue activities in the ^{225}Ac studies described in this dissertation. These effects may warrant consideration for high-activity applications.

4.3.2 Acquisition modes

iQID list-mode data reports the spatiotemporal coordinates (x, y, t) of scintillation light clusters detected on its CMOS camera. These list-mode coordinates are obtained on-the-fly as the attached GPU filters each frame and identifies cluster centroids through a series of protocols called frame parsing [135]. During this process, the $n \times n$ image in the neighborhood around each light cluster is evaluated for its centroid as well as properties such as the eccentricity, kurtosis, number of triggered pixels, and total signal intensity, among others. Different acquisition modes record different sets of information:

- Compressed Processed Listmode: the default acquisition mode for most applications.

List-mode data contains spatiotemporal coordinates and various properties of scintillation light clusters in a compressed file.

- Cropped Listmode: an analytical development mode in which the original scintillation light cluster images are saved to disk alongside the list-mode data. Consumes more data storage. Recommended for research on event selection.
- Full Listmode: a simple acquisition mode recording every triggered pixel value and its intensity. Minimal uses for most users, except when used with Offset Listmode.
- Offset Listmode: an add-on to the full or compressed listmode files tracking several meta-data parameters during the acquisition, including the real elapsed time, number of missed images, and device temperature. Necessary for debugging and for research that relies on precise timing.

Unless otherwise mentioned, all studies use the Compressed Processed Listmode acquisition mode to analyze the activity distribution of the sample. Several applications of the Cropped and Offset Listmode acquisition modes are discussed in Chapter 8.

4.3.3 Frame-rate correction

Many αRPT isotopes have complex decay chains with α-emitting progeny. Since the effective iQID pixel size is larger than the nuclear recoil range ($< 100\,\text{nm}$), if the progeny half-life is on the order of the iQID frame-rate, it is possible for multiple α-particles to be emitted in the same frame and same pixel. These will be recorded as only one event with the second particle effectively missed. A scalar correction based on the frequency of this occurrence is derived below.

iQID frame-rate correction: Let an iQID exposure window be defined by a start time of $t_0 = 0$ and end time t_1. What is the probability that a parent decay at time $t \in [0, t_1]$ will be followed by a progeny decay in the same window?

The probability of a radioactive decay as a function of time t' is $P(t') = 1 - e^{-\lambda t'}$. This will apply to the decay of the short-lived progeny. Assuming the parent half-life is long compared to t_1, there is uniform probability for its decay to occur at time dt within $[0, t_1]$. Let the progeny decay with constant $\lambda = \ln(2)/t_{1/2}$. Explicitly:

(A) Probability that decay of the parent happens within the window at time dt : $\dfrac{dt}{t_1}$

(B) Probability that a subsequent progeny decay occurs by t_1 : $P(t_1 - t)$

The probability of a double-decay P_d in the same exposure window is the integral of (A) multiplied by (B).

$$P_d = \int_0^{t_1} P(t)\frac{dt}{t_1} = \frac{1}{t_1}\int_0^{t_1}(1 - e^{-\lambda(t_1 - t)})dt$$
$$= 1 - \frac{1}{\lambda t_1}e^{\lambda(t-t_1)}\Big|_0^{t_1} = 1 - \frac{1}{\lambda t_1}(1 - e^{-\lambda t_1}).$$

^{225}Ac case study: Let us apply this derivation in the case of ^{225}Ac measurements in a typical iQID acquisition at 25 FPS (40 ms exposure). The decay from ^{221}Fr to ^{213}Bi through ^{217}At emits two α-particles with a $^{221}\text{Fr} \longrightarrow {}^{217}\text{At}$ half-life of 4.8 min and a $^{217}\text{At} \longrightarrow {}^{213}\text{Bi}$ half-life of 32.3 ms. The above derivation applies:

1. The "parent" half-life is long compared to the exposure window: 4.8 min >> 40 ms
2. The "progeny" half-life is on the order of the exposure window: 32.3 ms ∼ 40 ms

Therefore, $P_d = 1 - \frac{1}{\lambda t_1}(1 - e^{-\lambda t_1}) = 0.329$.

Let us now determine the scalar correction factor for the measurement. The probability of an α-particle event being attributable to ^{221}Fr is one in four, $P_f = 0.25$. However, due to this frame-rate "overlap" effect, a proportion of ^{217}At events are systematically not detected. The true probability of a *detected* α-particle event being attributable to ^{221}Fr is renormalized according to P_d:

$$P_f^* = P_f/(P_f + 0.25 + 0.25(1 - P_d) + 0.25) = 0.272.$$

Therefore, in 27.2% of measured events, $P_d = 32.9\%$ of these have a missing associated ^{217}At decay. The scalar correction factor is $1 + P_d P_f^* = 1.09$. □

4.4 Image processing

We process iQID activity autoradiographs into dose-rate images using a combination of open source Python libraries, including scikit-image (0.18.1) [136], OpenCV (4.0.1) [137], PyStackReg (0.2.5) [138], and other open source image processing software, including FIJI-ImageJ [139] and 3D Slicer [140]. Figure 4.4 shows the workflow of processing steps required.

4.4.1 Tissue slice ROI segmentation

Multi-slice autoradiographs must be segmented into regions of interest (ROIs) corresponding to the discrete tissue slices. We used an automated segmentation algorithm on the whole-FOV image that consists of the following steps.

1. (Optional) Combine bins to increase SNR for ROI detection;

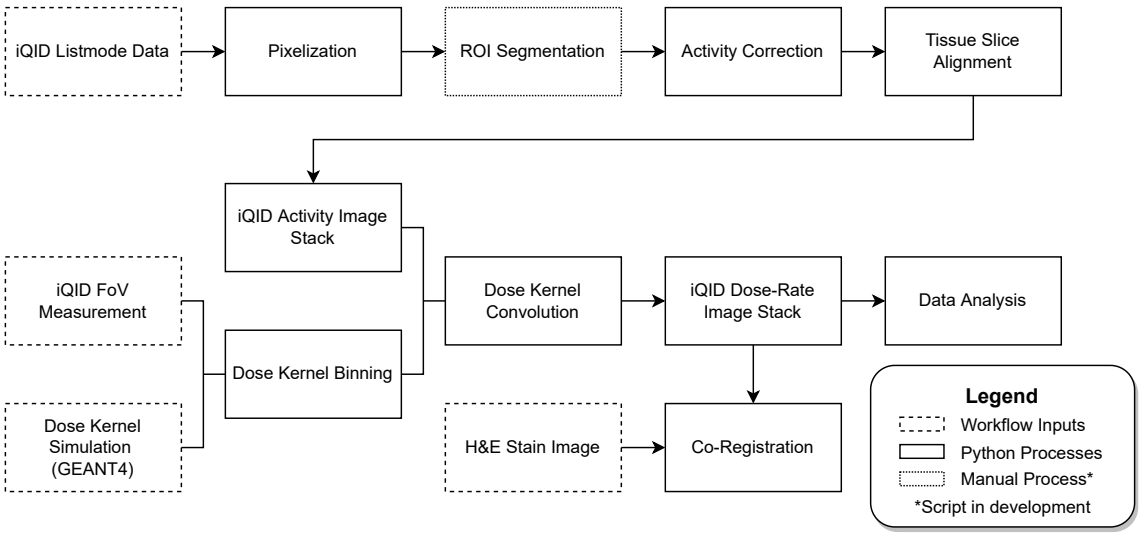

Figure 4.4: Detailed image processing flowchart showing sequence of automated and semi-automated image processing steps.

2. Binarize image above a manually defined or Otsu threshold;
3. Apply a Gaussian blur filter;
4. Identify image contours (tissue outlines) with the `cv2.findContours` method;
5. Select contours based on a minimum area size;
6. Generate masks corresponding to the interior of the slice contours; and
7. Categorize list-mode events according to their corresponding ROI.

Figure 4.5 shows a screenshot of the in-house Jupyter Notebook widget we developed for segmentation, labeling, and sorting of tissue slices within an iQID FOV. The three main parameters (rebinning factor, Gaussian filter size, and minimum area size) are manually selected according to the dataset.

The auto-segmentation procedure can struggle to identify sparse or low-signal images, as well as tissue slices with damage or breaks in them. In these cases, manual identification and masking of ROIs can be conducted using FIJI-ImageJ instead.

4.4.2 Activity estimation

Detected events in each ROI are binned in time and fit with a least-squares residual optimization exponential function to the temporal histogram of counts over the course of imaging. Two examples of tumor xenografts in mice treated with ^{225}Ac are shown in Fig. 4.6, with Fig. 4.6A displaying a standard example. The decay parameter was constrained to within 5% of the ^{225}Ac half-life, and the intercept of the exponential fit is related to to the instan-

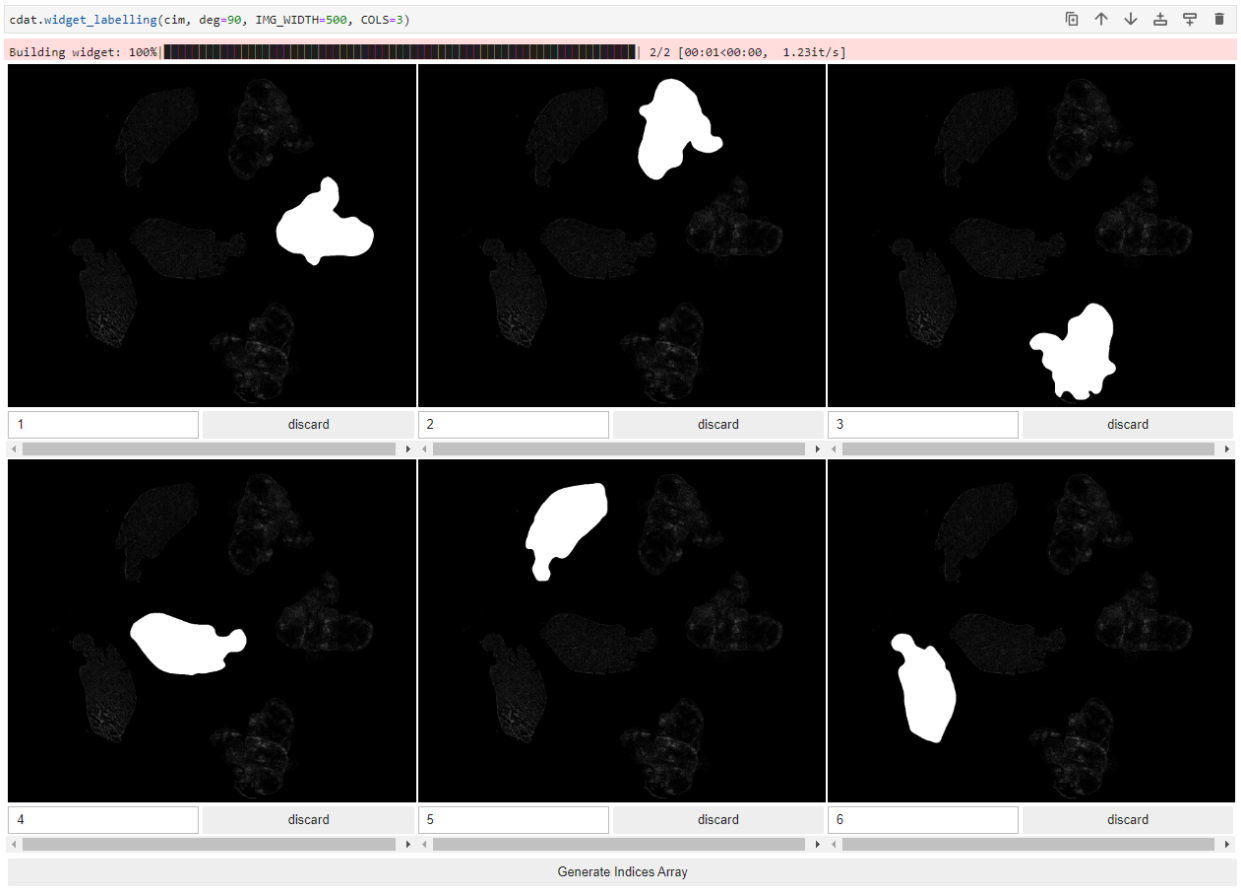

Figure 4.5: In-house Jupyter Notebook widget for segmentation, labeling, and sorting of tissue slices within an iQID FOV. Images show segmentation of tumor xenograft and liver slices from a mouse treated with ^{225}Ac.

taneous activity of the ROI at the start of imaging $A(0)$.[1] This quantity was exponentially corrected for isotope decay from the time of imaging to the time of sacrifice, and the total activity was distributed over the image proportional to the intensity of each pixel, resulting in a spatial activity snapshot of each tissue slice at the time of biopsy.

Some iQID data sets can show temporal histograms with non-physical rates, such as in Fig. 4.6B, where the event rate drops dramatically mid-acquisition before recovering later on. The exact reason for this occurrence is not known, but we suspect that it can happen when the attached laptop computer has processing or memory limitations. Frame parsing is a GPU-intensive process that might experience slowdowns when other operations, such as an operating system update, take place during acquisition. In such cases the fit was

[1] With 1000 s bins, the intercept is exactly equal to $A(0)$ in units of mBq. A unit correction factor must be applied for other bin sizes.

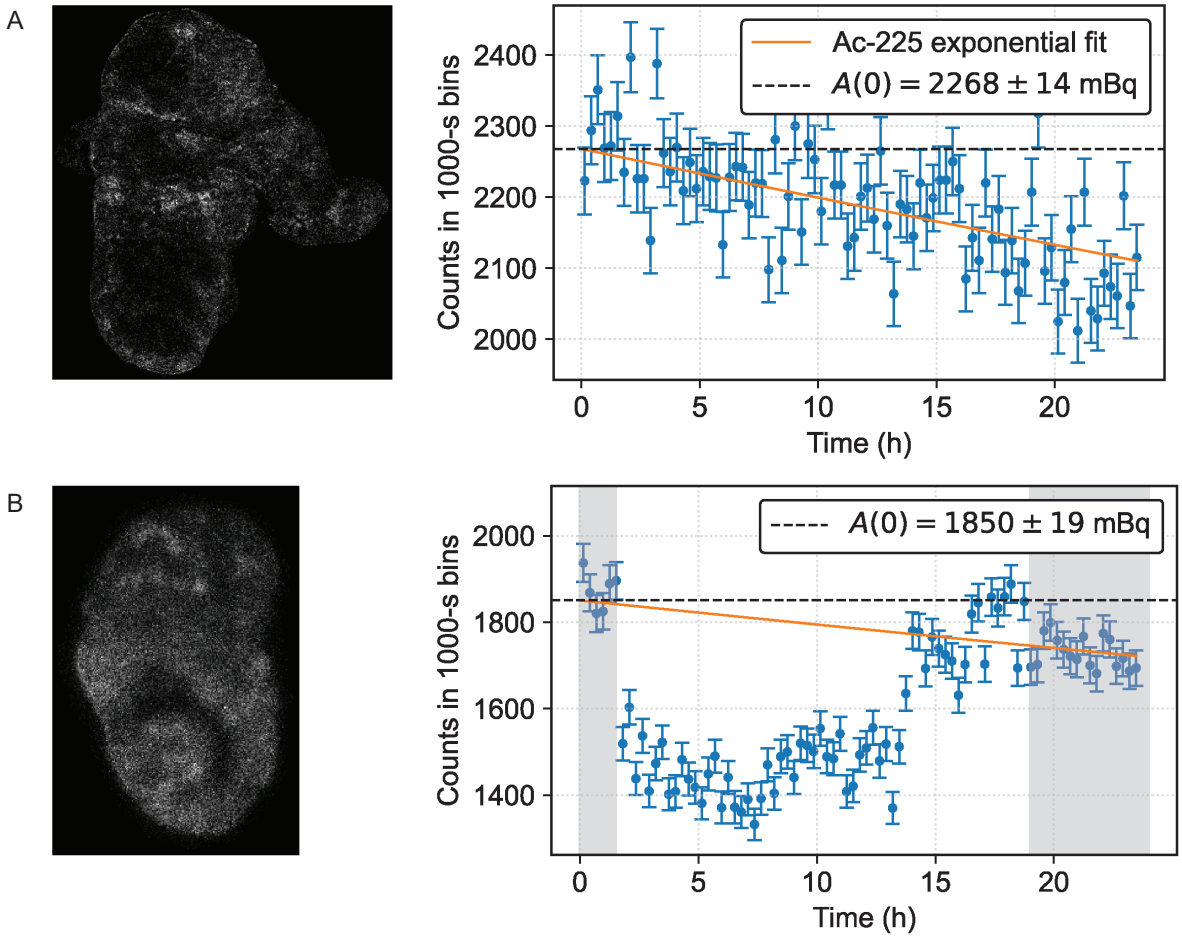

Figure 4.6: Temporal binning of iQID events to determine initial activity in tumor xenografts from mice treated with ^{225}Ac. (A) Standard example showing that the sample decays over the course of the iQID acquisition with half-life equal to that of ^{225}Ac. Activity at the start of imaging is estimated from the exponential fit. (B) Example in which the event rate drops unphysically during the acquisition, possibly due to memory or processing limitations of the attached computer. The estimate is compensated by selectively windowing the event histogram and using only a subset of the data for the fit (shaded gray regions).

estimated by selectively windowing the event histogram and using only a subset of the data that retained the full event rate.

4.4.3 Stack registration

Activity images of consecutive slices within a 3D volume were registered by approximating each thin slice as a minimally distorted 2D transformation of its neighbor. The orientation

was roughly obtained by minimizing the mean-squared error (MSE) between image intensities through rotation angles. A packaged method for optimal rigid-body transformations (translation and rotation) was then applied for precise alignment (PyStackReg). Small errors in the cumulative activity introduced by rotation were recorded and corrected for with a scalar compensation factor.

4.5 Dose-rate estimation

Spatial dose rates in tissues were computed from activity image stacks using a dose-point-kernel (DPK) convolution method. Monte Carlo (MC) simulation was used to generate an energy deposition kernel $K(r)$ that describes the mean energy distribution to a surrounding voxelized volume from a centrally located decay of an isotope. Convolution of the 3D activity image volume $A(r)$ with $K(r)$, and inclusion of mass through voxel density $\rho(r)$ and volume $V(r)$, produces an instantaneous 3D dose-rate snapshot $\dot{D}(r)$:

$$\dot{D}(r) = \int \frac{K(|r' - r|)}{\rho(r)V(r)} A(r')d^3r'. \tag{4.1}$$

The nomenclature here follows ICRU Report 96 [31], where r represents the source position and r' represents the target position. The (discrete) convolution integral is calculated using a Fast Fourier Transform (FFT)-based packaged Python method. Fig. 4.7 compares an iQID activity image to its corresponding dose-rate DAR after DPK convolution (^{225}Ac, 22Rv1 mouse tumor xenograft). As shown, DPK kernel convolution is inherently a smearing operation.

4.6 Monte Carlo kernel

A separate DPK must be generated for each measured isotope. In general, we generate the energy deposition kernel with 1-µm voxels using the GATE Monte Carlo framework [141], simulating 10^6 to 10^7 primary particles using the emstandard_opt3 physics list and 10-nm range cuts. iQID DAR measurements record only α-events, so we simulate only the α-particles as primaries. The energies and branching ratios of the α-particle primaries are sourced from the Lund/LBNL Nuclear Data Search [50]. Unless otherwise specified, iQID measurements were taken long enough after sacrifice for secular equilibrium to be achieved between parent and progeny isotopes. The emissions and volumes for ^{211}At and ^{225}Ac kernels used in our studies are provided in Table 4.2.

To apply in a DPK convolution, the energy deposition kernel is radially averaged and binned to the voxel size of the iQID image stack. Figure 4.8A shows a cross-section of an ^{211}At kernel generated with 10^7 primaries, binned to 12-µm voxels (Fig. 4.8B). The inverse-square component dominates the energy fall-off, as shown in the radial profile in Fig. 4.9A–B. Multiplication by a factor of r^2 shows the Bragg peaks associated with the ^{211}At and ^{211}Po decays of different energies more clearly (Fig. 4.9C).

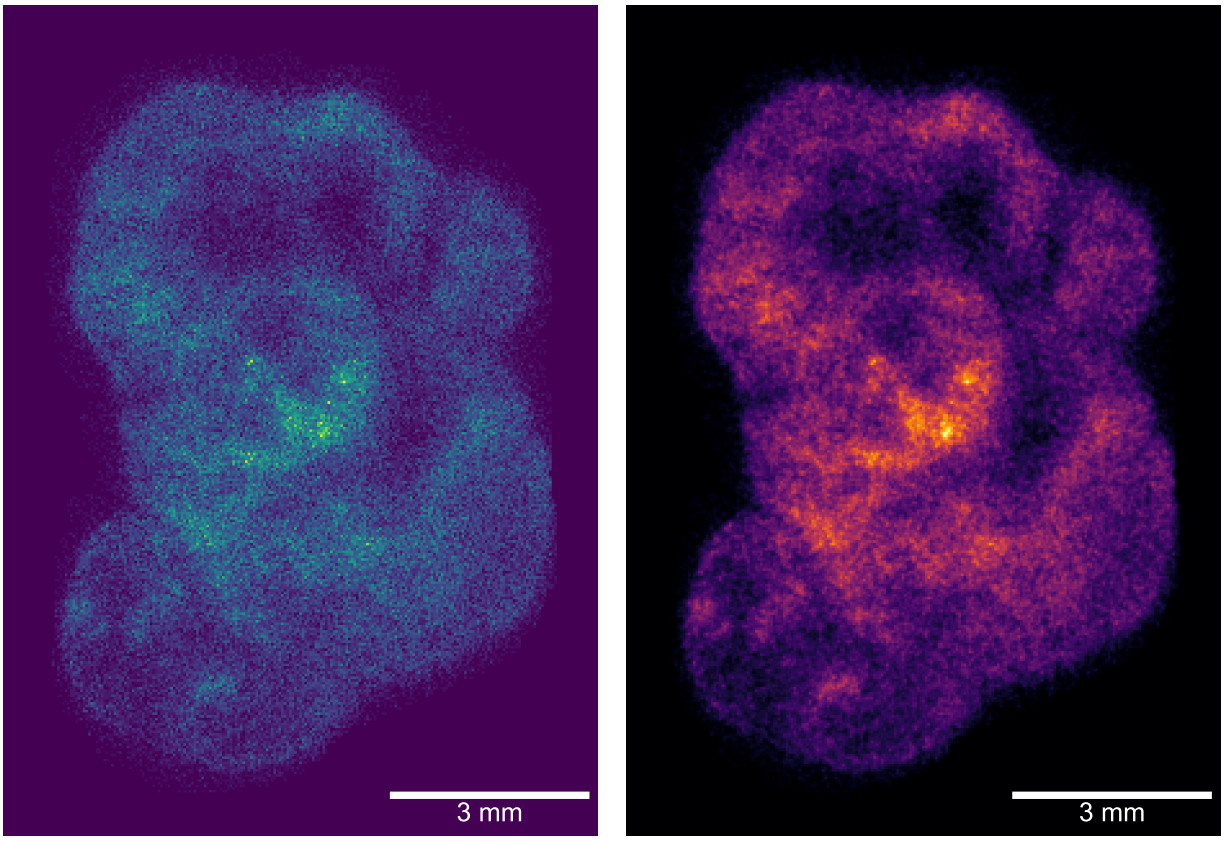

Figure 4.7: Comparison of iQID activity image (left) of ^{225}Ac in a 22Rv1 mouse tumor xenograft to its corresponding dose-rate DAR after DPK convolution (right).

Table 4.2: Parameters for dose-point-kernel simulations using GATE v9.0. Alpha-emission energies are provided by the weighted average of emissions from that isotope with intensities exceeding 0.1%.

Isotope	**∝-Emissions (MeV)**	**Physics**	**Volume**
^{211}At	^{211}At: 5.869 (41.8%) ^{211}Po: 7.450 (57.6%)	emstandard_opt3 10 nm range cut	151-µm water cube
^{225}Ac	^{225}Ac: 5.788 (100%) ^{221}Fr: 6.301 (100%) ^{217}At: 7.067 (100%) ^{213}Bi: 5.847 (2.1%) ^{213}Po: 8.376 (97.9%)	emstandard_opt3 10 nm range cut	181-µm water cube

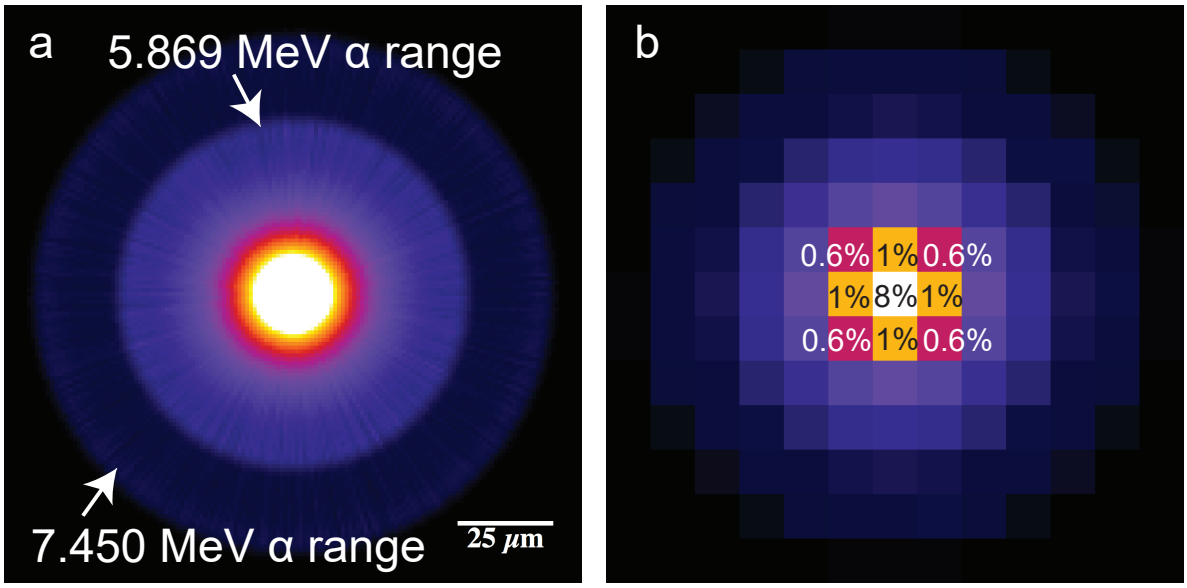

Figure 4.8: Monte Carlo energy deposition kernel for ^{211}At alpha-particles in water (10^7 events). (A) 1-µm voxel kernel (151 µm × 151 µm × 151 µm) showing two α-decay pathways. (B) Kernel with percentage energy deposition in voxels binned to 12 µm. Energy deposition falls rapidly beyond adjacent 12-µm tissue slices.

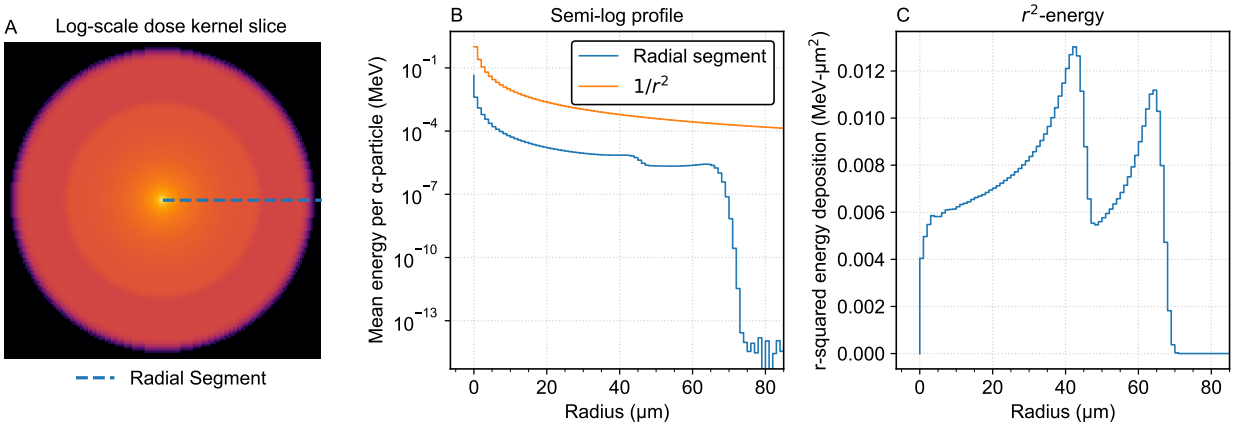

Figure 4.9: Radial profiles of an ^{211}At DPK. (A) Log-normalized, radially averaged cross-section with radial segment indication. (B) Semi-log profile of radial segment and relative contribution of inverse-square law to the profile. (C) Radial segment as in (B), multiplied by r^2, shows Bragg peaks associated with the two α-emissions in the ^{211}At decay chain.

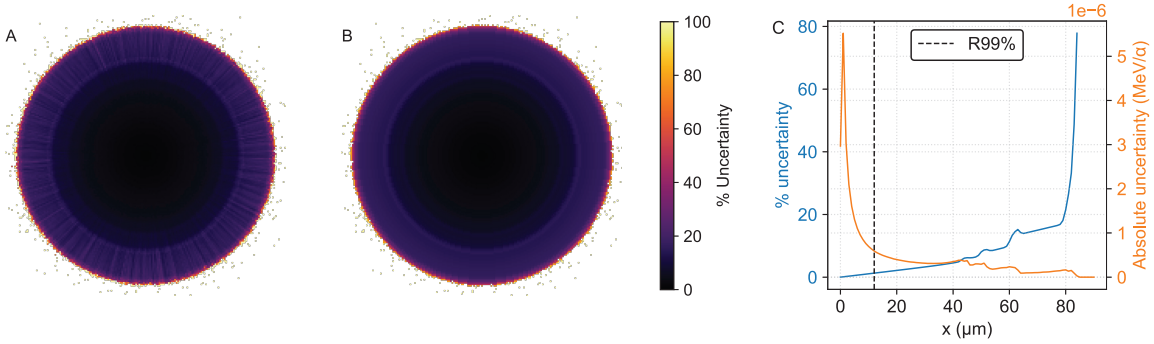

Figure 4.10: Relative voxel-wise uncertainties for ^{225}Ac DPK simulated with 10^7 primaries, (A) before and (B) after radial averaging. (C) Radial profiles of relative and absolute uncertainties. Relative uncertainty at $R_{99\%}$ (12 µm) is 1.3%.

4.6.1 Statistical uncertainty

The statistical uncertainty a voxel k of the energy deposition kernel, $s_{\bar{d}_k}$, is calculated according to

$$s_{\bar{d}_k} = \sqrt{\frac{1}{N-1}\left(\frac{\sum_i^N {d_{k,i}}^2}{N} - \left(\frac{\sum_i^N d_{k,i}}{N}\right)^2\right)}, \tag{4.2}$$

where, using the notation described by [142], $d_{k,i}$ is the energy deposited in voxel k by independent history (primary particle) i, and N is the total number of primary particles. When using GATE, this computation is easily produced by toggling on the `DoseActor` flags for `enableSquaredEdep` and `enableEdep`. These two output metrics report the sum contributions from all primary particles in the run per voxel, and thereby provide the two sums $\sum_i^N {d_{k,i}}^2$ and $\sum_i^N d_{k,i}$, respectively.

An example of the relative uncertainty map for an ^{225}Ac DPK simulated with 10^7 primaries is shown in Fig. 4.10A. The mean relative uncertainty associated with any non-zero 1-µm voxel was 17.4% after radial averaging (Fig. 4.10B). This metric is dominated by low-dose division in peripheral regions of the kernel. At the radius of 99% cumulative energy deposition ($R_{99\%}$, 12 µm), the relative uncertainty was 1.3% (Fig. 4.10C). All statistics reported thus far apply prior to image-specific binning. Binning the 1-µm voxels to 10–30 µm is typical for iQID measurements and improves the statistical precision.

4.6.2 Nuclear recoil energy

Use of α-particle primaries only for the DPK overlooks any energy contributions from the recoiling progeny nucleus, as described in Section 1.3. Since the range of the recoil nucleus

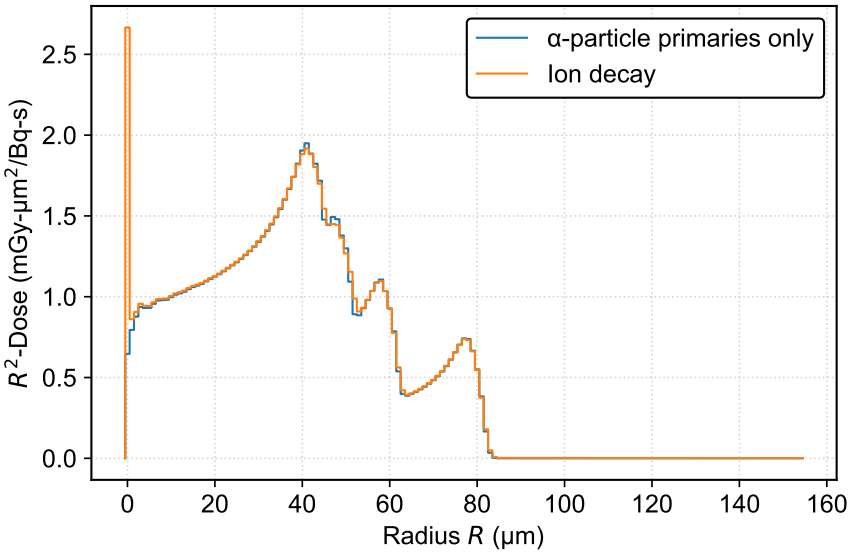

Figure 4.11: Comparison of α-primary DPK with full ion-decay DPK. Recoil energy of the progeny nucleus increases dose in the center voxel by a factor of 4. However, this discrepancy results in only 0.59% relative error in a typical binned voxel.

in tissue is around 100 nm, this energy is predominantly localized in the central voxel of the DPK.

Figure 4.11 compares the radial profiles from two DPKs, one computed with only α-particle primaries and the other using the GATE v9.0 ion-decay database for ^{225}Ac. The α-primary kernel estimates the center-voxel energy deposition as 43.4 keV per decay, compared to the four-times higher 182.1 keV for the ion-decay kernel. The difference of 138.7 keV is well explained by the missing recoil energy, which has a weighted average of 149.4 keV from the Q-value not included in the α-primary calculation. An extended minimal-dose tail (mainly observable in log-scale) also reflects the presence of β-particle and γ-emissions in the ion decay kernel.

Despite the dramatic discrepancy in the center voxel, binning of the DPK to a typical iQID resolution of 39 µm × 39 µm × 10 µm voxels significantly smooths out the difference, resulting in a center voxel error of 0.59%. The ion source is more complete than the α-primary source for computation of absorbed dose, but may complicate analyses that depend on RBE or weighting factors due to the difference in biological effect of α-particles, β-particles, γ-emissions, and recoil progeny. The biological impact of the nuclear recoil likely depends on geometry, where recoil from an isotope localized on the cell membrane would be unlikely to traverse the nucleus or cause DNA damage. At least one comparison study between non-recoiling (^{210}Po) and recoiling (^{212}Pb) α-particle emitters has suggested that recoiled nuclei had negligible impact on cellular damage [143].

4.7 Measurement time

The limited throughput of digital autoradiography can bottleneck data collection, commonly resulting in a back-up of frozen tissue samples awaiting measurements. As the isotope decays in storage, iQID image SNR decreases. Noise is reduced by improving counting statistics, either by measuring immediately after preparation or extending acquisition time. Table 4.3 is a simple reference that illustrates the exponential decay of several common isotopes. Percentages from 90% to 10% indicate how much of the signal remains for the isotope in that row after the indicated amount of time. For example, a sample of ^{225}Ac will have 90% of its signal remaining if measured within 1.5 d, but around 10% if there is a delay interval of 1 month before iQID measurement.

Table 4.3: Reference table evaluating exponential decay of common isotopes over time.

Isotope	Half-life	90%	80%	70%	60%	50%	40%	30%	20%	10%	Unit
Ac-225	9.92 d	1.5	3.2	5.1	7.3	9.9	13.1	17.2	23.0	33.0	d
Zr-89	3.27 d	0.5	1.1	1.7	2.4	3.3	4.3	5.7	7.6	10.9	d
Ce-134	3.16 d	0.5	1.0	1.6	2.3	3.2	4.2	5.5	7.3	10.5	d
Lu-177	6.65 d	1.0	2.1	3.4	4.9	6.6	8.8	11.6	15.4	22.1	d
Ra-223	11.43 d	1.7	3.7	5.9	8.4	11.4	15.1	19.9	26.5	38.0	d
Th-227	18.7 d	2.8	6.0	9.6	13.8	18.7	24.7	32.5	43.4	62.1	d
Cu-64	12.7 h	1.9	4.1	6.5	9.4	12.7	16.8	22.1	29.5	42.2	h

Figure 4.12 shows four ^{225}Ac-containing tumor slices measured at various times post-sacrifice (24 h acquisitions). Image graininess and noise increases with reduced counting statistics, which affects the quantitative accuracy as increasingly large decay corrections are applied to noise. Small-scale spatial activity heterogeneities are also obscured. Extended acquisition time to collect more counts can alleviate some of these effects, but the delay similarly worsens the image quality of subsequent tissues awaiting acquisition.

4.8 Sequential sectioning

Digital autoradiography of a single tissue slices yields a quantitative 2D activity image of α-particle emissions in that plane. For quantitative dosimetry, this isolated measurement is insufficient since it lacks information about the crossfire dose contributions from surrounding tissue. As discussed in Chapter 3, the simplest approach for αRPT is to consecutively slice and measure the surrounding volume spanning the range of the α-particle of interest, which we label as the sequential method. The cross-dose-rate can then be computed using a dose kernel, voxel S-values, or Monte Carlo simulation.

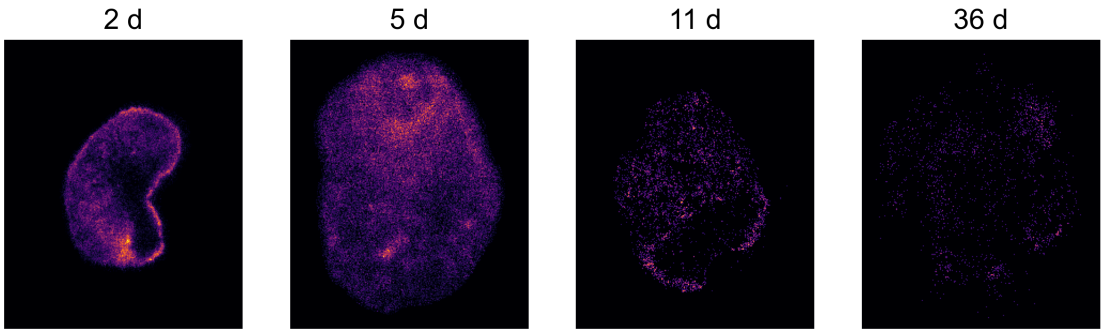

Figure 4.12: Impact of measurement delay on image sparsity. ^{225}Ac-containing tumor slices collected from identically prepared mice were measured at increasing times post-sacrifice. Time delays between sample collection and iQID measurement reduce the SNR of iQID images, which can obscure the spatial activity heterogeneity of αRPs.

The sequential method is the measurement and use of a series of consecutive tissue slices spanning the particle range, along with subsequent data processing and computational steps, to determine the absorbed dose rate in a central tissue slice. Since the α-particle range is a sliding window around each tissue slice, the dose-rate computation can only evaluate the central slice of the tissue volume. Compared to modeling methods that use blurring functions or 2D-to-3D calibrations, this approach may be considered to be the most accurate, since the actual spatial location of emissions in the 3D structure are measured. Practical challenges with this procedure include:

- **labor:** 10–20 tissue slices may be required per input volume, depending on slice thickness and particle range.
- **sample damage:** a damaged (torn/sheared/incomplete) slice must be discarded and approximated by an adjacent slice, reducing the accuracy of the computation.
- **measurement volume:** numerous slices per sample reduces measurement throughput and limits the number of tissues that can be measured in a given study or time. To accommodate the increased slice number, a larger device FOV may be used (at the cost of spatial resolution).
- **registration:** the spatial accuracy of this method is only as good as the registration procedure, where misregistration can blur the calculated dose distribution.

4.9 Slice minimization

Dosimetry studies that investigate multiple time points and tissue types can be bottlenecked by the requisite preparation of 10–20 tissue slices needed for the DPK convolution input

volume. A typical preclinical study investigates several organs and/or tumors per subject, with several subjects at each of multiple time points. The device field of view limits imaging throughput, while the decay of the radiopharmaceutical limits the time that tissues can be stored before measurement. Moreover, cryotoming is a laborious process that leaves the sample prone to tears and folds. While damaged samples can be discarded and re-cut for single-slice activity measurements, each sample in a dose computation input volume is needed to provide spatial cross-dose information. We have examined across several studies whether dose-rate estimates may be obtained using fewer slices using simulated variations of the DPK convolution procedure.

We hypothesized that our dosimetry routine would yield similar results whether a few surrounding slices (1–3 total) or a full set (up to 10 on either side of the center slice) were used to calculate the central-slice dose-rate map. Figs. 4.8–4.9 illustrate the reasoning: energy distribution in the dose kernel radial profile falls off rapidly with distance due to the dispersion of the α-particle flux in the 3D medium. Minimal energy is deposited beyond the maximum α-particle range, R_α. Therefore, decay events more than n slices of thickness t away, where $n = R_\alpha/t$, would not contribute significant dose to the measured slice, and slices up to that point contribute diminishing dose compared to those near the center. Two methods were developed to minimize the requisite slices and tested using preclinical iQID data. Cartoon schematics illustrating both methods are shown in Fig. 4.13A.

The slice contribution method is a limited-slice measurement strategy in which only one or several consecutive slices are acquired from the center of the tissue to form the input volume for DPK convolution. The resulting dose-rate image is quantitatively corrected through comparison to a calibration data set. In this method, the spatial dose-rate calculations are identical to those described previously (sequential method), except that only $N = 1, 3, 5, ...N_{\max}$ central slices are used in the 3D activity image stack, whereas $N_{\max}$ slices would be used in the sequential method. DPK convolution would then proceed as described above.

To assess the validity of the method using preclinical iQID data, the summed dose rate of all voxels in the calculated central slice, $\dot{D}_N$, was recorded for comparison to the dose rate calculated via the sequential method using all available slices, $\dot{D}_0$. To preserve symmetry in the central slice measurement, we simulated trials at odd slice numbers by adding one additional slice on each side to increment N. Comparison with the sequential method on a control data set yields a correction factor to scale the limited-slice data, obtained by empirically fitting $\dot{D}_N/\dot{D}_0$ with respect to N. A separate correction factor must be measured for each combination of tissue type, slice thickness, and radioisotope with a full set (10–20 slices) of data.

The cloning method is a limited-slice measurement strategy in which only one or several consecutive slices are acquired from the center of the tissue, and the outermost slices are digitally replicated out to the α-particle range to complete the input volume for DPK convolution. This methods relies on an identical slice approximation, in which one assumes that neighboring slices are nearly identical since the slice thickness is small. This is an implicit assumption in DAR analyses that use only one representative slice for a given organ or tis-

sue. Unlike the slice contribution method, the cloning method does not require a complete sequential-slice characterization of each tissue and organ. For a limited-data measurement of $N = 1, 3, 5, ...N_{\max}$ central slices, the remaining $N_{\max} - 1, N_{\max} - 3, N_{\max} - 5, ...0$ slices would be formed as duplicates of the external slices on either side before application of DPK convolution as described above.

4.9.1 Case study: ^{211}At in canine lymph nodes

Figure 4.13 summarizes our investigation of the two slice minimization methods in a study of ^{211}At in lymph nodes of healthy canines with 12-µm slice thickness (see Ch. 5 for the complete study). Fourteen biopsies from eight canine models were assessed ($n = 14$). In the slice contribution method, studies limited to N slices had slice contributions $\dot{D}_N$, shown as fractions of the all-slices (control study) total dose rate $\dot{D}_0$ (Fig. 4.13B, left). An exponential fit through this data ($\chi^2/\nu = 1.73$) provided an empirical scalar correction factor C_N to yield a corrected dose-rate estimate $\dot{D}_e = C_N \dot{D}_N$. The efficacy of the fit-scaling procedure was evaluated (Fig. 4.13B, right) by comparing $\dot{D}_e$ to $\dot{D}_0$. Loss of accuracy past $N = 11$ (130 µm) reflects that an asymptotic model was used to fit data that reaches unity at sufficient N. Across all biopsies, the mean deviation of the slice contribution method $\dot{D}_e$ from $\dot{D}_0$ was 9.5% using one slice and 2.4% using three slices.

For the same cohort, the mean deviation of single-slice $\dot{D}_e$ from $\dot{D}_0$ using the cloning method was 4.8% using one slice and 1.8% using three slices. The cloning method attempts to obtain quantitatively accurate dose rates without having the spatial information of multiple slices and assumes that surrounding tissue contains identical features in the same spatial locations. We tested this assumption by assessing the same dose-rate comparison metric within several data subsets, defined by the proximity of voxel values to the mean of the whole tissue. Data for high-dose-rate ($> x + 2\sigma$, "hot"), low-dose-rate ($< x - 1\sigma$, "cold"), and whole-lymph node regions are shown in Fig. 4.13C. (See Ch. 5, Fig. 5.1 for detail on this segmentation.)

The mean deviations of $\dot{D}_e$ from $\dot{D}_0$ for hot and cold regions, respectively, were 7.9%/3.9% and 6.5%/4.3% (single/triple slices). This bias, which decreases with N, demonstrates dose-rate overestimation (above the $\dot{D}_e/\dot{D}_0 = 1$ line) in hot regions and underestimation (below the $\dot{D}_e/\dot{D}_0 = 1$ line) in cold regions. Both methods showed similar convergence at higher slice numbers, but the cloning method had superior single-slice accuracy in our ^{211}At trials (4.8% vs 9.5%).

4.9.2 Case study: ^{225}Ac in murine kidneys and tumor xenografts

We also characterized the cloning method in a study of ^{225}Ac in mouse tumors and kidneys with 10-µm slice thickness (see Ch. 6 for the complete study). Ten consecutive slices ($10 \times 10\,\mu m = 100\,\mu m$ total) from each mouse kidney and tumor were cut, imaged, and digitally re-registered ($n = 4$ mice). The dose rate of the central slice was compared between the sequential and cloning methods.

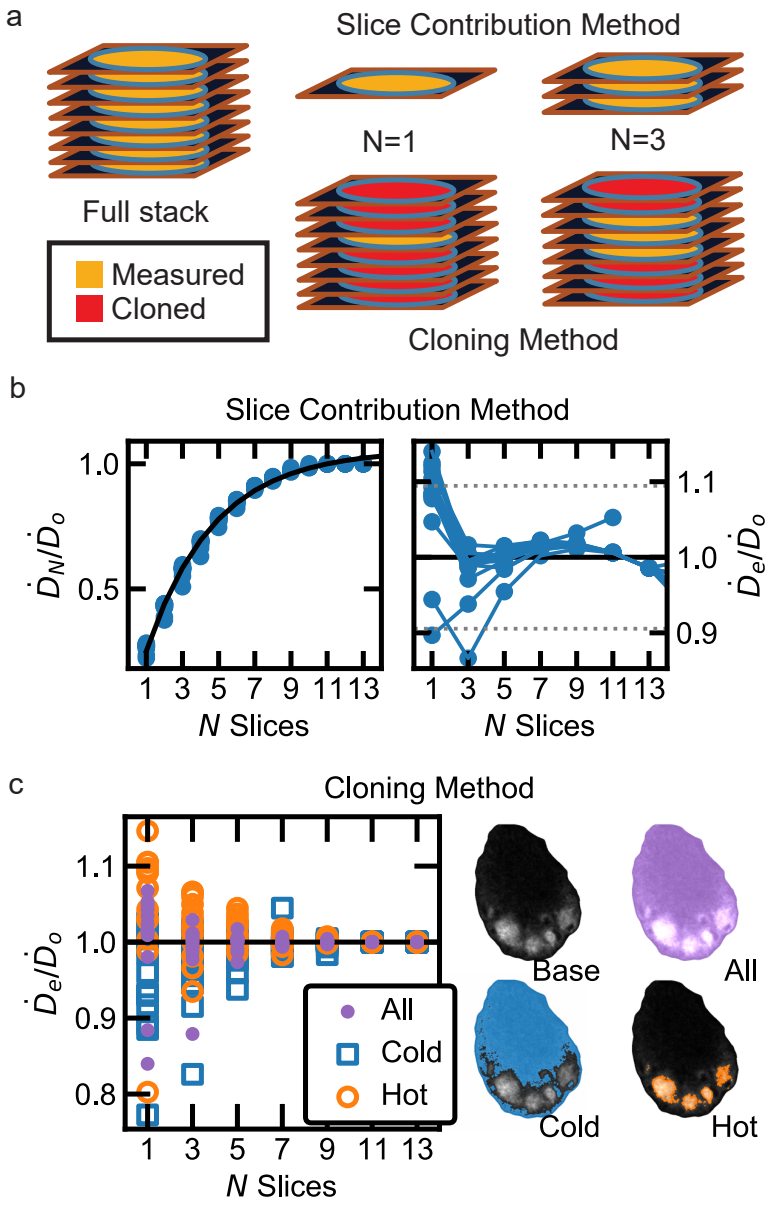

Figure 4.13: Slice reduction methods for ^{211}At in canine lymph nodes. (A) Cartoons showing slice contribution and cloning methods. (B) (Left) Cumulative contribution of N slices $\dot{D}_N$ towards central-slice dose rate $\dot{D}_0$ with an exponential fit (black line, $\chi^2/\nu = 1.73$) provided a method to scale up a low-slice dose-rate image. (Right) After correction, the mean deviation of $\dot{D}_e$ from $\dot{D}_0$ using once slice was 9.5% (gray dashed lines). (C) Evaluation of the cloning method in hot and cold data subsets with mosaic of lymph node slices highlighted to show evaluated regions. The mean deviation of single-slice $\dot{D}_e$ from $\dot{D}_0$ was 4.8%. High density of hot data points above, and of cold data points below, the $\dot{D}_e/\dot{D}_0 = 1$ line reflects overemphasis of features from the measured slice.

Fig. 4.14A–B shows an example comparison between the absorbed-dose-rate DAR calculated using the sequential and cloning methods for a 24 h p.i. tumor. Across subjects (kidneys and tumors at both time points), the cloning method calculated the mean dose rate of the sequential method with an accuracy of $4.1\,\% \pm 3.7\,\%$ (Fig. 4.14C). Gross features were captured, but the approximation was noisier and over- or under-emphasized high-activity regions. We assessed the spatial accuracy with γ analysis, a difference- and distance-based metric for similarity between two dose distributions that is used to evaluate clinical external-beam radiation therapy plans [144, 145]. $97\,\% \pm 3\,\%$ of dose-rate pixels in kidneys were accurately calculated ($\gamma < 1$), using a tolerance of 10% within three pixels (117 µm) and local normalization (Fig. 4.14D). Higher discrepancy was observed in tumors ($\gamma < 1$: $87\,\% \pm 6\,\%$), which reflects the fact that heterogeneities between slices are not preserved when using the cloning method approximation.

4.9.3 Discussion

The cloning method does not require a full data set to develop an empirical correction factor—unlike the slice contribution method—and is convenient to apply to limited-data studies without prior experience. The main limitation of the cloning method is the assumption that the spatial distribution of radioactive hotspots does not vary significantly with tissue depth, which results in a systematic overemphasis of features in the measured slice. Differences in morphological architecture and physiology from one section to the next will thus affect the accuracy of the cloning method. The observed difference was small for the canine lymph node and mouse kidney data, but tumors and other tissue types may exhibit greater structural inhomogeneity. Anatomically diverse tissues may require a full range of slices for accurate dose calculations using the slice contribution or full sequential methods instead. However, all DPK methods are ill posed to measure samples with small-scale, heterogeneous material structures (such as bone marrow trabeculae) because the interfaces between tissue and non-tissue (e.g., air or bone) would be inaccurately reflected. A full Monte Carlo simulation of the anatomy would be required to model such effects.

Conversely, dosimetry calculations for a single slice may not characterize the rest of the biopsy beyond the α-particle range. Multiple sparse samples are needed to assess the 3D dose distribution in a whole organ (see Chapter 6). Cryosections should be cut at a consistent location to minimize geometric effects (e.g., increased uptake in outer tissue layers) and structural effects (e.g., increased presence of cortical follicles along a longitudinal compared to a transverse plane).

4.10 Histological image segmentation and registration

Digital autoradiographs are often correlated with histological stains, typically hematoxylin and eosin (H&E), to draw relations between agent uptake, absorbed dose, and tissue pathology. In our work, this is accomplished by staining a tissue slice consecutive with the DAR

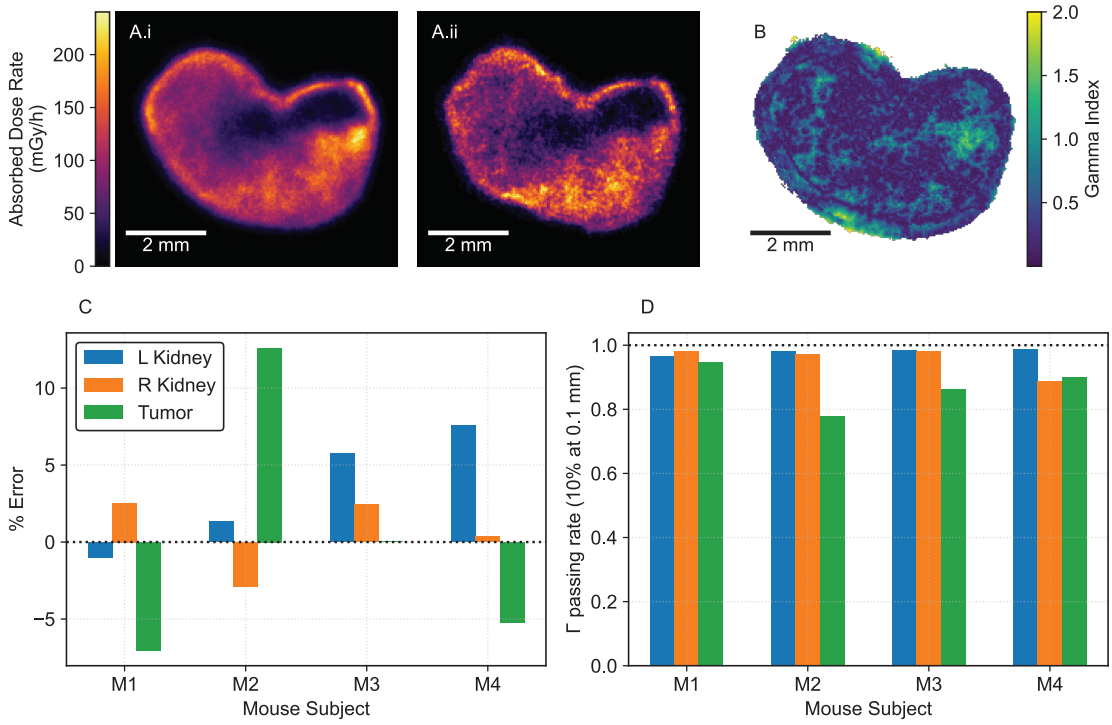

Figure 4.14: Cloning method characterization for ^{225}Ac in mice. (A) Example dose-rate images (24 h p.i. tumor) calculated using the sequential (i) and cloning (ii) methods. (B) Gamma index analysis (local normalization, 0.1 mm, 10%). (C) Percentage error of the mean voxel dose rate of cloning method compared to sequential method images from DAR mouse studies at 1 d (subjects M1, M2) and 7 d (M3, M4) post-injection. (D) Gamma index passing rates.

slice and digitally co-registering the two images. Our methods for multi-modal registration evolved over the course of several studies, depending on the goals of the subsequent analyses and required precision.[2]

4.10.1 Multi-modal gross registration

The goal of multi-modal registration in our initial study of ^{211}At was gross correlation between agent uptake and pathological damage. Since H&E slices were collected sequentially after the entire activity-volume stack, they were spatially separated from iQID-measured

[2]Researchers at Washington University in St. Louis have developed a procedure in which a single tissue slice is first measured with autoradiography, then subsequently stained and imaged, to avoid the registration challenge and minimize uncertainty associated with changes in tissue anatomy between slices [110].

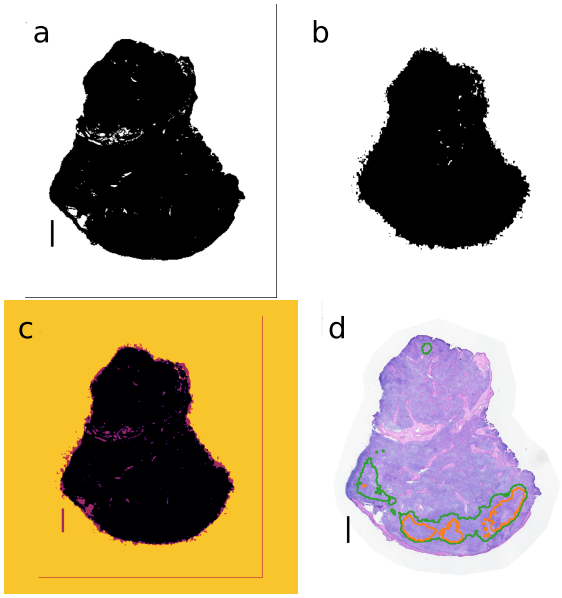

Figure 4.15: Registration procedure between iQID dose-rate images and H&E-stained images. (A) H&E thresholded binary image. (B) iQID dose-rate-map thresholded binary image. (C) Co-registration of (A) and (B) using scale factors and 2D transformations. (D) Contours of high-activity regions overlaid on H&E image (Fig. 5.1). Scale bars show 1 mm.

central slices by 50–100 µm. Therefore, we permitted some misalignment and shear transformations during co-registration. Threshold detection, scaling factors, and 2D transformations were all calculated and applied automatically, with manual corrections for reflections (slices face-up versus face-down).

Our approach was to down-sample the high-resolution H&E images (50–200 MB) to compute the appropriate transformation between the two images, then map the transformed iQID images onto the full-resolution H&E stains. Figure 4.15 outlines the registration procedure. We first cast all images to binary for alignment (Fig. 4.15A–B). Thresholds for the down-sampled H&E images were obtained using Otsu's method (`scikit-image`), a variance-based procedure that separates an image by clustering the intensity histogram [146]. A smaller threshold (one-tenth of the Otsu threshold) was used for the sparser iQID images to obtain binaries covering the whole spatial extent of the lymph node. We obtained pixel sizes from scale bars (H&E) and field-of-view measurements (iQID), then scaled the iQID images by the corresponding factor using `scikit-image`'s `rescale` function. The same-dimension images were co-registered using the described methods for slice alignment, including MSE intensity comparison and 2D transformations (Fig. 4.15C). Contours of high-dose-rate regions were overlaid on the H&E image for pathological comparison (Fig. 4.15D).

4.10.2 Sub-organ kidney segmentation

In our study of ^{225}Ac in mice, we investigated dosimetry at the sub-kidney scale. Kidney H&E images were manually segmented into four regions: cortex; the combined inner and outer stripes of medulla (ISOM/OSOM); the combined inner medulla and papilla (IM/Pa); and the combined vasculature and renal pelvis (V/Pe), using the reference histology images provided by NIH's National Toxicology Program [147]. Masks were created and saved using 3D Slicer [140]. We reduced the uncertainty in segmentation by combining the outer and inner stripes of medulla into one segment, and defined the boundary with the cortex as the presence or absence of glomerules. Similarly, we did not distinguish where the inner medulla and papilla ended or began and masked them as one segment. The automated rigid-body transformations based on binarized masks and external outlines of the kidneys as described above were sufficient for approximate alignment of the sub-organ regions when registering anatomical masks with 3D DARs.

4.10.3 Tumor segmentation and registration

To study tumor control probability in mice treated with ^{225}Ac (Sec. 4.11), more precise registration and segmentation methods were required to estimate the number of tumor cells in each voxel. Cell nuclei in tumor H&E images were segmented using a custom FIJI/ImageJ macro based on watershed segmentation and the Analyze Particles function (Fig. 4.16). These cell nuclei maps and iQID images were initially co-registered using automated rigid-body transformations with mean-squared-error intensity comparison, as described previously, but more precise registration was needed to match n_i cells in a voxel to dose D_i to calculate TCP. After the initial rigid-body registration, the two images were manually aligned with affine transformations using Bigwarp [148], a landmark-based deformation tool in ImageJ-Fiji [139]. To minimize interpolation errors, the DAR was treated as the reference image where possible. When DARs were transformed, the sum of pixel values was preserved using a scaling factor according to the difference before and after transformation. External edges of the tissue were preferred as landmarks to avoid biasing co-registration of internal structures receiving dose.

Tissue slices from both modalities (iQID and H&E) sometimes contained damaged or folded sections from the cryosectioning procedure. Identifiable damage was masked out of the TCP calculations, but the difference in total tissue extent sometimes hindered the registration. If a visibly adequate co-registration could not be achieved, the slice was omitted from analysis. To reduce the sensitivity of the calculation to registration error, we applied a $5\,\text{px} \times 5\,\text{px}$ erosion mask to the edge of the contour outlining $n_i > 0$ pixels.

4.11 Tumor control probability

Tumor control probability (TCP) is a statistical predictor of treatment efficacy based on whether tumor cells survive the treatment, where TCP = 1 indicates that all malignant cells

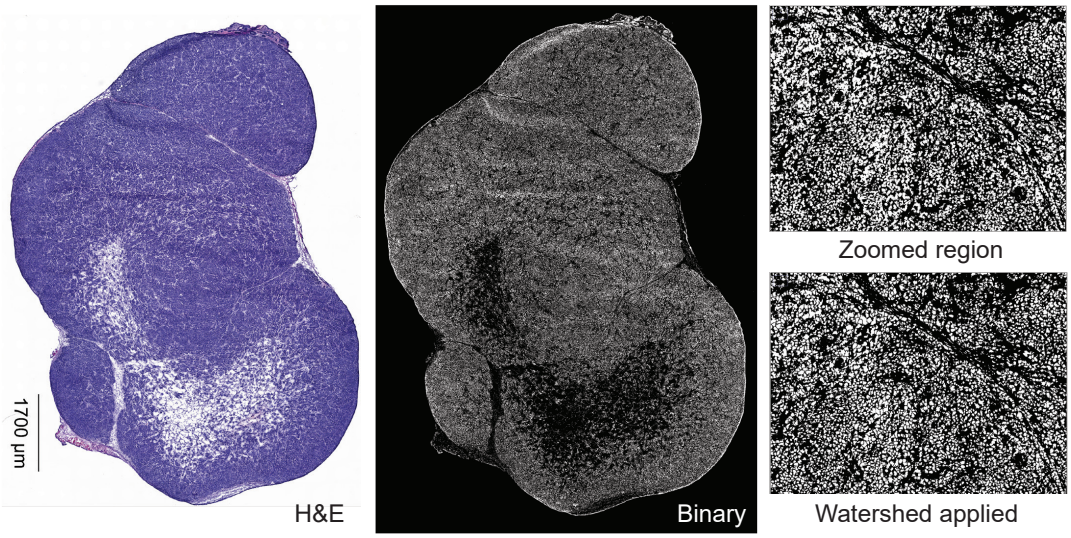

Figure 4.16: Illustration of tumor segmentation using ImageJ/FIJI.

die. We use the formalism reviewed by Spoormans et al [112], where TCP in a heterogeneous DAR is the product of voxel control probabilities (VCPs).

In a uniform-dose distribution, for n_0 clonogenic tumor cells, the Poisson-model uniform-dose TCP is given by

$$\begin{aligned} \mathrm{TCP} &= e^{-n_0 S}, \\ S &= e^{-\alpha D - \beta D^2} \approx e^{-\alpha D}, \end{aligned} \tag{4.3}$$

where S is the linear quadratic (LQ) probability model of survival for the cells receiving uniform dose D. The above simplification is reasonable for ^{225}Ac RPs, which mainly deliver dose through high-LET α-particle emissions for which the radiosensitivity parameter $\alpha >> \beta$. α must be measured or estimated for the cell type and α-particle of interest.

To compute a similar metric in a heterogeneous DAR, which we will call TCP*, a voxel i containing n_i cells is assumed to contain uniform dose D_i. TCP* is therefore calculated as the product of the uniform voxel control probabilities (VCPs):

$$\begin{aligned} \mathrm{VCP}(D_i) &= e^{-n_i S(D_i)} \\ \mathrm{TCP}^* &= \prod_i \mathrm{VCP}(D_i). \end{aligned} \tag{4.4}$$

The distinction between TCP* and TCP reflects the subtlety that the uniform-TCP value is *not* recovered in the case of a VCP-based calculation in a uniform dose distribution. An example of the numeric consequences of this fact is discussed in the ^{225}Ac xenograft case

study (Ch. 6). However, for convention and clarity, all mentions of TCP in the remainder of the text refer to VCP-product TCP* as above.

Chapter 5

Small-scale dosimetry of ^{211}At in canine lymph nodes

This chapter presents a brief but illustrative example of small-scale tissue dosimetry conducted with the framework presented in Chapter 4. The methods are applied to a study of lymph node biopsies from healthy canines treated with ^{211}At-labeled anti-CD45 monoclonal antibodies (mAbs), where the underlying preclinical goal is the assessment of the treatment viability for allogeneic hematopoietic cell transplantation (HCT) conditioning. We illustrate how nonuniformity of the agent uptake results in an inhomogeneous distribution of absorbed dose (Sec. 5.3), demonstrate temporal integration of aggregated dose-rate data to determine the mean absorbed dose over the treatment (Sec. 5.4), and comment on the relevance and limitations of the approach (Sec. 5.5). Material for this case study was published in Paper 1 alongside material in Chapter 4.

Paper 1 Abstract: Targeted radiopharmaceutical therapy with α-particle emitters (αRPT) is advantageous in cancer treatment because the short range and high local energy deposition of alpha particles enable precise radiation delivery and efficient tumor cell killing. However, these properties create sub-organ dose deposition effects that are not easily characterized by direct gamma-ray imaging (PET or SPECT). We present a computational procedure to determine the spatial distribution of absorbed dose from α-emitting radionuclides in tissues using digital autoradiography activity images from an ionizing-radiation quantum imaging detector (iQID). Data from ^{211}At-radioimmunotherapy studies for allogeneic hematopoietic cell transplantation in a canine model were used to develop these methods. Nine healthy canines were treated with 16.9-30.9 MBq ^{211}At/mg monoclonal antibodies (mAbs). Lymph node biopsies from early (2–5 h) and late (19–20 h) time points (16 total) were obtained, with 10-20 consecutive 12-µm cryosections extracted from each and imaged with an iQID device. iQID spatial activity images were registered within a 3D volume for dose-point-kernel convolution, producing dose-rate maps. The accumulated absorbed doses for

high- and low-rate regions were 9 ± 4 Gy and 1.2 ± 0.8 Gy from separate dose-rate curves, respectively. We further assess uptake uniformity, co-registration with histological pathology, and requisite slice numbers to improve microscale characterization of absorbed dose inhomogeneities in αRPT.

5.1 Introduction

Astatine-211 (^{211}At) anti-CD45 mAb radioimmunotherapy (RIT) conditioning is a promising substitute for external-beam total-body irradiation (TBI) in hematopoietic cell transplantation (HCT) preparative regimens for hematologic malignancies, including leukemias and non-Hodgkin's lymphoma [4, 149]. Canine lymphoma is a practical and clinically relevant model used in therapy studies due to its similarities to human lymphoma in anatomic forms, clinical presentations, cellular surface markers, and therapeutic response [150, 151]. Here, the digital autoradiography dosimetry framework articulated in Chapter 4 is demonstrated on data from sixteen canine lymph nodes following administration of ^{211}At-labeled anti-CD45 mAb for allogeneic HCT conditioning. The main preclinical finding is that mean dose metrics did not accurately characterize dose distribution, and therefore therapeutic effects, in tissues with inhomogeneous target expression.

5.2 Methods

5.2.1 Ethics approval

All procedures conducted were approved by the Fred Hutchinson Cancer Center Institutional Animal Care And Use Committee (IACUC). Fred Hutchinson is registered as a research facility with the USDA (91-R-0081), has a Letter of Assurance on file with PHS/OLAW (D16-00142), and is fully accredited by AAALAC International. The study design and methods reported previously [4], combined with the reporting in the current manuscript, follow recommendations in the ARRIVE guidelines.

5.2.2 Alpha-RIT imaging experiments

Data were collected as described elsewhere [4]: nine healthy canines were treated with 16.9–30.9 MBq ^{211}At/mg mAb (Table 5.1). Lymph node biopsies were obtained at early (2–5 h) and late (19–20 h) time points ($n = 16$). Subjects weighed between 7.9–13 kg and received either 0.5 or 0.75 mg/kg of ^{211}At-labeled anti-CD45 mAb CA12.10C12-B10 (8.44–23.2 MBq/kg injected activity, IA). iQID imaging and activity, dose-rate, and absorbed dose calculations were conducted.

Table 5.1: Dogs treated with ^{211}At-anti-CD45 radioimmunotherapy.

Canine ID	Subject Weight (kg)	Injected ^{211}At Activity (MBq/kg)	Antibody Dose (mAb mg/kg)	Specific Activity (MBq ^{211}At/ mg mAb)
H695	12.4	8.44	0.50	16.9
H700	13.0	23.2	0.75	30.9
H707	9.7	14.1	0.75	18.7
H714	10.1	14.5	0.50	29.0
H719	7.9	13.7	0.75	18.2
H741[a]	12.3	14.0	0.50	28.0
H751	9.5	12.9	0.50	25.8
H764	10.9	14.6	0.50	29.2
H765	9.6	11.4	0.50	22.7

[a]Biopsies from this study were discarded from analysis because torn and folded samples outnumbered usable samples.

5.2.3 iQID dosimetry

The ^{211}At decay series contains two α-particle emissions from ^{211}At and progeny radionuclide ^{211}Po, with respective energies of 5.87 and 7.45 MeV that correspond to ranges in water of 48 and 70 µm [152]. 10–20 consecutive 12-µm cryosections were collected from each tissue and measured for as long as possible before the next biopsy to reduce statistical uncertainty and utilize available imaging time (about 15 hours, or twice the 7.2-h half-life of ^{211}At). 40- and 115-mm diameter iQID configurations were used, resulting in effective voxel sizes of 10–30 µm XY and 12-µm Z dimensions. We discarded samples with major tears or folds from post-processing analysis and replaced them with duplicates of neighboring slices. Two full biopsies from one canine were not analyzed because the discarded samples outnumbered the acceptable ones. The 3D energy deposition kernel is shown and discussed in Sec. 4.6. ^{211}At and ^{211}Po were assumed to be in secular equilibrium, and only the alpha particles were generated as primaries.

5.3 Uptake uniformity

Our studies confirmed localized high-activity regions in a background of low-activity tissue. Tissues were digitally segmented from non-tissue background with an automatically generated contour mask. Voxel values of instantaneous dose rate at biopsy were binned into a dose-rate-area histogram (Fig. 5.1A), which we partitioned into three regions defined by standard deviations σ from the mean value x. Areas corresponding to these regions were

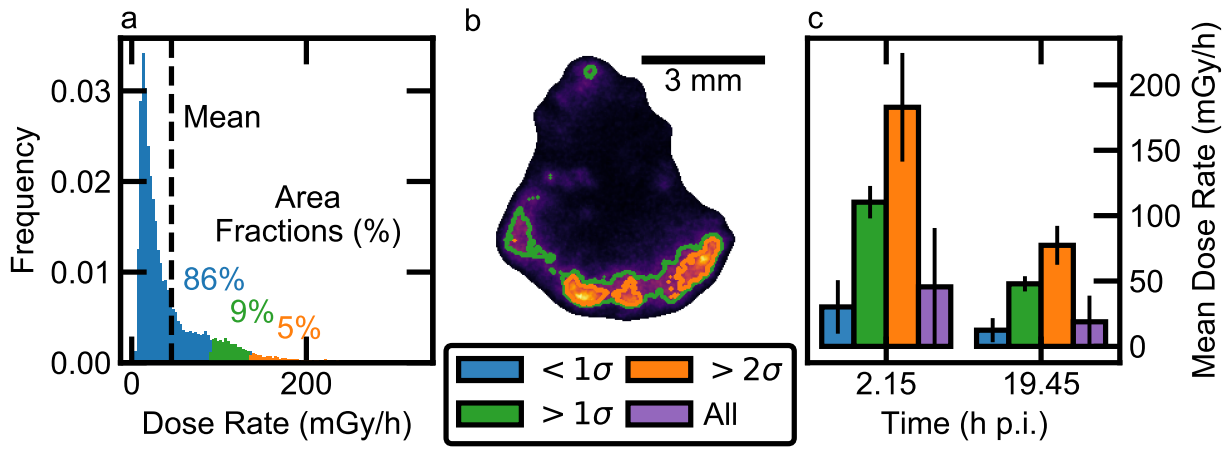

Figure 5.1: Uniformity analysis of ^{211}At dose rates in canine lymph nodes. (A) Dose-rate-area histogram of a slice of canine lymph node with regions segmented by deviation from the mean (dashed line). (B) Corresponding regions highlighted on the dose rate image in same colors. (C) Dose rates from two biopsies at different time points from the same canine. A mean value assessed over the whole organ underestimated the dose imparted to certain regions of tissue (5–6% of area) by a factor of three.

highlighted on the corresponding dose-rate image (Fig. 5.1B).

In a two-biopsy study from one representative canine, the respective mean dose rates were 46 ± 45 mGy/h (at 2.15 h p.i.) and 19 ± 20 mGy/h (at 19.45 h p.i.). The uncertainties, which represent one standard deviation σ, reflect the long high-dose tail of the dose-rate-area histogram (Fig. 5.1A). Therefore, 14% and 13% of the tissue area ($> 1\sigma$ from the mean) showed dose rate values over double the whole-organ mean in the respective biopsies, and 5% and 6% of the tissue area ($> 2\sigma$) exceeded three times the whole-organ mean. Figure 5.1C shows these discrepancies, with mean dose rates in each sub-region ($< 1\sigma$, $> 1\sigma$, $> 2\sigma$, and over the whole lymph node) in the two biopsies from early and late time points.

5.4 Absorbed dose estimation

Dose rates were estimated with a batch script for 16 biopsies at early and late time points with two biopsies discarded for sample flaws ($n = 14$). We assumed that uptake and decay kinematics were similar between canine subjects to compare IA-normalized dose rates across studies. Since uniformity analysis suggested that the mean dose rate may not be a representative metric for all regions in a sample, the measurement data was separated into high- ($> x + 2\sigma$, "hot") and low- ($< x - 1\sigma$, "cold") dose-rate regions of each lymph node section. The mean dose rate within each subset is plotted with time in Fig. 5.2.

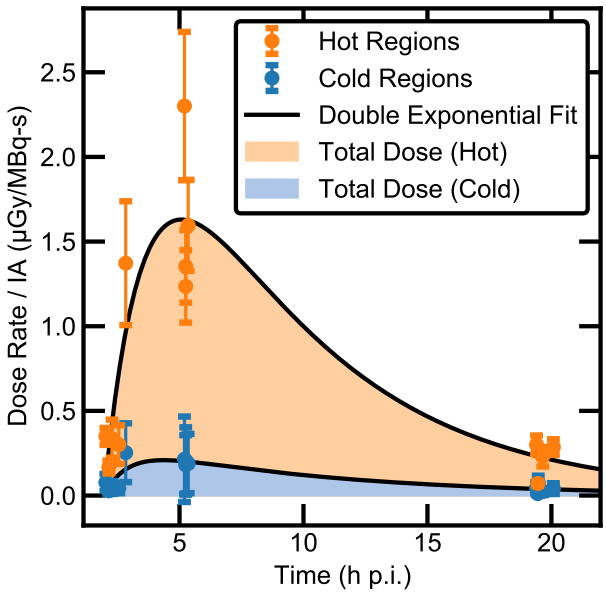

Figure 5.2: Dose-rate curves separated into high-dose-rate (orange, "hot") and low-dose-rate (blue, "cold") regions. Double-exponential fits ($y = ae^{-b(x-m)} - ce^{-d(x-n)}$, $\chi^2/\nu = 19.5, 2.2$ for hot and cold, respectively) use data from 14 biopsies across eight canine models, normalized to the injected activity of each study (8.44–23.2 MBq/kg). Shaded regions show curve-integration to estimate total absorbed dose, yielding hot-region doses of 9 ± 4 Gy and cold-region doses of 1.2 ± 0.8 Gy.

To estimate dose, the data were fit to a double exponential function using least-square residual optimization (Fig. 5.2). Standard deviations were calculated within each data subset for each biopsy and used as error to obtain reduced chi-squared values of 19.5 and 2.2 for the hot and cold regions. These quality-of-fit values deviate from unity more than typically expected for quantitative analysis, particularly for the high-activity regions. However, this result is not surprising given the limited sample points ($n = 14$ for a six-parameter fit) and variability within the data set. The study was not controlled to address specific regions within lymph nodes, resulting in samples with a variety of cuts (coronal, sagittal, transverse) and volumes (half- or whole-node). Segmentation of the regions by dose rate may therefore result in comparisons between different lymph node structural regions with high uptake.

Integration of the hot and cold dose-rate curves to six ^{211}At half-lives yielded upper and lower bounds for the absorbed dose received in the lymph node tissue slice. Uncertainties were roughly estimated by calculating the dose from a hypothetical dose-rate curve scaled to pass through the maximum value in the data set. For a mean IA of 150 ± 60 MBq (4.1 ± 1.6 mCi), the doses received in hot and cold regions were found to be 9 ± 4 Gy and 1.2 ± 0.8 Gy, respectively.

5.5 Discussion

This short chapter provides a condensed illustration of the metrics and information that DAR-based dosimetry can provide. Paper 1 was significant for its articulation of the methods described in Chapter 4, which added to the DAR tools developed by Bäck, Jacobsen, and Miller [130, 134, 153]. Since the preclinical data had already been assessed previously [4], the value of the material in this chapter lies more in the demonstrated feasibility of dosimetry-based analysis than the assessment of any biological outcome. The clear delineation of a small-scale dosimetry framework supports the ongoing paradigm shift from biodistribution absorbed dose measurements, which are not spatially sensitive within organs, to pharmacokinetic studies that utilize quantitative digital autoradiography dosimetry. The following discussion accompanied the original publication (which included methodological development, as in Chapter 4, alongside the ^{211}At dosimetry in this chapter).

Our work constitutes an improvement to previous DAR-based αRPT dosimetry [4, 153] in three ways:

1. The computational and image processing methods, including ROI segmentation, activity correction, slice registration, and MC DPK convolution, have not been fully described in previous works to our knowledge;

2. The iQID camera is a self-contained system that measures activity directly (event-by-event) rather than using a secondary gamma-counting measurement, as with the α-camera. Therefore, the uncertainty associated with dosimetry measurements is reduced;

3. We have introduced elements of automation to improve efficiency of data collection and processing, incorporated histogram segmentation for assessment of non-uniformity, and proposed methods to reduce prohibitive slice requirements of these studies. Scripts are available as an in-development Python package on Github at `https://github.com/robin-peter/iqid-alphas` (DOI: `https://doi.org/10.5281/zenodo.7117835`).

Our procedure does not trace individual α-particle tracks or their stochastic effects in specific cells but rather calculates absorbed dose with a mean Monte Carlo (MC) energy deposition kernel. We thus classify our approach as small-scale (sub-organ and cellular level) rather than a true stochastic microdosimetric method, using the titular convention [154]. Use of the DPK kernel allows for extension of this method to other radionuclides [155] or non-water-like tissues such as bone and lungs [156] by generating a new kernel. The authors are currently conducting studies of therapeutically conjugated ^{225}Ac and ^{227}Th in a murine model with these methods.

Direct MC, DPK convolution, and MIRD S-coefficients (or S-values) are the three current dosimetry methodologies identified by ICRU Report 96 as relevant for calculation of absorbed dose in RPT [31]. The S-coefficient method is often regarded as the most practical and closest to a clinical standard, but it usually assumes uniform distribution of dose within an

organ, which is often inaccurate in αRPT. Our procedure uses MC and DPK convolution in a procedural workflow, mostly contained in one non-proprietary software (Python), that can be replicated to obtain dosimetry results in systems of other radionuclides and tissues by tuning only a few specific components. Future work should compare DPK methods using iQID with actively researched S-coefficient approaches that model dose inhomogeneity, such as cellular-scale S-values (i.e. MIRDcell simulation) [31, 132, 157]. However, MIRDcell simulation results may be challenging to map to the non-cellular iQID device. The comparison between DPK and micro-scale S-value methods for iQID is therefore a non-trivial task.

Alpha-particle dose varies widely at the cellular level because the short particle range results in dose localized around expression of the target antigen. We confirmed that exclusively reporting the mean dose, as is common in biodistribution studies, may insufficiently characterize therapeutic effects in sub-organ tissues with inhomogeneous radiopharmaceutical uptake. Research that investigates the relationship between this microscale dose nonuniformity and biologic effect has been identified as a key avenue for progress in αRPT [31]. Our method of digital dose segmentation and co-registration with pathological information allows dose estimation on the scale of nonuniformities and promotes co-investigation of biologic effects. The methods presented in this work can also be generalized to report the RBE-weighted dose distribution for endpoints such as DNA double strand break induction [158] and reproductive cell survival [159] to further assess the clinical impact of αRPT.

In informal terms, the methods discussed here should be considered a suggested recipe, rather than a fixed prescription, for αRPT dosimetry using digital autoradiography. Follow-up studies should aim to optimize the components, including the registration procedure, microdosimetry model (DPK or otherwise), and experimental parameters. The dose contribution of the ^{211}At electron-capture branch was not quantified in the dose kernel and may be investigated in future work. A simple algorithm was sufficient to align the canine lymph nodes in this study, but more robust procedures may be needed for complex tissues. Rigid 2D transformations were applied assuming that each slice did not distort significantly in 12 µm, which may not be the case with thicker slices. This assumption is untrue at distances as low as 50 µm away, as was observed in the registration of iQID images with H&E-stained slices. Thicker slices also degrade depth resolution and detection efficiency as fewer alpha particles escape the tissue, but they are easier to cut from biopsies without sample handling errors. Quantifying the trade-offs between spatial resolution and precise dose localization, and between slice thickness and detection efficiency, would provide insight into the optimal field-of-view and cryotome setups.

5.6 Summary

Paper 1 had two main contributions: 1) the development and articulation of methods to obtain quantitative, spatially sensitive ex vivo α-particle absorbed dose measurements needed for the clinical translation of αRPT (Ch. 4), and 2) the demonstration of these methods as an illustrative example on previously collected data from ^{211}At-mAb treatment in canine lymph

nodes (Ch. 5). Efforts to streamline and standardize small-scale dosimetry improve the feasibility of preclinical and clinical biopsy absorbed dose measurements, which are required to further our understanding of α-particle radiopharmaceuticals and their biologic effects at both cellular and macroscopic scales.

Contribution 1 encompassed the development of advanced and automated tools to quantify cellular-scale absorbed dose and dose rates with single-particle DAR imaging and assess uptake uniformity, histological pathology, and requisite slice numbers. These tools provided a foundation for the continued development of micro-scale αRPT dosimetry methods in Papers 2 and 3. Although the small-scale dosimetry results from Contribution 2 were informative, no further biological outcomes were investigated as a result of the dosimetry metrics evaluated in this study. In the following chapter, we begin to contextualize preclinical dosimetry findings with treatment study observations and investigate whether small-scale dosimetry can assess organ toxicity or tumor control.

Chapter 6

3D digital autoradiography and dosimetry of ^{225}Ac in mouse kidneys and prostate cancer xenografts

This chapter reports the development of 3D digital autoradiography methods and their use in the analysis of a novel αRP, [^{225}Ac]Ac-Macropa-PEG$_4$-YS5, in a prostate cancer xenograft model in mice. Methods from Chapter 4 are applied as a baseline and expanded to 3D to evaluate whole tumors and mouse kidneys, with focuses on sub-kidney compartmental dosimetry and tumor control probability. The text and data in this chapter are reproduced from Paper 2 with edits and additions [2].

Paper 2 Abstract: Radiopharmaceutical therapy using α-emitting ^{225}Ac is an emerging treatment for patients with advanced metastatic cancers. Measurement of the spatial dose distribution in organs and tumors is needed to inform treatment dose prescription and reduce off-target toxicity, at not only organ but also sub-organ scales. Digital autoradiography with α-sensitive detection devices can measure radioactivity distributions at 20–40 µm resolution, but anatomical characterization is typically limited to 2D. We collected digital autoradiographs across whole tissues to generate 3D dose volumes and used them to evaluate the simultaneous tumor control and regional kidney dosimetry of a novel therapeutic radiopharmaceutical for prostate cancer, [^{225}Ac]Ac-Macropa-PEG$_4$-YS5, in mice. 22Rv1 xenograft-bearing mice treated with 18.5 kBq of [^{225}Ac]Ac-Macropa-PEG$_4$-YS5 were sacrificed at 24 h and 168 h post-injection for quantitative α-particle digital autoradiography and hematoxylin and eosin staining. Gamma-ray spectroscopy of biodistribution data was used to determine temporal dynamics and ^{213}Bi redistribution. Tumor control probability and sub-kidney dosimetry were assessed. Heterogeneous ^{225}Ac spatial distribution was observed in both tumors and kidneys. Tumor control was maintained despite heterogeneity if cold spots coincided with necrotic regions. ^{225}Ac dose rate was highest in the cortex

and renal vasculature. Extrapolation of tumor control suggested that kidney absorbed dose could be reduced by 41% while maintaining 90% TCP. The 3D dosimetry methods described allow for whole tumor and organ dose measurements following ^{225}Ac radiopharmaceutical therapy, which correlate to tumor control and toxicity outcomes.

6.1 Introduction

Digital autoradiographs (DARs) are often correlated with other modalities such as histological stains, gamma-ray spectroscopy, and even high-resolution MRI data to interrogate sub-organ and sub-tumor effects [123, 127]. Labor or instrument field-of-view constraints encourage the assessment of only one or a few representative slices, so observable features are limited to a single plane per slice due to the 2D nature of the modality. However, the content of a DAR can vary with the spatial position of the slice within the tissue. In the mouse kidney example in Fig. 6.1A, the peripheral slice does not pass through the medulla and lacks dosimetry information about that sub-organ compartment. While the obvious solution is to conduct the experiment with central slices, it may not be trivial to select a representative sampling location for irregular structures such as tumors.

The potential benefit to full 3D investigation of αRPs in tissues and tumors has not been previously evaluated. It is theoretically possible to collect enough consecutive DARs from a tissue to assemble a 3D absorbed dose rate distribution [131], but the procedure is practically prohibitive: imaging a typical 5-mm diameter tissue at 10 µm slice thickness would require 500 cryotome sections (Fig. 6.1B). Sparse sampling results in loss of the 3D activity information necessary to calculate absorbed dose from surrounding tissue cross-fire.

In Paper 2, we demonstrated that the identical slice approximation described in Chapter 4 can facilitate 3D quantitative digital autoradiography with sampling (Fig. 6.1B). By accepting some inaccuracy at each sampling point, 3D quantification of the activity distribution over an entire anatomical tissue or organ can be obtained. The procedure is straightforward: instead of consecutive tissue sections, single slices are cut from the frozen tissue at regularly determined intervals, on the order of twice the particle range to avoid crossfire between samples. The identical slice approximation, cloning method, and quantitative dosimetry procedures described in Chapter 4 are applied to each single-slice measurement. Registration of the slices yields a 3D absorbed dose profile. This procedure is referred to as 3D digital autoradiography (3D DAR) and produces 3D digital autoradiographs (3D DARs). Specific details such as slice thickness, slicing interval, and uncertainty associated with the approximation must be determined for each application.

The proposed 3D DAR methodology was combined with quantitative methods for DAR dosimetry (spatial information), gamma-ray biodistribution (temporal information), and H&E stain analysis (morphological information) to study [^{225}Ac]Ac-Macropa-PEG$_4$-YS5 in murine tumors and kidneys and relate the 3D sub-organ absorbed dose distribution to predicted biological outcome. YS5 is a human monoclonal antibody that binds to a tumor-

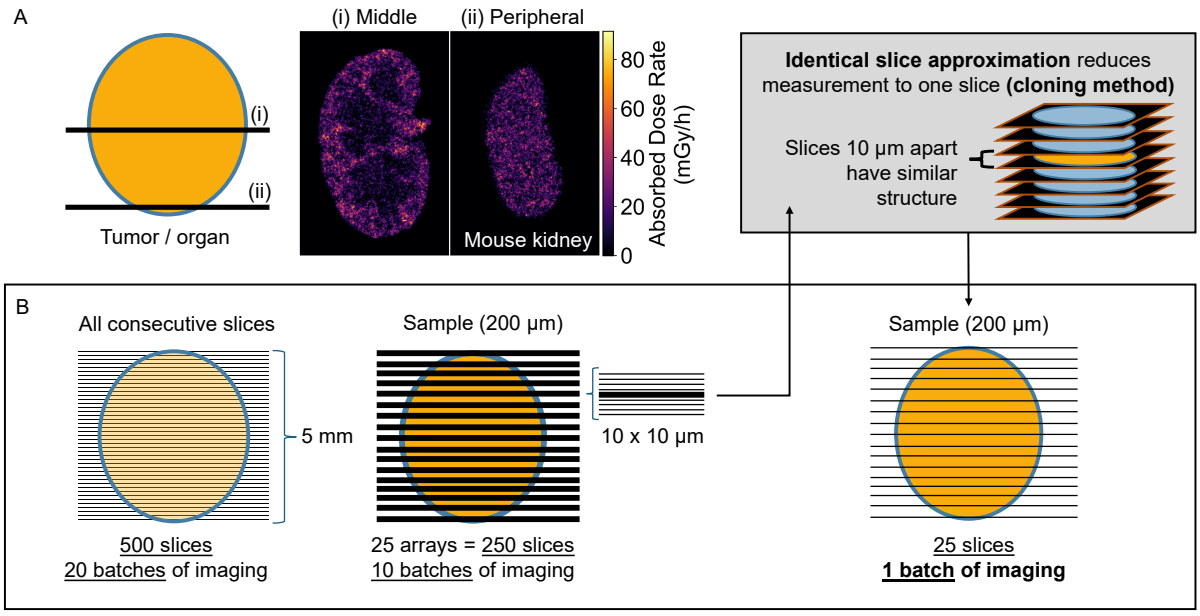

Figure 6.1: Visual overview of 3D DAR rationale and procedure. (A) A tissue slice sample represents a single plane in a 3D organ. The information contained in the slice autoradiograph depends on the anatomy of the sample in that plane. (B) Without sampling, or with sampling and sequential DAR dosimetry methods, 3D DAR requires prohibitive numbers of tissue slices. By accepting some inaccuracy from the cloning method, a 3D distribution of the activity distribution over an entire anatomical tissue or organ can be obtained within finite time.

selective epitope of CD46 [160]. Researchers at UC San Francisco, who originally identified YS5, have since developed several novel α-radiopharmaceutical agents utilizing it, including [^{225}Ac]Ac-Macropa-PEG$_4$-YS5, which has shown specific uptake in prostate cancer models and demonstrates promise for ^{134}Ce/^{225}Ac theranostic development with ^{134}Ce as the PET diagnostic and ^{225}Ac as the therapeutic agent [59, 161].

6.2 Methods

6.2.1 Ethics approval

The animal experiments were approved by and carried out in compliance with the Institutional Animal Care and Use Committee (IACUC) and established guidelines at the Laboratory Animal Resource Center (LARC), University of California, San Francisco, CA. The

study design and methods follow recommendations in the ARRIVE guidelines.

6.2.2 Experimental design

Immunocompromised Nu/nu mice (5-6 weeks old, Strain: 002019, Jackson Laboratories) were used for subcutaneous xenografts. Each mouse was subcutaneously inoculated with 2.5 million 22Rv1 cells mixed with Matrigel (Corning, #354230) in a 1:1 ratio. Tumor growth was monitored for 21 days until the tumors reached a volume of 0.4 to 0.6 cc. All animals for prostate cancer models used in our studies were male mice.

22Rv1 xenograft-bearing mice received an intravenous injection of 18.5 kBq of [^{225}Ac]Ac-Macropa-PEG$_4$-YS5 via the tail vein and were sacrificed at two time points: 24 h post-injection (p.i.) and 168 h (7 d) post-injection. ^{225}Ac was in equilibrium at the time of injection. Blood, tumors, kidneys, and other selected organs were collected for biodistribution (BioD: NaI AMG, Hidex), and only tumors and kidneys were subjected for autoradiography (iQID, QScint Imaging Solutions, LLC). Consecutive tissue slices were stained with hematoxylin and eosin (H&E) using a standard protocol. Antibody conjugation, ^{225}Ac radiolabeling, and [^{225}Ac]Ac-Macropa-PEG$_4$-YS5 synthesis followed the procedure in [161].

In total, four cohorts of identically prepared mice were described in this study: animals for DAR method comparison ($N = 4$), animals for 3D DAR ($N = 4$), animals for BioD-based ^{213}Bi corrections ($N = 8$), and animals in a 7-d BioD study to determine the time-dose-rate curves for [^{225}Ac]Ac-Macropa-PEG$_4$-YS5 in the mice ($N = 17$).

6.2.3 iQID digital autoradiography imaging

An iQID camera DAR device was used to obtain high-resolution (voxel size 39 µm × 39 µm × 10 µm) images of the instantaneous spatial distribution of α-particle emitters in tissues at the start of the acquisition. A larger stage (80 mm diameter) was used to increase the number of tissue samples that could be measured simultaneously, with the trade-off of increasing the effective voxel size to 39 µm.[1]

After sacrifice, tissue samples were prepared in an Optimum Cutting Temperature (OCT) medium, sliced using a cryotome to 10 µm thickness, and mounted on the iQID camera for imaging. A correction factor (1.09) for the device frame-rate (25 FPS), discussed in Section 4.3.3, was derived for ^{225}Ac due to the rapid decay of progeny ^{217}At ($t_{1/2}$ = 32 ms). The 3D energy deposition kernel for ^{225}Ac is described in Sec 4.6. Progeny were assumed to be in secular equilibrium, since iQID measurements were taken long enough after sacrifice for free ^{213}Bi to decay significantly (> 5 h). The kernel was averaged radially and binned to the voxel size of the iQID image stack (XY: 39 µm; Z: 10 µm).

[1] As compared to a 40-mm FOV with 19.5 µm effective voxel size.

6.2.4 2D to 3D DAR

The cloning method was validated for [^{225}Ac]Ac-Macropa-PEG$_4$-YS5 in a mouse model using ten consecutive slices ($10 \times 10\,\mu m = 100\,\mu m$ total) from each mouse kidney and tumor ($N = 4$ mice). The dose rate of the central slice was compared between the sequential and cloning methods. The results for the validation study are shown in Fig. 4.14 and discussed in Section 4.9.

To assess 3D dose volumes, mice were identically prepared ($N = 4$), but instead single tissue slices were extracted at 200 µm intervals from kidneys and tumors to yield 3D volumes of 20–30 slices per tissue (voxel size 39 µm × 39 µm × 210 µm). Spatial dose rates were estimated in each slice using the cloning method and DPK convolution. At 200 µm spatial sampling rate in a 5-mm diameter tissue (i.e., one slice collected every 200 µm of tissue), the cloning method reduces the slices that must be prepared for 3D DAR from 250 to 25. 3D DAR figures were rendered with 3D Slicer [140].

6.2.5 Radiosensitivity parameter and TCP

To compute TCP, we used $\alpha = 1.8\,Gy^{-1}$ based on a cell-killing assay (Fig. 4B in Bobba et al [161]) to estimate the α-radiosensitivity parameter of 22Rv1 cells to [^{225}Ac]Ac-Macropa-PEG$_4$-YS5. Relevant method details are quoted here:

> 22Rv1 cells were cultivated in 96-well plates at a density of 2,000 cells per well. The cells were treated with varying concentrations of [^{225}Ac]Ac-Macropa-PEG$_4$-YS5 (ranging from 3.7×10^{-7} to 3.7 kBq) for 96 h. After the treatment, cell viability was measured using the cell titer glo reagent (Fisher scientific, Mfr. No. Promega G7570) per the manufacturer's instructions.

The plate (Corning Inc. Costar REF 3603 96 Well Assay Plate) had a bottom growth area of $0.32\,cm^2$, and 100 µL of total liquid volume was applied. As a first-order approximation, cells were assumed to receive the same dose as the water, assuming full energy deposition of all α-particles in the ^{225}Ac decay chain over 96 h. This assumption likely underestimates the cell kill due to the actual accumulation of the labeled radiopharmaceutical on the cell membrane rather than as a dispersed solution.

The linear quadratic model, which is well established in literature for cell survival assays, does not predict saturation at high dose, as was observed in Bobba et al, Fig. 4B. However, there is binding saturation in a cell culture, shown in Bobba et al, Fig. 4A. For the cell survival curve, we excluded the last data point at 50 nCi/mL, as this value falls well beyond the threshold for 90% binding saturation (22 nCi/mL, calculated from Bobba et al, Fig. 4A). The resulting curve is shown in Fig. 6.2. A linear-quadratic model fit applied to the values yields $\alpha = 1.8\,Gy^{-1}$. A fit without the last (likely also saturated) data point yields $\alpha = 5.8\,Gy^{-1}$, but we used $\alpha = 1.8\,Gy^{-1}$ for our model to maintain a conservative approach (underestimating rather than overestimating tumor control).

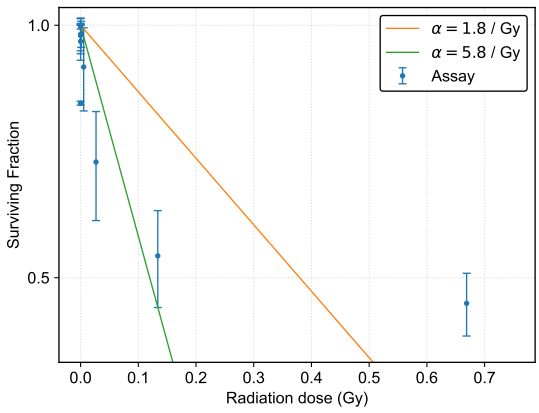

Figure 6.2: Converted cell survival curve of [^{225}Ac]Ac-Macropa-PEG$_4$-YS5 in 22Rv1 cells, based on Fig. 4B from [161].

Literature values of α-particle radiosensitivity parameters tend to vary widely [31]. Several conservative assumptions underlie the final selection of $\alpha = 1.8\,\mathrm{Gy}^{-1}$ as the radiosensitivity parameter in this study, and we acknowledge from the the data shown that the model is a poor fit that should only serve as a first-pass estimate. A clonogenic assay using a non-membrane permeable chelator such as EDTA/DTPA, in conjunction with a Monte Carlo simulation accounting for the geometry and α-particle range, would be a more accurate approach to compute the cell survival curve. For this study, we accepted the cell kill underestimates from both the saturation and homogeneous dose assumption as a conservative approach to therapy optimization.

6.2.6 Gamma-ray spectroscopy

Gamma-ray emissions from organs and tumors were counted in a Hidex NaI(Tl) automatic gamma counter between 0.5–3 h post-sacrifice, allowing 60 s active counting time per tissue, as described in Chapter 2. Net counts were recorded in energy windows corresponding to ^{221}Fr (168–268 keV) and ^{213}Bi (370–510 keV), using a least-squares Gaussian distribution with linear background to correct for ambient background (^{213}Bi) and down-scatter (^{221}Fr) in each energy window (Fig. 6.3). Counts were corrected by their respective branching ratios, decay times, and energy-dependent detector efficiencies, determined by a known-activity detector calibration using the same procedures. The formalism described in Section 2.6 for separation of ^{225}Ac and ^{213}Bi was applied.

6.2.7 Macro-to-micro dosimetry

The temporal evolution of activity was estimated using macroscopic gamma counting measurements and a macro-to-micro approach [107]. The absorbed dose value in each DAR voxel was extrapolated by scaling the dose-rate curve measured within whole tumors and kidneys by a factor c based on the mean dose rate of the DAR measurement at one time-point (24 h or 168 h p.i.), assuming that the activity did not significantly redistribute over time. The

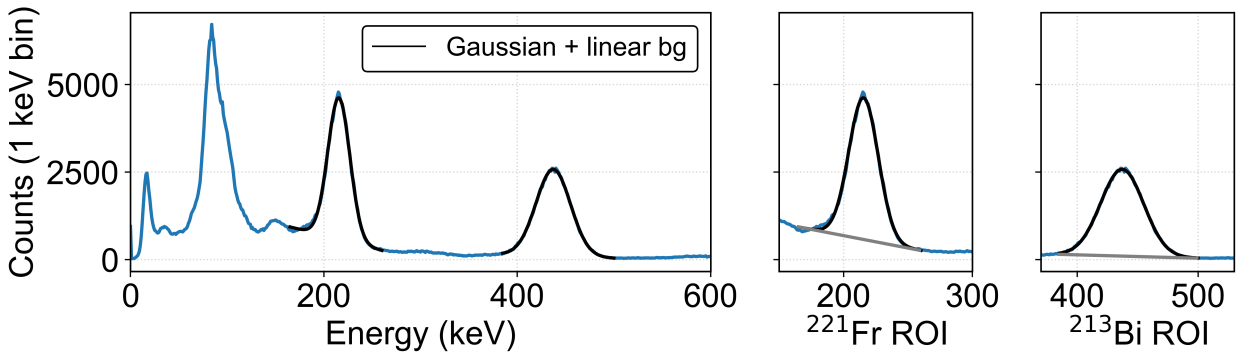

Figure 6.3: Illustration of counting and fitting procedure for gamma-ray spectroscopy measurements.

dose-rate curve was modeled with time-dependent BioD from 1 d, 2 d, 4 d, and 7 d p.i. ($N = 17$).

Energy from the ^{225}Ac decay chain was assumed to deposit entirely within the tumor (which showed $A_b(t)/A_a(t) = 1$ within uncertainties), but in kidneys, we separated ^{225}Ac contributions from free ^{213}Bi and its products. Resulting dose rates were fit to bi-exponential curves using least-squares optimization. We extracted extrapolation factors c_{24h} and c_{168h},

$$c_{24h} = D/\dot{D}_{24h}, \qquad c_{168h} = D/\dot{D}_{168h}, \tag{6.1}$$

where D was the total integrated dose under the time-dose-rate curve (TRC) to six half-lives, and $\dot{D}_{24h}$ and $\dot{D}_{168h}$ were the dose rates measured at 24 h and 168 h p.i by BioD. iQID dose-rate DARs from 24 h p.i. were scaled by c_{24h} to obtain the voxel distribution of total absorbed dose D_i, and similarly for 168 h p.i. DARs by c_{168h}.

6.2.8 Histological staining

Tissue slices consecutive with each sample series (sequential-method validation mice) or with each tissue slice (3D DAR mice) were stained with H&E using a standard protocol. Images were acquired with an Octopus-Versa Slide Scanner (Leica).

6.2.9 Statistical analysis

Results reported as $x \pm \sigma$ describe the mean value x and one standard deviation σ. Results of the form x (x_1, x_2) show asymmetric uncertainties, where x_1 is the lower bound and x_2 is the upper bound propagated from dose calculations. For sub-organ dosimetry using H&E stains, damage to the kidneys during cryotome slicing resulted in only $N = 1$ mouse per time point, for which x and σ are calculated using contralateral samples (left and right kidneys). All mentions of *dose* refer to absorbed dose (Gy), with no radiation weighting or relative biological effectiveness factor.

Table 6.1: $A_b(t)/A_a(t)$ ratios for selected tissues at approximately 1 h post-sacrifice (first bar in Fig. 6.4). Kidneys showed significant deviation from secular equilibrium at both time points.

Tissue	$t = 24$ h p.i.	$t = 168$ h p.i.
Tumor	0.97 ± 0.04	1.06 ± 0.04
Kidneys	6.1 ± 0.3	5.3 ± 0.6
Blood	0.62 ± 0.01	1.03 ± 0.10

6.3 ^{213}Bi redistribution

BioD results from 24 h p.i. are shown in Fig. 6.4A ($N = 4$). The ratio $A_b(t)/A_a(t)$ was compared to unity at $t = 1$ h post-sacrifice (first bar in each 4-bar set) to determine deviation from secular equilibrium in tissues. Values of the ratio from both the 24 h p.i. and 168 h p.i. subjects are summarized in Table 6.1. Note that this ratio must always be reported with a specific post-sacrifice time to be meaningful, and should only be compared to ratios collected at the same time (unless decay corrections using the Bateman equations are applied to normalize all values to a certain post-sacrifice time, as calculated below).

In kidneys, $A_b/A_a = 6.1 \pm 0.3$ and $5.3 \pm 0.6 > 1$ indicated substantial free redistributed ^{213}Bi at both time points. Blood measurements were deficient in ^{213}Bi at 24 h p.i. ($A_b/A_a = 0.62 \pm 0.01 < 1$), which suggests that ^{213}Bi was cleared from blood through the kidneys, but had equilibrated by the late time point ($A_b/A_a = 1.03 \pm 0.10$). Both early and late time points showed tumors at or near secular equilibrium between ^{225}Ac and ^{213}Bi ($A_b/A_a = 0.97 \pm 0.04, 1.06 \pm 0.04 \approx 1$).

The decay of $A_b(t)/A_a(t)$ in kidneys post-sacrifice followed Eqn. 2.9 with a goodness-of-fit coefficient of determination $r^2 = 0.996$ ($N = 4$ mice, 60 s active counting per tissue). The decreasing signal in the kidneys was used to measure the free ^{213}Bi using Eqns. 2.9 and 2.10. $A_b(0)/A_a(0)$ was calculated from Eqn. 2.9 and Eqn. 2.10 for 24 h p.i. mice as 14.7 ± 0.2 and 14.0 ± 1.2, respectively, which agree within 1σ. Agreement was also observed at 168 h p.i. (17.1 ± 1.8 and 15.6 ± 2.4). In both cases, the more precise result was used for subsequent analyses. Greater uncertainties for the experimental fit at 168 h p.i. are attributable to the lower overall activities remaining in the system and a poorer exponential fit due to an oversight in the 168 h p.i. data that resulted in a narrower time window for the measurements (only 8 min between mice).

6.4 Single-time-point dosimetry

Figure 6.4B shows time-dose-rate curves (TRCs) using the approach illustrated in Fig. 6.4A to separate kidney absorbed dose contributions into ^{225}Ac and free ^{213}Bi components. No

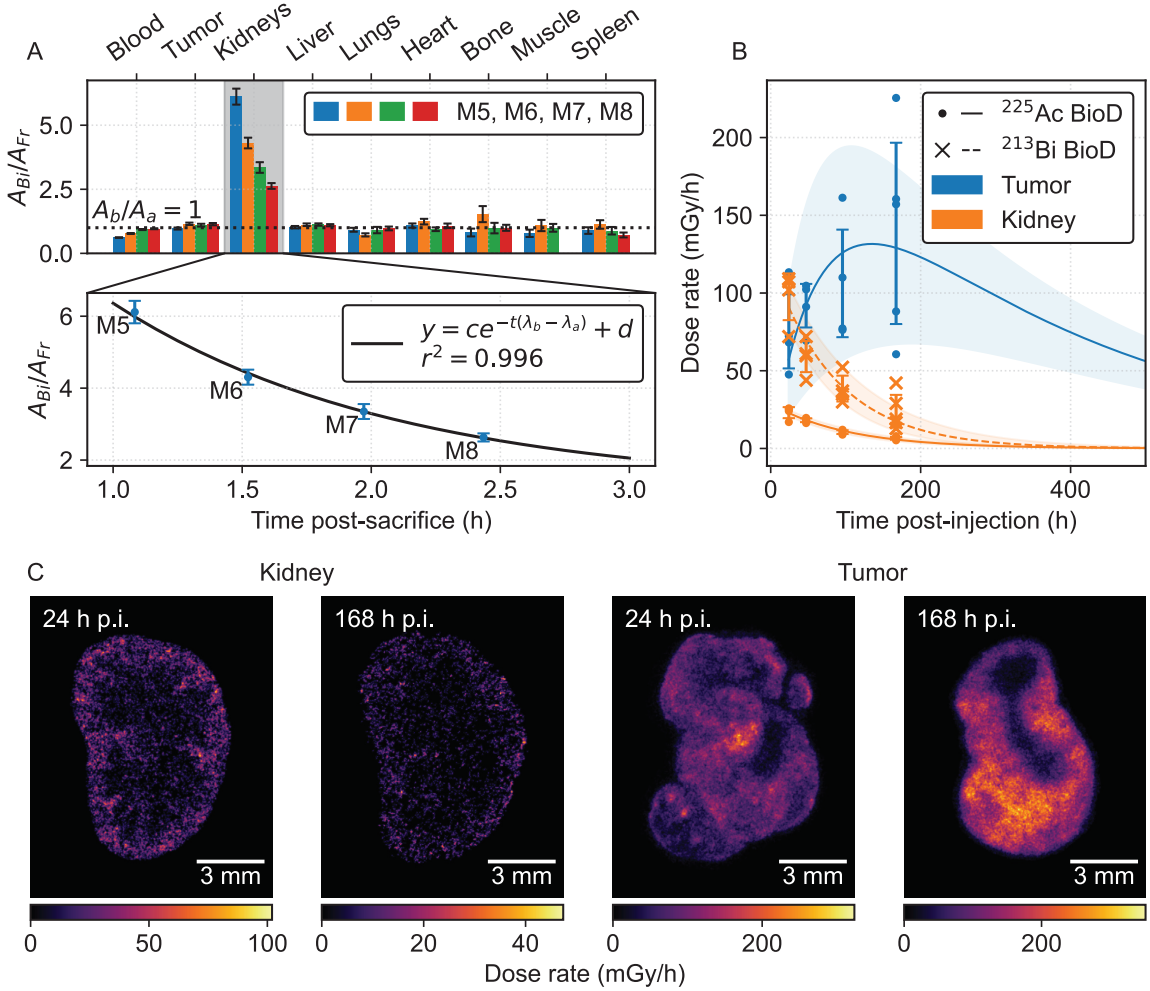

Figure 6.4: Temporal studies of [^{225}Ac]Ac-Macropa-PEG$_4$-YS5 in 22Rv1 xenograft-bearing mice. (A) ^{213}Bi correction example using gamma-ray spectroscopy for 24 h p.i. mice (subjects M5–M8). Activity ratios of the two ^{225}Ac daughters demonstrate clearance of free ^{213}Bi in the blood through the kidneys ($N = 4$). The decay of the $A_b(t)/A_a(t)$ ratio following sacrifice follows Eqn. 2.9 despite variable uptake between subjects. (B) Time-dose-rate curves (18.5 kBq, $N = 17$), with contributions from free ^{213}Bi and ^{225}Ac in kidneys separated. (C) Representative DARs from kidneys and tumors at two time points.

^{213}Bi data from 24 h p.i. were available from this cohort due to a 7-h delay in measurement. The 24 h p.i. data shown were extrapolated from the measured ^{225}Ac activity A_a and the calculated correction factor $A_b(0)/A_a(0)$.

The dominant uncertainty in the TRCs was the variable uptake between animal subjects, shown as 1σ error bars around the mean absorbed dose rate. Individual subject data points

Table 6.2: Absorbed dose calculations and correction factors from integration of BioD dose-rate curves (Fig. 6.4B).

Tissue	Radioisotope	Dose (mGy/kBq)	$c_{24h} = D/\dot{D}_{24h}$ (mGy/mGy-h)	$c_{168h} = D/\dot{D}_{168h}$ (mGy/mGy-h)
Tumor	^{225}Ac	3540 (2120, 4840)	870 (520, 1190)	474 (283, 647)
Kidneys	^{225}Ac	142 (121, 168)	114 (97, 135)	406 (345, 480)
Kidneys	^{213}Bi	466 (349, 627)	84 (63, 113)	361 (271, 486)

are shown instead of the mean dose rates themselves. We calculated the total absorbed dose for each TRC as the integrated area, with uncertainties as the dose from upper- and lower-bound curves defined by modulating the fitting parameters by $\pm 1\sigma$. Table 6.2 summarizes the calculated doses and conversion factors c for each TRC with bound-based uncertainties.

Use of the extrapolation factor assumes that the intra-organ and intra-tumor spatial activity do not change over time. Figure 6.4C shows representative DARs for kidneys and tumors at 24 h and 168 h post-injection. The ratio between mean absorbed dose rates in each renal compartment (cortex, ISOM/OSOM, IM/papilla, and V/Pe) was (1, 0.50, 0.88, 1.19) at 24 h p.i., and (1, 0.60, 0.83, 1.06) at 168 h p.i., indicating that similar compartmental distribution was preserved. (Segmentation details are described in Sec. 4.10.2.) In tumors, both time-points exhibited morphology-dependent activity distribution with low dose in the necrotic core, but higher tumor saturation was observed at 168 h post-injection.

6.5 3D kidney dosimetry

The mean kidney absorbed dose from 18.5 kBq [^{225}Ac]Ac-Macropa-PEG$_4$-YS5 was 6.4 (4.6, 8.9) Gy and 7.5 ± 2.2 Gy from DAR and BioD, respectively (Table 6.3). 75% (73%, 78%) (DAR) and 78 ± 7 % (BioD) of the total mean dose was due to the decay of free ^{213}Bi, where the ^{213}Bi correction to iQID DARs was provided by the $A_b(0)/A_a(0)$ ratio. The spatial distribution of free ^{213}Bi was not obtained from these DARs, which were imaged several days post-sacrifice. The reported mean values of the two modalities differed by 15% and agree within 1σ of BioD statistical uncertainties.

Figure 6.5A illustrates an example H&E stained slice, the anatomically segmented regions (cortex, ISOM/OSOM, IM/papilla, and V/Pe), and the corresponding iQID DAR. All 23 slices from a 24 h p.i. kidney were combined to create the 3D DAR and co-registered 3D anatomical model in Fig. 6.5B.

Dose-rate volume histograms (DrVHs) from each anatomical compartment are shown in Fig. 6.5C. Average ^{225}Ac dose rate in the renal cortex doubled that in the medulla at 24 h p.i. (16.6 ± 0.1 mGy/h vs. 8.2 ± 0.1 mGy/h) and was 67% higher at 168 h p.i. (4.24 ± 0.04 mGy/h vs. 2.53 ± 0.07 mGy/h). The inner medulla and papilla mean dose

Table 6.3: Absorbed dose comparisons between modalities and tissues using single-point dosimetry.

Tissue	Modality	^{225}Ac Dose (Gy/kBq)	^{213}Bi Dose (Gy/kBq)*	Total Dose (Gy/kBq)
Kidneys	DAR ($N = 2$)	0.09 (0.07, 0.11)	0.26 (0.18, 0.37)	0.35 (0.25, 0.48)
Kidneys	BioD ($N = 8$)	0.08 ± 0.02	0.32 ± 0.14	0.40 ± 0.14
Tumor	DAR ($N = 3$)	2.8 ± 0.2	—	2.8 ± 0.2
Tumor	BioD ($N = 8$)	3.1 ± 1.0	—	3.1 ± 1.0

*Dose due to α-particles from redistributed free ^{213}Bi and its associated progeny ^{210}Po. For DAR, separation of ^{213}Bi (and ^{210}Po) dose is based on $A_b(0)/A_a(0)$ ratio calculated in Sec. 6.3. Significant redistribution was not observed to tumors (Fig. 6.4A).

rate was similar to that in the cortex (13%, 18% less for respective time-points). Blood vessels and the renal pelvis collected comparatively high amounts of ^{225}Ac at the two time points (20 ± 1 mGy/h, 4 ± 1 mGy/h). These results show high ^{225}Ac concentrations at key transport locations: blood vessels, cortex, and the renal pelvis. Intact antibody-based radiopharmaceutical compounds such as [^{225}Ac]Ac-Macropa-PEG$_4$-YS5 may be too large for filtration and thus stagnate in the glomeruli or remain in the blood.

We evaluated our DAR-based sub-organ dosimetry results from 24 h p.i. next to a regional S-value dosimetry model developed by Vargas et al [127]. This model takes the total activity as measured by BioD and distributes it according to the relative activity ratios in each compartment. We calculated this ratio using DARs from across the whole kidney volume and applied the published S-value calculations according to the procedure described by the authors. Since we did not separate the ISOM and OSOM, or the IM from the papilla, these segments were combined and their S-values averaged. Vasculature was assigned to the compartment within which it was found for this analysis, since it was not segmented in the reference.

The iQID DAR and regional S-value methods agreed within uncertainties for cortex and ISOM/OSOM regions (Fig. 6.5D). However, the S-value calculation indicated an IM/Pa dose rate exceeding 5 times that of the DAR method (bar extends beyond figure limits). The BioD mean dose rate (23.1 ± 3.6 mGy/h), which assumed full energy deposition of all decay products within the tissue, was naturally uniform and higher than the iQID and S-value estimates, except for the IM/Pa.

6.6 3D tumor dosimetry and TCP

Tumors received an average of 50.8 ± 4.1 Gy (DAR) and 57.4 ± 18.5 Gy (BioD) between the two modalities (2.8 ± 0.2 Gy/kBq or 3.1 ± 1.0 Gy/kBq: Table 6.3). Figure 6.6A–D summarizes

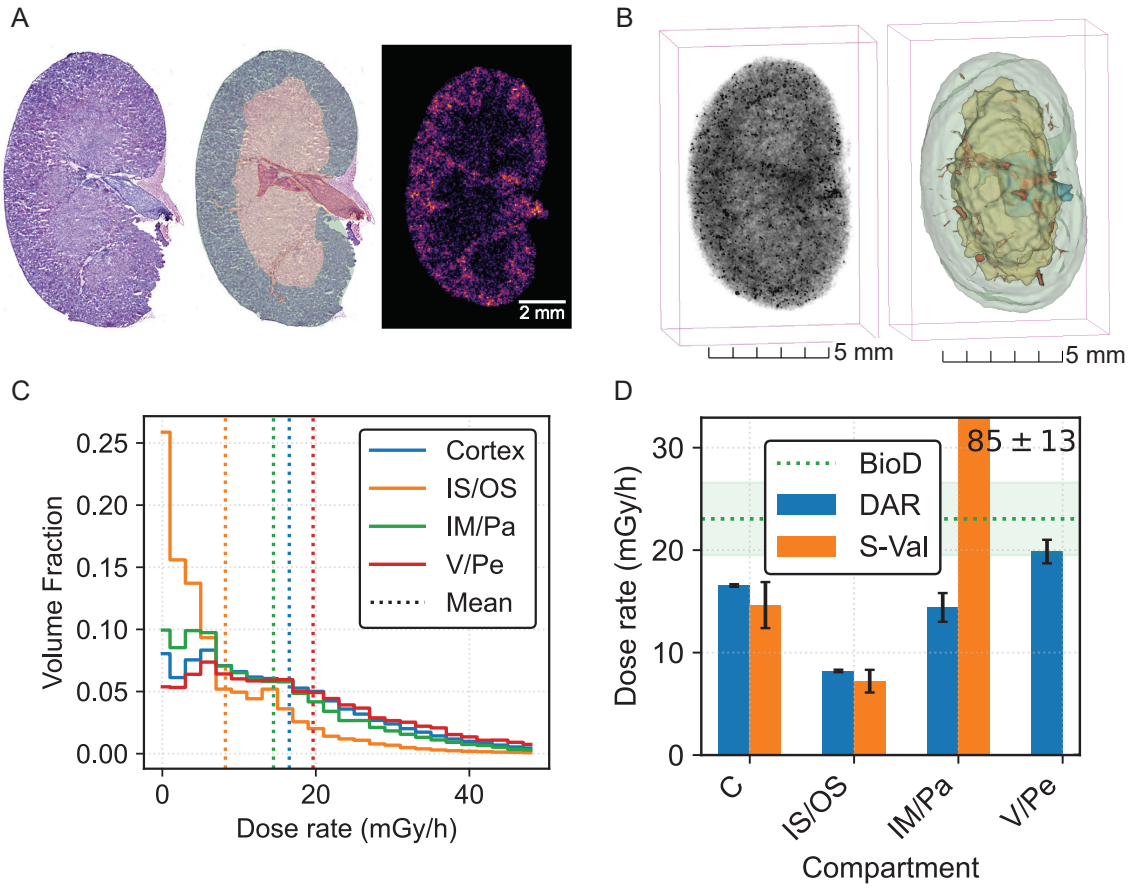

Figure 6.5: 3D kidney dosimetry and segmentation. (A) Example sub-organ dosimetry slice from a 24 h p.i. kidney, showing H&E image, anatomical mask, and 2D iQID DAR. (B) 3D DAR and H&E-based anatomical mask for the whole kidney, comprising 23 slices. (C) ^{225}Ac DrVH for segmented regions of both kidneys at 24 h p.i. (D) Comparison between iQID DAR, regional S-values [127], and BioD for kidney dosimetry.

tumor dosimetry and the TCP calculation process for a 24 h p.i. tumor, including the 3D DAR (Fig. 6.6A), example registered iQID and cell density images from H&E (Fig. 6.6B), TCP values for individual slices (Fig. 6.6C), and DrVHs for individual slices and the total volume for an example 24 h p.i. tumor (Fig. 6.6D). This analysis was conducted for $N = 3$ mice (labeled M9, M10, and M11), including two at 24 h p.i. (TCP: 1.00 ± 0.01, 0.88 ± 0.25) and one at 7 d p.i. (0.71 ± 0.39). Values are cited as the mean and standard deviation of TCP calculated for individual slices.

Despite heterogeneous dose distribution and cold spots, high tumor control was attained in mouse M9 because low-dose regions corresponded to the necrotic core of the tissue with few cell nuclei (Fig. 6.6B). Between the two 24 h p.i. mice, lower mean dose (17% less) and heterogeneous uptake of the radiopharmaceutical in non-necrotic regions resulted in decreased TCP. The red dashed circle in the 3D DAR (Fig. 6.6E) indicates a region of reduced uptake in one lobe of the tumor. Fig. 6.6F shows a representative gray-scale DAR with low slice-TCP (0.00), with voxels with $\mathrm{VCP}_i < 0.95$ indicated in red. Fig. 6.6G shows the same for a low-TCP slice from 7 d p.i.

The mean slice-TCP and kidney dose were estimated for a range of injected activities (IA) from 0 to 18.5 kBq, assuming that dose scales linearly with IA and maintains the same organ and sub-organ spatial distribution (Fig. 6.6A). We then calculated a predictive de-escalation scheme using the highest TCP tumor (M9, Fig. 6.6B). In this simple model, a reduced IA of 10.9 kBq maintained a TCP of 0.9 with a 41% reduction in kidney dose. 75% IA reduction (4.625 kBq) was predicted to yield non-controlled tumors (TCP= 0). To test this, one additional mouse was prepared and analyzed with 4.625 kBq IA. We observed sparse radiopharmaceutical uptake, in comparison to the 18.5 kBq cohort, and TCP was calculated to be zero for all slices in agreement with the model (Fig. 6.7B). This calculation is consistent with a previous therapy and survival study with [^{225}Ac]Ac-Macropa-PEG$_4$-YS5 in mice, which found that 4.625 IA treatment extended survival and inhibited tumor growth for 41 days compared to saline, followed by tumor regrowth [161]. Subjects M10 and M11 did not reach 0.9 TCP and were not evaluated for de-escalation.

6.7 Discussion

Microdosimetry and small-scale dosimetry are crucial to understanding the treatment strategy of α-particle radiopharmaceuticals by linking spatial absorbed dose distributions to tumor kill or organ toxicity [75, 103, 162]. Here, we demonstrated how three staples of preclinical RP studies—gamma-ray biodistribution, immunohistological stains, and digital autoradiography—may be combined to assess tumor control probability and produce DrVHs of anatomical compartments. To our knowledge, this was the first study to generate and analyze 3D DAR in entire organs and tumors, and to calculate voxel-based TCP for experimental ^{225}Ac αRP measurements simultaneously with sub-organ kidney dosimetry. Since tumor dose from radiotherapeutics is limited by the tolerance of normal tissues, it is necessary and natural that small-scale tumor and organ dosimetry should be evaluated concurrently.

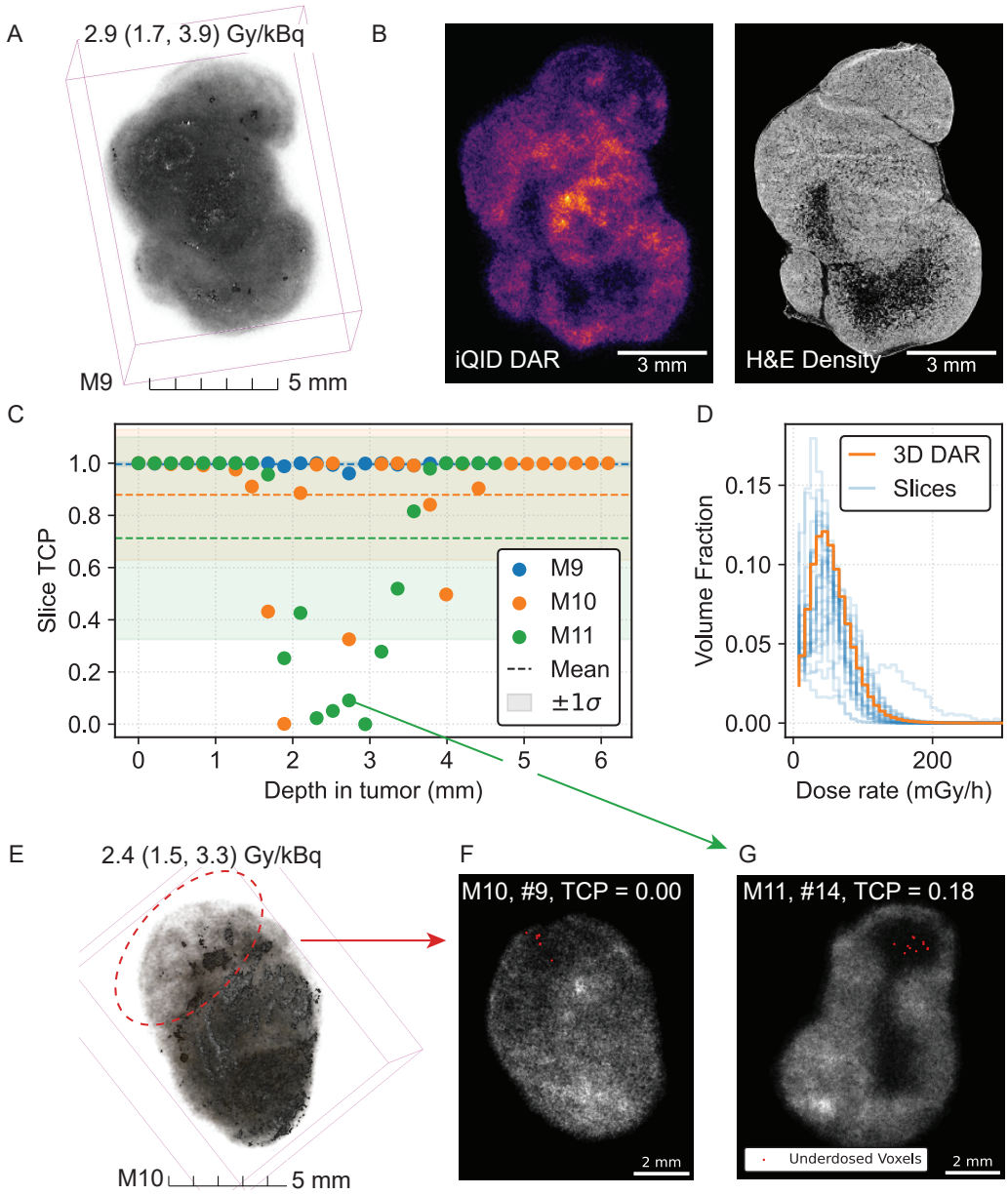

Figure 6.6: 3D tumor dosimetry and TCP calculation. (A) 3D DAR of 24 h p.i tumor (M9). (B) Co-registered iQID dose-rate DAR with corresponding cell nucleus density image segmented from H&E. (C) Slice-by-slice TCP ($N = 3$ mice with 21–27 slices each). (D) Tumor DrVH for individual slices compared to 3D DAR volume. (E) 3D DAR of 24 h p.i. tumor (M11). (F–G) Illustrative low-TCP slices. Dose-rate DAR is shown in gray-scale, with underdosed voxels (< 0.95 VCP) indicated.

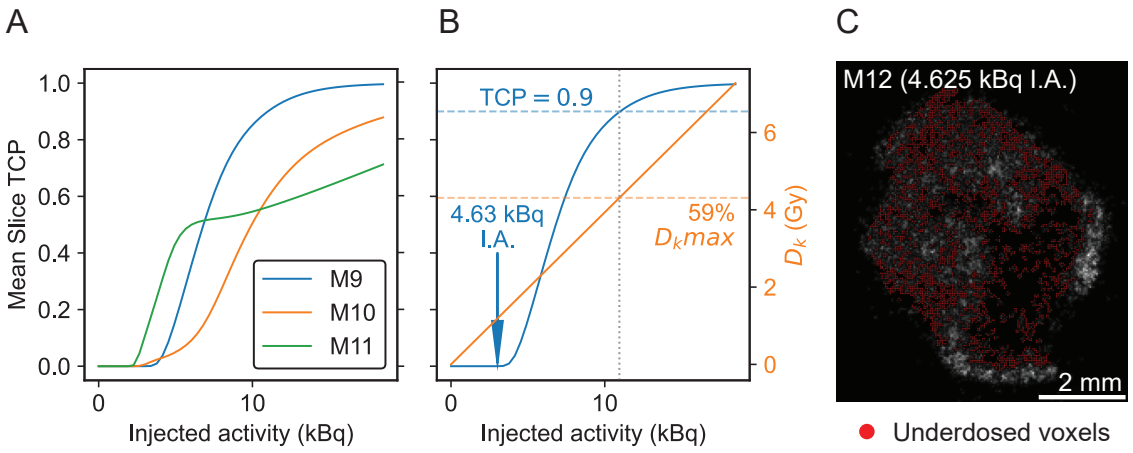

Figure 6.7: De-escalation predictive calculation. (A) Calculation of mean-slice TCP for a range of injected activities. (B) In subject M9, de-escalation calculation suggests that kidney dose may be reduced by 41% while maintaining 90% TCP. For 4.625 kBq I.A., the model predicts 0% TCP. (C) Slice from 4.625 kBq I.A. experiment, showing gray-scale dose-rate DAR with underdosed voxels (< 0.95 VCP) indicated. The calculated TCP of 0% is consistent with the model's prediction.

The study was mainly limited by the fact that no survival-and-treatment study of [^{225}Ac]Ac-Macropa-PEG$_4$-YS5 was conducted at the 18.5 kBq IA level, and therefore we could not draw direct conclusions about the treatment outcome and toxicity. However, results from 4.625 kBq treatments were available and provided some insight to our results [161]. The 4.625 kBq [^{225}Ac]Ac-Macropa-PEG$_4$-YS5 treatment extended survival and inhibited tumor growth for 41 days compared to saline, but tumors ultimately regrew. This was consistent with our simple predictive model and the added 4.625 kBq mouse assessed with the DAR-TCP method. For sub-organ dosimetry, we found that [^{225}Ac]Ac-Macropa-PEG$_4$-YS5 was predominantly located in the cortex, vasculature, and pelvis-adjacent structures. This agreed with the survival study, which observed mild to moderate renal toxicity and histopathological reduction and atrophy of the cortical glomerules and tubules. The simple de-escalation scheme was calculated for only one mouse with high TCP (> 0.9), since de-escalation is not a goal for sub-controlled tumors. Therefore, we could only treat this method as a proof of concept. With the DAR-TCP and sub-organ methodological framework established, future treatment studies can both utilize and validate the method by calculating TCP in cohorts treated at several injected activity levels and identifying potential correlation to disease progression and mortality. Exploration of these methods is increasingly relevant given the positive outcomes reported by clinical de-escalation trials [163].

We found several important nuances when using VCP-product TCP as a metric for

αRP treatment efficacy. In this framework, if every 10-µm slice has a high TCP = 0.95, where TCP = 1 is complete tumor control, then the cumulative 3D TCP of a 5-mm tumor would be $(0.95)^{50} = 0.08$. Given the tumor inhibition observed in treatment studies, we suspect that the mean TCP per slice may better reflect the treatment efficacy [161]. The TCP metric is conservative, formulated based on the probability of 100% cell kill, and thus does not necessarily capture meaningful non-curative outcomes such as prolonged survival, as we found with our comparison to the 4.625 kBq study. Additionally, we used conservative assumptions to estimate the radiosensitivity parameter α, so the actual biological impact and tumor control are likely to be higher than predicted when correcting for binding saturation, sterilized cells, well geometry, and dose delivered by recoiling nuclei. We did not consider hypoxia, variable radiosensitivity, or repopulation and repair [112].

An inherent drawback of ex vivo DAR and BioD studies is that the animal must be sacrificed to conduct a measurement, precluding monitoring of the same animal over time and demanding costly increases in sample size to minimize inter-subject variability. Moreover, the treatment cannot be adjusted on a subject-specific basis unless tissue biopsies are obtained. In this study, we utilized the minimum number of mice feasible to obtain a representative data set, resulting in large uncertainties attributable to single-point pharmacokinetics and the resulting inter-subject variability (Fig. 6.4B). These challenges are characteristic of the macro-to-micro dosimetry approach. Although the animal cohort was small, each tissue or tumor was assessed over 20–30 independent slices to evaluate intra-subject variability and the benefit of a 3D DAR approach. We demonstrated that a single 2D slice might not include structural or dose-distribution features present elsewhere in the 3D volume.

An in vivo study of the αRP characterizing the continuous pharmacokinetics over time within subjects, if one can be achieved given the low administered activities, could improve the precision of the macro-to-micro approach. Our group is working to develop ultra-high-sensitivity gamma-ray imaging techniques for αRPT [81, 91, 92, 164]. In vivo PET and SPECT imaging surrogates for ^{225}Ac RPs are also under investigation in our group and elsewhere [27, 161]. These imaging strategies are complementary to the methods described here, and can be used for in vivo imaging and ultimately for applications in clinical dosimetry [162, 165].

This work complements the study by Mellhammar et al, who used a MC-simulation DAR-TCP approach with ^{177}Lu-PSMA-617 extrapolated to [^{225}Ac]Ac-PSMA-617 [123]. We demonstrated experimentally that, as the authors simulated, low tumor penetration reduces TCP for the same IA level. Our approach differed in that quantitative single-particle DARs of the α-emitting RP were measured, instead of using a relative-intensity β-particle DAR as a proxy for the spatial distribution of α-particles. We also used 3D DAR for TCP (improving statistical count and morphological assessment), included concurrent sub-organ kidney dosimetry, and accounted for both biological and physical clearance with an experimental TRC for the macro-to-micro conversion.

These voxel-TCP approaches may help estimate the biological outcome of doses in de-escalation studies. Although tumor dose is heterogeneous in Fig. 6.6B, the low-dose region corresponds to the necrotic core of the tissue with few cell nuclei, resulting in high tumor

control. Conversely, de-escalation reduces tumor penetration and increases RP sparsity, affecting tumor management, as shown in Fig. 6.7B. DAR-based studies can explore these effects during drug development. Although we demonstrated the concept for de-escalation analysis in Fig. 6.7, a rigorous de-escalation model would require more refined uncertainty analysis and a larger cohort, as described above.

For ^{225}Ac RPT, off-target toxicity rather than cytotoxic efficacy may be the current challenge limiting routine clinical use. The high tumor control observed here was accompanied by 350–400 mGy/kBq (6.4–7.5 Gy) absorbed dose to kidneys. Gamma-ray spectroscopy suggested that this was largely attributable to redistributed ^{213}Bi. Inclusion of a biological weighting factor such as relative biological effectiveness (RBE) or radiation weighting (w_R) representing the double-strand breaks from α-particles could bring the 6.4–7.5 Gy α-particle dose above the 15 Gy threshold associated with nephropathy in external-beam radiation therapy [37]. Since our spectroscopy approach only predicts the total activity correction and not the sub-organ spatial distribution of free ^{213}Bi, early-time DAR or other separation techniques might reveal different critical sub-structures than those we identified (Chs. 3, 8).

We characterized the cloning method performance to evaluate the assumption in DAR dosimetry that adjacent slices are functionally identical. The method was accurate within 10% for mean dose rates, but differences between slices did affect spatial dose distribution in tumors ($87\,\% \pm 6\,\%$ γ-passing rate). Still, the approximation procedure allowed the rapid collection of 3D DARs, which revealed spatial variation in [^{225}Ac]Ac-Macropa-PEG$_4$-YS5 dose within tissues. The identical-slices assumption thus appears suitable, and perhaps necessary, to generate 3D DARs for sub-organ anatomical dosimetry, but stochastic cellular microdosimetry would require a high-resolution, multi-slice source volume for accurate results. We speculate that this method only holds because of the "small-scale" (not truly microdosimetric) nature of the analysis. If a higher-resolution iQID setting or device were used, such that individual kidney tubules or glomeruli were identifiable, then the assumption that adjacent slices are replicates of each other is unlikely to be true.

6.8 Summary

We developed a method for 3D digital autoradiography (3D DAR) and combined it with advanced gamma-ray spectroscopy and histological segmentation to conduct small-scale dosimetry in murine studies of α-emitting [^{225}Ac]Ac-Macropa-PEG$_4$-YS5. Tumor control and 3D sub-organ kidney absorbed dose distributions were evaluated at the voxel level ($39\,\mu m \times 39\,\mu m \times 210\,\mu m$). These methods provide an important framework to assess treatment outcomes and organ risk for ^{225}Ac radiopharmaceutical studies.

Chapter 7

3D digital autoradiography and dosimetry of ^{225}Ac in systemic prostate cancer microtumors

The 3D DAR framework developed in Chapter 6 is applied to evaluate [^{225}Ac]Ac-Macropa-PEG$_4$-YS5 in a model of prostate cancer micrometastases. 3D DAR proves itself a powerful and necessary tool to investigate the utility of αRPs for treatment of metastatic lesions. [^{225}Ac]Ac-Macropa-PEG$_4$-YS5, characterized with 3D DAR, shows remarkable affinity for microtumors within healthy liver tissue but incomplete dose penetration within larger tumors. These effects may be overlooked with conventional 2D DAR. Selected data and text from Paper 3 is reproduced with edits [3]. The introduction, discussion, and additional analysis are original to this dissertation.

7.1 Introduction

Prostate cancer (PCa) is the most common noncutaneous cancer in men, with a lifetime development risk of 11.6% and annual incidence of 112 per 100,000 men [166]. It is fortunate that many prostate tumors are indolent, and localized disease is usually manageable through active surveillance, surgery, and external radiation [167]. However, 30%–40% of patients develop biochemical recurrence[1] after surgery or radiation treatment, and around 8% face metastatic disease at diagnosis [5, 169]. Metastatic disease is significantly more challenging to control: the five-year survival rate for localized PCa is over 99%, but only 31% for metastatic PCa [166].

Androgen deprivation therapy, the standard treatment for metastatic PCa, lowers male hormone levels to slow tumor growth [167]. In 21 in 100,000 men per year, the disease

[1] Biochemical recurrence: increase in the level of prostate-specific antigen (PSA) in the blood, which can indicate return of the disease [168]. PSA is the main biomarker used to evaluate the presence of PCa in screening and endpoint evaluations [7].

progresses despite testosterone reduction and is classified as metastatic castration-resistant prostate cancer (mCRPC) [170]. Various novel chemo- and hormone therapies have been investigated and approved in Phase 3 clinical treatment trials, but the survival prognosis for this aggressive disease remains poor—with 50% mortality in six months [17, 171]. Radiopharmaceuticals have also been identified as candidates to improve mCRPC care. In 2022, the FDA approved β-emitting [^{177}Lu]Lu-PSMA-617 for PSMA-positive patients. However, around 13% of mCRPC patients do not show PSMA expression, and of the PSMA-positive treated population, 20%–40% do not respond [172, 173]. In such cases where alternative targeting moieties are needed, or mechanisms of β-particle radioresistance occur, αRPT may improve therapeutic outcomes [174]. It is a common refrain that the shorter range of the α-particle ($< 100\,\mu m$) may also reduce off-target toxicity in treatment of micrometastatic lesions, although this hypothesis requires further verification with imaging and dosimetry.

In the previous chapter, the antibody-targeted α-particle agent [^{225}Ac]Ac-Macropa-PEG$_4$-YS5 was shown to have high affinity and efficacy in patient-derived 22Rv1 xenografts. Here, the agent is studied in a metastatic progression model to better evaluate its utility for mCRPC cases. Paper 3 investigated several candidate cell lines to disperse in mouse subjects via intracardiac injections and tracked their distribution in vivo using bioluminescent imaging (BLI) and [^{89}Zr]^{89}Zr-DFO-YS5 PET imaging. The confirmed model was utilized in several treatment studies at different injected activities (4.6 kBq and 9.2 kBq) and timings (early and late: 1 or 3 wk post-inoculation treatment). A complete response was observed at both dosages in the early treatment group, precluding quantitative dosimetry of tumors, which were not visible. The low-dosage, late treatment group was assessed with quantitative digital autoradiography methods to characterize the on- and off-target dose distributions in prostate cancer micrometastases.[2] We focus on these DAR results and analyses in this chapter.

7.2 Methods

In brief, 22Rv1 prostate cancer cells were transduced with a Luciferase (Luc)-containing lentivirus to confirm tumor cell dissemination through BLI. The resulting 22Rv1-Luc cells were injected in the left ventricle of each mouse (100k cells per mouse). 4.6 kBq [^{225}Ac]Ac-Macropa-PEG$_4$-YS5 was administered at three weeks post-inoculations. The liver received the bulk of 22Rv1-Luc tumor burden and was investigated with quantitative DAR dosimetry. Liver tissues from one mouse were collected at 96 h (4 d) p.i., and the whole liver was sectioned into 10-µm slices spaced 200 µm apart (19 slices total).

Quantitative activity images were acquired using a digital autoradiograph (iQID, QScint Imaging Solutions, LLC) and converted to dose-rate maps using the dose-kernel protocol for single slices described in Chapter 6. Adjacent H&E slices were collected and imaged through the same standard protocol, then manually segmented into normal liver and tumor regions.

[2] Due to the intracardiac dissemination method, the tumors studied here lack a primary tumor and may be better categorized as systemic microtumors rather than true micrometastases. For convenience, we use both terms interchangeably in this chapter.

Co-registration of spatial dose-rate maps and H&E slices was conducted through automated rigid body (translation and rotation) intensity maximization followed by manual landmark-to-landmark affine transformation (translation, rotation, and shear) (ImageJ BigWarp). In selected micro-tumors, the number of cell nuclei were counted using watershed segmentation and ImageJ Analyze Particles on the H&E cross-section.

To evaluate the activity and dose distribution over time, the experiment was repeated with the DAR protocol performed on days 7, 10, and 14 after 4.6 kBq [^{225}Ac]Ac-Macropa-PEG$_4$-YS5 injections. Subject preparation was identical, and treatments occurred 3 weeks following inoculation of the 22Rv1-Luc metastatic tumor cells. Detail about the procedures used in the broader study are described in Paper 3 [3].

7.2.1 3D DAR renders

Minor adjustments to the 3D DAR rendering procedure used in Chapter 6 allowed quantitative visualization of 3D dose rates with a perceptually uniform colormap. As before, stacks of 2D dose-rate autoradiographs or segmented H&E images were centered and registered using only rigid-body transformations by matching microtumor landmarks between slices (ImageJ BigWarp). Minor misalignments that may have been introduced by sample stretching or spacing between slices did not affect results, since this 3D registration was only used for visualization. Once registered, images were loaded into Slicer 3D. Slices in the image space were assigned a thickness of 210 µm (10 µm tissue thickness + 200 µm spacing). The render was produced using the default VTK GPU Ray Casting protocol from Slicer 3D v5.6.2 with nearest-neighbor interpolation and without shading. The color mapping was synchronized to the Volumes module, which uses the quantitative image intensities of individual slices. Since the 3D render was produced simply by stacking independent 2D DARs, no other reconstruction algorithm was required.

7.3 3D DAR of liver micrometastases

Figure 7.1 shows a representative distribution of the absorbed dose rate due to [^{225}Ac]Ac-Macropa-PEG$_4$-YS5 in the liver and microtumors at 4 d following administration of the therapy (post-injection, or p.i.). Co-registration of the dose-rate map (Fig. 7.1A) with H&E images of consecutive sections confirmed the uptake of [^{225}Ac]Ac-Macropa-PEG$_4$-YS5 in 22Rv1 microtumors, which showed differential H&E dye uptake compared to normal liver tissue (Fig. 7.1B–C).

The 2D H&E liver-tumor masks and dose-rate maps were further Z-stacked to generate a 3D view of the liver and microtumors within (Fig. 7.2). The 3D renders of histology and dose-rate maps illustrate that [^{225}Ac]Ac-Macropa-PEG$_4$-YS5 penetrated the liver tissue to distribute the α-particle agent even at depth. A dose-rate volume histogram (Fig. 7.3) summarizes the absorbed dose rate in lesion (microtumor) and non-lesion areas (4.6 kBq

IA), revealing mean values of 231 ± 153 mGy/h and 11 ± 35 mGy/h across the 3D volume, respectively—significantly higher in the microtumors.

The cell-level H&E image of a sample microtumor is shown in Fig. 7.4A. Its diameter and volume were determined to be 863 µm and 0.34 mm^3, respectively, assuming a spherical shape. Over all lesions, microtumors ranged in diameter from 0.1 mm to 1.8 mm. The total amount of radioactivity deposited in the sample microtumor cross-section was measured to be 608.9 mBq (0.016 nCi), corresponding to a mean activity of 0.107 mBq (2.9×10^{-3} pCi) per cell based on the watershed segmentation count (Fig. 7.4B). Some tumors showed relatively uniform intratumoral dose deposition, while others demonstrated heterogeneous dose deposition with central areas of reduced radiopharmaceutical accumulation (Fig. 7.4C–D).

Examination of additional slices in 3D provided comprehensive insights into the heterogeneity within lesions (Fig. 7.5). In most large lesions, the activity distribution was a thick spherical shell, reduced in the tumor core but uniformly distributed in edge slices (Fig. 7.5A). In contrast, small-diameter tumors received relatively uniform radiation doses throughout (Fig. 7.5B). Across $N = 13$ individual microtumors evaluated, the volume-normalized activity was inversely related to tumor volume (Fig. 7.6). Heterogeneous dose rates resulted in a lower amount of DNA damage compared to the relatively uniform dose rate distribution, as measured by the presence of DNA damage foci [3].

7.4 Temporal evolution and total dose

The correlation between tumor size and dose-rate heterogeneity seen in the single-time-point experiment at 4 d p.i. persisted when the livers were collected on days 7, 10, and 14 post-injection. Representative examples of both heterogeneously dosed and more uniformly dosed microtumor slices are shown in Fig. 7.7.

Between 9–17 microtumors per mouse, with $N = 1$ mouse per time point, were assessed at days 4, 7, 10, and 14 to compute the mean value and standard deviation for tumor and liver dose rates over time (Fig. 7.8A). Over the 10-day period, the mean absorbed dose rate in microtumors followed a mono-exponential decay with an effective half-life t_{eff} of 5.29 ± 0.05 d. The biological half-life t_b, representing the rate of biological clearance of [^{225}Ac]Ac-Macropa-PEG$_4$-YS5 through the mouse system, was calculated to be

$$\lambda_{\text{eff}} = \lambda_b + \lambda_p, \qquad t_b = \frac{\ln 2}{\lambda_b} = 11.4 \pm 0.2\,\text{d}, \tag{7.1}$$

since the physical half-life of ^{225}Ac is known ($t_p = 9.9$ d). Similarly, the surrounding liver tissue mean dose-rate effective half life was $t_{\text{eff}} = 4.02 \pm 0.03$ d with biological half-life $t_b = 6.8 \pm 0.1$ d. Thus, [^{225}Ac]Ac-Macropa-PEG$_4$-YS5 was better retained in tumor cells compared to normal liver tissue.

The total average absorbed dose from the [^{225}Ac]Ac-Macropa-PEG$_4$-YS5 treatment to microtumors and normal liver tissue was estimated by integrating the extended time-dose-

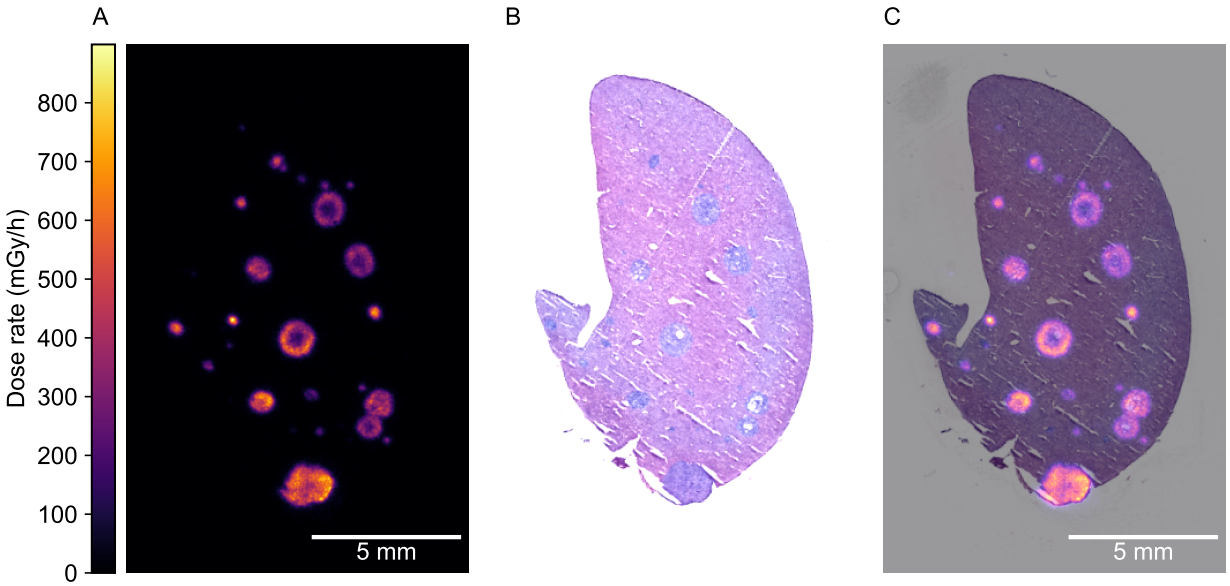

Figure 7.1: Digital autoradiography of liver tissues shows accumulation of [^{225}Ac]Ac-Macropa-PEG$_4$-YS5 corresponding to 22Rv1 tumor micrometastases, identifiable with differential dye uptake in H&E images. (A) Dose-rate map generated from quantitative α-particle digital autoradiography. (B) H&E image produced from adjacent tissue section. (C) Co-registration of the dose-rate map and H&E image.

rate curve (TRC) to $6.6t_{\text{eff}}$. Since data was not collected from before 4 d p.i., the TRC was modeled in two ways as shown in Fig. 7.8B to represent lower- and upper-bound estimates for total dose. In the lower-bound model, the dose rate at 4 d p.i. was assumed to be the maximum, motivating a piecewise linear function from the origin followed by the fitted exponential curve as the integrable TRC. For the upper-bound model, the αRP injection was assumed to fully internalize in the tumor by 1 h p.i. and the fitted exponential was extended to that point, connected to a linear function from the origin. Previous studies in patient-derived xenografts (PDXs) have shown that [^{225}Ac]Ac-Macropa-PEG$_4$-YS5 accumulates at a moderate rate as a bi-exponential function (Fig. 6.4), so the true TRC is likely to fall in between these two extremes, although the translation between PDXs and micrometastases has not been confirmed. Table 7.1 summarizes the absorbed dose calculation from both models in microtumors and liver tissue. In the lower and upper bound models, the average microtumor received 24.9 and 22.5 times the average liver dose, respectively.

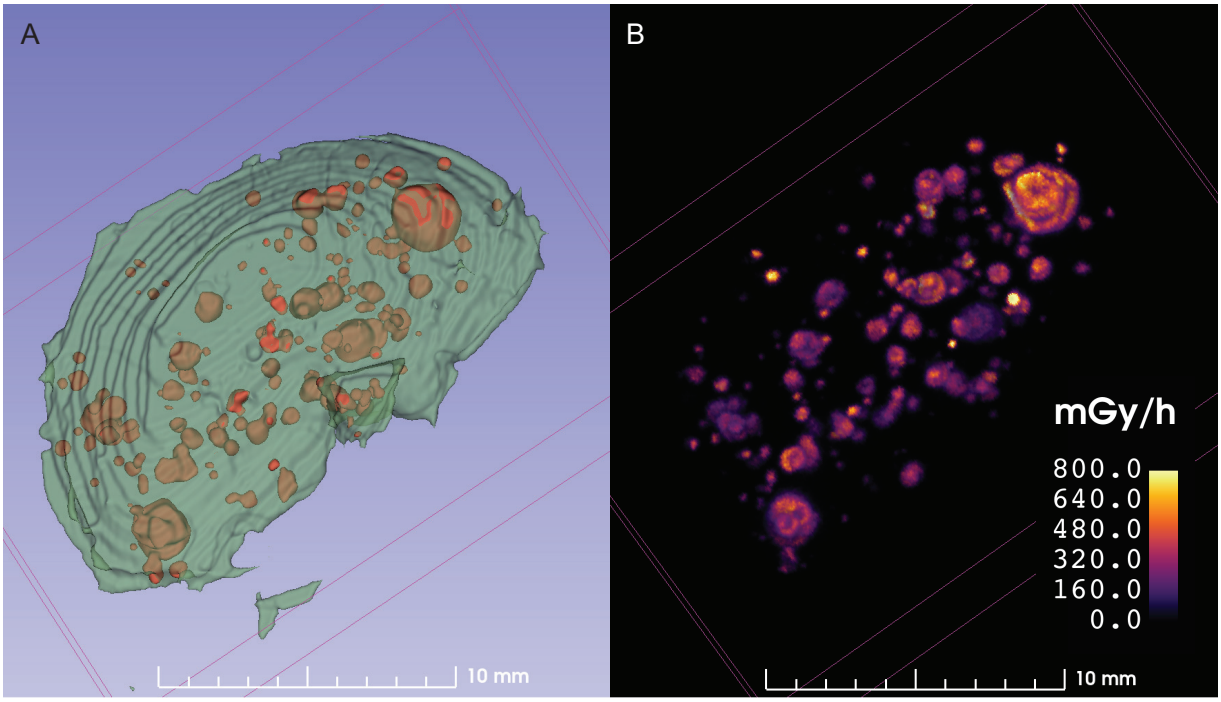

Figure 7.2: 3D digital autoradiography of [^{225}Ac]Ac-Macropa-PEG$_4$-YS5 targeting 22Rv1 micrometastases in mouse liver, stacking 2D images to generate 3D images. (A) 3D render of normal liver tissue (green) and microtumors (red), obtained from segmented H&E images. (B) 3D dose-rate map showing microtumor-targeted dose in the complete liver volume.

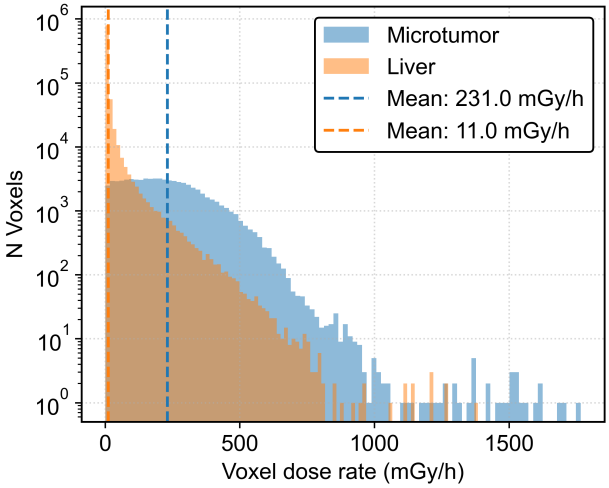

Figure 7.3: Dose-rate volume histogram summarizing voxels in all liver slices.

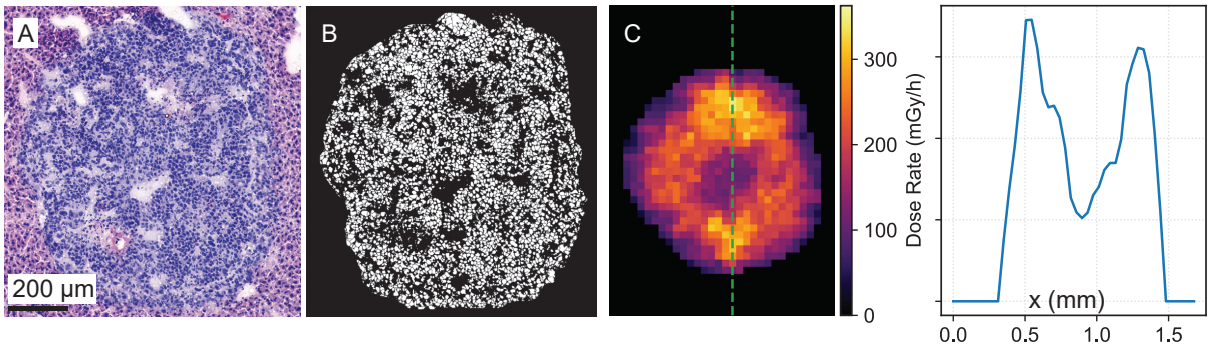

Figure 7.4: Sample microtumor morphology and dose-rate distribution. (A) Close-up H&E of differential dye uptake corresponding to tumor cells. (B) Watershed segmentation of tumor cell nuclei. (C) Unregistered dose-rate image of same microtumor with line profile showing reduced penetration in the center.

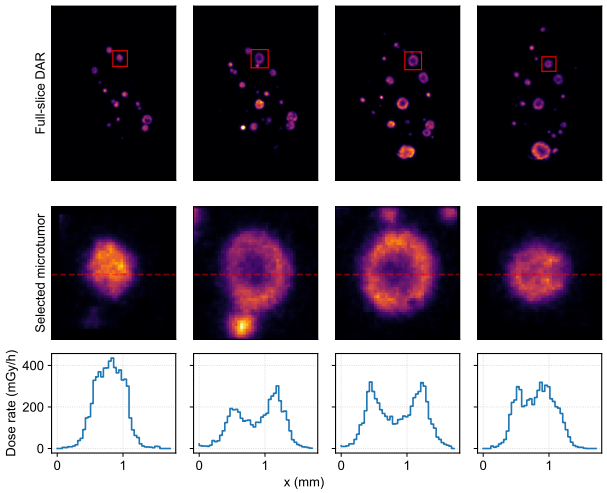

(A) Sample microtumor with heterogeneous dose-rate distribution.

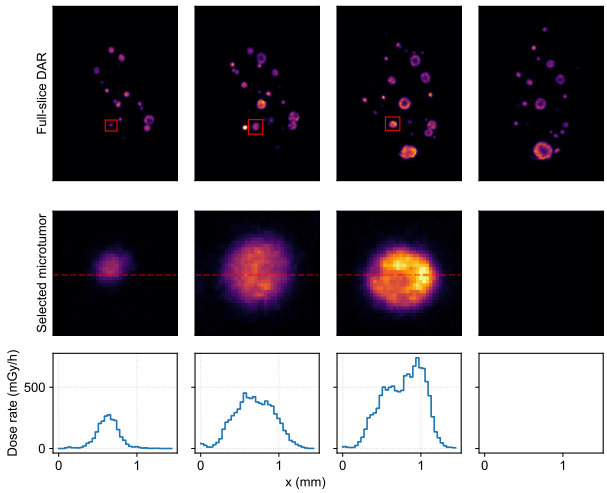

(B) Sample microtumor with internally saturated dose-rate distribution.

Figure 7.5: 3D digital autoradiography shows different dose-rate penetration in two microtumors. Uniformly dosed slices in tumor (A) were found to be peripheral and not representative of the actual shallow-depth penetration, whereas uniform slices in tumor (B) persisted in three dimensions.

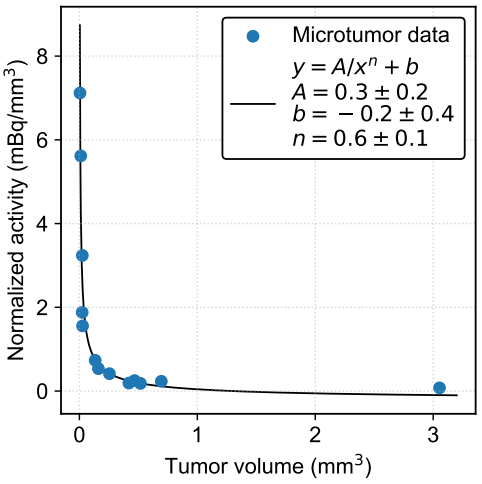

Figure 7.6: Inverse relation between tumor volume and volume-normalized activity. Smaller tumors received more complete radiopharmaceutical penetration throughout the volume compared to larger ones.

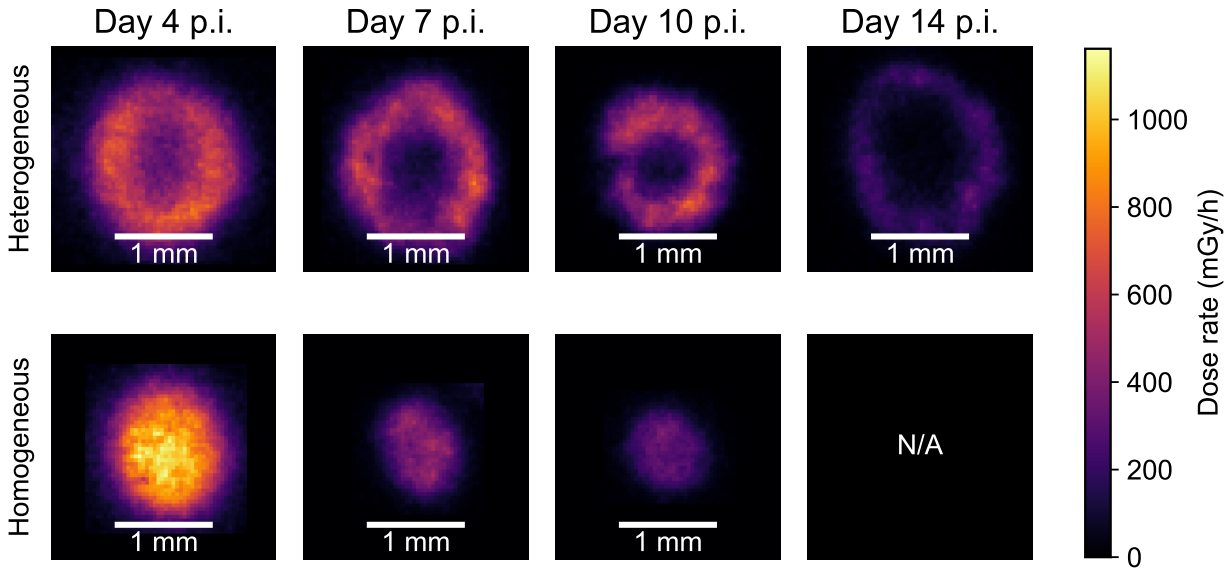

Figure 7.7: Sample DAR regions of interest showing presence of both heterogeneous and homogeneous microtumor slices when the [^{225}Ac]Ac-Macropa-PEG$_4$-YS5 treatment was replicated in 3-week-old 22Rv1 tumors at 7, 10, and 14 d post-injection of [^{225}Ac]Ac-Macropa-PEG$_4$-YS5. Larger microtumors received relatively lower absorbed dose to the core as compared to the edge at all time points.

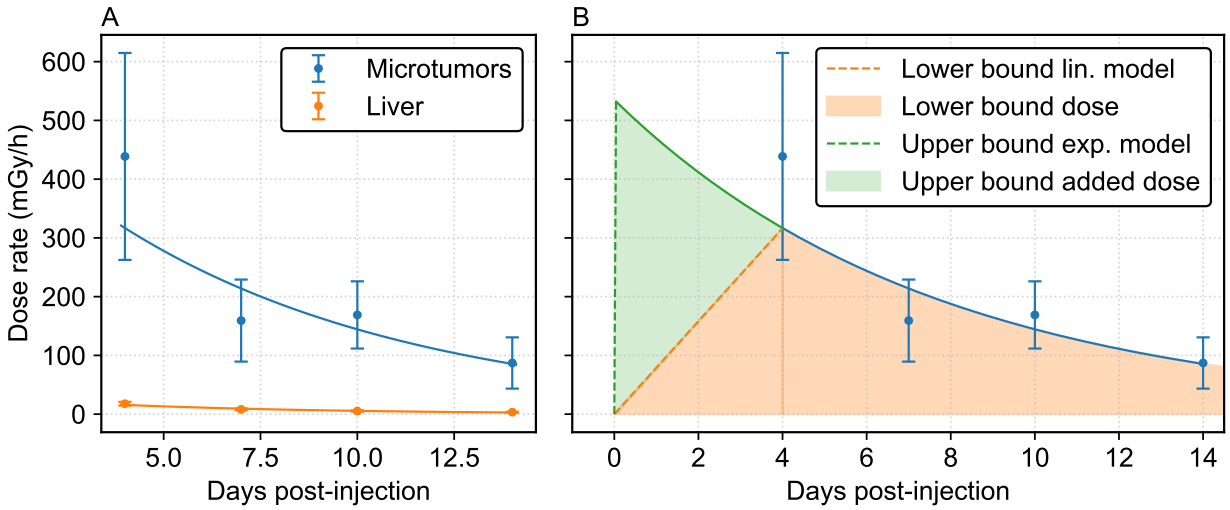

Figure 7.8: Time-dose-rate curves (TRCs) for microtumors and livers from 4–16 d post-injection. (A) After 4 d p.i., mean dose rate in microtumors and the surrounding liver decayed exponentially with half-lives of 5.29 ± 0.05 d and 4.02 ± 0.03 d, respectively. (B) Extrapolation models for microtumor TRC to calculate total absorbed dose. A linear fit to the maximum at 4 d p.i. is used for a lower-bound estimate of integrated dose, and continuation of the exponential fit to 1 h p.i. is used for an upper bound estimate.

Table 7.1: Total absorbed dose during [^{225}Ac]Ac-Macropa-PEG$_4$-YS5 treatment for liver microtumors and normal tissue, calculated with linear (lower-bound) and exponential (upper-bound) extrapolation models.

Tissue	Dose, Lower (Gy (Gy/kBq))	Dose, Upper (Gy (Gy/kBq))
Microtumors	72.2 (15.6)	96.8 (20.9)
Liver	2.9 (0.6)	4.3 (0.9)

7.5 Discussion

Quantitative 3D digital autoradiography in this chapter informs a broader study conducted in Paper 3 on the development of metastatic PCa models and their treatment with [^{225}Ac]Ac-Macropa-PEG$_4$-YS5. Selective targeting and localized radiation delivery are often-cited potential advantages of αRPT, but they must be confirmed in the preclinical phase of drug discovery. Figures 7.1 and 7.2 re-emphasize the utility and necessity of DAR for verification of these effects. The highly nonuniform uptake of [^{225}Ac]Ac-Macropa-PEG$_4$-YS5 in the liver identically corresponded to the microtumor distribution observed in histological stains. Ex vivo autoradiography is the only imaging method currently available to observe spatial variation of radioactivity at this scale, in lesions as small as 100 µm in diameter.

Use of a digital system with this framework also enabled quantification of the crossfire dose delivered to normal tissue. The DrVH in Fig. 7.3 shows strong separation between dose delivery to targeted microtumors and nontargeted liver cells. When the experiment was repeated to monitor a two-week period, [^{225}Ac]Ac-Macropa-PEG$_4$-YS5 cleared faster from healthy liver tissue than the microtumors. This sub-organ information is only available through autoradiography, and not when employing conventional methods of preclinical dosimetry such as whole-organ BioD studies.

The 3D procedure that we developed enabled a comprehensive view of micrometastatic lesions that could be missed with conventional 2D DAR. When conducting 2D DAR in normal organs, a central plane is usually selected to provide the most representative view of the anatomical structures. However, it is not possible to identify the representative plane of internal micrometastases a priori. Figure 7.5 illustrates this idea. In some slices, a heterogeneously dosed tumor appears similarly saturated to a a uniformly dosed tumor because the plane intersects the outer section of a thick spherical shell. Only observation across several planes in 3D reveals the lower αRP penetration in the center.

The major limitation of ex vivo methodology, discussed in Chapter 6, is that it is not possible to track the dose rate of a single specific lesion over time nor directly calculate its total absorbed dose. We estimated the mean dose rate across all microtumors using a dataset spanning the treatment time. However, the concept of a mean dose relies on an assumption of an "average microtumor," when we conversely demonstrated that the size of a lesion affected the quality and quantity of radiopharmaceutical uptake. Further segmentation of the cohort by microtumor size might be required for a robust analysis.

Although DAR analysis was only conducted in the late-treatment cohort, since lesions were not detectable when treated early, our findings can provide insight into outcomes from both groups. In the original Paper 3 study, both 4.6 kBq and 9.2 kBq [^{225}Ac]Ac-Macropa-PEG$_4$-YS5 administrations procured complete responses for a mouse cohort treated at 1 wk post-inoculations. However, the late cohort treated at 3 wk post-inoculations required higher dosage (9.2 kBq) for complete response in 100% of animals. 75% of late-cohort mice treated with only 4.6 kBq experienced tumor regrowth. These results can be partially explained by the findings of the DAR study. [^{225}Ac]Ac-Macropa-PEG$_4$-YS5 penetration was incomplete in larger tumors, with normalized activity (activity per tumor volume) falling off roughly as

a $x^{-0.6}$ relation with tumor size (Fig. 7.6). The low-dose core received around 100 mGy/h at 4 d post-injection, about one-half of the mean dose rate to microtumors at that time point, which was insufficient to control the disease in all animals. We can hypothesize that in the early-treatment group, tumors were not permitted to expand to sizes that would result in deficiency of [^{225}Ac]Ac-Macropa-PEG$_4$-YS5 in the core. Therefore, microtumors were consistently dosed in full and a complete response was maintained. The micro-scale insights provided by DAR help explain the macroscopic treatment outcomes that we observed and may inform future directions for drug development.

We only discussed data from the 4.6 kBq IA group, but the DAR-H&E procedure was also conducted for one subject in the 9.2 kBq cohort at 4 d post-injection. DARs showed qualitatively similar patterns of targeting and penetration at higher dose rates compared to the 4.6 kBq group. However, the H&E images were folded and unfocused, hindering accurate segmentation of the liver and tumor regions for quantitative evaluation. Repetition of the study could clarify whether increased injection activity affects the spatial microdistribution or only the magnitude of absorbed dose. For example, one could investigate whether the penetration depth of the αRP into larger microtumors is increased with greater injected activities.

7.6 Summary

[^{225}Ac]Ac-Macropa-PEG$_4$-YS5 demonstrated high affinity for and localization in microscopic 22Rv1 PCa lesions in a metastatic mouse model as seen by small-scale digital autoradiography images. Quantitative DAR dosimetry showed that the αRP delivered minimal crossfire to normal liver tissue, which received 22 to 25 times less dose over the treatment compared to micrometastatic tumors. However, 3D DAR revealed low-dose cores in larger tumors due to incomplete [^{225}Ac]Ac-Macropa-PEG$_4$-YS5 penetration, an effect which could be missed by single-slice 2D DAR. This finding can explain results of treatment studies, in which mouse cohorts treated later, with more developed tumors, required greater injected activities to avoid recurrence. DAR is an increasingly valuable tool in the preclinical phase of αRPT drug discovery, and this case study illustrates how findings at the micro-scale can explain and inform results such as tumor response or recurrence at the macro-scale.

Chapter 8

Developments towards multi-isotope and parent-progeny separation in iQID autoradiographs

This chapter investigates two novel methods to enable separation of different isotopes using the iQID camera, developed with the intent of discriminating ^{225}Ac from its long-lived progeny ^{213}Bi at the sub-organ scale. First, we evaluate the spectral capabilities of the iQID camera and use scintillation light cluster metrics to identify β-particles from the ^{213}Bi decay chain (Sec. 8.2). We then engineer a hybrid system incorporating a synchronized HPGe detector to "tag" high-spatial-resolution α-decays in an iQID autoradiograph with simultaneous γ-ray emissions (Sec. 8.3). Both approaches are exploratory with high potential for future work. As such, the structure of this chapter is less formal, with methods, results, and discussion together by section as needed.

8.1 Introduction

Isotope-agnostic α-particle counting has thus far been sufficient to quantify dose distributions of ^{211}At and equilibrium ^{225}Ac. When dose due to redistributed progeny is a concern, however, differentiation of emissions is required. Off-target dose due to progeny redistribution can sometimes be quantified with ex vivo BioD or in vivo imaging measurements (Ch. 2), but the drawbacks of photon-based methods apply. Only isotopes with favorable γ- or x-ray emissions can be measured, there is limited signal due to low αRPT activities, and the dosimetric information is confined to the organ-level. The same theme of αRPT dosimetry underscored in previous chapters returns here: progeny relocalization to specific organ sub-compartments can result in toxicity effects that differ from the predictions of mean dose measurements. A digital autoradiography system that can perform α-particle spectroscopy is thus desirable for αRPT drug development. As we reviewed in Chapter 3, currently available energy-discriminating semiconductor autoradiographs that might meet this need

typically have FOV limitations that limit their utility as workhorse devices in preclinical laboratories.

Here, we explore two avenues for isotope separation in the iQID camera. The energy resolution limitations of standard iQID operation prevent true α-particle energy spectroscopy, but joint detection of β- or γ-emissions from the same decay chain may provide information about progeny distributions. We show that adjustment of the iQID acquisition parameters allows synchronous detection of both β- and α-particles, potentially enabling discrimination of β-emitting progeny from α-emitting parents. In a separate investigation, we propose a method to "tag" α-particles detected in iQID with simultaneous γ-rays using a HPGe detector with synchronized timing. Both methods are designed and discussed with the ^{225}Ac/^{213}Bi decay series in mind, but are generalizable to other in vivo generators with β- or γ-emitting progeny.

8.1.1 Radioactive check sources

Three check sources were used in our experiments, all produced by Spectrum Techniques LLC (Oak Ridge, TN). ^{210}Po modeled a pure α-emitter; ^{90}Sr, a pure β-emitter; and ^{22}Na, a β^+-photon coincidence emitter. These sources and their emissions energies are compared to emissions from the ^{225}Ac decay chain in Table 8.1.

8.2 Feasibility of ^{225}Ac/^{213}Bi separation using scintillation clusters

Because tissue washout, incomplete stopping, and intensifier smearing dramatically reduce the iQID energy resolution, energy information is not reported in the device list-mode file by default. However, the size and intensity of the scintillation light cluster correlates with the energy of the charged particle and can be used to discriminate large energy gaps. Elimination of events below a simple threshold is already the default procedure to reduce noise in iQID α-particle measurements. Miller et al have also used a threshold-based approach to separate α-particles and fission fragments from ^{252}Cf [128]. Since there is a large energy difference between the α- (> 5.8 MeV) and β-emissions (200–500 keV) from the ^{225}Ac and ^{213}Bi decay chains, we hypothesized that a scintillation light threshold could separate them in a single acquisition. All β-particle emissions in the decay series occur downstream from ^{213}Bi (Fig. 1.4), so a sufficiently sensitive simultaneous measurement could determine the distribution and quantity of redistributed ^{213}Bi at a sub-organ scale.

iQID can detect both α- and β-particles, but quantitative acquisition optimized to both simultaneously can prove challenging, especially at αRPT-levels of injected activity. Past efforts have used physical attenuation materials to selectively block α-particles from reaching the scintillator, necessitating two separate acquisitions to obtain an α-image and a β-image [128]. A recent collaboration between Cornell Medicine and MSKCC has shown simultaneous imaging of ^{177}Lu and ^{225}Ac in tumor xenografts in mice with a 3400:1 ratio between respective

Table 8.1: Check sources for iQID isotope separation experiments compared with select emissions from the ^{225}Ac decay chain.

Isotope	Emission	Energies[a]	Initial Activity
^{210}Po	α (99.999%)	5.3 MeV	0.01 µCi
^{90}Sr	β^- (100%)	196 keV (546 keV)	0.10 µCi
^{90}Y	β^- (99.99%)	932 keV (2.28 MeV)	
^{22}Na	β^+ (89.9%)	216 keV (547 keV)	0.01 µCi
	photon, γ	511 keV, 1.27 MeV	
^{225}Ac[b]	α (100%)	5.8 MeV, 6.3 MeV, 7.1 MeV	
^{221}Fr	γ (11.44%)	218 keV	
^{213}Bi[c]	α (2%, 98%)	5.8 MeV, 8.4 MeV	
	β^- (30.1%, 66.8%)	320 keV, 492 keV (982 keV, 1.42 MeV)	
	γ (25.9%)	440 keV	
^{209}Tl	β^- (97%)	660 keV (1.83 MeV)	

[a]Energies indicated as mean (endpoint) for β-emissions.
[b]Includes decay chain until ^{213}Bi (^{225}Ac, ^{221}Fr, ^{217}At).
[c]Includes decay chain after ^{213}Bi(^{209}Tl, ^{213}Po, ^{209}Pb.) Only select γ-emissions are included.

injected activities (1.7 mCi to 0.5 µCi) [129]. In the ^{225}Ac/^{213}Bi redistribution use-case, the activity ratio in tissues is likely no greater than 10:1 (Sec. 8.2.3).

Our goals in this section were to: (1) verify the energy resolution (or lack thereof) for α-particle measurements using iQID scintillation light cluster metrics; (2) characterize and optimize iQID parameters for simultaneous α/β-imaging; and (3) demonstrate and articulate the feasibility and limitations for ^{225}Ac/^{213}Bi separation in a single acquisition.

8.2.1 Scintillator comparison

Beta-particle detection with iQID typically uses a gadolinium oxysulfide (Gd_2O_2S:Tb, Gadox, or GOS) film rather than the ZnS:Ag phosphor screen used in previous chapters for α-particle detection. Table 8.2 compares the physical properties of these two materials, which are both commercially available from QScint. (The QScint ZnS:Ag screen is similar to EJ-440, which was used in previous studies, with a thinner plastic layer to restrict light spread and improve spatial resolution.) We assessed both scintillators' energy resolution and light characteristics to select the one with superior qualities for simultaneous detection of both particles.

Table 8.2: Physical properties of the tested ZnS:Ag and GOS scintillators.

Scintillator	**Commercial name**	**Density** (g/cm^3)[a]	$\mathbf{Z_{eff}}$[b]	**Phosphor**	**Plastic**
ZnS:Ag	QSCINT-02-0005	4.09	24.9	25 µm	50 µm
Gd_2O_2S:Tb	QSCINT-02-0001	7.34	47.0	40 µm	100 µm

[a]Density of the crystal, which is greater than that of the phosphor..
[b]Calculated as $Z_{\text{eff}} = \sqrt[2.94]{\Sigma_i f_i Z_i^{2.94}}$ [175].

Cluster-based energy resolution

We first evaluated the iQID energy resolution for α-particles with standard imaging parameters to verify that more complex discrimination would be necessary. The iQID Compressed Processed Listmode and Cropped Listmode data sets (Ch. 4) provide two cluster metrics that can serve as proxies for energy:

- Cluster sum: the sum scintillation light intensity of all pixels in the detected cluster.
- Cluster area: the total number of triggered pixels above the user-set threshold for cluster identification.

Figure 8.1 shows event-normalized distributions for these two metrics in sample acquisitions of ^{225}Ac (5.8–8.4 MeV) and ^{210}Po (5.3 MeV) α-particles using ZnS:Ag. We used default settings for α-particle detection, reported in Table 8.3. Although ^{210}Po is an essentially monoenergetic emitter, the FWHM cluster sum and cluster area metrics in ZnS were large, about 7000 intensity units and 78 px, respectively. GOS showed a more restricted spread, with 1300 intensity units and 40 px FWHM, respectively. In both scintillators, the discrete α-particle energies from ^{225}Ac were difficult to identify and unusable for quantitative analysis. Cluster-based energy discrimination with the default configuration was, consistent with expectations, insufficient to discern α-particles of different energies. We used cluster area over cluster signal sum for subsequent analyses because of the superior FWHM.

Energy washout and particle stopping

Figure 8.2 compares the range and energy deposition profiles for ^{225}Ac α-particles in water, GOS, and ZnS, simulated using GATE with 10^6 particles each as described in Chapter 4. The ranges for energy deposition in each material are roughly 70, 30, and 125 µm, respectively. Three range thresholds are worth consideration with respect to energy deposition and blurring effects in iQID.[1]

[1]We consider tissue to be a water-like material. Because we were unable to source the exact density of the GOS phosphor for simulation, the range profile for GOS likely overestimates the stopping power relative to the less dense phosphor.

Table 8.3: Default iQID acquisition settings for α-particle detection.

Parameter	**Quantity**
Frame rate	25 FPS
CMOS camera gain	35 dB
Filtering kernels	Median 3×3 px, Gaussian 3×3 px
Recorded cluster size	11×11 px
Pixel trigger threshold	15
Cluster size threshold	5 px

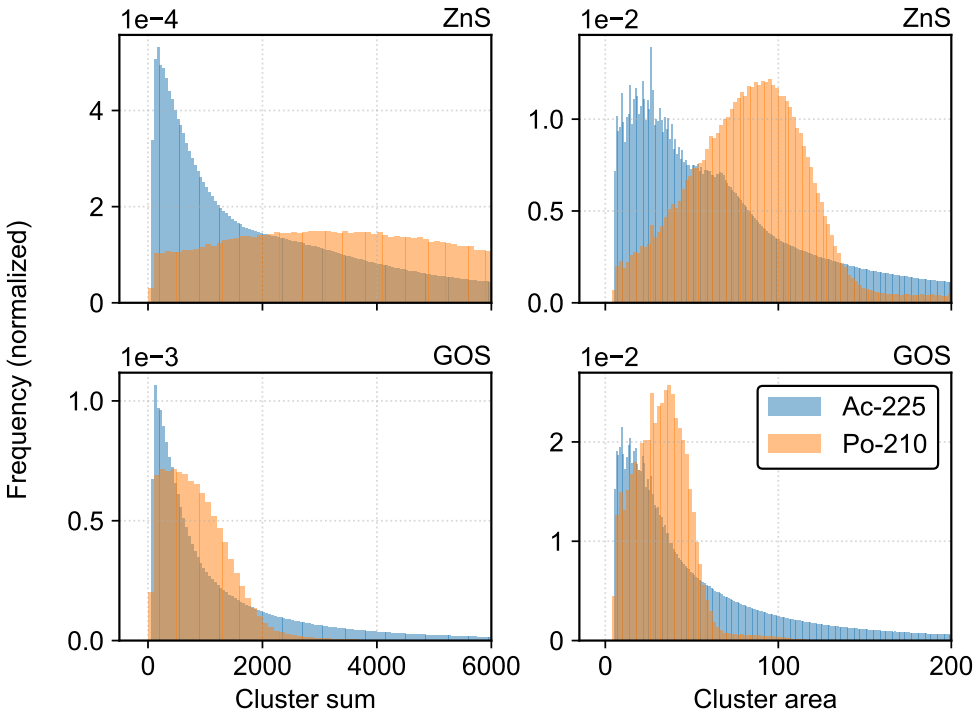

Figure 8.1: Cluster-based energy spectra for ^{225}Ac and ^{210}Po in ZnS (above) and GOS (below) using default α-particle acquisition parameters in iQID (Table 8.3).

- **Tissue washout:** tissue slices are cut 10–20 µm thick for digital autoradiography. The energy loss of heavy charged α-particles is continuous over the particle track, so a portion of the α-energy will deposit in the tissue instead of the scintillator. More oblique emissions result in longer path lengths and greater lost signal. An α-particle traveling perpendicularly through the entire slice will lose about 23.5% of its energy before reaching the scintillator.

- **Incomplete stopping in ZnS:** ZnS has a relatively low density and effective Z despite its excellent α-detection efficiency in iQID. Full-energy α-particles from the ^{225}Ac chain only deposit about 22% of their energy in a normal path through the 25 µm-thick ZnS phosphor. However, this figure also varies based on the obliquity, path length, and degree of prior tissue washout. The amount of information carriers generated in the scintillator is thus variable and difficult to predict.

- **Complete stopping in GOS:** In comparison with ZnS, GOS has a higher density and stopping power ($\propto Z_{\text{eff}}$), and fully stops full-energy ^{225}Ac-chain α-particles by 40 µm, the thickness of the QScint phosphor.

These simulations suggest that the α-particle energy resolution of GOS should be superior to ZnS due to the improved yield of information carriers inside the scintillator. The results are consistent with our findings in Fig. 8.1.

Operating voltage and detector efficiency

Lacking the option to discriminate ^{225}Ac chain α-particles directly, we investigated the feasibility of simultaneous detection of α- and β-emissions. A candidate scintillator must identify both with reasonable efficiency.

iQID uses threshold filtration that allows the device to operate essentially noiseless for pure α-particle imaging. In this acquisition mode at 1.5 V (applied to the multichannel plate image intensifier, MCP), lower-energy β-particles are also undetected. For β-autoradiography, the control voltage is raised to 2 V, increasing the gain and triggering β-detection on the CMOS camera. We hypothesized that increasing the operating voltage from 1.5 to 2 V may allow simultaneous detection of the two particle types, but could also increase noise events due to gain amplification.

We examined the relation between operating voltage, detected events, and noise in Fig. 8.3, using ^{210}Po as a pure α-emitter and ^{90}Sr (^{90}Y) as a pure β-emitter. Fig. 8.3A assesses the normalized event detection as a function of voltage, distinguished from a true measure of efficiency because of the possibility of false noise triggers being registered. Figures 8.3B–C investigate the cluster size histograms for GOS and ZnS over the voltage range.

As the gain (MCP voltage) is increased from 1.5 V to around 1.85 V, the efficiency for α-particle detection increases to a plateau, and the cluster size distribution shifts right. Further increase to 2.0 V results in more detections, but these may not be actual α-particle events: they add to a new low-energy spike in the cluster size histogram. The inset axis in Fig. 8.3B,

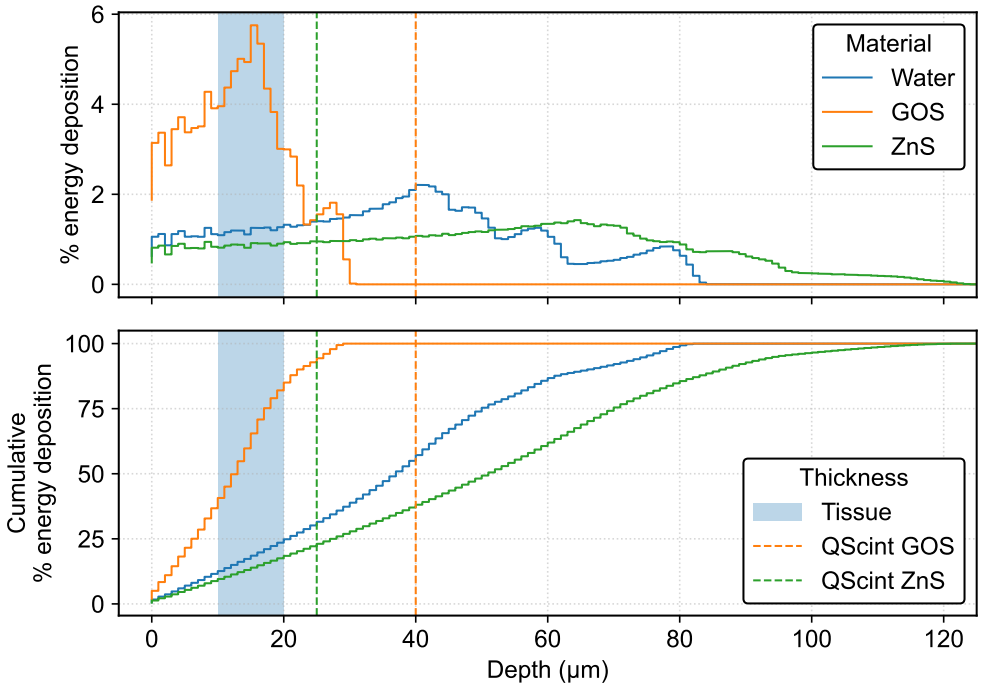

Figure 8.2: Energy deposition and range profiles for ^{225}Ac α-particles in water, GOS, and ZnS. Energy washout in the tissue slice and incomplete stopping in the ZnS scintillator render the expected energy deposition unpredictable. GOS shows a higher stopping power.

left, highlights the emergence of this spike above 1.85 V. These events are investigated in the next section.

The overall efficiency for β-particle detection is lower and does not start until 1.7 V, after which there is a nearly linear rise (Fig. 8.3A, right). The cluster size distribution remains stable over the voltage range, with some flattening as the high-energy tail extends to larger sizes. Between the two scintillators, ZnS has higher detection efficiency for α-particles, whereas GOS is superior for β-particle detection.

Scintillator selection summary

Overall, the GOS scintillator was better suited to α/β detection than ZnS. While ZnS was minorly advantageous for α-particle detection efficiency (ε_α), GOS showed better efficiency for β-detection (ε_β). GOS could also be operated at higher voltages before triggering extra noise in the α-particle spectrum, allowing further optimization of ε_β since $\varepsilon_\beta \propto V$. Use of GOS at 1.85 V appeared to optimize ε_β while minimizing α-noise.[2]

[2]For pure α-particle detection, ZnS has one other advantage: price. At the time of writing, QSCINT-02-0005 is priced at \$50 / 10 × 10 cm sheet, compared to \$220 for the same size sheet of QSCINT-02-0001.

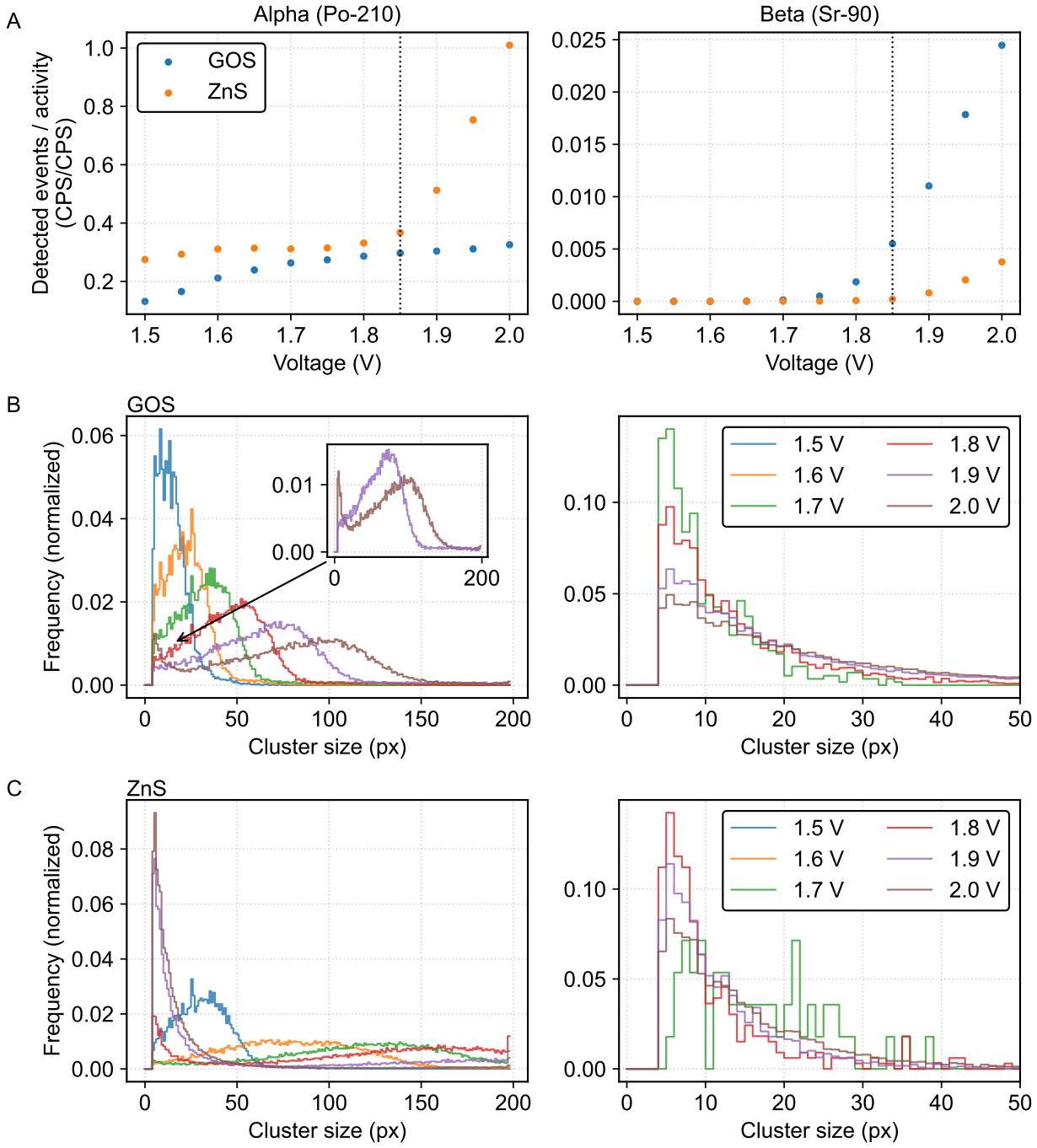

Figure 8.3: Relation between iQID operating voltage, detected events, and noise for α- and β-particle detection. (A) Normalized event detection as a function of voltage. Alpha-particle efficiency plateaus at 1.8 V, then rises with added noise triggers. Beta-particle efficiency increases linearly after threshold at 1.7 V. 1.85 V (dashed line) was selected to enable detection of both particles. (B) Cluster size histograms for GOS and (C) ZnS. Beta-particle histograms remain stable with voltage, whereas α-particle events show left-side spikes representing noise triggers at high gain.

8.2.2 Proof-of-concept experiment

At higher voltages, β-particle cluster sizes remained in the range of about 5–20 px, whereas α-particle cluster sizes were pushed to larger bins (Fig. 8.3B). We conducted a proof-of-concept experiment with simultaneous acquisition of ^{210}Po and ^{90}Sr to investigate whether this difference could be used to separate the two particle types. Figure 8.4 shows the experimental setup and example 21 × 21 px cluster images from each source. In general, ^{210}Po α-particles appeared as bright, bold clusters, and ^{90}Sr/^{90}Y β-particles were less intense and noisier, consistent with the histogram observations. Beta-particles sometimes showed multiple interaction positions, which we speculate could result from delta-rays produced by the higher-energy ^{90}Y emission. In this configuration at 1.85 V, ε_α and ε_β were 31% and 1.2%, respectively.

Center-of-mass filtration

Figure 8.5A shows the normalized frequency of each α- and β-particle cluster sizes in this setup at 1.85 V and 2.0 V. As before, higher gain yielded additional events in the low-size α-particle bins. These events overlapped with the low-energy β-particle region of the spectrum and would hinder their separation. Although the experiment could be run at 1.85 V to circumvent this issue, we briefly explored the individual cluster profiles here to investigate whether the low-area events were indeed noise. If the noise events could be selectively discarded, then this would allow for increased voltage acquisitions to improve ε_β.

Examples of individual clusters with area under 10 px are shown in Fig. 8.5B. Some were similarly shaped but smaller than the typical α-particle profile (Fig. 8.4), possibly due to tissue washout. Others were noisy, off-center, or showed multiple interaction positions. Regardless of whether these were true α-particle events or faulty triggers, the cluster size measurement was artificially lowered because the iQID frame parsing crop did not encompass the full light distribution.

We applied a center-of-mass (CoM) filtration algorithm to the cluster images to eliminate these events from analysis. The CoM was calculated on an Otsu binarization of the cluster image. Events with CoMs outside of a user-selected boundary square in the center, 7 px × 7 px in this experiment, were discarded. Annotations to Fig. 8.5B show the boundary square, calculated CoMs, and exclusion decision for each of the example events. CoM filtration reduced the size of the added peak in the 2.0 V cluster area histogram with no effect on the 1.85 V histogram (Fig. 8.5A). Since the peak was not eliminated completely, we conducted the remaining analysis on the 1.85 V acquisition only.

Calibration and selection

The scintillation light cluster size histograms in Fig. 8.5A provide a calibration function to select the most probable type for an unknown particle of measured cluster area. We tested two straightforward methods for this first-pass experiment. In both cases, we used the

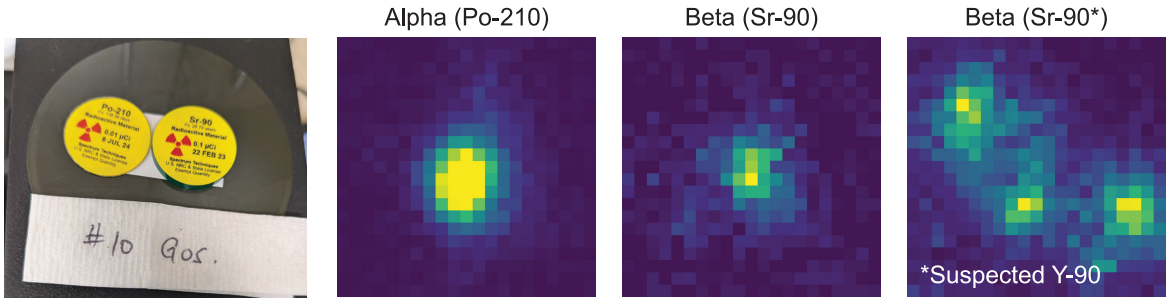

Figure 8.4: Setup and example cluster images from ^{210}Po/^{90}Sr experiment. Alpha-particles appear larger and bolder compared to the noisier beta-particles. Beta-particles can appear with multiple interactions, which we speculate are from delta-rays produced by the higher-energy ^{90}Y emission.

probability density functions (PDFs) obtained by normalizing each cluster size distribution such that the total area integrated to unity.

- Most-probable binary: At each cluster size x, the higher PDF(x) determines the assigned particle type.
- Probability distribution: At each cluster size x, the event is assigned each particle type according to their relative probabilities. For example, if $\text{PDF}_\alpha(x) = 0.04$ and $\text{PDF}_\beta(x) = 0.01$, then the pixel containing the event is assigned an α-particle with 80% intensity and a β-particle with 20% intensity.

We imposed a minimum threshold for bin content, in which cluster sizes with fewer than two recorded events were not included in the look-up table because of the lack of data. Events at these sizes were discarded. Each look-up function was then re-applied to an unassigned version of the data set.

The original iQID image with both sources is compared to the images obtained through binary assignment in Fig. 8.6A. The ^{210}Po signal was enhanced and the ^{90}Sr signal was reduced by α-selection, and vice versa for β-selection. Images using probability distribution assignment were qualitatively similar (not shown). Note that the orientation of the sources is inverted in the iQID image compared to Fig. 8.4, and that the ^{90}Sr source was stronger than the ^{210}Po source (0.10 µCi vs. 0.01 µCi).

Figure 8.6B collects the results of the two selection methods. Each selection image is evaluated with the fraction $f = N_s/N_t$, where N_s is the number of events selected as a specific particle type (α or β), and N_t is the true number of events from that type as dictated by the spatial location of the sources. Both methods enhanced the desired particle type and suppressed the other but incurred some false positive events. The binary assignment method performed better, preserving 83% of intended events with 17% falsely identified events on average, compared to 75% and 25%, respectively.

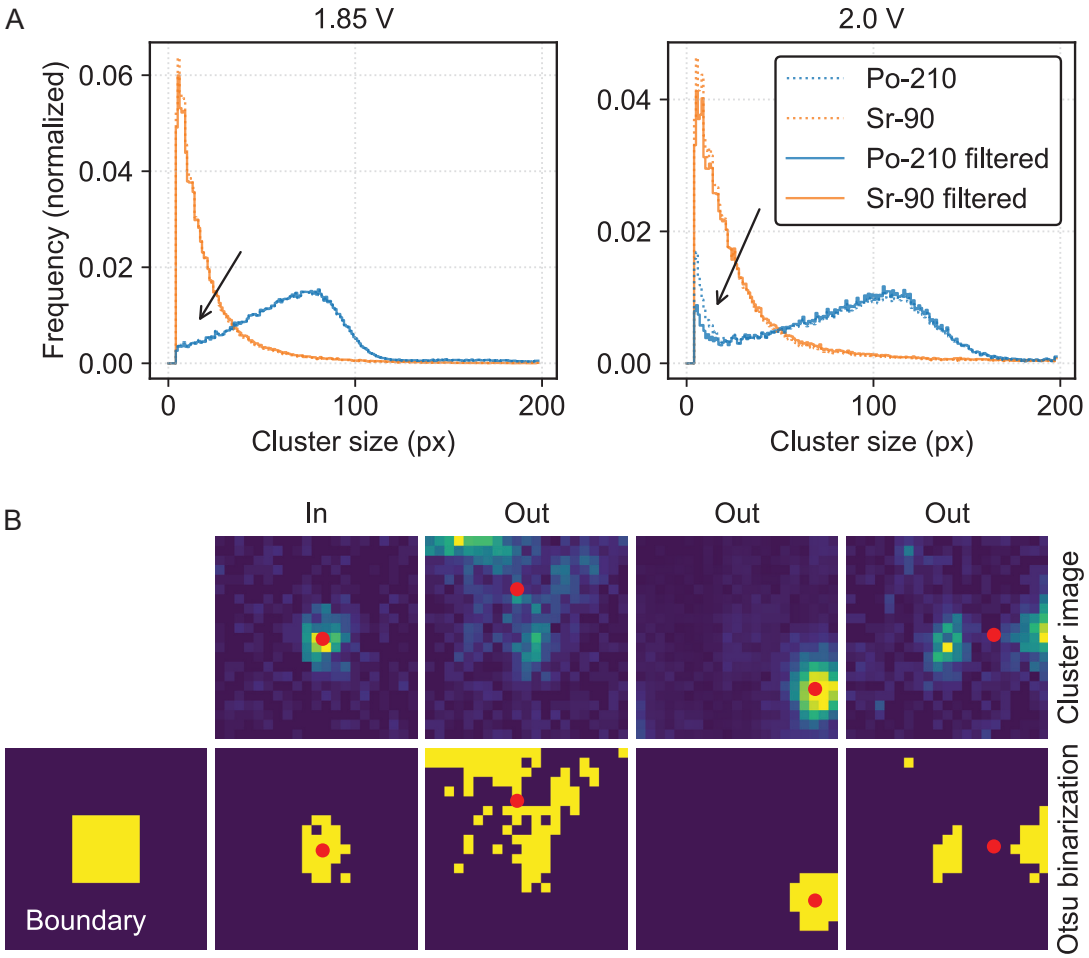

Figure 8.5: Center-of-mass (CoM) filtration for scintillation clusters in ^{210}Po/^{90}Sr experiment. (A) Acquisition at 2.0 V yields additional low-size clusters that interfere with α/β separation. CoM filtration eliminates off-center events with area artificially reduced due to cropping. (B) Examples of CoM filtration on 2.0 V α-particle scintillation clusters with cluster area < 10 px. Events with CoM outside of the boundary square were discarded ("Out").

Figure 8.7 shows an initial measurement for application of the separation method to ^{225}Ac at 1.6 V,[3] where the most-probable binary method was used and selectively emphasized the α- and β-particle sources (Fig. 8.7A). When applied to an ^{225}Ac droplet in secular equilibrium ($\sim$ 2.5 nCi), we observed retention of both α- and β-particles, with over ten times as many α- as β-detections. This result was not proportional to the expected four-to-two distribution of α- and β-particles in the ^{225}Ac decay chain, even after the efficiency of the method (as measured by the check sources) was considered.

The discrepancy can be explained as an artifact of the frame rate and spatial activity concentration of the droplet, which appears overly concentrated in its center in Fig. 8.7A. When several events appear in the same frame and are too close together, iQID frame parsing will recognize them as one merged entity, recording only one event with very large cluster area instead of several smaller ones. To confirm, we measured the same sample at 1.5 V, which reduced signal from α- and eliminated β-particle events. The ^{225}Ac droplet exhibited a uniform distribution of activity without the artifact. Thus, this measurement should be considered preliminary, since the particle efficiencies are not accurate due to the spatial pile-up.

8.2.3 Discussion

In this section, we explored iQID capabilities for α/β-particle discrimination using two commercially available scintillator screens, ZnS and GOS. We confirmed that default acquisition settings with either material did not have energy resolution sufficient to discriminate the α-particles in the ^{225}Ac decay chain, and showed that a raised-voltage acquisition mode using GOS could acquire both α- and β-particles simultaneously. ZnS was superior for α-particle detection efficiency but fell short in β-particle detection efficiency. A calibrated scintillation cluster size metric selectively enhanced or suppressed α- or β-particle signal in postprocessing. We demonstrated the principle and showed the feasibility for simultaneous detection on a sample of ^{225}Ac in secular equilibrium.

Reproducibility is crucial for quantitative measurement, and we alluded to some difficulties with the device efficiency on different days of acquisition. For example, our calibration in Fig. 8.3 identified 1.85 V as a sufficient compromise between β-efficiency and false positives. We repeated the calibration on another day and found similar results for efficiency and cluster size distributions, but at lower voltages by a shift of roughly 0.2 V. Anecdotally, the behavior can change before and after device or software restart, but we were not able to consistently reproduce the observed changes. To avoid inconsistencies, we did a short calibration before each separation experiment and selected the operating voltage that appeared to produce the desired behavior as chosen by Fig. 8.3. This behavior should be investigated in the future, as the calibration process can be time-consuming, and all quantitative iQID acquisitions (including isotope-agnostic ones) assume consistency in the device efficiency.

[3] We encountered some inconsistencies with the applied voltage and response, and on this particular day found 1.6 V to achieve similar results as the 1.85 V setting from Fig. 8.3. See discussion for more details.

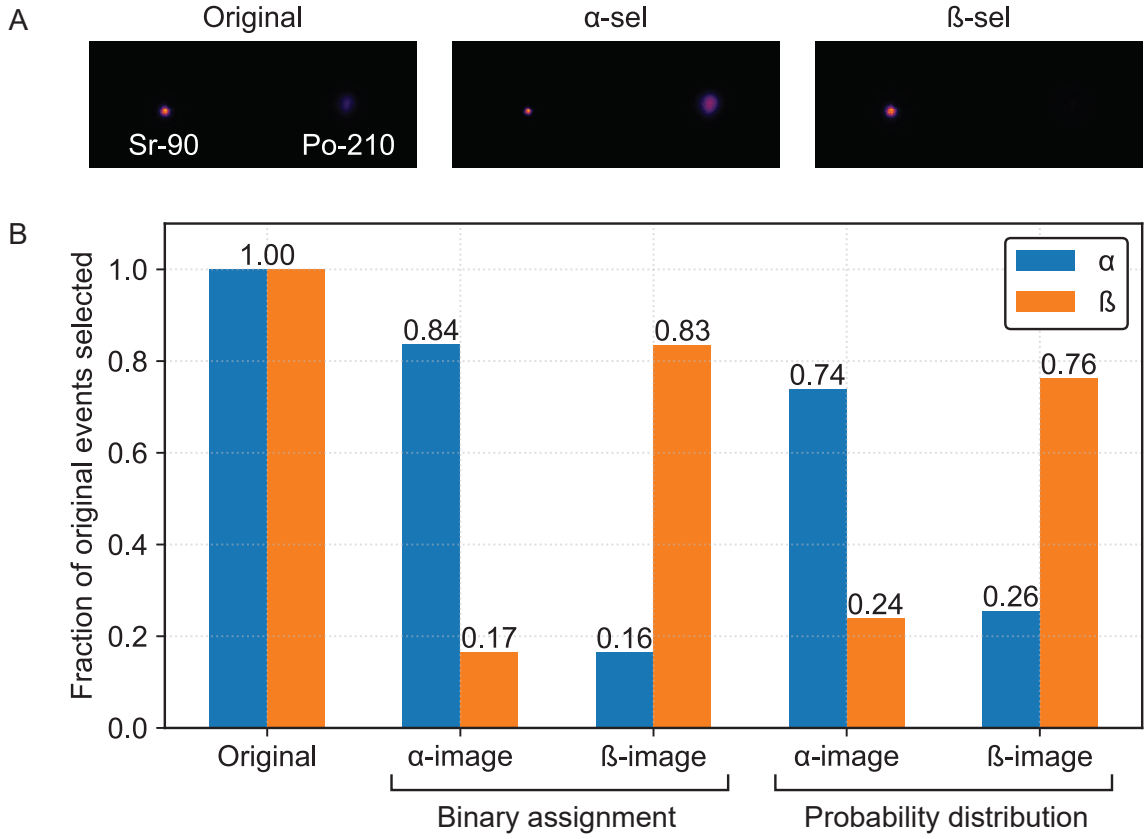

Figure 8.6: Segmentation of a ^{210}Po/^{90}Sr iQID acquisition by scintillation cluster size. (A) Original iQID image with both sources, compared to the images obtained through binary assignment. (B) Effectiveness of most-probable binary and probability distribution assignment methods. Both methods enhanced the desired particle type and suppressed the other but incurred some false positive events.

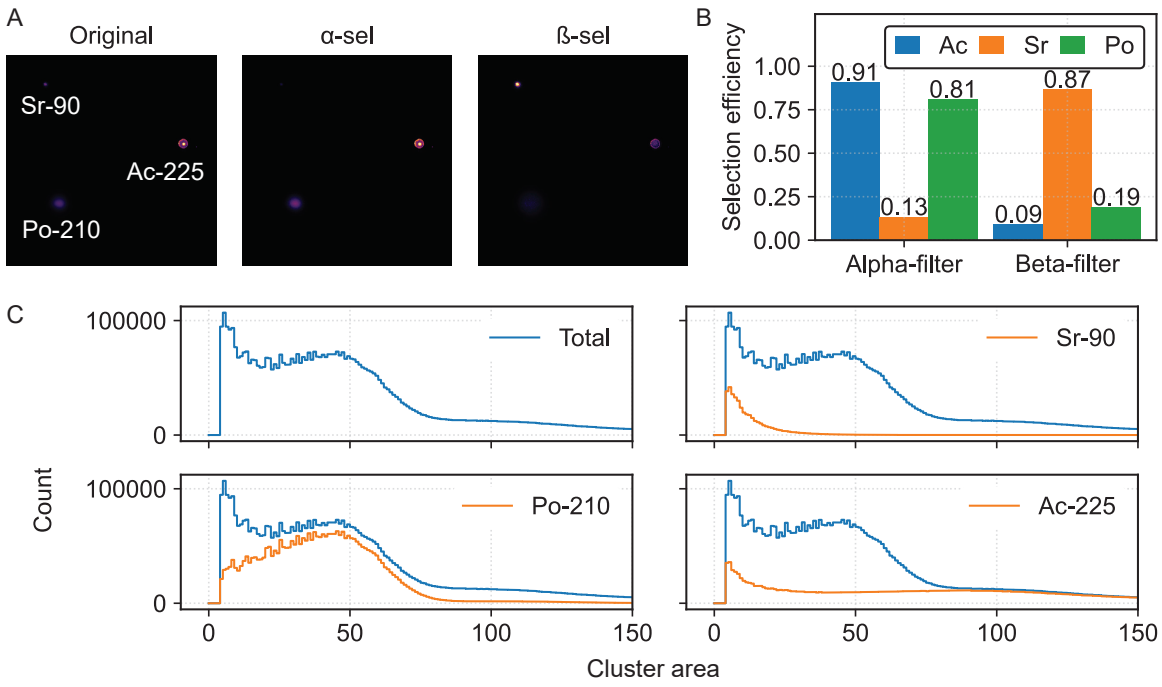

Figure 8.7: Preliminary measurement with ^{90}Sr and ^{210}Po check sources alongside an ^{225}Ac droplet. (A) Acquisition image, unmodified and as filtered by α-particle and β-particle segmentation thresholds. (B) Fraction of original events obtained by the segmentations for each isotope. (C) Cluster area histograms for each contribution to the entire acquisition. Note that the over-concentration of activity in the center of the ^{225}Ac droplet indicates spatial pile-up that can be eliminated by higher frame rates.

The iQID β-particle detection efficiency must be carefully considered for separation of ^{225}Ac and ^{213}Bi in real tissues. βRPT does not demand extreme sensitivity from iQID because injected activities are relatively high in mice (∼mCi). In αRPT, however, injected activities are sub-microcurie and can result in picocurie-levels of activity in thin tissue slices. Measurement is also constrained to the approximately 5-hour period before equilibration of ^{213}Bi.[4] Extending the acquisition time is thus not a viable method to improve the collected statistics, as it is with measurements of ^{225}Ac only.

We recorded about 1% detection efficiency for ^{90}Sr/^{90}Y β-particles in the 1.85 V GOS configuration. Back-of-the-hand calculations can assess whether this sensitivity is sufficient for a typical case:

- Assume the device has 1% β-particle detection efficiency and 31% α-particle detection efficiency, as measured in our 1.85 V GOS acquisition.

[4] Bi-213 activity is within 99% of the ^{225}Ac activity within 292 min.

- All events must be collected in the first five hours of acquisition.
- Let the tissue slice contain 0.5 Bq (13 pCi) ^{225}Ac, based on kidney slice measurements in the [^{225}Ac]Ac-Macropa-PEG$_4$-YS5 study described in Chapter 6.
- Over the 5-h acquisition, there would be (0.5 Bq)(5 h) = 9000 ^{225}Ac decays, with four α- and two β-emissions per decay.
- iQID would detect around 11000 α-events and fewer than 200 β-events.
- We can consider the noise floor to be the false positive rate corresponding to α-particles incorrectly identified as β-particles by the separation method. A rate of 17% (Fig. 8.6) results in over 1800 false β-events.
- The false β-events (1800) would overwhelm the true β-signal (200) unless excess ^{213}Bi were present in at least a 9:1 ratio over ^{225}Ac. Around 6:1 excess has been observed in kidneys from mice treated with [^{225}Ac]Ac-Macropa-PEG$_4$-YS5 (Fig. 6.4).

The method as performed here is not sensitive enough for this use case, but it is already on the right order of magnitude. Sensitivity depends on the β-detection efficiency and false positive rate, for which there are several actionable avenues for improvement. The camera gain, filtration, and thresholds all provide tuneable knobs that can be adjusted to improve the efficiency of detection of either particle, but we only tested MCP voltage adjustment. Additionally, if the CoM filtration can be improved or expanded to better discard unsuitable events, the MCP can be operated at higher gains with superior β-efficiency (Fig. 8.3A).

The cluster size distributions for ^{225}Ac and ^{213}Bi were not identical to those of ^{210}Po and ^{90}Sr. The difference could be advantageous, since the higher-energy α-particles from ^{225}Ac are more right-shifted to reduce overlap with lower-energy β-particles. The absence of a high-energy β-particle in the ^{213}Bi chain may also reduce overlap compared to the ^{90}Sr/^{90}Y test case. However, it could be non-trivial to perform a calibration between ^{225}Ac and ^{213}Bi, which would require purified samples of both isotopes or post-processing calculations to account for the ingrowth of ^{213}Bi during acquisition. We have begun to investigate measurement of an ^{225}Ac sample at voltages above and below the threshold for β-particle detection. Care must be taken to account for the right-shift of the α-particle cluster size distribution under voltage adjustment in this case.

Future work could explore other metrics besides the cluster size histogram and simple assignment methods discussed here. Cluster variance, eccentricity, skewness, and kurtosis are all evaluated by the iQID frame-parser and could be used for multi-variable data analysis. We believe that machine learning classifiers might be particularly powerful, given the ease of data acquisition (enabling large swaths of training data) and ability to automatically label data sets (separate acquisitions with a single particle type).

8.3 Feasibility of ^{225}Ac/^{213}Bi separation using coincident γ-rays

iQID lacks energy discrimination but provides ultra-high spatial resolution for the position of α-particle emissions in ex vivo tissue samples. On the other hand, γ-ray counting and imaging methods provide energy fingerprints associated with specific isotopes, but are as yet unable to resolve spatial heterogeneities characteristic of αRPT. These two datasets provide complimentary information, if they could be combined.

Within the time resolution of our devices, γ-ray emission following α- or β-decay occurs simultaneously (picoseconds). We hypothesized that an energy-discriminating HPGe detector in synchrony with the iQID device could detect these coincident emissions and "tag" a proportion of detected α-particles as belonging to specific γ-emitting progeny, either ^{221}Fr or ^{213}Bi. This section details our efforts to engineer a hybrid system with this capability.

8.3.1 Methods

The goal of this approach was the synchronization of two detectors, an iQID digital autoradiograph and an ORTEC IDM 200-V HPGe detector (described in Chapter 2). iQID cannot be operated with an external trigger, so we explored post-processing software developments to co-register the two sets of list-mode data according to a common clock.

Below is a step-by-step description of the protocol. The physical setup for data acquisition and considerations regarding each step are elaborated on in the following sub-sections.

Procedure

1. Collect digital autoradiography listmode (iQID) and gamma spectroscopy listmode (IDM) data simultaneously from a sample.
2. Load iQID Compressed Listmode data and record acquisition time t_0(iQID).
3. Load iQID Offset Listmode data. Correct iQID data for missed frames.
4. Convert corrected iQID frames to timestamps using FPS (exposure time).
5. Load IDM data and record acquisition time t_0(IDM).
6. Apply event selection criteria (energy, events per frame, etc).
7. Align IDM data timestamps to iQID timeline by adding $dt = t_0(\text{IDM}) - t_0(\text{iQID})$.
8. Bin IDM events to the iQID framerate.
9. Identify coincident frames as those containing both an iQID α-particle and IDM γ-ray.
10. Repeat (7–9) with 1-ms shifts of dt over a specified interval to account for potential misregistration in the initial start times.
11. Evaluate results to locate the correct registration and tagged events.

Physical setup

The basic system geometry used a custom-built stand to support a detector-down orientation of the IDM above the iQID camera.[5] Minor modifications to this design evolved over several experiments (Fig. 8.8). The detector was initially set above the entire iQID housing structure, including the light-tight sample enclosure (Fig. 8.8A). Greater geometric efficiency for the γ-ray emissions was obtained by adjusting the stand to bring the HPGe head closer to the iQID sample plane, which necessitated removal of the cover (Fig. 8.8B–D). An opaque tarp was wrapped around the entire setup to prevent damage to the image intensifier.[6] In a later experiment, the tarp was used to cover only the iQID component to allow manipulation of a sealed disk source resting on top of it (Fig. 8.8E). Eventually, the system was transported to a room with lower ambient γ-ray background, and a lead shield was fixed in front of the HPGe head (Fig. 8.8F). The experiments motivating each setup are described in Section 8.3.2.

iQID timing information and corrections

Use of a CMOS camera to record scintillation light makes iQID an integrating detector over intervals defined by the device frame rate. In standard operation with low-activity samples, pile-up is a minimal concern and timing requirements are lax. Typical frame rates are around 20–40 FPS (25–50 ms exposure). The CMOS camera (Point Grey Research Grasshopper 3, GS3-U3-51S5M-C) can operate up to 75 FPS (13.3 ms) in the full-field view. Reduction of the capture ROI permits a corresponding increase in framerate, up to about 400 FPS (2.5 ms). At higher rates, the iQID software crashes during acquisition.

Figure 8.9 details the timing of processes between the iQID camera and the connected laptop computer. The former acquires images, while the latter parses frames, records timestamps, and writes list-mode data. The time associated with each iQID listmode event is reported by the device in two ways (Compressed Processed Listmode data): the current frame index i, and the elapsed time in milliseconds t_i. While the camera itself constantly acquires images F_i at the user-defined FPS, the timestamp $t_i = t - t_0$ is based on the time t at which the computer loads the image data from the buffer and is rounded to the nearest millisecond. The acquisition start time t_0 is recorded in the header, rounded to the nearest whole second. When the workload is below the capacity of the laptop processor and GPU, images move in and out of the buffer quickly. Typical acquisition modes measuring the decay time of long-lived isotopes (e.g. Fig. 4.6) do not require sub-second precision from t_0 and are relatively unaffected by the processing and transfer overheads that affect t_i.

For coincidence identification, the precision is insufficient. Two consecutive frames are sometimes labeled with the same millisecond t_i value because it is dictated by the buffer

[5] The stand was designed and built for this purpose from aluminum rails and rubber bumpers by Benjamin Huang in the Vetter lab at UC Berkeley.

[6] The iQID camera has magnetic interlocks to prevent operation without the cover. These were overridden using weak ceramic disc magnets. This operation mode is not sanctioned by QScint and voids the iQID camera warranty.

Figure 8.8: Evolution of physical system design for hybrid iQID-HPGe detection. The basic geometry stayed consistent, with the HPGe IDM supported in a detector-down orientation above the iQID sample stage as in the initial setup, (A). (B) Light-tight tarp wrapped around the setup allows iQID to be operated without the cover. (C) Inside view of (B). Adjustment of the stand brings the IDM closer to the iQID stage. (D) Close-up view of (C) showing the proximity of the HPGe head to the sample. (E) Alternative tarp placement allowing for manipulation of a sealed source on top of it. (F) Relocation of the setup to a lower-background environment with lead shielding from one direction.

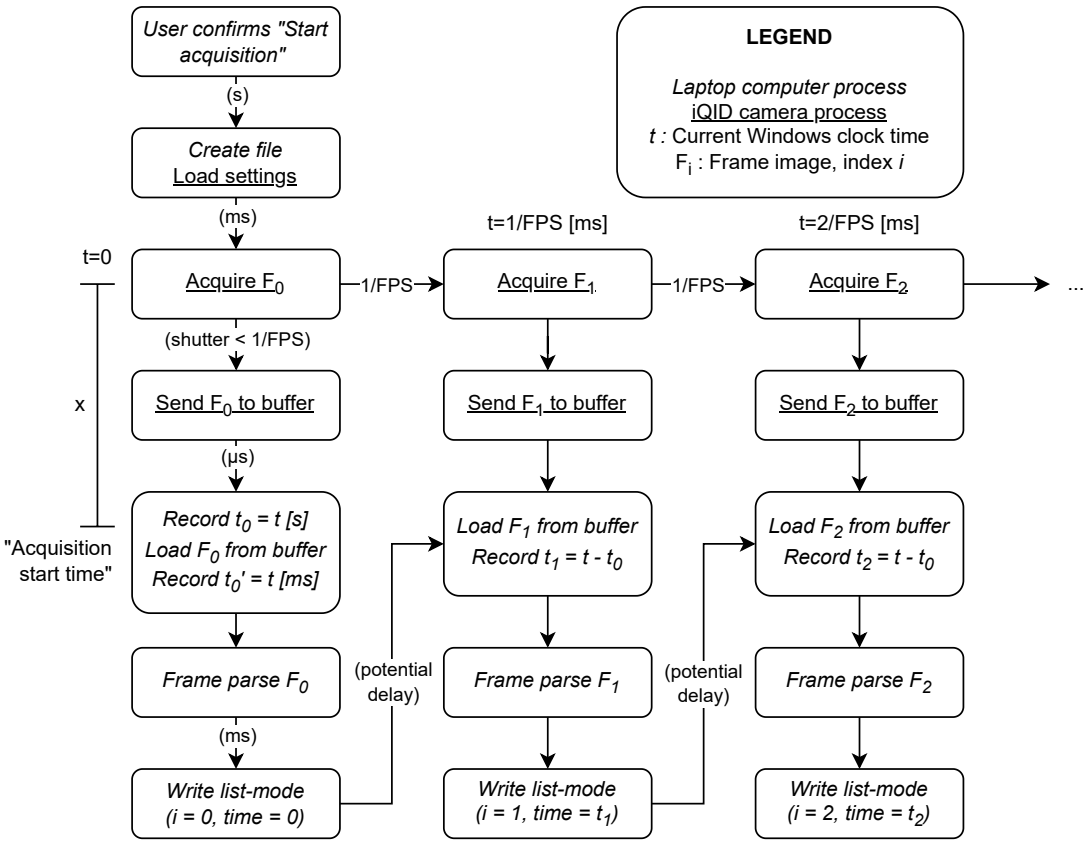

Figure 8.9: Timing and processes in the iQID camera readout.

pull-time. Moreover, t_0 is too imprecise to coordinate with another detector. iQID software patch 2.2.28 (introduced Feb 2024) was installed to add an additional millisecond-precision t_0' to the data header. We then obtained an event timestamp by multiplying the immutable frame index containing the event by the exposure window time (1/FPS). For example, an event that occurred in frame 9 at 400 FPS was timestamped at $(9)(2.5\,\text{ms}) = 22.5\,\text{ms}$ after the start of acquisition. The first frame, frame 0, definitionally corresponded to 0 ms after the start of acquisition.

An important inconsistency to note is that the acquisition start time t_0' is not recorded until frame 0 has been acquired and loaded by the laptop computer, instead of at the start of its exposure. There is thus a delay x = (exposure time) + (transfer time) + (load time) of a few milliseconds that is challenging to quantify precisely. We handle this challenge in the synchronization section below.

Very high activities or frame rates can overwhelm the laptop, sending images to the buffer faster than the computer can parse the frames. The camera continues to collect images, but

Packet index	PC computer time (s)	PC time, normalized to 1st timestamp (s)	Detector time (s)	Calculated dt (s)
Acquisition start	42.45 - dt = 42.2	-dt	0	Average = 0.25
0	42.45	0	0.25	0.25
1	42.60	0.15	0.39	0.24
2	42.85	0.40	0.64	0.26

Figure 8.10: Schematic for estimation of IDM acquisition start time with example data, where arrows indicate calculations. List-mode data provides the difference between PC computer time and corresponding detector time, which are averaged to determine the mean delay (vertical arrow). The acquisition start time is estimated as the PC time at which a command would have produced the detector time of zero based on the average delay dt and the first PC timestamp (horizontal arrow).

those sent to a full buffer are immediately discarded without recording data. Skips of a few frames are not problematic in typical acquisitions, because missing data from several seconds does not affect the ability to fit the half-life of isotopes with half-lives of hours to days. The arrival-time t_i is also used in these applications, which is read directly from the computer rather than calculated with the frame index. However, the frame index does not increment during skips, rendering our precise timestamp calculation inaccurate if they occur.

We corrected this effect using the Offset Listmode data, which reports the current number of skipped frames at any given frame index. This information is not reported in the Compressed Processed Listmode data, although the iQID header file records the total number of missed frames over the acquisition to allow one to easily determine whether a correction is necessary. For an array of recorded frame indices i and missed frame totals $m(i)$, the true frame numbers $f(i)$ were calculated as $f(i) = i + m(i)$, then multiplied by the exposure window as described above to yield corrected timestamps.

IDM timing information and list-mode parser

List-mode readout from the ORTEC IDM 200-V produces a binary file described in its user manual and supporting documentation. We wrote an open-source Python script to read and

parse this file, available at https://github.com/robin-peter/gamma-bits, which provides the timestamp in 10-ns increments and ADC value (corresponding to energy) of each event. Like iQID, the IDM has variable buffer read-out overhead but a constantly ticking internal clock. The internal timestamps are exact with reference to the acquisition start time as measured by the detector clock, but it can be challenging to determine this value in computer (PC) time because the overhead between a PC command and the detector receipt is not constant. Figure 8.10 illustrates ORTEC's approach as we understand it.[7] The Windows timestamp of each data pull request and the corresponding detector time at the instant of request receipt are recorded in the list-mode data. When the file is parsed, the average delay between command and receipt is calculated over the whole acquisition. Then, the acquisition time start is estimated as the PC time at which the initiation command would have produced the detector time of zero based on the average delay and first PC-detector timestamp pair. We reproduced this logic and applied it in our experiments.

Post-processing synchronization

Both devices were attached to the same Windows laptop computer for readout, resulting in two data timelines recorded on the same Windows clock. Figure 8.11A illustrates the conceptual approach to synchronizing the data. Since the start times were on the same reference timeline, a simple correction $dt = t_0(\text{iQID}) - t_0(\text{IDM})$ was applied to timestamps in the IDM data to obtain IDM timestamps in the iQID time frame. (The nomenclature here assumes that the iQID acquisition was started first, followed by the IDM. The procedure can be carried out with a negative sign in experiments where the order is reversed.) iQID α-events and IDM γ-events that occur at the same time would be labeled as in coincidence.

The schematic in Fig. 8.11A is idealized for two detectors with perfect time resolution. Figure 8.11B reflects that iQID cannot operate faster than with 2.5 ms exposures, and events detected in a frame may have occurred at any time during the open window. The IDM detector was assumed to be a perfect instrument by comparison. To determine coincidences in the more realistic configuration, IDM events were binned to the time of iQID camera frames, and the data was searched to locate coincident frames rather than coincident events.

The start times $t_0(\text{iQID})$ and $t_0(\text{IDM})$ are crucial to accurate registration of the two timelines. As described above, both detectors have some uncertainty associated with the start time that they report. In iQID, t_0' is delayed from the actual start of the first frame by the time taken to acquire, transfer, and load the image prior to the clock check on the computer. For the IDM, the variable overhead can be estimated by averaging over many packets, but the actual jitter of the first initiation command is not knowable. Our procedure needed to be robust to some misregistration in the timestamp.

We devised a post-processing procedure to accommodate misregistration in the start times, where the coincidence identification was performed in shifted increments over a user-defined range of possible offsets and coincidences were evaluated for each possible shift (Fig.

[7] We compared this procedure against a list-mode parser provided by ORTEC support but were unable to confirm with any engineers.

8.11C). We hypothesized that true coincidences would spike above a background level of random coincidences ("randoms") at the "correct" registration, and used this criterion to evaluate the registration of each experiment. The code re-generates the frame-binned IDM histogram at each shift, so the procedure can become computationally expensive for many events and long acquisitions, in which cases the shift arrays were split into portions and evaluated on a computer cluster.

Event selection

The two-flag coincidence protocol naturally yields a large number of random hits because of the long time window of the iQID frame. Several event selection criteria were imposed to reduce false positive events. Figure 8.12 summarizes the main ways in which we discarded events to minimize false positives.

- (Fig. 8.12A) High-background time periods were eliminated from analysis, since there was no intrinsic background rejection. For example, cyclotron production in the early morning caused an influx of 511 keV annihilation photons that down-scattered into a ^{213}Bi region of interest.
- (Fig. 8.12A) Only gamma-ray events from the isotope photopeak were included.
- (Fig. 8.12B) Only iQID frames with a single particle were included, as there is no method to choose which event from a set of multiple within an iQID frame would correspond to a given γ-emission.

Evaluation metrics

Two metrics were used over the experiments to evaluate whether the approach had accurately identified α/γ coincidences:

- Spatial separation: Experiments utilizing two spatially separated sources could be evaluated for event identification accuracy compared to the ground truth, as in Fig. 8.6. The emphasis and suppression effects of the analysis were compared over the range of offset shifts, where the correct registration would yield maximal difference from the original image.
- Coincidence counts: Experiments of a single source with known activity (e.g. ^{22}Na coincidence tests) were expected to produce predictable numbers of random coincidences corresponding to the length of the iQID frame window. The number of detected coincidences was compared over the range of offset shifts, where the correct registration would yield maximal true detections over the random coincidence noise floor.

The number of random coincidences expected from an acquisition is a function of the two event rates r_1 and r_2 and the length of the exposure window τ. We derive this following

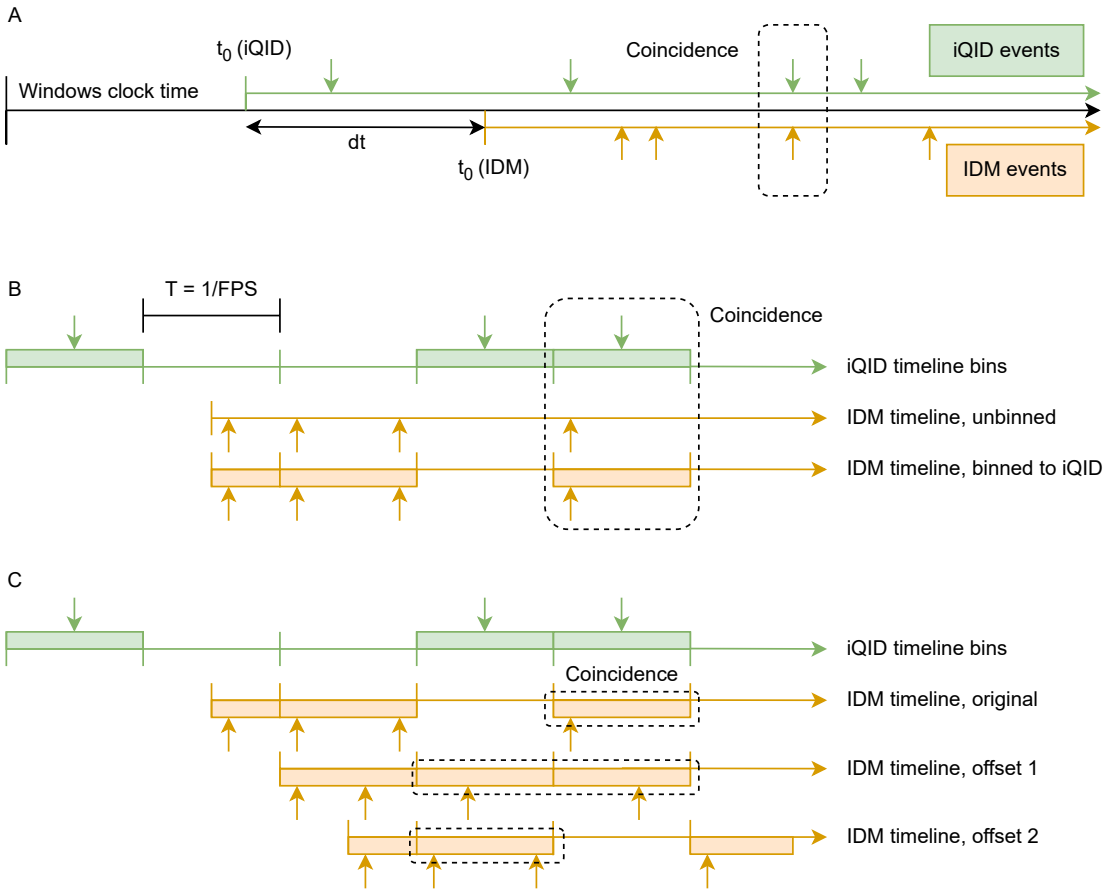

Figure 8.11: Schematics showing approaches to data synchronization between iQID α-particle and HPGe IDM γ-ray events. (A) Conceptual schematic with idealized detectors. Two data sets are obtained on the same reference timeline (Windows clock) and can be co-located with respect to each other using a known difference dt. (B) Realistic schematic accounting for finite iQID exposure time (down to 2.5 ms at 400 FPS). IDM events are binned to the iQID frame rate, and coincidences are identified in frames with positive flags in both devices. (C) Timeline-offset procedure to accommodate possible misregistration in the start times. Coincidence identification is performed for a range of shift increments.

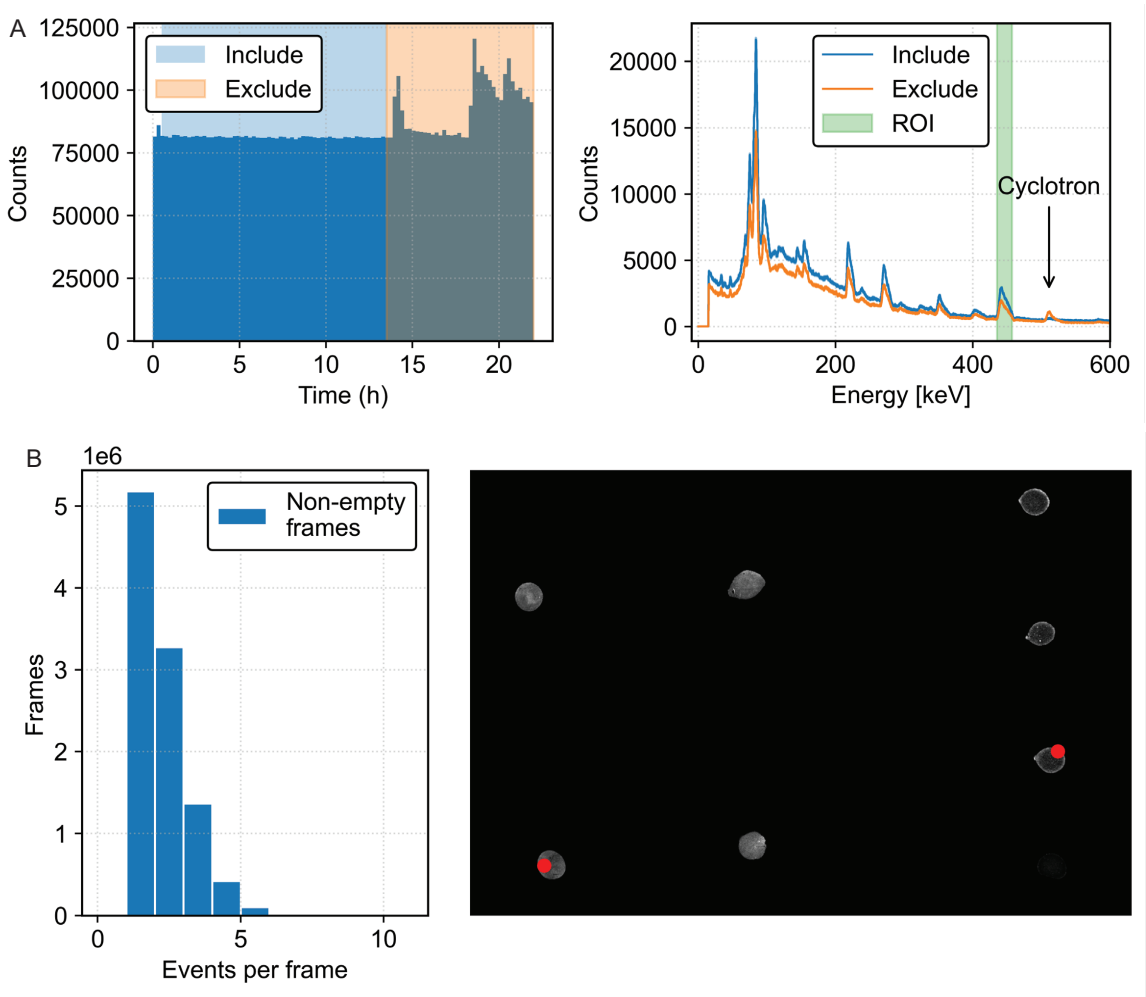

Figure 8.12: Examples of event selection for gamma-tag analysis. (A) Events during periods of high background were discarded, such as during an early-morning period of cyclotron production. The energy spectrum from the discarded events were disproportionately high in the 511-keV window due to positron-emitters, which also contributed to downscatter background in the selected region of interest. (B) Only iQID frames with a single charged-particle event were used. It cannot be discerned which spatial location corresponds to an emitted gamma-ray, as shown in this example frame with one event from an ^{225}Ac droplet and another from a ^{223}Ra droplet.

the nomenclature in [176], which describes random coincidences in a two-detector trigger system. Unlike the system in the reference, in which an event in either detector can trigger a window, the iQID-IDM hybrid detector has a rolling iQID frame window that "opens" every $\tau = 1/\text{FPS}$ seconds. Our derivation changes accordingly: the gate is considered to only trigger from Detector A (iQID) at the detection rate r_1. The random coincidence event rate R is the product of r_1 with the probability that Detector B triggers in the interval τ opened by a detection in A (i.e., the iQID frame):

$$R = r_1(1 - e^{-r_2\tau}). \tag{8.1}$$

Here, r_1 and r_2 are given by the detected rate of events in iQID and the HPGe IDM, respectively, *after* event selection and binning to the iQID frames, because these are the actual counts used in the coincidence detection algorithm. To compare the expected random rate R to the expected true signal rate T, the particular isotope and branching ratios of the experiment must be considered. These calculations are shown in each section as necessary.

8.3.2 Iterative experiments

Here, we discuss some of the experiments conducted to examine the feasibility of an iQID-HPGe hybrid gamma-tagging system. We were ultimately unable to identify coincident events above the expected random threshold, but improved on the system's efficiency, random coincidence rate, and processing algorithm over the course of several experimental iterations. Since we lack a conclusive result, this section reads as a progress report that details the challenges encountered, solutions discovered, and motivation behind each step.

Droplet experiments

Our initial experimental setup used two swatches of ZnS:Ag scintillator for α-particle detection mounted on iQID in the system setup in Fig. 8.8A. Four droplets of either ^{225}Ac or ^{223}Ra (approx. 1 nCi per droplet) were prepared on each scintillator piece (Fig. 8.13A–B).[8] The spatial separation provided a ground-truth control to evaluate the accuracy of the gamma tagging procedure. These two isotopes were used because of their availability in our lab and because they both emit simultaneous γ-rays in coincidence with α-particles (Fig. 8.13C). Note that ^{223}Ra emits a γ-ray at 445 keV with 1.3% intensity that interferes with the ^{213}Bi ROI about 440 keV (25.9%). We believed that the ^{213}Bi ROI would still have superior signal-to-background in this controlled experiment compared to the ^{221}Fr peak because of the downscatter background at 218 keV.

Data was acquired for 21 h at 90.9 FPS (11 ms frames), but only the first 12.5 h was used for analysis due to the flood of background activity from cyclotron production in the

[8] The exact activities were not known precisely. They were estimated from an argon dose calibrator as 1 nCi per ^{225}Ac droplet and 0.8 nCi per ^{223}Ra droplet, with greater uncertainty associated with the ^{223}Ra sample, which was prepared from a residual quantity of material. These quantities are known to be below the accurate range of the calibrator, even at the level of the macroscopic solution prepared for dilution.

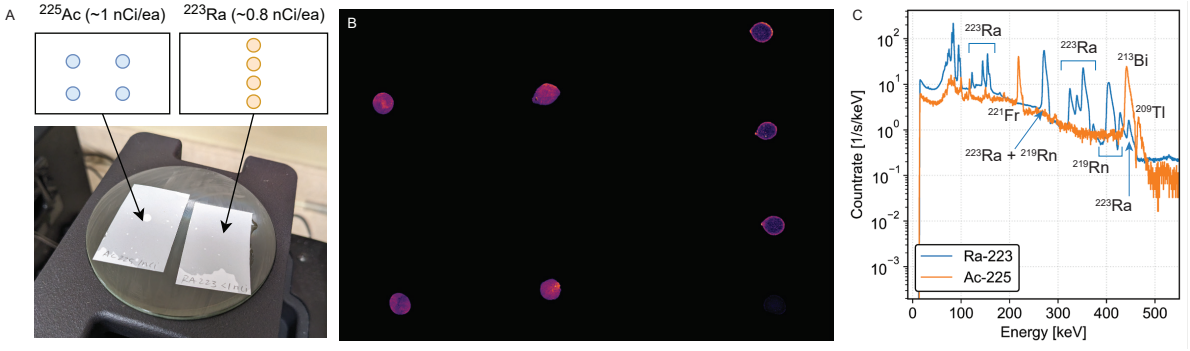

Figure 8.13: Droplet experiment setup with ^{225}Ac and ^{223}Ra. (A) Two ZnS swatches are prepared with four droplets each at approx. 1 nCi per droplet. Spatial separation provides ground truth. (B) Unprocessed iQID image of both isotopes. One ^{223}Ra droplet appears not to have been completely pipetted. (C) Energy spectra for (other samples of) equilibrium ^{225}Ac and ^{223}Ra as measured by the HPGe IDM, with select peaks annotated.

early morning. Figure 8.14A summarizes the time cut (i), energy spectrum and ROI at (435, 457) keV corresponding to the 440-keV emission from ^{213}Bi (ii), signal-to-background in the peak ROI (iii), and singles-frame event selection (iv). Both the proportion of singles frames in iQID ($f_s = 0.05$) and the ratio of net to gross counts in the ^{213}Bi ROI ($N/G = 0.29$) were low. Based on the detected event rates, we expected 2700 random coincidences and 300 true detections (Box 8.1). Across 90 arbitrarily selected frame shifts, we observed 2700 ± 50 detected coincidences (max: $2878 = 2720 + 3\sigma$) and decided to improve the setup before more extensive coincidence analysis.

To improve the proportion of usable events and the signal-to-background rate, the HPGe detector head was brought close to the iQID sample stage by removal of the light-tight cover, which necessitated enclosure of the entire setup with an opaque tarp (Fig. 8.8B–D). Figure 8.14B shows the metrics for the new configuration, which used a similar time cut (i) and energy ROI (ii) but yielded yielded a significantly better net-to-gross ratio, ((iii), $N/G = 0.66$). To improve the singles rate, we increased the frame rate to 180.6 FPS (5.5 ms frames) and allowed the sample to decay for a week, reducing the activity by a factor of $\exp(-7 \ln 2/9.9) = 0.61$. These adjustments yielded a seven-fold increase in usable single-alpha frames ((iv), $f_s = 0.36$) and an additional benefit to random coincidence reduction by lowering τ (Eqn. 8.1). In comparison to the previous setup, in which the predicted true-to-random coincidence ratio was $T/R = 287/2702 = 10.6\%$, the new setup had $T/R = 18472/37785 = 48.8\%$. Note also that the experiments took similar amounts of time (21, 22 h) but sixty times more usable frames were obtained in the second version.

Figure 8.14C shows the results of shift-based coincidence analysis for the improved droplet setup with registration differentials assessed from -3 s to $+3$ s in increments of 1 ms. At each registration, the number of coincidences was recorded, as well as the number of tagged

events assigned to each side of the frame (^{225}Ac side or ^{223}Ra side). In an ideal case without background interference, a working algorithm would correctly assign all of the tagged events to the ^{225}Ac side, since the ^{213}Bi energy window was used.

Across 6000 registrations, the mean value of coincidences in the 440 keV ROI was 39 790± 160. None produced coincidences in excess of 670 events of the random value (maximum: 40450), well below the expected true coincidences of 18500. The ratio of assigned events, $R = N_{\mathrm{Ac}}/N_{\mathrm{Ra}}$, was 2.10 in the original image, but did not deviate greater than 5.3% (2.21) with any coincidence filtration. Similar results were observed for the 218 keV window. Notably, the best registrations for each energy ROI (218 keV and 440 keV) were not matched (1.855 s, 1.359 s). In a similar experiment later on using ^{225}Ac droplets and a ^{210}Po check source (without γ-emission), we again did not identify coincidences in significant excess of the random rate (Fig. 8.14D). Failure to identify coincidences above background in these droplet studies motivated a series of check-source experiments below.

^{22}Na experiments

This set of experiments was designed to troubleshoot the timing and synchronization. It was actually during these experiments that we developed the shift protocol detailed above. Although we have already relayed results from the droplet experiments in these terms, we include these experiments to fully detail what we know about the two systems. ^{22}Na was advantageous for troubleshooting because the dual back-to-back annihilation photon emission nearly guaranteed that each detected positron was accompanied by a synchronous 511 keV photon emitted towards the solid angle of the HPGe detector.

The 7.34 µCi ^{22}Na source available in our lab was quickly found to be too strong for the experimental setup of the droplet samples. Only about 1% of the frames in the 10-minute test acquisition were single-event, with 0.2% empty. Moreover, the proximity of the source to the HPGe crystal put the detector at 79% deadtime, and even when acquiring at the maximal 400 FPS (2.5 ms frames), the devices registered simultaneous events in every frame. We examined a few other geometries, such as operation with and without the cover, detection of the 511 keV photon in iQID instead of the positron, and reduced-rate geometries using coincidence between the 511 keV photon and the 1275 keV gamma-ray. Many of these setups did reduce the deadtime issues, but overcorrected to yield extremely low rates of anticipated true coincidences.

We borrowed a lower activity (82 nCi) ^{22}Na source (Spectrum Techniques) and repeated the experiment in the highest-efficiency geometry (Fig. 8.8B–D). The shift protocol was applied over ±5 s at 1-ms increments for energy windows around 511 keV and 1275 keV (Fig. 8.15A). Results for the two windows are shown in Fig. 8.15B. At no shift did the detected 511 keV coincidences exceed 1000 events over the mean random value, where 24000 true coincidences were expected. Similarly, 10400 true coincidences were expected in the 1275 keV window with a 63000-count noise floor. Note that our random calculation model predicted around 1300 random coincidences fewer (0.6%) than measured in the 511 keV

Box 8.1: True and randoms rate estimation for ^{225}Ac and ^{223}Ra droplets. Let the acquisition time be t. Rates r_1 and r_2 are given from the binning procedure as

$$r_1 = (\text{number of valid iQID frames})/t; \quad r_2 = (\text{number of valid IDM events})/t$$

The valid iQID frames are those meeting the singles selection criteria, and the valid IDM events are those in the energy ROI prior to iQID frame binning. Note also that

$$r_2 = r_N + r_B = G/t,$$

where r_N is the actual rate of ^{213}Bi emissions detected in the ROI at the detector's efficiency, and r_B is the rate of background (or ^{223}Ra 445 keV) emissions contaminating the peak, which combine to obtain gross counts G. The expected randoms rate R is calculated from Eqn. 8.1.

To calculate the expected number of true coincidences, we take the activity from the ^{225}Ac and ^{223}Ra droplets to be $A_{Ac} = 4\,\text{nCi}$ and $A_{Ra} = (3)(0.8\,\text{nCi}) = 2.4\,\text{nCi}$ (assuming minimal activity from the fourth ^{223}Ra droplet, based on Fig. 8.13B). The actual rate of α-particle emission A_α is

$$A_\alpha = 4(A_{Ac} + A_{Ra}),$$

because both decay chains emit four α-particles per decay series. The iQID efficiency ε_{iQID} is

$$\varepsilon_{iQ} = r_1/A_\alpha,$$

assuming the same efficiency for α-particles from the two isotopes. (One could split the calculation into two iQID efficiencies, but we proceed as described for simplicity.) Similarly, the IDM efficiency for γ-rays in the ^{213}Bi photopeak is approximately

$$\varepsilon_{IDM} = \frac{r_2(N/G)}{A_\alpha},$$

where the ratio N/G represents the fraction of net ^{213}Bi counts atop the background. From the true rate of ^{213}Bi γ-rays emitted from the sample, $A_{Bi} = 0.259A_{Ac}$, we calculate the expected true coincidence rate in our system T:

$$T = \varepsilon_{iQ}\varepsilon_{IDM}A_{Ac}.$$

The expected random and true coincidences for the acquisition can be calculated as Rt and Tt, respectively.

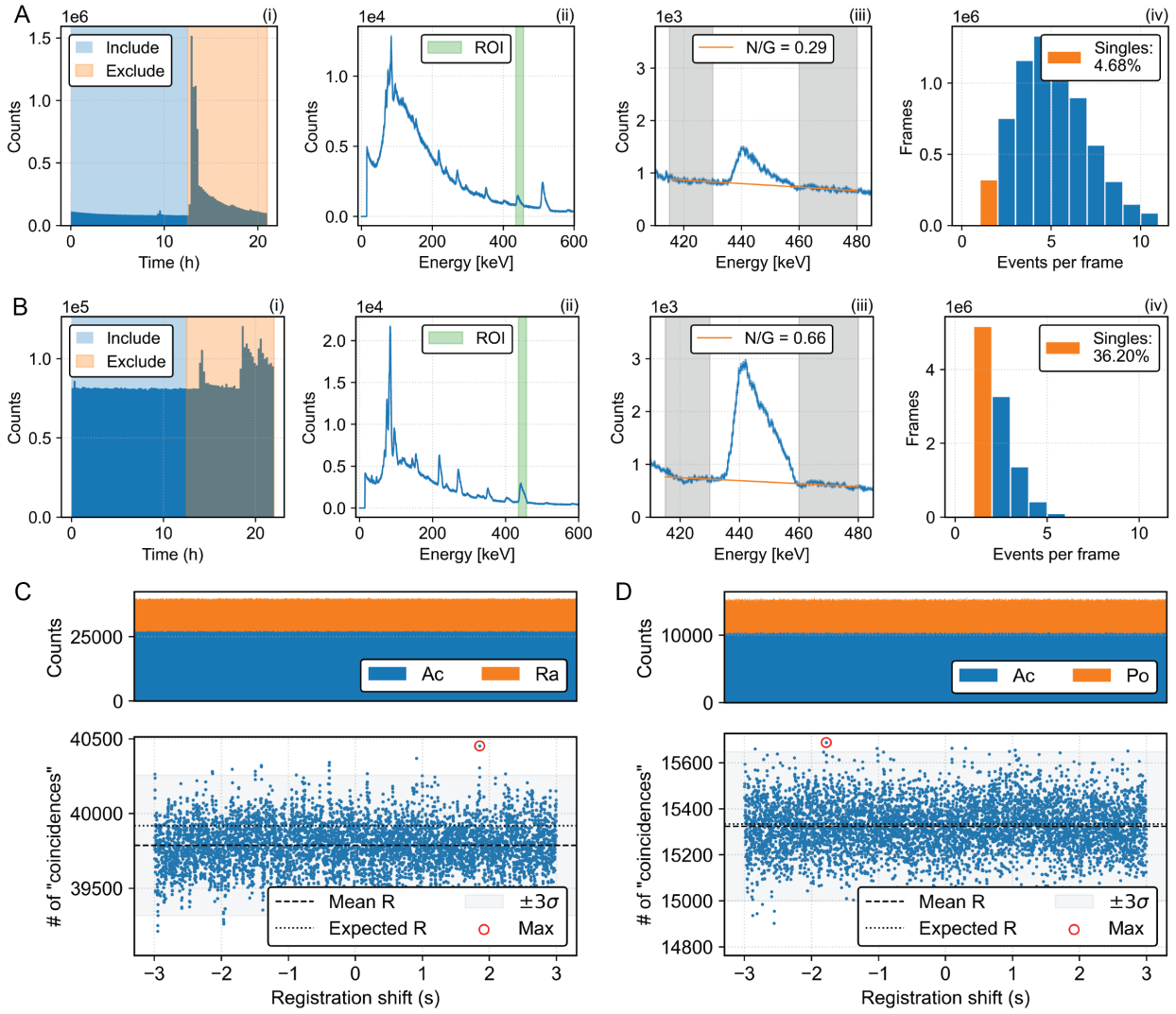

Figure 8.14: Characteristics and results for several iterations of droplet experiments. (A) Time cut (i), energy spectrum and ^{213}Bi ROI (ii), signal-to-background in the ROI (iii), and singles-frame event selection (iv) for initial experiment, corresponding to setup in Fig. 8.8A. (B) Similar metrics indicating improvement to geometry and efficiency by adjusting setup as in Fig. 8.8B. (C) Shift protocol showing event assignment (above) and total coincidences (below) for ^{225}Ac/^{223}Ra droplet experiment. (D) Shift protocol for ^{225}Ac/^{210}Po droplet experiment.

Box 8.2: True and randoms rate estimation for ^{22}Na experiments. As in Box 8.1, we have r_1 and r_2 as the valid iQID and IDM rates over acquisition time t. The actual rate of β^+ and 511-keV photon emissions are calculated according to their branching ratios [50]:

$$A_{\beta^+} = 0.89955 A_{Na}, \qquad A_{511} = 1.7991 A_{Na}.$$

These provide an iQID efficiency and energy-specific IDM efficiency. All subsequent calculations in Box 8.1 follow analogously.

window. We are unsure of the reason and did not observe similar deviation from prediction in other experiments (Figs. 8.14, 8.16).

We questioned whether the device timeline misregistration could exceed the set ±5 s interval. The shift protocol is not computationally optimized and somewhat time-consuming, so we devised a simple tabletop experiment to co-locate the timelines to within one second. Unlike α-particles, the β^+ emissions from ^{22}Na can penetrate some thin materials, such as the opaque sheet used to protect the iQID components in the coverless geometry. We migrated the tarp to only cover the iQID itself, with the sealed check source resting atop it (Fig. 8.8E). Acquisitions from the two detectors were initiated as close together as possible, and at the approximately one-minute mark, the tarp and source together were pulled off of the sample stage (Fig. 8.16A). This action mimicked a step function where signal was immediately lost from iQID and quickly dropped in the IDM with a time delay related to the $1/r^2$ geometric falloff and the speed at which the source was pulled away (Fig. 8.16B). The two event timelines were manually registered with our best estimate of the location of these steps, which we believe was accurate within an uncertainty of ±1 s (Fig. 8.16C). Therefore, a shift protocol over ±3 s would capture misregistration quantifiable to 1-ms increments (less than one-half of a frame). Only events captured prior to the source-pull were used in analysis.

The results from this approach were similarly inconclusive to previous experiments (Fig. 8.16D). We assessed a ±3 s window to guarantee that the anticipated ±1 s registration would be contained within our search range, but both the 511 keV and 1275 keV analyses identified maximum coincidences closer to the 3-s boundary (2.697 s and 2.142 s, respectively). These maximum values were not statistically convincing. For the 511 keV ROI, the maximum 1317 coincidences was 79 greater than the expected randoms, with 152 true coincidences expected. The 1275 keV ROI maximum at 411 counts was 63 greater than the expected randoms, with 57 expected. Moreover, the maximum values for the two ROIs did not occur at the same shift increment, as would be expected if the protocol correctly identified an offset in the two timelines. We repeated this experiment identically a second time with similar results.

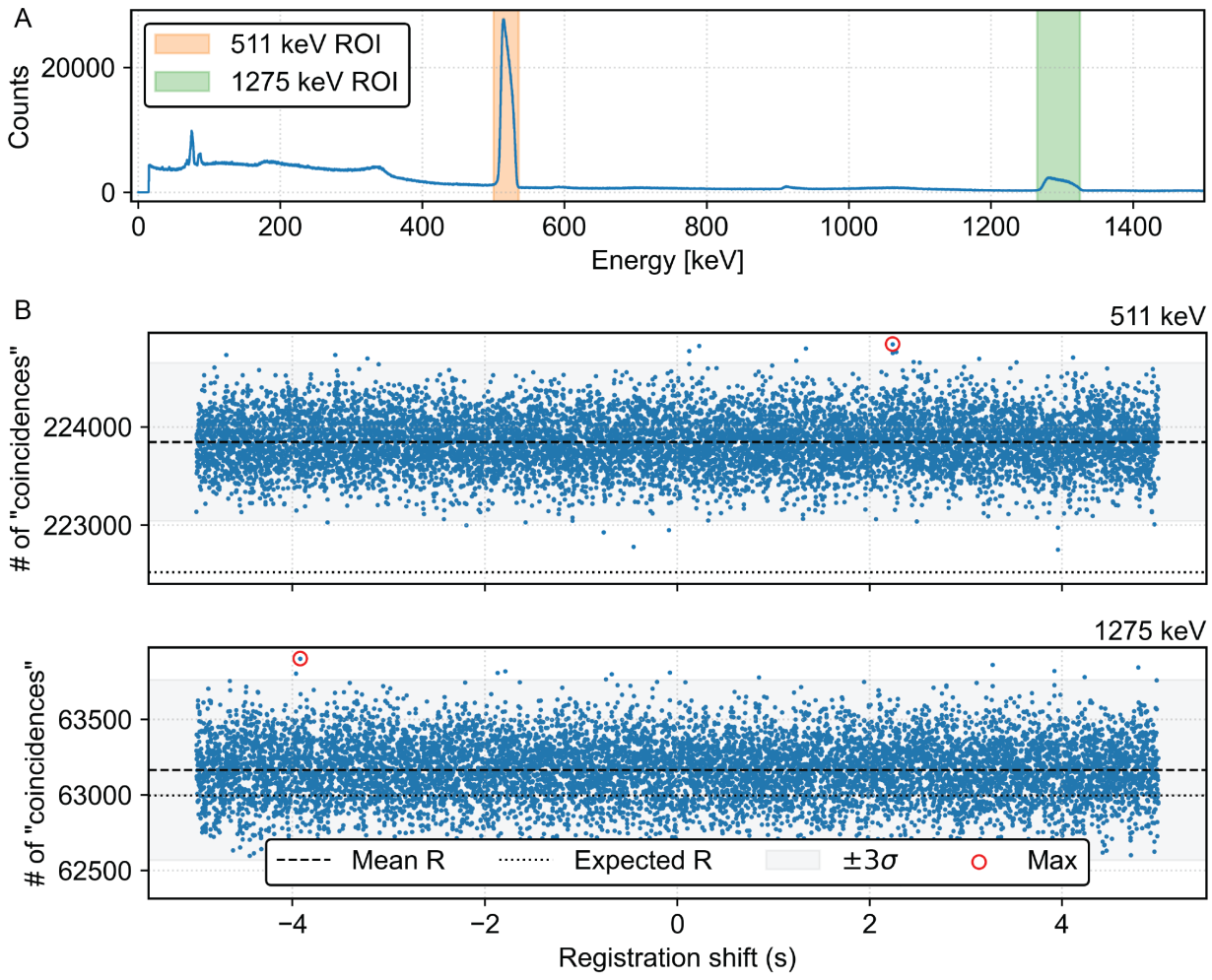

Figure 8.15: Shift protocol results for ^{22}Na coincidence experiment. (A) HPGe IDM energy spectrum showing regions of interest used at 511 keV and 1275 keV. (B) Registration shift diagrams for each energy window. At no shift did the detected 511 keV coincidences exceed 1000 events over the mean random value, where 24000 true coincidences were expected.

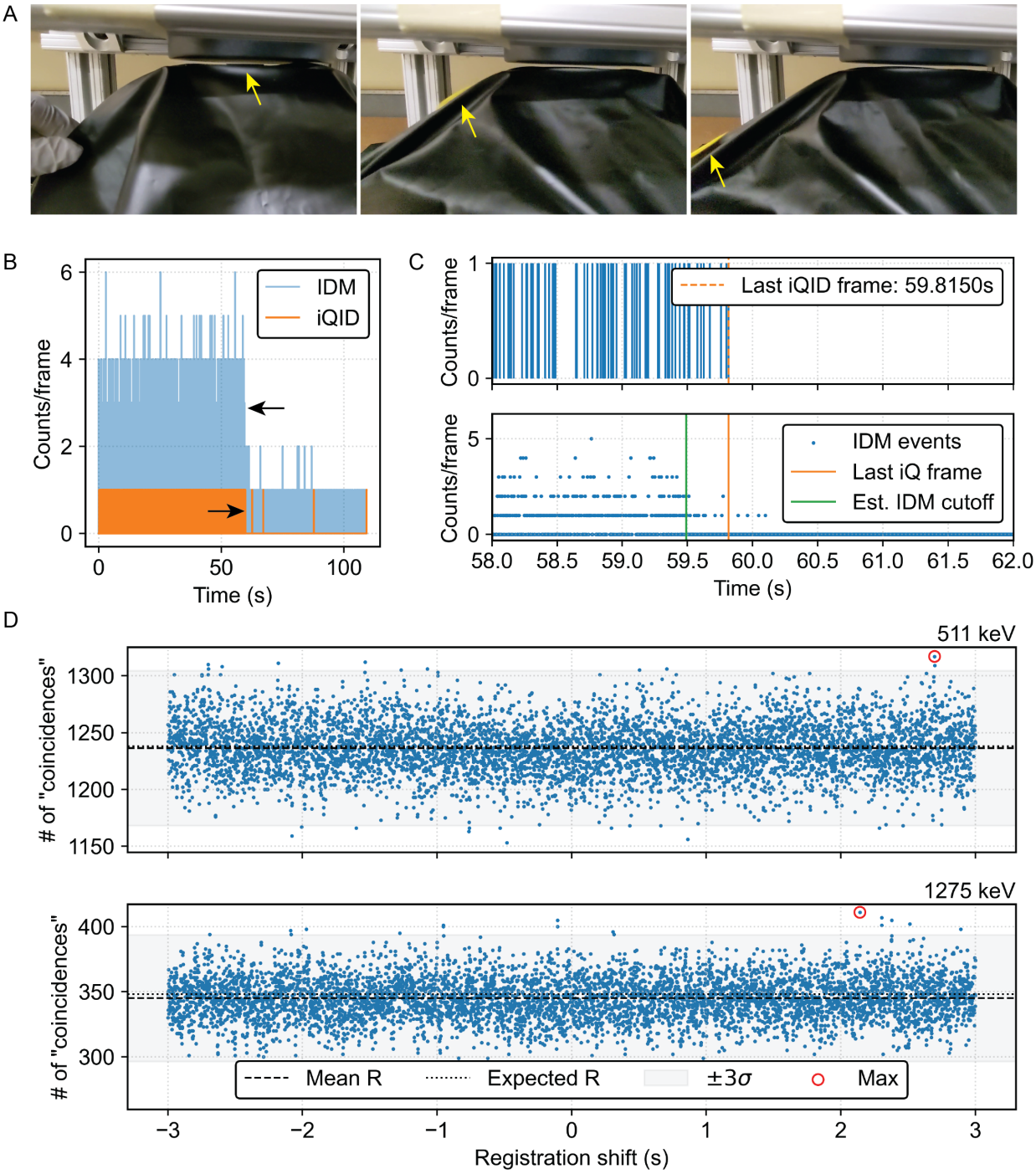

Figure 8.16: Tabletop ^{22}Na experiment for coarse timeline registration. (A) Video frames showing the ^{22}Na source (emphasis, yellow arrow) pulled out from the sample stage to create (B) step functions in the iQID and IDM responses. (C) Manual registration of the two timelines to within 1 s by identification of the step location. (D) Shift-protocol for coincidence identification is still inconclusive in both 511 keV and 1275 keV ROIs.

8.3.3 Discussion

This section detailed our efforts to engineer a hybrid α/γ (or β/γ) system combining an iQID camera with an HPGe IDM-200-V detector to tag spatially detected charged particles with simultaneously emitted photons. We investigated the timing, reporting, and sources of overhead in the list-mode data in depth for both systems. Several of the tools that we developed, including the iQID missed-frame correction and ORTEC list-mode parser, may be useful in their own right for conventional applications of each detector.

Despite improvements over multiple iterations of ^{225}Ac/^{223}Ra droplet and ^{22}Na coincidence experiments, in which we optimized the geometry and acquisition parameters to increase detection efficiency and the proportion of usable events, we were ultimately unable to realize the concept envisioned at the start of the experiment. Several possible lines of investigation may provide insight into the feasibility or flaws of the approach overall.

iQID inconsistency at high frame rates. The iQID CMOS camera is intended for operation up to around 90 FPS in the full 2448 px × 2048 px field-of-view, which we pushed to higher frame rates by restricting the acquisition area to a smaller region of interest. Increased frame rate shortens the exposure window of the CMOS camera, improves the discrimination against random coincidences, and increases the activities that can be accurately measured by reducing the number of counts in each frame for a given sample. Software crashes limited our maximum frame rate to 400 FPS (2.5 ms frame). However, we also encountered a rate consistency issue with iQID operation over the course of troubleshooting. The same source could be measured at two different times on the same day with identical settings but show count rate differences by factors of four to six, even in cases where no missed frames were recorded. We were unable to identify the exact steps to replicate the error. Similarly, several shutter settings could be obtained for different acquisitions with identical frame rates. (We believe that the time between frame initiation was held constant in such cases, but the "live" acquisition time would vary.) These unpredictable behaviors cast uncertainty not only on the rates reported in this chapter but on the timing accuracy overall. The fact that there is a timing issue related to high frame-rate operation that we do not understand raises the question of whether there are other key timing facets that we have overlooked. These issues should be the priority for investigation in any continued work.

External trigger troubleshooting. Although we modeled the expected coincidence rates for each experiment in Boxes 8.1 and 8.2, we did not have ground-truth information for coincident triggers received by both devices. The reason that we used a post-processing approach is because iQID does not have the capability to utilize or provide an external trigger. Industry collaboration with QScint allowing access to some of the lower-level behaviors of the device would be useful to troubleshoot the coincidence timing, provide ground truth using simple pulse modules, and confirm the timing in Fig. 8.9.

Gamma-ray detector timing. We developed the shift protocol in order to permit some inaccuracy in our timing registration, but it bears repeating that the acquisition start timestamp from the ORTEC IDM-200-V appears to be an average estimate based on the typical jitter and overhead time for the device. Essentially, the exact start time is not provided by the device. There is potential work in troubleshooting the time reporting in the gamma-ray detector through external trigger and pulse processing modules. We have begun efforts to synchronize two such detectors with our post-processing methods. Similarly, we have obtained some preliminary data using an M400 CZT gamma-ray detector (H3D) instead of the ORTEC HPGe IDM, although we have found that data acquisition code adjustments would be required to obtain higher precision timestamps. The results of these approaches would rule out whether lack of consistent timing synchrony is due to the behavior of the gamma-ray detector instead of the iQID device.

Background reduction. One flaw that we identified during the iterative experiments was the lack of background rejection in the system. The setup was unshielded and susceptible to contamination by γ-rays in the environment. A peak at 909 keV is visible in Fig. 8.16A, corresponding to the γ-ray emission from ^{89}Zr, a PET isotope tracer being studied in neighboring laboratory spaces. It seems unlikely that the quantities of annihilation photons from the small ^{89}Zr background substantially affected our conclusions, given the persistence of results at 1275 keV and in the droplet experiments, but background reduction is still an area to be improved. We started to characterize a lower-background setup in which the system was relocated to another room with lower and largely directional background from across the hall, where a tall lead shield was propped up to reduce the flux from the known background source (Fig. 8.8F). We did not obtain significantly different results in this setup. Nonetheless, a more stable configuration with greater shield thickness would be desirable in the next iteration.

Code viability. It should not be overlooked that the scripts written for coincidence identification could contain fatal errors. We have attempted to troubleshoot with increasingly simplified experimental conditions and several rounds of code re-writing, but a more rigorous review that clarifies the structure and introduces proper unit tests may prove useful.

8.4 Summary

We investigated two approaches to separate different isotopes utilizing the iQID camera: a simultaneous α/β iQID acquisition and a hybrid iQID-HPGe gamma-tagging system. Both systems were characterized at a low level and then tested using a proof-of-concept experiment with ^{225}Ac for separation from long-lived progeny ^{213}Bi.

For the α/β iQID system, the acquisition efficiency and cluster sizes were characterized as functions of operating voltage to select acquisition parameters with sufficient β-efficiency while preserving specificity for α-particles. Filtration using cluster area in an

image of ^{90}Sr and ^{210}Po check sources recovered detected α-particles with 84% sensitivity (83% specificity) and β-particles with 74% sensitivity (76% specificity). A test measurement with an ^{225}Ac droplet showed high α-particle efficiency and non-negligible β-particle detection, but spatial pileup due to low frame-rates hindered quantitative analysis. Overall, the experiments showed that the α/β iQID method is already usable for samples with high discrepancy between ^{225}Ac and ^{213}Bi, but efficiency improvements are necessary to detect typical ^{213}Bi quantities in tissues above the noise floor.

We spent considerable effort troubleshooting the iQID-HPGe system and recorded our findings about the intrinsic timing and behaviors of both component devices. Although we were unable to show successful co-registration of the two device timelines in post-processing with either proof-of-concept experiment (^{22}Na or ^{225}Ac), several tools have been produced by this work and are available for future investigations. These include software for iQID frame corrections, IDM-200-V list-mode data parsing and manipulation with energy and time cuts, and coincidence analysis between the two devices. We speculate that low-level troubleshooting using external trigger systems will be needed to uncover the flaw in our system setup.

Chapter 9

Conclusion

9.1 Summary

Interest in α-particle radiopharmaceutical therapy continues to grow in clinical, commercial, and academic spheres. Encouraging clinical trials and appealing physical properties for selective targeting have bolstered hopes that the modality may transform the space of metastatic cancer treatment. However, translation of αRPT agents from promising trial candidates to standard-of-care therapies may require more rigorous understanding of their effects and mechanisms.[1] Existing treatment planning and verification schemes are rudimentary compared to those in photon-based modalities because limited data regarding α-particle dose distributions and effects prevent clinical implementation of a dosimetry-based framework. Dose heterogeneity, produced by the short α-particle range, is a major unknown obscuring the relation between absorbed dose and outcome, and it must be studied ex vivo. In this work, we presented the suite of digital-autoradiography-based small-scale dosimetry tools that we have developed to improve the feasibility, accuracy, accessibility, and interpretation of ex vivo absorbed dose measurements on scales matching the α-particle range.

The backbone of this dissertation is the implementation of αRPT dosimetry procedures with an iQID digital autoradiography system. Quantitative autoradiography and dose kernel calculations are not new to the field. However, production of meaningful dosimetry information with iQID required device characterization, scripts for data handling, quantitative corrections, image processing, and isotope-specific kernel simulations that were not previously articulated in literature. These protocols, developed in Paper 1, provided a foundation that we improved in Paper 2 and utilized to illustrate the differences between macroscopic and micro-scale dosimetry measurements in three preclinical studies (^{211}At in canine lymph nodes, ^{225}Ac in mouse kidneys and tumor xenografts, and ^{225}Ac in mouse liver micrometastases). All methods have been detailed with reproducibility in mind. The impact of this framework is to enable radiopharmaceutical researchers to incorporate small-scale dosimetry

[1] The presence of FDA-approved ^{223}Ra in the clinical setting should not be overlooked, although it is a palliative rather than a curative therapy.

into their preclinical workflows, aiding the evaluation of αRPT drug candidates and encouraging the growth of a knowledge base about their biological effects.

Among commercially available DAR devices for preclinical studies, the iQID camera provides high throughput, which we enhanced with slice-minimization approaches. Assuming that a single measured tissue slice can approximate the spatial distribution in an adjacent one dramatically improves the ability to conduct robust, large-volume preclinical research, although the inevitable loss of information increases dose uncertainty. The most significant outcome of these investigations was the capacity for 3D digital autoradiography. At its core, 3D DAR is straightforward plane-by-plane sampling of 3D tissues, but quantitative absorbed dose calculations of single tissue slices can only be accomplished with approximations like the one used in this work. A 3D approach had the greatest marginal utility over a 2D one in the study of tumor micrometastases in healthy liver tissue, in which the relationship between the geometric distribution of absorbed dose and lesion size may have been missed with conventional DAR. The preclinical study assessing PCa xenografts in a mouse model was, to our knowledge, the first to generate and analyze 3D DAR in entire organs and tumors.

All three preclinical examples reaffirmed that the mean absorbed dose, as measured by a gamma counter or most in vivo imaging systems, does not accurately reflect the dose delivered to sub-structures in organs or tumors. Elevated ^{211}At uptake was observed in canine lymph nodes follicles in a HCT conditioning regimen study, but the biological impact of this finding was not determined. In the preclinical studies of ^{225}Ac in mice, further analyses were added to probe the biological effect. These included region-segmented dose-rate-volume histograms, a tumor control probability metric, and corroborative treatment monitoring. The ^{225}Ac studies provide two examples for how small-scale dosimetry can inform preclinical research: by modeling injected activity levels to simultaneously optimize tumor and organ-at-risk absorbed dose, or by assessing the underlying reason for differences in response between controlled cohorts.

In contrast to the relatively user-ready DAR dosimetry package, we made exploratory progress towards isotope separation using the iQID camera. One method focused on the the low-level scintillation light information provided by the system to separate α-emitters from β-emitters, while another added an HPGe gamma-ray spectrometer in temporal coincidence to identify emissions associated with specific energy lines. The systems were characterized and then tested using proof-of-concept experiments to separate ^{225}Ac from long-lived progeny ^{213}Bi. The α/β-separation approach showed promising sensitivity and specificity, with room for efficiency improvements to detect typical quantities of redistributed ^{213}Bi in tissues. We were unable to demonstrate coincidence synchronization in the hybrid iQID-gamma system, but the software for iQID frame corrections, list-mode data handling, and data analysis that we produced may find use in future investigations.

9.2 Future outlook and remarks

Although the ex vivo methods developed here are readily translatable to clinical biopsies [66], patient-specific personalized dosimetry for αRPT is unlikely to use them directly because of the cost, invasiveness, and varied feasibility of biopsy procedures. A personalized dosimetry framework would use in vivo imaging measurements and rely on knowledge mapping the data to tumor and tissue responses (Fig. 1.6). Modulation of therapy injections after the first is only possible with accurate dosimetry models that incorporate sub-structure dose heterogeneity, and autoradiography-based dosimetry is the way to establish those models.

The most impactful addition that could be made to this body of work would be a comprehensive preclinical study assessing the value of small-scale dosimetry for prediction of a specific treatment outcome. While we established a framework for this procedure in Chapter 6, the pilot DAR study evaluated only three mice and did not include data about subject survival at the same administered activity. DAR dosimetry of liver micrometastases in Chapter 7 suggested that micro-scale αRP penetration contributed to the differences observed between early- and late-treatment cohorts, but interpretation was similarly limited by sample size. Paralleling a current concern for clinical RPT, in which despite evidence of correlation few studies directly show that use of dosimetry improves patient survival, it remains to be seen whether small-scale dosimetry predicts preclinical efficacy and toxicity better than macroscopic methods. The implementation of small-scale dosimetry with DAR and the information it provides have been articulated here. Now, these analyses must be shown to be useful.

Preclinical ex vivo measurements face the inherent limitation that the animal must be sacrificed to conduct a measurement, preventing monitoring of the same animal over time and requiring large sample sizes to assess results because of inter-subject variation. Effects are only understood through the review of averages between experimental cohorts rather than individuals. Research questions might include, what is the characteristic small-scale distribution in specific organs or tumors? Are dose differences observed between cohorts, and do they correlate with meaningful differences in treatment outcome? Temporal dose evolution is similarly challenging to estimate using ex vivo measurements. In vivo studies of αRP pharmacokinetics, perhaps achievable with the next generation of specialized imaging systems (Sec. 1.4.1), would provide complementary information to stabilize the calculation of total absorbed dose over time. Ideally, small-scale information could be correlated with in vivo imaging of the same structures, allowing the effects of dose heterogeneity to be estimated from macroscopic measurements in well-understood models.

Achieving the rigor with which absorbed dose is calculated and delivered in external-beam radiation therapy is a challenging task in RPT. The fundamental inability to control the radioactive source after administration to a patient creates substantial barriers to prediction and treatment verification. Given the current prognosis for late-stage metastatic cancer, there is much to be gained by pursuing promising modalities like αRPT despite these challenges. Small-scale dosimetry plays a niche but essential role towards understanding the mechanisms and realizing the therapeutic potential of αRPT.

References

1. Peter, R. *et al.* Small-Scale (Sub-Organ and Cellular Level) Alpha-Particle Dosimetry Methods Using an iQID Digital Autoradiography Imaging System. *Sci Rep* **12,** 17934 (2022).
2. Peter, R., Bidkar, A. P., *et al.* 3D Small-Scale Dosimetry and Tumor Control of ^{225}Ac Radiopharmaceuticals for Prostate Cancer. *Sci Rep* **14,** 19938 (2024).
3. Bidkar, A. P., Peter, R., *et al.* Effective Treatment of Prostate Cancer Micrometastases Using CD46-targeted ^{225}Ac Therapy. *In revisions* (2024).
4. Frost, S. H. L. *et al.* α-Imaging Confirmed Efficient Targeting of CD45-Positive Cells After ^{211}At-Radioimmunotherapy for Hematopoietic Cell Transplantation. *Journal of Nuclear Medicine* **56,** 1766–1773 (2015).
5. U.S. Department of Health and Human Services, Centers for Disease Control and Prevention and National Cancer Institute. *U.S. Cancer Statistics Data Visualizations Tool* 2024.
6. Surveillance, Epidemiology, and End Results Program (SEER). *SEER*stat Database: Mortality - All COD, Aggregated with State, Total U.S. (1969-2022)* 2024.
7. American Cancer Society. Cancer Treatment & Survivorship Facts & Figures 2022-2024. *CA: A Cancer Journal for Clinicians* (2024).
8. Ye, J. C., Horne, S., Zhang, J. Z., Jackson, L. & Heng, H. H. Therapy Induced Genome Chaos: A Novel Mechanism of Rapid Cancer Drug Resistance. *Front. Cell Dev. Biol.* **9** (2021).
9. van den Boogaard, W. M. C., Komninos, D. S. J. & Vermeij, W. P. Chemotherapy Side-Effects: Not All DNA Damage Is Equal. *Cancers* **14,** 627 (2022).
10. Nurgali, K., Jagoe, R. T. & Abalo, R. Editorial: Adverse Effects of Cancer Chemotherapy: Anything New to Improve Tolerance and Reduce Sequelae? *Front. Pharmacol.* **9** (2018).
11. Edeline, J., Gilabert, M., Garin, E., Boucher, E. & Raoul, J.-L. Yttrium-90 Microsphere Radioembolization for Hepatocellular Carcinoma. *Liver Cancer* **4,** 16–25 (2014).

12. Azeredo-da-Silva, A. L. F. *et al.* Selective Internal Radiation Therapy Using Y-90 Resin Microspheres for Metastatic Colorectal Cancer: An Updated Systematic Review and Network Meta-Analysis. *Adv Ther* **41,** 1606–1620 (2024).

13. Parker, C. *et al.* Alpha Emitter Radium-223 and Survival in Metastatic Prostate Cancer. *New England Journal of Medicine* **369,** 213–223 (2013).

14. Wissing, M. D., van Leeuwen, F. W., van der Pluijm, G. & Gelderblom, H. Radium-223 Chloride: Extending Life in Prostate Cancer Patients by Treating Bone Metastases. *Clinical Cancer Research* **19,** 5822–5827 (2013).

15. Deshayes, E. *et al.* Radium 223 Dichloride for Prostate Cancer Treatment. *Drug Design, Development and Therapy* **11,** 2643–2651 (2017).

16. Saad, F. *et al.* Radium-223 and Concomitant Therapies in Patients with Metastatic Castration-Resistant Prostate Cancer: An International, Early Access, Open-Label, Single-Arm Phase 3b Trial. *The Lancet Oncology* **17,** 1306–1316 (2016).

17. Jang, A., Kendi, A. T. & Sartor, O. Status of PSMA-targeted Radioligand Therapy in Prostate Cancer: Current Data and Future Trials. *Ther Adv Med Oncol* **15,** 17588359231157632 (2023).

18. Kratochwil, C. *et al.* ^{213}Bi-DOTATOC Receptor-Targeted Alpha-Radionuclide Therapy Induces Remission in Neuroendocrine Tumours Refractory to Beta Radiation: A First-in-Human Experience. *Eur J Nucl Med Mol Imaging* **41,** 2106–2119 (2014).

19. Kratochwil, C. *et al.* ^{225}Ac-PSMA-617 for PSMA-Targeted α-Radiation Therapy of Metastatic Castration-Resistant Prostate Cancer. *Journal of Nuclear Medicine* **57,** 1941–1944 (2016).

20. Tauber, R. L. *et al.* 872P - Safety and Efficacy of Ac-225-PSMA-617 in Metastatic Castration Resistant Prostate Cancer (mCRPC) after Failure of Lu-177-PSMA. *Annals of Oncology. Abstract Book of the 44th ESMO Congress (ESMO 2019) 27 September – 1 October 2019, Barcelona, Spain* **30,** v342 (2019).

21. Ballal, S., Yadav, M. P., Bal, C., Sahoo, R. K. & Tripathi, M. Broadening Horizons with ^{225}Ac-DOTATATE Targeted Alpha Therapy for Gastroenteropancreatic Neuroendocrine Tumour Patients Stable or Refractory to ^{177}Lu-DOTATATE PRRT: First Clinical Experience on the Efficacy and Safety. *Eur J Nucl Med Mol Imaging* **47,** 934–946 (2020).

22. Ku, A., Facca, V. J., Cai, Z. & Reilly, R. M. Auger Electrons for Cancer Therapy – a Review. *EJNMMI Radiopharmacy and Chemistry* **4,** 27 (2019).

23. Bolcaen, J. *et al.* Marshalling the Potential of Auger Electron Radiopharmaceutical Therapy. *Journal of Nuclear Medicine* **64,** 1344–1351 (2023).

24. Miederer, M. *et al.* Alpha-Emitting Radionuclides: Current Status and Future Perspectives. *Pharmaceuticals* **17,** 76 (2024).

25. Robertson, A. K. H. *et al.* Multi-Isotope SPECT Imaging of the ^{225}Ac Decay Chain: Feasibility Studies. *Phys. Med. Biol.* **62,** 4406 (2017).
26. Makvandi, M. *et al.* Alpha-Emitters and Targeted Alpha Therapy in Oncology: From Basic Science to Clinical Investigations. *Targ Oncol* **13,** 189–203 (2018).
27. Nelson, B. J. B., Wilson, J., Andersson, J. D. & Wuest, F. Theranostic Imaging Surrogates for Targeted Alpha Therapy: Progress in Production, Purification, and Applications. *Pharmaceuticals* **16,** 1622 (2023).
28. Berger, M., Coursey, J. & Zucker, M. *ESTAR, PSTAR, and ASTAR: Computer Programs for Calculating Stopping-Power and Range Tables for Electrons, Protons, and Helium Ions (Version 1.21)* 1999.
29. Sgouros, G., Bodei, L., McDevitt, M. R. & Nedrow, J. R. Radiopharmaceutical Therapy in Cancer: Clinical Advances and Challenges. *Nature Reviews Drug Discovery* **19,** 589–608 (2020).
30. Elgqvist, J., Frost, S., Pouget, J.-P. & Albertsson, P. The Potential and Hurdles of Targeted Alpha Therapy - Clinical Trials and Beyond. *Front Oncol* **3,** 324 (2014).
31. Sgouros, G. *et al.* ICRU REPORT 96, Dosimetry-Guided Radiopharmaceutical Therapy. *JICRU* **21,** 1–212 (2021).
32. Knoll, G. F. *Radiation Detection and Measurement* 4th ed., 217 (Wiley, Hoboken, 2010).
33. Bethe, H. Zur Theorie Des Durchgangs Schneller Korpuskularstrahlen Durch Materie. *Annalen der Physik* **397,** 325–400 (1930).
34. Bloch, F. Zur Bremsung Rasch Bewegter Teilchen Beim Durchgang Durch Materie. *Annalen der Physik* **408,** 285–320 (1933).
35. Hall, E. J. & Giaccia, A. *Radiobiology for the Radiologist* 7th ed., 455–466 (Lippincott Williams & Wilkins, Philadelphia, 2011).
36. Friesen, C. *et al.* Breaking Chemoresistance and Radioresistance with [^{213}Bi]Anti-CD45 Antibodies in Leukemia Cells. *Cancer Research* **67,** 1950–1958 (2007).
37. Wessels, B. W. *et al.* MIRD Pamphlet No. 20: The Effect of Model Assumptions on Kidney Dosimetry and Response—Implications for Radionuclide Therapy. *Journal of Nuclear Medicine* **49,** 1884–1899 (2008).
38. Abbas, N. *Comparison of High- and Low-LET Radioimmunotherapy in HER-2 Positive Carcinomas* Doctoral Thesis (Oslo University Hospital, 2013).
39. Bäck, T. *et al.* ^{211}At Radioimmunotherapy of Subcutaneous Human Ovarian Cancer Xenografts: Evaluation of Relative Biologic Effectiveness of an α-Emitter In Vivo. *Journal of Nuclear Medicine* **46,** 2061–2067 (2005).

40. Behr, T. M. *et al.* High-Linear Energy Transfer (LET) α versus Low-LET β Emitters in Radioimmunotherapy of Solid Tumors: Therapeutic Efficacy and Dose-limiting Toxicity of ^{213}Bi- versus ^{90}Y-labeled CO17-1A Fab′ Fragments in a Human Colonic Cancer Model1. *Cancer Research* **59,** 2635–2643 (1999).

41. Dahle, J., Bruland, Ø. S. & Larsen, R. H. Relative Biologic Effects of Low-Dose-Rate α-Emitting ^{227}Th-Rituximab and β-Emitting ^{90}Y-Tiuexetan-Ibritumomab Versus External Beam X-Radiation. *International Journal of Radiation Oncology*Biology*Physics* **72,** 186–192 (2008).

42. Eychenne, R., Chérel, M., Haddad, F., Guérard, F. & Gestin, J.-F. Overview of the Most Promising Radionuclides for Targeted Alpha Therapy: The "Hopeful Eight". *Pharmaceutics* **13,** 906 (2021).

43. De Kruijff, R. M., Wolterbeek, H. T. & Denkova, A. G. A Critical Review of Alpha Radionuclide Therapy—How to Deal with Recoiling Daughters? *Pharmaceuticals* **8,** 321–336 (2015).

44. Zimmermann, R. Is ^{212}Pb Really Happening? The Post-^{177}Lu/^{225}Ac Blockbuster? *Journal of Nuclear Medicine* (2024).

45. Mausner, L. F., Srivastava, S. G. & Straub, R. F. *In Vivo Generator for Radioimmunotherapy* tech. rep. H000545 (Brookhaven National Laboratory (BNL), Upton, NY (United States), 1988).

46. Edem, P. E., Fonslet, J., Kjær, A., Herth, M. & Severin, G. In Vivo Radionuclide Generators for Diagnostics and Therapy. *Bioinorganic Chemistry and Applications* **2016,** 6148357 (2016).

47. Sanderson, R. *Chemical Bonds and Bonds Energy* (Elsevier, 2012).

48. Pelepenko, L. E., Janini, A. C. P., Gomes, B. P. F. A., de-Jesus-Soares, A. & Marciano, M. A. Effects of Bismuth Exposure on the Human Kidney—A Systematic Review. *Antibiotics* **11,** 1741 (2022).

49. Slikkerveer, A. & de Wolff, F. A. in *Toxicology of Metals, Volume I* (CRC Press, 1996).

50. Center, N. N. D. *Information Extracted from the NuDat Database* 2024.

51. Teze, D. *et al.* Targeted Radionuclide Therapy with Astatine-211: Oxidative Dehalogenation of Astatobenzoate Conjugates. *Sci Rep* **7,** 2579 (2017).

52. Wilbur, D. S. [^{211}At]Astatine-Labeled Compound Stability: Issues with Released [^{211}At] Astatide and Development of Labeling Reagents to Increase Stability. *Current Radiopharmaceuticals* **1,** 144–176 (2008).

53. Suzuki, H., Kannaka, K. & Uehara, T. Approaches to Reducing Normal Tissue Radiation from Radiolabeled Antibodies. *Pharmaceuticals* **17,** 508 (2024).

54. Mirzadeh, S., Kumar, K. & Gansow, O. A. The Chemical Fate of 212Bi-DOTA Formed by β- Decay of ^{212}Pb(DOTA)2-***. *Radiochimica Acta* **60,** 1–10 (1993).

55. Meredith, R. F. *et al.* Safety and Outcome Measures of First-in-Human Intraperitoneal α Radioimmunotherapy With ^{212}Pb-TCMC-Trastuzumab. *American Journal of Clinical Oncology* **41,** 716 (2018).

56. Kokov, K. V. *et al.* ^{212}Pb: Production Approaches and Targeted Therapy Applications. *Pharmaceutics* **14,** 189 (2022).

57. Jaggi, J. S., Seshan, S. V., McDevitt, M. R., LaPerle, K., Sgouros, G. & Scheinberg, D. A. Renal Tubulointerstitial Changes after Internal Irradiation with α-Particle–Emitting Actinium Daughters. *Journal of the American Society of Nephrology* **16,** 2677 (2005).

58. Schwartz, J. *et al.* Renal Uptake of Bismuth-213 and Its Contribution to Kidney Radiation Dose Following Administration of Actinium-225-Labeled Antibody. *Phys. Med. Biol.* **56,** 721 (2011).

59. Bidkar, A. P. *et al.* Treatment of Prostate Cancer with CD46-targeted ^{225}Ac Alpha Particle Radioimmunotherapy. *Clinical Cancer Research,* OF1–OF13 (2023).

60. Banerjee, S. R. *et al.* Preclinical Evaluation of ^{213}Bi- and ^{225}Ac-Labeled Low-Molecular-Weight Compounds for Radiopharmaceutical Therapy of Prostate Cancer. *Journal of Nuclear Medicine* **62,** 980–988 (2021).

61. Tronchin, S., Forster, J., Hickson, K. & Bezak, E. Modeling the Effect of Daughter Migration on Dosimetry Estimates for Unlabeled Actinium-225. *Medical Physics* **51,** 5032–5044 (2024).

62. Satapathy, S., Sharma, A., Sood, A., Maheshwari, P. & Gill, H. J. S. Delayed Nephrotoxicity After ^{225}Ac-PSMA-617 Radioligand Therapy. *Clinical Nuclear Medicine* **47,** e466 (2022).

63. Pelletier, K., Côté, G., Fallah-Rad, N., John, R. & Kitchlu, A. CKD After ^{225}Ac-PSMA617 Therapy in Patients With Metastatic Prostate Cancer. *Kidney International Reports* **6,** 853–856 (2021).

64. Feuerecker, B. *et al.* Clinical Translation of Targeted α-Therapy: An Evolution or a Revolution? *Journal of Nuclear Medicine* **64,** 685–692 (2023).

65. Abou, D. S., Ulmert, D., Doucet, M., Hobbs, R. F., Riddle, R. C. & Thorek, D. L. J. Whole-Body and Microenvironmental Localization of Radium-223 in Naïve and Mouse Models of Prostate Cancer Metastasis. *JNCI: Journal of the National Cancer Institute* **108,** djv380 (2016).

66. Benabdallah, N. *et al.* Beyond Average: α-Particle Distribution and Dose Heterogeneity in Bone Metastatic Prostate Cancer. *Journal of Nuclear Medicine* (2023).

67. Carrasquillo, J. A. *et al.* Phase I Pharmacokinetic and Biodistribution Study with Escalating Doses of ^{223}Ra-dichloride in Men with Castration-Resistant Metastatic Prostate Cancer. *Eur J Nucl Med Mol Imaging* **40,** 1384–1393 (2013).

68. Henriksen, G., Fisher, D. R., Roeske, J. C., Bruland, Ø. S. & Larsen, R. H. Targeting of Osseous Sites with α-Emitting ^{223}Ra: Comparison with the β-Emitter 89Sr in Mice. *Journal of Nuclear Medicine* **44,** 252–259 (2003).

69. Jacene, H., Gomella, L., Yu, E. Y. & Rohren, E. M. Hematologic Toxicity From Radium-223 Therapy for Bone Metastases in Castration-Resistant Prostate Cancer: Risk Factors and Practical Considerations. *Clinical Genitourinary Cancer* **16,** e919–e926 (2018).

70. Frantellizzi, V. *et al.* Targeted Alpha Therapy with Thorium-227. *Cancer Biotherapy and Radiopharmaceuticals* **35,** 437–445 (2020).

71. Washiyama, K. *et al.* ^{227}Th-EDTMP: A Potential Therapeutic Agent for Bone Metastasis. *Nuclear Medicine and Biology* **31,** 901–908 (2004).

72. Favaretto, C. *et al.* Terbium-149 Production: A Focus on Yield and Quality Improvement towards Preclinical Application. *Sci Rep* **14,** 3284 (2024).

73. Bayer. *Xofigo Administration Guide* tech. rep. (2020).

74. Strigari, L. *et al.* The Evidence Base for the Use of Internal Dosimetry in the Clinical Practice of Molecular Radiotherapy. *Eur J Nucl Med Mol Imaging* **41,** 1976–1988 (2014).

75. Dieudonné, A. *et al.* Dosimetry for Targeted Radionuclide Therapy in Routine Clinical Practice: Experts Advice vs. Clinical Evidence. *Eur J Nucl Med Mol Imaging* **51,** 947–950 (2024).

76. O'Donoghue, J., Zanzonico, P., Humm, J. & Kesner, A. Dosimetry in Radiopharmaceutical Therapy. *Journal of Nuclear Medicine* **63,** 1467–1474 (2022).

77. Levillain, H. *et al.* International Recommendations for Personalised Selective Internal Radiation Therapy of Primary and Metastatic Liver Diseases with Yttrium-90 Resin Microspheres. *Eur J Nucl Med Mol Imaging* **48,** 1570–1584 (2021).

78. Bouchareb, Y. *et al.* Technological Advances in SPECT and SPECT/CT Imaging. *Diagnostics* **14,** 1431 (2024).

79. Vastenhouw, B. & Beekman, F. Submillimeter Total-Body Murine Imaging with U-SPECT-I. *Journal of Nuclear Medicine* **48,** 487–493 (2007).

80. Moses, W. W. Fundamental Limits of Spatial Resolution in PET. *Nuclear Instruments and Methods in Physics Research Section A: Accelerators, Spectrometers, Detectors and Associated Equipment* **648,** S236–S240 (2011).

81. Seo, Y. Quantitative Imaging of Alpha-Emitting Therapeutic Radiopharmaceuticals. *Nucl Med Mol Imaging* **53,** 182–188 (2019).

82. Hindorf, C., Chittenden, S., Aksnes, A.-K., Parker, C. & Flux, G. D. Quantitative Imaging of ^{223}Ra-chloride (Alpharadin) for Targeted Alpha-Emitting Radionuclide Therapy of Bone Metastases. *Nucl Med Commun* **33,** 726–732 (2012).

83. Pacilio, M. *et al.* The Italian Multicentre Dosimetric Study for Lesion Dosimetry in ^{223}Ra Therapy of Bone Metastases: Calibration Protocol of Gamma Cameras and Patient Eligibility Criteria. *Physica Medica* **32,** 1731–1737 (2016).

84. Vatsa, R. *et al.* 225Ac-PSMA-617 Radioligand Posttherapy Imaging in Metastatic Castrate-Resistant Prostate Cancer Patient Using 3 Photopeaks. *Clinical Nuclear Medicine* **45,** 437 (2020).

85. Gosewisch, A. *et al.* Image-Based Dosimetry for ^{225}Ac-PSMA-I&T Therapy Using Quantitative SPECT. *Eur J Nucl Med Mol Imaging* **48,** 1260–1261 (2021).

86. Usmani, S., Rasheed, R., Al kandari, F., Marafi, F. & Naqvi, S. A. R. ^{225}Ac Prostate-Specific Membrane Antigen Posttherapy α Imaging: Comparing 2 and 3 Photopeaks. *Clinical Nuclear Medicine* **44,** 401 (2019).

87. Meredith, R. F. *et al.* Pharmacokinetics and Imaging of ^{212}Pb-TCMC-trastuzumab after Intraperitoneal Administration in Ovarian Cancer Patients. *Cancer Biother Radiopharm* **29,** 12–17 (2014).

88. Yang, C. *et al.* Quantitative Multi-Isotope Imaging of Alpha-Emitter Radiopharmaceutical Therapy with the Alpha-SPECT-Mini System. *Journal of Nuclear Medicine* **65,** 242352–242352 (2024).

89. Encarnação, P. M., Correia, P. M., Caravaca, J., Veloso, J. F. & Seo, Y. *In-Vivo Imaging of Therapeutic Radiopharmaceuticals with a Developmental CZT-based SPECT* in *2024 IEEE Nuclear Science Symposium (NSS), Medical Imaging Conference (MIC) and Room Temperature Semiconductor Detector Conference (RTSD)* (2024), 1–2.

90. Das, B., Mehrdel, B., Seo, Y., Goodman, D., Streicher, M. & Caravaca, J. *Compton Imaging of Therapeutic Radionuclides with a CZT Camera* in *2024 IEEE Nuclear Science Symposium (NSS), Medical Imaging Conference (MIC) and Room Temperature Semiconductor Detector Conference (RTSD)* (2024), 1–1.

91. Caravaca, J. *et al.* A Technique to Quantify Very Low Activities in Regions of Interest with a Collimatorless Detector. *IEEE Transactions on Medical Imaging,* 1–1 (2024).

92. Frame, E. *et al.* Coded Aperture and Compton Imaging for the Development of ^{225}Ac-based Radiopharmaceuticals. *Medical Physics* **n/a** (2023).

93. Fanchon, L. M. *et al.* Feasibility of in Situ, High-Resolution Correlation of Tracer Uptake with Histopathology by Quantitative Autoradiography of Biopsy Specimens Obtained under 18F-FDG PET/CT Guidance. *J Nucl Med* **56,** 538–544 (2015).

94. Siegel, J. A. *et al.* MIRD Pamphlet No. 16: Techniques for Quantitative Radiopharmaceutical Biodistribution Data Acquisition and Analysis for Use in Human Radiation Dose Estimates. *J Nucl Med* **40,** 37S–61S (1999).

95. Hidex. *Hidex Automatic Gamma Counter Specifications* tech. rep. (Oy, Mustionkatu 2, FIN-20750 Turku, Finland, 2015).

96. Kletting, P. *et al.* Molecular Radiotherapy: The NUKFIT Software for Calculating the Time-Integrated Activity Coefficient. *Medical Physics* **40,** 102504 (2013).

97. Kratochwil, C. *Treating Prostate Cancer with ^{225}Ac-PSMA-617 plus ^{177}Lu-PSMA-617 "Cocktail" Therapy* Cape Town, South Africa, 2023.

98. Bateman, H. The Solution of a System of Differential Equations Occurring in the Theory of Radioactive Transformations. *Proceedings of the Cambridge Philosophical Society* **15,** 423–427 (1910).

99. Krane, K. S. *Introductory Nuclear Physics* (John Wiley & Sons, Inc., 1988).

100. Castillo Seoane, D. *et al.* Gamma Counting Protocols for the Accurate Quantification of ^{225}Ac and ^{213}Bi without the Need for a Secular Equilibrium between Parent and Gamma-Emitting Daughter. *EJNMMI Radiopharmacy and Chemistry* **7,** 28 (2022).

101. LabLogic. *Spec-RAM CZT Benchtop Gamma Spectrometer*

102. Bandstra, M. S. *et al.* RadMAP: The Radiological Multi-sensor Analysis Platform. *Nuclear Instruments and Methods in Physics Research Section A: Accelerators, Spectrometers, Detectors and Associated Equipment* **840,** 59–68 (2016).

103. Tronchin, S., Forster, J. C., Hickson, K. & Bezak, E. Dosimetry in Targeted Alpha Therapy. A Systematic Review: Current Findings and What Is Needed. *Phys. Med. Biol.* **67,** 09TR01 (2022).

104. Lassmann, M. & Nosske, D. Dosimetry of ^{223}Ra-chloride: Dose to Normal Organs and Tissues. *Eur J Nucl Med Mol Imaging* **40,** 207–212 (2013).

105. O'Donoghue, J. A., Baidoo, N., Deland, D., Welt, S., Divgi, C. R. & Sgouros, G. Hematologic Toxicity in Radioimmunotherapy: Dose-Response Relationships for I-131 Labeled Antibody Therapy. *Cancer Biotherapy and Radiopharmaceuticals* **17,** 435–443 (2002).

106. Sciuto, R. *et al.* The Role of Dosimetry and Biological Effects in Metastatic Castration–Resistant Prostate Cancer (mCRPC) Patients Treated with ^{223}Ra: First in Human Study. *Journal of Experimental & Clinical Cancer Research : CR* **40,** 281 (2021).

107. Hobbs, R. F., Song, H., Huso, D. L., Sundel, M. H. & Sgouros, G. A Nephron-Based Model of the Kidneys for Macro-to-Micro α-Particle Dosimetry. *Phys. Med. Biol.* **57,** 4403 (2012).

108. Marusyk, A. & Polyak, K. Tumor Heterogeneity: Causes and Consequences. *Biochimica et Biophysica Acta (BBA) - Reviews on Cancer* **1805,** 105–117 (2010).

109. Mirzayans, R. & Murray, D. What Are the Reasons for Continuing Failures in Cancer Therapy? Are Misleading/Inappropriate Preclinical Assays to Be Blamed? Might Some Modern Therapies Cause More Harm than Benefit? *International Journal of Molecular Sciences* **23,** 13217 (2022).

110. Bastiaannet, R. *Generalized Alpha Particle Microdosimetry: Insights at the Cellular Level* Los Angeles, 2024.

111. Hofmann, W. *et al.* Internal Microdosimetry of Alpha-Emitting Radionuclides. *Radiat Environ Biophys* **59,** 29–62 (2020).

112. Spoormans, K., Crabbé, M., Struelens, L., De Saint-Hubert, M. & Koole, M. A Review on Tumor Control Probability (TCP) and Preclinical Dosimetry in Targeted Radionuclide Therapy (TRT). *Pharmaceutics* **14** (2022).

113. Miller, B. W. Radiation Imagers for Quantitative, Single-particle Digital Autoradiography of Alpha- and Beta-particle Emitters. *Seminars in Nuclear Medicine. Instrumentation* **48,** 367–376 (2018).

114. Solon, E. G., Schweitzer, A., Stoeckli, M. & Prideaux, B. Autoradiography, MALDI-MS, and SIMS-MS Imaging in Pharmaceutical Discovery and Development. *AAPS J* **12,** 11–26 (2010).

115. Örbom, A., Miller, B. W. & Bäck, T. in *Handbook of Nuclear Medicine and Molecular Imaging for Physicists* (CRC Press, 2022).

116. Miller, B. W., Bowen, J. M. & Morrison, E. C. High-Resolution, Single-Particle Digital Autoradiography of Actinide Sources Using Microcapillary Array Collimators and the iQID Camera. *Applied Radiation and Isotopes* **166,** 109348 (2020).

117. Jakubek, J., Cejnarova, A., Holy, T., Pospisil, S., Uher, J. & Vykydal, Z. Pixel Detectors for Imaging with Heavy Charged Particles. *Nuclear Instruments and Methods in Physics Research Section A: Accelerators, Spectrometers, Detectors and Associated Equipment. Radiation Imaging Detectors 2007* **591,** 155–158 (2008).

118. Yamamoto, S. *et al.* Development of an Ultrahigh Resolution Real Time Alpha Particle Imaging System for Observing the Trajectories of Alpha Particles in a Scintillator. *Sci Rep* **13,** 4955 (2023).

119. Janesick, J. R. *Scientific Charge-Coupled Devices* (SPIE, 1000 20th Street, Bellingham, WA 98227-0010 USA, 2001).

120. Kuk, K. *et al.* Projection Imaging with Ultracold Neutrons. *Nuclear Instruments and Methods in Physics Research Section A: Accelerators, Spectrometers, Detectors and Associated Equipment* **1003,** 165306 (2021).

121. Broisat, A. *et al.* Mapping of Brain Tissue Hematocrit in Glioma and Acute Stroke Using a Dual Autoradiography Approach. *Sci Rep* **8,** 9878 (2018).

122. Johnston, R. F., Pickett, S. C. & Barker, D. L. Double-Label Image Analysis Using Storage Phosphor Technology. *Methods* **3,** 128–134 (1991).

123. Mellhammar, E., Dahlbom, M., Vilhelmsson-Timmermand, O. & Strand, S.-E. Tumor Control Probability and Small-Scale Monte Carlo Dosimetry: Effects of Heterogenous Intratumoral Activity Distribution in Radiopharmaceutical Therapy. *Journal of Nuclear Medicine* (2023).

124. Örbom, A. *Preclinical Molecular Imaging Using Multi-Isotope Digital Autoradiography: Techniques and Applications* PhD thesis (Department of Medical Radiation Physics, Lund University, Lund, 2013).

125. Al Darwish, R., Marcu, L. & Bezak, E. Overview of Current Applications of the Timepix Detector in Spectroscopy, Radiation and Medical Physics. *Applied Spectroscopy Reviews* **55,** 243–261 (2020).

126. AL Darwish, R., Staudacher, A. H., Bezak, E. & Brown, M. P. Autoradiography Imaging in Targeted Alpha Therapy with Timepix Detector. *Computational and Mathematical Methods in Medicine* **2015,** e612580 (2015).

127. Vargas, C. S., Struelens, L., D'Huyvetter, M., Caveliers, V. & Covens, P. A Realistic Multiregion Mouse Kidney Dosimetry Model to Support the Preclinical Evaluation of Potential Nephrotoxicity of Radiopharmaceutical Therapy. *Journal of Nuclear Medicine* **64,** 493–499 (2023).

128. Miller, B. W., Gregory, S. J., Fuller, E. S., Barrett, H. H., Bradford Barber, H. & Furenlid, L. R. The iQID Camera: An Ionizing-Radiation Quantum Imaging Detector. *Nuclear Instruments and Methods in Physics Research Section A: Accelerators, Spectrometers, Detectors and Associated Equipment* **767,** 146–152 (2014).

129. Rinne, S. S. *et al.* ^{177}Lu/225Ac Pretargeted Dual-Isotope Therapy for Treatment of GPA33(+) Colorectal Cancer. *Journal of Nuclear Medicine* **65,** 241498–241498 (2024).

130. Bäck, T. & Jacobsson, L. The α-Camera: A Quantitative Digital Autoradiography Technique Using a Charge-Coupled Device for Ex Vivo High-Resolution Bioimaging of α-Particles. *J Nucl Med* **51,** 1616–1623 (2010).

131. Timmermand, O. V., Nilsson, J., Strand, S.-E. & Elgqvist, J. High Resolution Digital Autoradiographic and Dosimetric Analysis of Heterogeneous Radioactivity Distribution in Xenografted Prostate Tumors: Digital Autoradiographic and Dosimetric Analysis of Prostate Tumors. *Med. Phys.* **43,** 6632–6643 (2016).

132. Vaziri, B., Wu, H., Dhawan, A. P., Du, P., Howell, R. W. & Committee, I. c. w. t. S. M. MIRD Pamphlet No. 25: MIRDcell V2.0 Software Tool for Dosimetric Analysis of Biologic Response of Multicellular Populations. *Journal of Nuclear Medicine* **55,** 1557–1564 (2014).

133. Dorenbos, P. Light Output and Energy Resolution of Ce3+-Doped Scintillators. *Nuclear Instruments and Methods in Physics Research Section A: Accelerators, Spectrometers, Detectors and Associated Equipment* **486,** 208–213 (2002).

134. Miller, B. W., Frost, S. H. L., Frayo, S. L., Kenoyer, A. L., Santos, E. & Jones, J. C. Quantitative Single-Particle Digital Autoradiography with α-Particle Emitters for Targeted Radionuclide Therapy Using the iQID Camera. *Medical Physics* **42,** 12 (2015).

135. Miller, B. W., Barber, H. B., Furenlid, L. R., Moore, S. K. & Barrett, H. H. *Progress of BazookaSPECT* in *Penetrating Radiation Systems and Applications X* **7450** (SPIE, 2009), 69–83.

136. Van der Walt, S. *et al.* Scikit-Image: Image Processing in Python. *PeerJ* **2,** e453 (2014).

137. Bradski, G. The OpenCV Library. *Dr. Dobb's Journal of Software Tools* (2000).

138. Lichtner, G. *PyStackReg* 2021.

139. Schindelin, J. *et al.* Fiji: An Open-Source Platform for Biological-Image Analysis. *Nat Methods* **9,** 676–682 (2012).

140. Kikinis, R., Pieper, S. D. & Vosburgh, K. G. in *Intraoperative Imaging and Image-Guided Therapy* (ed Jolesz, F. A.) 277–289 (Springer, New York, NY, 2014).

141. Jan, S. *et al.* GATE: A Simulation Toolkit for PET and SPECT. *Phys. Med. Biol.* **49,** 4543–4561 (2004).

142. Chetty, I. J. *et al.* Reporting and Analyzing Statistical Uncertainties in Monte Carlo–Based Treatment Planning. *International Journal of Radiation Oncology, Biology, Physics* **65,** 1249–1259 (2006).

143. Azure, M. T., Archer, R. D., Sastry, K. S. R., Rao, D. V. & Howell, R. W. Biological Effect of Lead-212 Localized in the Nucleus of Mammalian Cells: Role of Recoil Energy in the Radiotoxicity of Internal Alpha-Particle Emitters. *Radiat Res* **140,** 276–283 (1994).

144. Low, D. A., Harms, W. B., Mutic, S. & Purdy, J. A. A Technique for the Quantitative Evaluation of Dose Distributions. *Med Phys* **25,** 656–661 (1998).

145. Miften, M. *et al.* Tolerance Limits and Methodologies for IMRT Measurement-Based Verification QA: Recommendations of AAPM Task Group No. 218. *Medical Physics* **45,** e53–e83 (2018).

146. Otsu, N. A Threshold Selection Method from Gray-Level Histograms. *IEEE Transactions on Systems, Man, and Cybernetics* **9,** 62–66 (1979).

147. National Toxicology Program. *Kidney - Nonneoplastic Lesion Atlas*

148. Bogovic, J. A., Hanslovsky, P., Wong, A. & Saalfeld, S. *Robust Registration of Calcium Images by Learned Contrast Synthesis* in *2016 IEEE 13th International Symposium on Biomedical Imaging (ISBI)* (2016), 1123–1126.

149. Chen, Y. *et al.* Durable Donor Engraftment after Radioimmunotherapy Using α-Emitter Astatine-211–Labeled Anti-CD45 Antibody for Conditioning in Allogeneic Hematopoietic Cell Transplantation. *Blood* **119,** 1130–1138 (2012).

150. Ito, D., Frantz, A. M. & Modiano, J. F. Canine Lymphoma as a Comparative Model for Human Non-Hodgkin Lymphoma: Recent Progress and Applications. *Veterinary Immunology and Immunopathology. Special Issue: Dual Purpose with Dual Benefit Research Models in Veterinary and Biomedical Research* **159,** 192–201 (2014).

151. Villarnovo, D., McCleary-Wheeler, A. L. & Richards, K. L. Barking up the Right Tree: Advancing Our Understanding and Treatment of Lymphoma with a Spontaneous Canine Model. *Current Opinion in Hematology* **24,** 359 (2017).

152. Berger, M., Coursey, J., Zucker, M., Chang, J., Seltzer, S. & Bergstrom, P. *Stopping-Power & Range Tables for Electrons, Protons, and Helium Ions* Text. 2009.

153. Bäck, T., Chouin, N., Lindegren, S., Jensen, H., Albertsson, P. & Palm, S. Image-Based Small-Scale 3D-dosimetry in Targeted Alpha Therapy Using Voxel Dose-Point Kernels and Alpha Camera Imaging of Serial Tissue Sections. *Journal of Nuclear Medicine* **55,** 50–50 (2014).

154. Hobbs, R. F. *et al.* Application of Small-Scale (Sub-Organ and Cellular Level) Alpha-Particle Specific Dosimetry Model in Tumors and Kidneys in a Pre-Clinical Model of Metastatic Prostate Cancer Using ^{211}At-YC-I-27, a PSMA-Targeting Ligand for Metastatic Prostate Cancer. *Brachytherapy* **15,** S196 (2016).

155. Graves, S. A., Flynn, R. T. & Hyer, D. E. Dose Point Kernels for 2,174 Radionuclides. *Med Phys* **46,** 5284–5293 (2019).

156. Khazaee Moghadam, M., Kamali Asl, A., Geramifar, P. & Zaidi, H. Evaluating the Application of Tissue-Specific Dose Kernels Instead of Water Dose Kernels in Internal Dosimetry: A Monte Carlo Study. *Cancer Biother Radiopharm* **31,** 367–379 (2016).

157. Katugampola, S., Wang, J., Prasad, A., Sofou, S. & Howell, R. W. Predicting Response of Micrometastases with MIRDcell V3: Proof of Principle with ^{225}Ac-DOTA Encapsulating Liposomes That Produce Different Activity Distributions in Tumor Spheroids. *Eur J Nucl Med Mol Imaging* (2022).

158. Stewart, R. D. *et al.* Rapid MCNP Simulation of DNA Double Strand Break (DSB) Relative Biological Effectiveness (RBE) for Photons, Neutrons, and Light Ions. *Phys. Med. Biol.* **60,** 8249–8274 (2015).

159. Stewart, R. D., Carlson, D. J., Butkus, M. P., Hawkins, R., Friedrich, T. & Scholz, M. A Comparison of Mechanism-inspired Models for Particle Relative Biological Effectiveness (RBE). *Med. Phys.* **45** (2018).

160. Su, Y. *et al.* Targeting CD46 for Both Adenocarcinoma and Neuroendocrine Prostate Cancer. *JCI Insight* **3,** e121497, 121497 (2018).

161. Bobba, K. N. *et al.* Development of CD46 Targeted Alpha Theranostics in Prostate Cancer Using ^{134}Ce/^{225}Ac-Macropa-PEG4-YS5. *Theranostics* **14,** 1344–1360 (2024).

162. Lawhn-Heath, C. *et al.* Dosimetry in Radionuclide Therapy: The Clinical Role of Measuring Radiation Dose. *The Lancet Oncology* **23,** e75–e87 (2022).

163. Rathke, H. *et al.* Deescalated ^{225}Ac-PSMA-617 Versus ^{177}Lu/^{225}Ac-PSMA-617 Cocktail Therapy: A Single-Center Retrospective Analysis of 233 Patients. *Journal of Nuclear Medicine* **65,** 1057–1063 (2024).

164. Caravaca, J., Huh, Y., Gullberg, G. T. & Seo, Y. Compton and Proximity Imaging of ^{225}Ac in Vivo with a CZT Gamma Camera: A Proof of Principle with Simulations. *IEEE Transactions on Radiation and Plasma Medical Sciences,* 1–1 (2022).

165. Delker, A. *et al.* Biodistribution and Dosimetry for Combined [^{177}Lu]Lu-PSMA-I&T/ [^{225}Ac]Ac-PSMA-I&T Therapy Using Multi-Isotope Quantitative SPECT Imaging. *Eur J Nucl Med Mol Imaging* **50,** 1280–1290 (2023).

166. Siegel, R. L., Miller, K. D. & Jemal, A. Cancer Statistics, 2020. *CA: A Cancer Journal for Clinicians* **70,** 7–30 (2020).

167. Litwin, M. S. & Tan, H.-J. The Diagnosis and Treatment of Prostate Cancer: A Review. *JAMA* **317,** 2532–2542 (2017).

168. Van den Broeck, T. *et al.* Prognostic Value of Biochemical Recurrence Following Treatment with Curative Intent for Prostate Cancer: A Systematic Review. *European Urology* **75,** 967–987 (2019).

169. Henríquez, I. *et al.* Current and Emerging Therapies for Metastatic Castration-Resistant Prostate Cancer (mCRPC). *Biomedicines* **9,** 1247 (2021).

170. Thurin, N. H. *et al.* Epidemiology of Metastatic Castration-Resistant Prostate Cancer: A First Estimate of Incidence and Prevalence Using the French Nationwide Healthcare Database. *Cancer Epidemiology* **69,** 101833 (2020).

171. Wallace, K., Landsteiner, A., Bunner, S., Engel-Nitz, N. & Luckenbaugh, A. Epidemiology and Mortality of Metastatic Castration-Resistant Prostate Cancer (mCRPC) in a Managed Care Population in the United States. *JCO* **38,** e13592–e13592 (2020).

172. Calais, J. & Czernin, J. PSMA Expression Assessed by PET Imaging Is a Required Biomarker for Selecting Patients for Any PSMA-Targeted Therapy. *Journal of Nuclear Medicine* **62,** 1489–1491 (2021).

173. Sun, M., Niaz, M. O., Nelson, A., Skafida, M. & Niaz, M. J. Review of ^{177}Lu-PSMA-617 in Patients With Metastatic Castration-Resistant Prostate Cancer. *Cureus* **12,** e8921 (2020).

174. Kauffman, N., Morrison, J., O'Brien, K., Fan, J. & Zinn, K. R. Intra-Arterial Delivery of Radiopharmaceuticals in Oncology: Current Trends and the Future of Alpha-Particle Therapeutics. *Pharmaceutics* **15,** 1138 (2023).

175. Murty, R. C. Effective Atomic Numbers of Heterogeneous Materials. *Nature* **207,** 398–399 (1965).

176. Pengra, D. *Counting Statistics of Random Events: A Tutorial* tech. rep. (University of Washington, 2006).